Cold, Controlled, Ion-Molecule Reactions

by

James Greenberg

B.S., University of Arizona, 2014

M.S., University of Colorado Boulder, 2017

A thesis submitted to the

Faculty of the Graduate School of the

University of Colorado in partial fulfillment

of the requirements for the degree of

Doctor of Philosophy

Department of Physics

2020

This thesis entitled:
Cold, Controlled, Ion-Molecule Reactions
written by James Greenberg
has been approved for the Department of Physics

_____

Prof. Heather Lewandowski

_____

Prof. Eric Cornell

Date _____

The final copy of this thesis has been examined by the signatories, and we find that both the content and the form meet acceptable presentation standards of scholarly work in the above mentioned discipline.

Greenberg, James (Ph.D., Physics)

Cold, Controlled, Ion-Molecule Reactions

Thesis directed by Prof. Heather Lewandowski

Coulomb crystals in linear Paul ion traps (LIT) have proven to be a fruitful environment to study gas-phase ion chemistry and spectroscopy of molecular ions. Recently, the capabilities of such apparatuses have been extended by (radially) coupling them to a time-of-flight mass spectrometer (TOFMS). The TOFMS enables simultaneous detection of all constituent masses in the ion trap. Thus, one can follow reactions both by the depletion of reactants, as well as growth of product channels, allowing for a more complete description of reaction kinetics. We have designed, built, and characterized a combined LIT-TOFMS apparatus for the purpose of studying cation-molecule reactions. This thesis provides an overview of ion trapping theory and basic reaction kinetics/dynamics. A detailed description of the apparatus and four ion-molecule reactions are also discussed. The first two ion-molecule reactions covered demonstrate quantum control over laser-cooled Ca^+ in the reactions $Ca^+ + NO$ and $Ca^+ + O_2$. The third ion-molecule reaction elucidates the isomer specific reaction mechanisms observed in the reaction ${C_2H_2}^+ + C_3H_4$. The last reaction covered is $CCl^+ + C_2H_2$, which reveals new pathways to ionic products important in chemistry of the interstellar medium. The thesis concludes with future prospects to extend the capabilities of the apparatus in pursuit of colder and more controlled ion-molecule reaction studies.

Dedication

To future graduate students who may read this. Don't panic.

Acknowledgements

It may take a village to raise a child, but it takes an entire institute, and then some, to raise an experiment. None of this work would not have been possible without the resources, expertise, dedication, and amazing people at JILA. First and foremost, thanks to my advisor, Heather, for being a great scientist, leader, and friend. Thanks to the Lewandowski group: Philipp, Katherine, Ben, Olivia, Kyle, Jason, John, Yomay, Cam, and Maya. Thanks to the amazing JILA machine shop who built the ion trap and many other parts: Hans, Kyle, Kim, Todd, and Calvin. Thanks to the JILA electronics shop who helped make the LIT-TOFMS electronics a reality: Terry and Karl. Thanks to the JILA administrative staff that keep the institute running, especially Agnieszka and Krista, for making my life so much easier. I also want to acknowledge our theory collaborators who gave so much of their effort to the research as well: John, James, and Lam. Thanks to Mathias and Barney for their advice and ideas. Thanks to MIT Tim for putting up with me in the lab for an entire week. Also thanks to the visiting professors who I got to know briefly: Bas, Tim, and Gary. An enormous number of my friends and family also were critical to my success in grad school. Thanks and much love to Greg, Bonnie, Mom, and Dad; my aunts, Mary, Kathy, and Susan along with my uncle George. I couldn't have even made it to Boulder without my best friend, Christian. As if the thesis wasn't enough, Kevin and I conquered some mountains. Summer forever, Amy! Thanks to my girlfriend Lotto for being so rad and supportive. So grateful for my fuzzy little Mugen :3 And cheers to all my other friends I've made in Boulder: Doug, Nathan, Quynh, Chris, Brendan, Kyle, Adam, Jeff, and all the members of STMP that I definitely don't have room to name. You all mean so much to me.

Contents

Chapter

1 Introduction **1**

1.1 Motivation 1

1.2 Cold ion-molecule collision experiments 3

1.3 Outline of this thesis 6

2 Ion trapping and ion-molecule reaction theory **7**

2.1 Ion trapping 7

2.1.1 Pseudo-potential approximation 10

2.1.2 Trapping stability 11

2.1.3 Ion kinetic energy 12

2.2 Laser cooling of Ca^+ 13

2.3 Coulomb crystals and sympathetic cooling 16

2.4 Time-of-flight mass spectrometry 19

2.5 Bimolecular reaction kinetics and dynamics 21

2.5.1 Kinetics 21

2.5.2 Dynamics 23

3 Experimental Apparatus **26**

3.1 Vacuum chamber 26

3.2 Linear ion trap – time-of-flight mass spectrometer (LIT-TOFMS) 27

3.3 Electronics . . . 32
3.3.1 LC tank circuit . . . 34
3.3.2 Quench circuit . . . 35
3.3.3 HV switches . . . 36
3.4 TOFMS performance . . . 37
3.5 Ion number calibration . . . 39
3.6 Calcium state population calibration . . . 41
3.7 Gas Handling . . . 43
3.7.1 Pulsed leak valve . . . 43
3.7.2 PZT valve . . . 47

4 Quantum controlled reaction with Ca^+ 49

4.1 $Ca^+ + NO$ . . . 49
4.1.1 Introduction . . . 49
4.1.2 $Ca^+ + NO$ reactions . . . 51
4.1.3 Ion trap apparatus . . . 52
4.1.4 Reaction Rate Measurements . . . 54
4.1.5 Discussion . . . 57
4.1.6 Conclusion . . . 59
4.2 $Ca^+ + O_2$ . . . 59
4.2.1 Introduction . . . 60
4.2.2 $Ca^+ + O_2$ Reactions . . . 61
4.2.3 Ion Trap Apparatus . . . 64
4.2.4 Reaction Rate Constant Measurements . . . 66
4.2.5 Discussion . . . 68
4.2.6 Summary . . . 72
4.2.7 $Ca^+ + H_2O$ . . . 73

4.2.8 Addendum 74

5 Isomer specific chemistry and isotopologue reactions of $C_2H_2^+ + C_3H_4$ **76**

5.1 Introduction 76

5.2 Methods 78

5.3 Propyne – HC_3H_3 82

5.3.1 Experimental results 82

5.3.2 Computational results 88

5.3.3 Discussion 90

5.4 Allene – $H_2C_3H_2$ 93

5.4.1 Experimental Results 93

5.4.2 Computational Results 97

5.4.3 Discussion 99

5.5 Summary and outlook 100

6 Translationally cold trapped CCl^+ reactions with acetylene (C_2H_2) **103**

6.1 Introduction 103

6.2 Experimental Methods 105

6.3 Computational Methods 107

6.4 Results and Discussion 108

6.4.1 $CCl^+ + C_2H_2$ reaction measurements 108

6.4.2 Modeling the $CCl^+ + C_2H_2$ reaction 111

6.5 Conclusions 113

6.6 Supplementary information 114

7 Conclusion **125**

7.1 Summary 125

7.2 Outlook 126

Bibliography **128**

Appendix

A Electronics circuit diagrams **144**

A.1 Ion trap driver . . . 144

A.2 HV switches and quench boards . . . 145

A.3 DC shim box . . . 147

A.4 RF secular excitation . . . 149

B Labview control and automation **151**

B.1 Automation . . . 151

B.2 Labview control code . . . 152

B.2.1 Producer consumer architecture . . . 153

B.2.2 Code hierarchy . . . 154

B.2.3 How to add a step . . . 157

B.2.4 How to add a module . . . 157

C MATLAB analysis code **159**

C.1 OBE global fit and model . . . 159

C.2 Reaction model fits . . . 165

C.3 TOFMS integrator . . . 169

C.4 Image fitting code . . . 172

Tables

Table

1.1 List of many cation-molecule reactions studied in linear Paul ion traps. 300K should be understood as room temperature. Reactions studied in this thesis are the first four entries. 5

3.1 Typical trapping parameters and trap geometry specifics. Also included are some calculated values (not measured) for $^{40}Ca^{+}$ using the typical trap parameters and the equations found in Ch. 2. 28

3.2 Variables used to calibrate OBE fit parameters with typical trap parameters in Tab. 3.1 43

4.1 Table of results for the two independent determinations of reaction rate constants and branching ratios. The listed uncertainties represent the statistical uncertainty. . 59

4.2 Measured reaction rate constants for pairs of Ca^{+} excited state populations shown in Fig. 4.9. The fractional populations in the $^{2}P_{1/2}$-state (f_P) and $^{2}D_{3/2}$-state (f_D) are shown with the corresponding measured effective rate constant (k_{eff}). The data point numbers correspond to measurements shown in Fig. 4.9. 68

4.3 The resulting rate constants k_P (k_D) for the three quantum states of Ca^{+}. Uncertainties are from the 90% confidence interval for the fit parameters, k_P (k_D) 68

4.4 The resulting reaction rates for the three quantum states of Ca^{+}. Uncertainties are from the 90% confidence interval for the fit parameters. 73

5.1 Reaction rate constants for all measured isotopologue reactions. All rate constants determined by fit of the loss of charged reactants. Uncertainties are derived from the 90% confidence interval of the fit and do not account for possible inaccuracies in the neutral concentration measurement. 85

5.2 Branching ratios for the reaction $C_2H_2^+ + HC_3H_3 \longrightarrow C_5H_5^+ + H$ and its isotopologues that led to $C_5H_xD_y^+$ $(x + y = 5)$. Numbers are the branching ratios (in %) for each mass channel as determined by the fit of the model. Uncertainties are the 90% confidence interval of the branching ratio fit. Blank spaces indicate the mass channel was either not populated or not statistically different from zero at the 10% significance level. 86

5.3 Branching ratios for the reaction $C_2H_2^+ + HC_3H_3 \longrightarrow C_3H_3^+ + C_2H_3$ and its isotopologues that led to $C_3H_xD_y^+$ $(x + y = 3)$. Numbers are the branching ratios (in %) for each mass channel as determined by the fit of the model. Uncertainties are the 90% confidence interval of the branching ratio fit. Blank spaces indicate the mass channel was either not populated or not statistically different from zero at the 10% significance level. 87

5.4 Estimated branching ratios for the reaction $C_3H_4^+ + HC_3H_3 \longrightarrow$ products and its selected isotopologues. Numbers are the branching ratios (in %) for each mass channel, as determined by the fit of the truncated model. Uncertainties are the 90% confidence interval of the branching ratio fit. Blank entries indicate the mass channel was not statistically different from zero at the 10% significance level. Detected mass-to-charge ratios that could not be assigned a unique chemical formula have been omitted. 88

5.5 Reaction rate constants for all measured isotopologue reactions. All rate constants determined by fit of the loss of charged reactants. Uncertainties are derived from the 90% confidence interval of the fit and do not account for possible inaccuracies in the neutral concentration measurement. 96

5.6 Branching ratios for the reaction $C_2H_2^+ + H_2C_3H_3 \longrightarrow C_3H_3^+ + C_2H_3$ and its isotopologues. Numbers are the branching ratios (in%) for each mass channel as determined by the fit of the model. Uncertainties are the 90% confidence interval of the branching ratio fit. Blank spaces indicate the mass channel was not statistically different from zero at the 10% significance level. 96

5.7 Selected isotopologue data for $C_6H_5^+$ and $C_6H_7^+$ products from allene. Numbers are the branching ratios (%) for each mass channel as determined by the fit of the truncated model. Uncertainties are the 90% confidence interval of the branching ratio fit. Blank spaces indicate the mass channel was not statistically different from zero at the 10% significance level. 97

6.1 Results from the fits to the pseudo-first order reaction rate models for the formation of intermediate and secondary products from the reaction of $CCl^+ + C_2H_2$. Included are the rate constants for the single pressure measurement of $C_2H_2 \approx 5(1) \times 10^6\,cm^3$. 110

6.2 Results from the fits to the pseudo-first order reaction rate models for the formation of intermediate and secondary products from the reaction of CCl^+ with C_2H_2 (from Table I in main text) and C_2D_2. Included are the rate constants for the single pressure measurement of $C_2H_2 \approx 5(1) \times 10^6\,cm^3$ and $C_2D_2 \approx 7(1) \times 10^6\,cm^3$. For the C_2D_2 case, rates extracted from the data are less certain and the majority of the reported error is due to the calcium ion number uncertainties, as the $C_3D_2^+$ product channel overlaps with the Ca+ channel 118

6.3 Previously measured and calculated constants of CCl^+ for comparison with current computational results. 119

6.4 Electronic energies and vibrational zero-point corrections from calculations at the CCSD/aug-cc-pVTZ level of theory with accompanying CCSD(T)/CBS single point energies, all in Hartrees. Stationary point numbers correspond to those on the $CCl^+ + C_2H_2$ potential energy surface in Figure 6.3. Structures 6 and 10-12 are energetically similar isomers where the HCl moiety rearranges along the *l*-C_3H^+ backbone. The other linear isomer of $C_3H_2{}^+$ is also included for reference. All structures are illustrated in Figure 6.8. 120

6.5 CCSD/aug-cc-pVTZ calculated geometries for stationary points on potential energy surface represented in Figure 6.5. Structures for each point are depicted in Figure 6.8 and electronic and zero point energies are provided in Table 6.4 122

Figures

Figure

2.1 Schematic representation (not to scale) of the ion trap geometry. The coordinate system is drawn for reference and orientation. To the left is an isometric view of the trap and to the right is an end-on view. 8

2.2 Mathieu Stability diagram for experimentally accessible values of $a_{x,y}$ and $q_{x,y}$. Stable trapping conditions are represented by the shaded region. The intercept on the $q_{x,y}$-axis is ~ 0.908. 12

2.3 Energy level diagram for $^{40}Ca^{+}$. Transition wavelengths are measured in air, the lifetimes are total excited state lifetimes, and g_j are the Landé g-factors. 15

2.4 False-color fluorescence microscope images of two separate coulomb crystals with different values of the plasma parameter. The top image shows the charged fluid phase and the bottom image shows the crystalline phase. 17

2.5 False-color fluorescence microscope images of a bi-component coulomb crystal containing Ca^{+} and $C_2H_2{}^{+}$ ions. 18

3.1 Exploded schematic of the ion trap and detection optics. The ion trap has four rods, which are broken into three segments each. RF potentials are applied to all 12 segments. In addition, small DC potentials are applied to form a trapping field along the longitudinal axis. Directly above the ion trap sits a 10x microscope objective to image the fluorescence from the Ca ions onto a EMCCD camera. The drift tube (not shown) of the TOFMS is located directly below the ion trap. 29

3.2 Laser breadboard layouts for diode lasers used in the experiment. 30

3.3 Optical beampaths of ionization lasers and cooling lasers used in this thesis. Two flipper mirrors are used in conjunction with the shutters to send one of the two ionization lasers into the chamber at a time or the radial cooling beam for the calcium. 31

3.4 Left: Schematic representation of the TOFMS. Shown in red and black are the repeller and extractor configuration of the trap rods for radial ejection of trapped ions into the TOFMS. Right: The corresponding repeller and extractor voltages as a function of time, required to go from trapping to TOFMS. Vertical dotted lines represent the timings of the quench and HV pulse control triggers. 33

3.5 A schematic diagram of the RF drive electronics. The diagram shows the three different parts (marked by colored boxes) required for ion trapping and extraction into the TOFMS (only single side of bifilar winding is shown). 34

3.6 A single-shot TOFMS mass spectrum (right) of trapped, laser-cooled $^{40}Ca^{+}$ and co-trapped $^{39}K^{+}$, $^{44}Ca^{+}$, $^{85,87}Rb^{+}$ and $^{133}Cs^{+}$. This Coulomb crystal (left) contained 986 ions with 594 of them being $^{40}Ca^{+}$. Apart from these ions, no further mass peaks can be identified. 38

3.7 Dependence of mass resolution on trapped ion numbers. Pure $^{40}Ca^{+}$ Coulomb crystals of different sizes are trapped and detected in the TOFMS. We observe a decrease of mass resolution with increasing ion number. 39

3.8 Calibration of the MCP signal to ion number. To calibrate the MCP signal, we start by loading small crystals into our trap and counting the number of ions on the image. Then, by extracting those ions into the TOFMS and integrating the resulting MCP signal, we determine how the MCP signal relates to the number of ions in the trap. Using this calibration, we can determine the absolute number of ions in the trap for subsequent experiments. 41

3.9 Determination of the ion density in our ion trap. We correlate the measured ion number from the TOFMS to the fitted Coulomb crystal volume taken from the recorded CCD images. From a fit to these data, we can determine the ion density in our trap. The inset shows a Coulomb crystal with an ellipsoidal fit. 42

3.10 Five calibration data sets to constrain the parameters of the OBE. These five plots are fit simultaneously (red lines) to determine the p-state population. The sixth plot is the global scaling of intensity to p-state population. **NOTE:** the detunings plotted are defined opposite from the majority of the literature, *i.e.:* $\Delta_{model} = -1 \times \Delta$. This is a holdover from the base code taken from [1]. 44

3.11 Schematic diagram of pulsed leak valve setup. The high precision all-metal leak valve is backed by a solenoid actuated 3-way valve. This arrangement allows pulsed gas admission into the UHV chamber. 45

3.12 UHV chamber pressure reacting to opening and closing of the PLV. These tests were performed with 10 PSIG of pure helium backing the valve. The plot on the right is a zoom in of the first pulse plotted to the left with markers to highlight the valve opening time. 46

4.1 Comparison of reactant and product energies for the $Ca^+ + NO$ system. The exothermicity of the reaction depends on the quantum state of Ca^+. Excited states of Ca^+ can be populated by excitation on the two cooling laser transitions at 397 nm and 866 nm. To achieve cooling, the 397 nm laser is red-detuned from resonance by an amount Δ. Only Ca^+ in the $P_{1/2}$ state is energetically allowed to react. The charge exchange product channel barrier is overcome by the thermal energy of neutral NO at 180 K.(Energies not to scale.) 52

4.2 NO^+ and CaO^+ measured ion numbers as a function of time. The ion numbers are normalized by the initial number of Ca^+ determined from the image captured at t = 0. The error bars represent the standard error of the mean of measured ion numbers from five experimental runs at each time point. The solid lines indicate fits to the data using a pseudo first-order reaction rate model. Also shown are three false-color fluorescence images of the Coulomb crystals taken immediately before ejecting the ions into the TOFMS. The images were taken at t = 50 s, 200 s, and 320 s. The dark bands in the center and along the outer edges of the crystals indicate the presence of ions that are lighter and heavier than Ca^+ respectively. These ions are the reaction products. 54

4.3 Measured reaction rates for the two product channels, NO^+ and CaO^+, as a function of Ca^+ $P_{1/2}$ state population. The NO concentration was $2.3(1)\times10^8$ cm^{-3} for all of these data. The initial number of Ca^+ ions in the trap was around 600. The slopes of the fit lines are used to determine the 180 K reaction rate constants. The statistical uncertainty in the $P_{1/2}$ state population is smaller than the points. There is a an offset for the reaction rate at zero excited state population. However, it corresponds to only a 1 – 2% offset in the $P_{1/2}$ state population, which is likely due to a small systematic in determining the absolute state population from the florescence. 55

4.4 Measured reaction rates for product channels NO^+ and CaO^+ as a function of neutral NO concentration in the chamber. The NO pressure in the chamber was varied between 3.4×10^{-9} and 1×10^{-8} torr to change the NO concentration. For all of these data, the $P_{1/2}$ state population was 19.1(1.8)%. The slopes of the fit lines correspond to the 180 K reaction rate constants. 57

4.5 Generalized valence-bond (GVB) diagrams that illustrate the processes whereby ^2P calcium atoms react with NO molecules to form CaO^+ and nitrogen atom in their ground states (top); and the charge exchange process that yields Ca atoms and ground state NO^+ (bottom). 58

4.6 Diagram of the Ca^+ energy structure and product channel energy (energies are not to scale). The main laser cooling transition for Ca^+ at 397 nm excites the ion to the $^2P_{1/2}$-state. The ion can decay to the ground $^2S_{1/2}$- or the excited $^2D_{3/2}$-state. A second laser at 866 nm repumps population that accumulates in the dark $^2D_{3/2}$-state back into the cooling cycle. Here, Δ_{397} and Δ_{866} represent the detuning of the cooling lasers with respect to the two cooling transition frequencies. The reaction with O_2 is energetically possible in either of the two excited states, but not in the ground state. 62

4.7 Predictions of the state distribution of the Ca^+ ion from the 8-level OBE with a fixed 866 nm detuning (+42 MHz). The state populations for the $^2S_{1/2}$, $^2P_{1/2}$, and $^2D_{3/2}$ states are shown. The vertical lines represent the parameters used for three measurements used to determine the rate constants presented in Section 4.2.4 (see Table 4.2). To obtain the other state distributions shown in Table 4.2, we also changed the 886 nm laser detuning. 63

4.8 Example reaction measurement showing the growth of CaO^+ product ions, normalized by the initial number of Ca^+ ions (~ 800). The fraction in the $^2P_{1/2}$-state is 0.16 and $^2D_{3/2}$-state is 0.22, with an O_2 density of $8.9\times10^7 cm^{-3}$. The solid line is a fit using Eqn. (4.6), where k_{eff} is the only free parameter. The error bars correspond to the standard error of the mean of 7 measurements at each time point. 67

4.9 Dependence of the effective rate constant, k_{eff}, on the $^2P_{1/2}$- and $^2D_{3/2}$-state populations of Ca^+. The experimental measurements are shown as diamonds, where the color of the point represents the value of k_{eff}. For all data shown, the O_2 concentration was kept constant at 8.9×10^7 cm^{-3}. We perform a two-dimensional fit to the data using Eqn. 4.7, which allows us to extract k_P and k_D. The contour lines represent constant k_{eff} values of the fit. 69

4.10 An energy-level diagram featuring electronic states of reactants, intermediates, and the observed $CaO^+ + O(^3P)$ product channel. All energies calculated at the CCSD(T) level, apart from those levels involving excited states of molecular oxygen, that use experimental excitation energies. 71

4.11 Dependence of the reaction rate on the $^2P_{1/2}$- and $^2D_{3/2}$-state populations of Ca^+ for the reaction $Ca^+ + H_2O$. The experimental measurements are shown as diamonds, where the color of the point represents the value of the rate. We perform a two-dimensional fit to the data, which allows us to estimate the state dependent rates. The contour lines represent constant reaction rate values of the fit. 74

4.12 Calibration data used to predict calcium p-state populations by coulomb crystal fluorescence. The red line is the output of the 3-level OBE model used in [2]. Retroactive use of the 8-level OBE is not possible and thus the y-axis scaling of the p-state is too large by as much as a factor of 2. 75

5.1 Schematic render of the LIT-TOFMS apparatus. A cross-sectional view of the spherical octagon vacuum chamber reveals the ion trap at the center of our experiment. The source of Ca^+ is an effusive beam of neutral calcium, generated by an oven. The source of molecular ions is a pulsed, supersonic gas jet of neutral acetylene seeded in a noble carrier gas. These neutral beams are intersected by pulsed ionization lasers in the center of our trap to load atomic and molecular ions. Ca^+ ions are addressed by the cooling lasers. To observe the laser induced fluorescence from Ca^+, a microscope objective (outside the UHV chamber) is implemented. A pulsed leak valve (also outside the UHV chamber) is used for the introduction of the neutral reactant. 79

5.2 Left: False-color fluorescence microscope image of a typical two-component Coulomb crystal and its corresponding TOFMS trace (right). The TOFMS data were produced by a single trap loading, i.e., not averaged over multiple experimental cycles. The mass spectrum shows ∼240 $C_2H_2^+$ ions were co-trapped with ∼600 Ca^+ ions. . 80

5.3 Primary products of the reaction $C_2D_2^+ + DC_3D_3$ as a function of time. Each point represents the mean and standard error of 12 measurements. Secondary reaction products have been omitted for clarity. Ion numbers are normalized to the initial number of acetylene ions in the trap (~ 200 ions). 82

5.4 Example detection of multiple orders of products from $C_2H_2^+ + HC_3H_3$. The product order is apparent by the delay of onset in appearance and their mass is too large to be a product of $C_2H_2^+ + C_3H_4$. $C_5H_5^+$ was first order, $C_6H_7^+$ second, and $C_7H_5^+$ was third. Ion numbers have been normalized to initial $C_2H_2^+$ number. Product channels have been multiplied by 4 to enhance clarity of the differences in reaction order. Note that not all measured product channels are shown in this plot. 83

5.5 Reaction model for propyne. Each arrow represents a bimolecular gas-phase reaction between the ion and a neutral propyne. Vertically stacked ions are of the same reaction order. The exact relationship between higher order products was undetermined and beyond scope of this work. This ambiguity is represented by the curly brackets. 84

5.6 Potential energy surface (PES) connecting the propyne and acetylene cation to experimentally observed primary products. The energy of each stationary point is calculated using CCSD(T) in the scheme described in the main text. All energies are relative to separated acetylene cation and propyne. Dashed lines between stationary points indicate reactions that occur via a barrierless process. Note that the initial point of the PES is given for after the first charge exchange has taken place already. 89

5.7 Primary product of the reaction $C_2D_2^+ + H_2C_3H_2$ as a function of time. Each point represents the mean and standard error of 10 measurements. Secondary and higher order products have been omitted for clarity. Ion numbers are normalized to the initial acetylene in the trap 120 ions. 94

5.8 Example detection of multiple orders of products from $C_2H_2^+ + H_2C_3H_2$. Which product order is apparent by delay of onset in appearance and their mass was too large to be a product of $C_2H_2^+ + C_3H_4$. $C_3H_3^+$ was first order, $C_6H_7^+$ second, and $C_7H_5^+$ was third. Ion numbers have been normalized to initial $C_2H_2^+$ number. Second and third order product channels have been multiplied by 20 to enhance the clarity of the differences in reaction order. Note that not all measured product channels are shown in this plot. 95

5.9 Reaction model for allene. Each arrow represents a bimolecular gas-phase reaction with the ion and a neutral allene. Vertically stacked ions are of the same reaction order. The exact relationship between higher order products was undetermined and beyond scope of this work. This ambiguity is represented by the curly brackets. . . . 95

5.10 Potential energy surface connecting the of allene and acetylene cation to experimentally observed primary products. The energy of each stationary point is calculated using the mHEAT+ method.[3] All energies are relative to separated acetylene cation and allene. 98

6.1 Ground-state structures of CCl^+ and C_2H_2. 104

6.2 Measured ion numbers of CCl^+ (blue ×), l-C_3H^+ (green ○), c-$C_3H_2^+$ (black □), and $C_5H_x^+$ (x = 2, 3, and higher; red ∗) as a function of time. Data are normalized by the initial ion number of CCl^+ (~ 100). Each data point represents the mean and standard error from four experimental runs per time point. The averaged data are fit using a pseudo-first order reaction rate model (solid lines). 109

6.3 The main features of the potential energy surface for $CCl^+ + C_2H_2$ calculated at the CCSD(T)/CBS level of theory. The favored Cl loss product, dissociates without a barrier, forming c-$C_3H_2^+ + Cl$ [8]. The HCl loss channel leading to l-$C_3H^+ + HCl$ [7] involves a few stationary points with lower energies than the dissociation limit of -0.1 eV. Here, the bare '+' indicates infinite separation. 112

6.4 Measured total ion numbers of the $CCl^+ + C_2H_2$ reaction as a function of time. Each data point represents the mean and standard error from 4 experimental runs per time point. The total ion data are fit using a 1st order polynomial giving a slope of -0.04 with an uncertainty of 0.3 (the 95% confidence interval of the fit parameter) indicating the number of ions are conserved over the reaction. 115

6.5 Measured ion numbers of CCl^+ (blue $\times$), C_3D^+ (green $\circ$), $C_3D_2{}^+$ (black $\square$), and C_5D_x (x = 2, 3 and higher; red $*$) as a function of time for the reaction of CCL^+ with duetrated acetylene C_2H_2. The product masses shift as expected due to deuterium substitution. Data are normalized by the initial ion numbers of CCl^+ (~ 100). Each data point represents the mean and standard error from 4 experimental runs per time point. The average data are fit using a pseudo-first order reaction rate model (solid lines). $C_3D_2{}^+$ (m/z 40) overlaps with the Ca^+ channel. To fit this channel, the initial average Ca^+ ion numbers are subtracted from the m/z 40 channel at each time step. There is some variability in the loaded numbers of Ca^+, making the ion numbers and rates extracted from the 40 channel less certain. 116

6.6 Measured total ion numbers of the $CCl^+ + C_2D_2$ reaction as a function of time. Each data point represents the mean and standard error from 4 experimental runs per time point. The raw total ion data are fit using a 1st order polynomial giving a slope of -0.09 with an uncertainty of 0.2 (the 95% confidence interval of the fit parameter) indicating the number of ions are conserved over the reaction. 117

6.7 Potential energy surface calculated at the CCSD/aug-cc-pVTZ level of theory for the reaction of CCl^+ with C_2H_2. Energies (in eV) are from single point CCSD(T)/aug-cc-pVTZ calculations extrapolated to the complete basis set limit. Structures, energies, and geometries are given in Figure 6.8 and Tables 6.4 and 6.5, respectively. . . 121

6.8 Structures of stationary points on the potential energy surface in Figure 6.7. In each case, energies are given relative to the $CCl^+ + C_2H_2$ limit [1]. Geometries were computed at the CCSD/aug-cc-pVTZ level. Structures 6 and 10-12 are the several minima with different rearrangements of the HCl moiety along the C_3H^+ backbone. Also included is the l-$C_3H_2{}^+$ isomer energy. Geometries for each stationary point are provided in Table 6.4. 122

7.1 Schematic render of the partially constructed coupling between a TWRD and the ion trap from this thesis. An in-vacuum molecular beam shutter separates the line of site from the TWRD to the guiding hexapole. The guiding hexapole delivers the molecular beamline to the trap center. 127

A.1 Main RF driver for the ion trap. Primary and secondary sides of the step-up transformer are separated by the dashed line. The quench boards and high-voltage switches are represented schematically as two and three-way switches, respectively. Connections to the DC shim box are also labeled. 145

A.2 High voltage switches and quench circuit diagrams. The floating power supply is a 12VDC NIHM battery pack that rests on a glass plate to allow it to float up to 2kV. 147

A.3 Circuit diagra for DC shim box PCB. Buffer amps for potentiometer control voltages feed into the summing matrix via dividing resistors. The summing amps then generate the buffered DC voltages that are applied to the rods. 149

A.4 Secular excitation relay circuit schematic. 150

A.5 Time sequence of the secular excitation and control trigger. 150

B.1 Block diagram of all the control electronics in the experiment. 152

B.2 Block diagram of all VI modules and what hardware they each control. 156

Chapter 1

Introduction

Collision studies are a common way to study physical interactions. The relationship between experiment and theory in such studies often plays out as follows: experiments prepare precise initial conditions for a collision and then accurately measure the outcome. A model of the interaction is built, and its predictions can be tested against the experimental data. This thesis describes an apparatus that was designed, built, and used to measure the outcome of carefully controlled collisions between ions and molecules, in the gas phase, in order to better understand the nature of their interactions. Atoms and molecules, whether neutral or charged, are complicated quantum mechanical systems. Their interactions display a diverse range of behaviors stemming from intrinsically quantum phenomenon. For example, the rearrangement of electronic structure is often the result of a collision. The ultimate goal of this research is to understand the mechanisms that drive such reactions in pursuit of building/refining models of the underlying quantum interactions.

1.1 Motivation

With knowledge and mastery of small systems comes the push to understand larger and more complicated ones. An enormous amount of work has been done studying the nature of atomic collisions. The next logical step was to include molecules. Molecular collisions, while not new, are enticing because they push the limits of known physics. Especially tantalizing are the quantum control aspects of molecules with the realization that "more is different." From a chemistry perspective, the most fundamental process is the formation and breaking of bonds.

Studying isolated reactions between small molecules serves as an ideal laboratory to build upon the foundational understanding of chemistry.

In a more applied direction, gas-phase reactions between ions and molecules play a role in the chemistry of interstellar medium (ISM). The combination of ionizing radiation from stars and the low molecular density found in the ISM is observed, through the use of spectroscopy, to produce many ionic species. Many-atom organic species ranging up to amino acids and the famous buckminsterfullerene ($C_{60}{}^{+}$) have also been detected [4]. Because the long-range potential between a charged and neutral molecule leads to a large reaction cross-section, ion-molecule reactions are believed to contribute to the observed diversity. To this end, large databases of ion-molecule reactions have been built to help with modeling of the chemistry of the ISM [5, 6]. Other environments where gas-phase reactions between ions and molecules play a role are planetary atmospheres [7, 8] and combustion [9, 10].

Another striking attribute of the ISM is that it is cold. Interstellar clouds are in, or close to, thermal equilibrium with the cosmic microwave background radiation (CMBR). Temperatures from 3K to 10K are typical for interstellar chemistry. To probe this regime, we must produce cold molecular samples in the lab.

In addition to understanding ISM chemistry, cold reactions dramatically reduce complexity. Molecules are many atom quantum systems with many degrees of freedom to distribute thermal energy. Less thermal energy available leads to fewer populated quantum states. As temperatures reduce below 10K, one can begin to think about fully-quantum state resolved interactions.

Fully quantum-state resolved collisions would place the most stringent bounds on theoretical interaction models to date. So-called, quantum chemistry, demonstrates the ultimate level of control on reactions. Quantum control has been achieved for many atomic systems and draws ever closer with molecular collision experiments. A multitude of techniques that have been successful in achieving atomic control have been applied to molecular systems as well [11].

1.2 Cold ion-molecule collision experiments

Crossed-beam and merged-beam experiments have successfully demonstrated cold, ion-molecule collisions spanning many energy regimes. These experiments typically produce a cold, neutral molecular beam via supersonic expansion to collide with a guided ion beam in vacuum. The collision energy can be adjusted by the relative angle of the the ion and neutral beams. The collision energy of crossed beams, expressed as a temperature, is typically between 10–1000K [12]. Merged-beam experiments explore the collision energy regime below 10K [13, 14]. Product detection typically employs a combination of spectroscopic, velocity-map imaging, and mass spectrometry techniques. While these experiments have been very successful in studying both cold and controlled ion-molecule reactions, they have very short reaction/interaction times. This limits detection sensitivity. Collisions studied inside an ion trap can dramatically extend the interaction time and thus increase sensitivity to measuring reactions. Ion traps also accumulate charged products which allow for simultaneous tracking of reactants and products. The rest of this section will detail a few experimental approaches that utilize ion traps for controlled collisions.

22-pole ion traps create cold ions via cryogenic buffer-gas cooling[15–17]. The large number of poles reduces the radio frequency (RF) micromotion heating of the ion trap to allow for buffer gas cooling of the trapped ions to low temperatures. Neutral species are added into the trap to react with the ions that also are cooled by the buffer gas. Charged products of the reaction are accumulated in the 22-pole trap and can be identified via action spectroscopy [16, 18]. The relatively high pressure of cryogenic buffer gas used in these systems is capable of stabilizing highly excited reaction complexes. Chemistry involving cations typically produce such unstable complexes, which are unlikely to stabilize in the ISM. Additionally, for thermodynamic reasons only recently elucidated [19], the ion temperatures cannot drop below 10K in these experiments. This fundamentally limits the collision energy range available to 22-pole trap experiments. Replacing buffer gas cooling with direct laser cooling creates the opportunity to study colder, cation-molecule reactions without a large background gas pressure.

Linear Paul ion traps (LIT) are particularly well-suited for direct laser cooling of ions because the geometry allows for good optical access. While atomic cations are the only current candidates for direct laser cooling, they sympathetically cool co-trapped molecular ions to translational temperatures <10 K [20, 21]. Sympathetic cooling does not address the internal degrees of freedom of a co-trapped molecular ion, which means it will not stabilize highly energetic reaction complexes. This makes the linear Paul ion trap an ideal workhorse for studying cation-molecule reactions relevant to the ISM [22, 23]. The translational energy of a neutral reactant typically sets the collision energy studied in these experiments.

One such realization of cold, controlled collisions involving a LIT are hybrid ion-atom traps. These overlap a linear Paul ion trap with a neutral magneto-optical trap (MOT), sometimes called MOTion traps [24–28]. Direct laser cooling of the MOT atoms achieves temperatures much lower than 1K and afford some degree of quantum-state control. Collision energies can be carefully controlled via ion or atom shuttling techniques up to about 1K [29–31]. Like in the 22-pole trap, charged products of a reaction are accumulated in the trap and are investigated via a mixture of spectroscopic and mass-spectrometry techniques. A drawback to this arrangement is the atomic MOT species is quite specific. Additionally, a molecular MOT has not been considered, to my knowledge, which limits these studies to ion-atom collisions.

Another realization of LIT experiments introduce the neutral reactant as a room temperature gas. This leads to average collision energies between the trapped ions and neutral gas on the order of 100–200K. As with all the ion trap studies mentioned so far, products of these reaction accumulate in the trap. These studies can be separated into two different detection schemes for reaction products. The first scheme utilizes optical detection with the help of secular mass excitation[32–34]. The second scheme adds a time-of-flight mass spectrometer (TOFMS) to compliment optical detection methods [35–38]. By using a room temperature gas as a neutral reactant, these experiments benefit from being able to investigate a wide range of species. The disadvantage is that the chemistry does not quite reach the temperatures of the ISM. Despite the higher collision energy, these experiments have contributed a lot to the scientific community as evidenced by the number of ion-molecule

Table 1.1: List of many cation-molecule reactions studied in linear Paul ion traps. 300K should be understood as room temperature. Reactions studied in this thesis are the first four entries.

Reactants	$T_{neutral}$ (K)	Reference
$Ca^+ + NO$	300	[2], Ch. 4
$Ca^+ + O_2$	300	[39], Ch. 4
$C_2H_2{}^+ + C_3H_4$	300	Ch. 5
$CCl^+ + C_2H_2$	300	[40], Ch. 6
$Mg^+ + H_2\,/D_2$	300	[32]
$Be^+/Mg^+ + HD$	$\geq$300	[33]
$Ba^+ + O_2\,/N_2O\,/CO_2$	300	[21]
$BaO^+/CaO^+ + CO$	300	[21]
$H_2{}^+/H_3{}^+ + H_2\,/HD\,/O_2$	300	[41]
$Ca^+ + H_2O$	300	[34]
$H_3O^+ + NH_3$	300	[42]
$Ca^+ + N_2O$	300	[37]
$Xe^+ + NH_3\,/ND_3$	300	[43]
$Be^+ + H_2O\,/D_2O\,/HOD$	300	[44, 45]
$C^+ + H_2O$	10,100,300	[46]
$Ca^+ + ND_3\,/H_2CO\,/CH_3CN$	<10	[47]
$N_2H^+ + CH_3CN$	<10	[47]
$Ca^+ + CH_3F$	2-4	[48]
$OCS^+ + ND_3$	300	[49]
$Ca^+ + 3$-Aminophenol	2*	[50, 51]
$N_2{}^+ + N_2$	2*	[52]
$N_2H^+ + p/o\text{-}H_2O$	2*	[53]
$Ca^+ + CH_3F\,/\,CH_2F_2\,/\,CH_3Cl$	5-243	[54]

* Neutrals introduced via supersonic beam.

reactions in Tab. 1.1 with room temperature reactant gasses. The level of control and specificity afforded by ion trapping techniques allows for better understanding of a large library of ion-molecule reactions studied via previous methods (e.g., ion cyclotron resonance or selected ion flow tubes). The reaction studies presented in this thesis fill some of the holes in that library by creating purified samples of highly reactive molecules.

LIT experiments have pursued a few additional techniques of achieving cold, controlled collisions. All these techniques come in the form of collisions between a neutral molecular beam and the ions in the trap. Stark velocity-selected beams have been demonstrated [47, 48, 55] as well as conformer selected beams [50, 51], and cold buffer gas beams [46]. Multiple groups are pursuing collisions with a Stark [56] or Zeeman [57] decelerated beam, though at time of writing, this has

yet to be demonstrated.

The apparatus we have built and characterized is a new combined LIT-TOFMS, which adds to a growing list of similar experiments. This list is growing because of the success the LIT-TOFMS has in characterizing cation-molecule reactions relevant to the ISM. We intend to extend the limits of cold-controlled reactions by coupling the LIT-TOFMS to a traveling-wave ring decelerator (TWRD). This will deliver a beam of neutral radical molecules with a specific quantum state into the ion trap with a tunable velocity, which will lead to collision energies from 1–300 K. With the ultimate goal of quantum control in mind, we can also pursue stimulated rapid adiabadic passage (STIRAP) methods to produce trapped molecular ions in specific quantum states [58].

1.3 Outline of this thesis

This thesis covers the work done to produce cold, controlled, ion-molecule reactions. Some basic theory is covered to understand the operation of a linear Paul ion trap and how to conceptualize the collisions/reactions that take place inside. Then, the physical apparatus is described and characterized. Afterwards, there are investigations into four different ion-molecule reactions: $Ca^+ + NO$, $Ca^+ + O_2$, $C_2H_2{}^+ + C_3H_4$, and $CCl^+ + C_2H_2$. The reactions involving Ca^+ display quantum control of photochemistry. Reactions with $C_2H_2{}^+$ show isomer specific chemistry resulting from the different arrangements of the neutral reactant C_3H_4. The reaction of CCl^+ uncovers astrochemically relevant reaction mechanisms. The thesis concludes with a summary of the work presented and a brief outlook on the future work: incorporation of the TWRD.

Since this experiment was built from the ground up over my time at JILA, there is a large amount of additional technical information that is not covered in detail in the thesis. Schematics of the trap electronics, LabVIEW code for experiment control, and MATLAB code written for data analysis have been relegated to the appendices.

Chapter 2

Ion trapping and ion-molecule reaction theory

This chapter summarizes the theory underlying our method of studying reactions in an ion trap. The detailed theory of each section has been covered in the literature in far greater detail than can be included here and will be referred to often. I will include a brief overview of the concepts to contextualize the experimental implementation described in the next chapter. All equations are derived using a Gaussian CGS unit system.

2.1 Ion trapping

Earnshaw's theorem guarantees that charged particles cannot be trapped in three dimensions via static potentials [59]. Ion trapping is thus achieved through use of sinusoidal time-varying quadrupole potentials. An intuitive understanding of this comes from the saddle point at the center of a static qudrupole potential. If the polarity is flipped, the saddle point rotates 90 degrees. By sinusoidaly varying the voltage, the saddle point rotation produces a local minimum in two dimensions. The third dimension is confined using a static potential.

There are many realizations of ion traps utilizing a variety of geometries to produce the desired time-varying quadrupole field. Our ion trap is a linear Paul trap [60], which is particularly well suited for laser cooling ions (covered in the next section). A schematic diagram of our trap geometry is depicted in Fig. 2.1. While hyperbolic electrodes produce an ideal quadrupole potential, cylindrical rods are easier to manufacture and produce an adequate approximation. This is true provided the radius of rods, R, and inscribed radius, r_0, of the trap are related by $R = 1.15\ r_0$

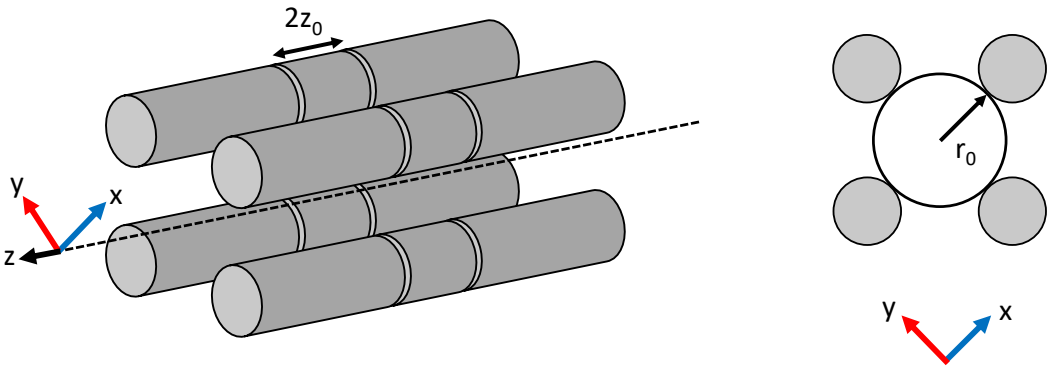

Figure 2.1: Schematic representation (not to scale) of the ion trap geometry. The coordinate system is drawn for reference and orientation. To the left is an isometric view of the trap and to the right is an end-on view.

[61, 62]. The four rods have three electrically isolated segments each, for a total of 12 rod segments. Radio-frequency (RF) voltage is applied to all six segments in a diagonal pair of rods. The opposite phase RF voltage (180°) is applied to the other diagonal pair of rods to produce the time-varying quadrupole potential

$$\phi_{RF}(x, y, t) = 2V_{RF}\sin(\Omega t)\frac{x^2 - y^2}{2r_0^2}. \tag{2.1}$$

V_{RF} is the amplitude (zero-to-peak) of the applied RF, Ω is the angular frequency of the RF, x, y, and t are two spatial coordinates and a temporal coordinate, respectively.

A DC voltage is also applied to the eight, longer electrodes on the ends of each rod (the so-called endcaps). This produces an approximately harmonic potential along the axial directions with a small radial dependence described by

$$\phi_{EC}(x, y, z) = \frac{\kappa V_{EC}}{z_0^2}\left(z^2 - \frac{x^2 + y^2}{2}\right). \tag{2.2}$$

κ (< 1) is a geometrical factor, V_{EC} is the DC voltage applied to the endcaps, and z_0 is half the length of the center electrode. Thus the total electrical potential is

$$\Phi(x, y, z, t) = \phi_{RF} + \phi_{EC}. \tag{2.3}$$

We can now derive the equations of motion for an ion in the trap. Unfortunately, solutions to the equations of motion cannot be obtained analytically for many ions in the trap. However,

insights from the single trapped ion picture that follow are a useful intuition to build on and provide a correct description (to lowest order) of the center-of-mass motion of many ions. Computational solutions for many ions are attainable where more accuracy is desired. The following derivation borrows elements of similar derivations given in [1, 63].

We exclusively trap cations, as they are laser coolable. To date our ionization methods only allow us to remove only a single electron, so we consider a particle of charge $+e$ and mass m,

$$\vec{F} = m\vec{a} = e\vec{\nabla}\Phi. \tag{2.4}$$

Or, separated into three differential equations, (for the three spatial coordinates)

$$\begin{aligned} \frac{\partial^2 x}{\partial t^2} + \left(-\frac{e}{m}\frac{\kappa V_{EC}}{z_0^2} + \frac{e}{m}\frac{2V_{RF}}{r_0^2}\sin(\Omega t)\right)x = 0 \\ \frac{\partial^2 y}{\partial t^2} + \left(-\frac{e}{m}\frac{\kappa V_{EC}}{z_0^2} - \frac{e}{m}\frac{2V_{RF}}{r_0^2}\sin(\Omega t)\right)y = 0 \\ \frac{\partial^2 z}{\partial t^2} + \left(\frac{e}{m}\frac{2\kappa V_{EC}}{z_0^2}\right)z = 0 \end{aligned} \tag{2.5}$$

It is worth noting that the equation in the z direction is that of a harmonic oscillator. The equations in every direction have been rearranged to match the form of the Mathieu equation, which has a well-known analytical solution. That form is

$$\frac{\partial^2 u}{\partial \tau^2} + (a_u - 2q_u\sin(2\tau)) = 0, \tag{2.6}$$

where u and τ are generalized coordinates; a_u and q_u are dimensionless parameters. The variable substitutions that cast Eq. (2.5) into the form of Eq. (2.6) are

$$u = \{x, y, z\}, \tag{2.7}$$

$$\tau = \frac{\Omega t}{2}, \tag{2.8}$$

$$a_x = a_y = -\frac{a_z}{2} = -\frac{e}{m}\frac{4\kappa V_{EC}}{z_0^2\Omega^2}, \tag{2.9}$$

$$q_x = -q_y = \frac{e}{m}\frac{4V_{RF}}{r_0^2\Omega^2}; \quad q_z = 0. \tag{2.10}$$

The solution of Eq. (2.6) can be expressed as a Fourier series. As long as $q_u \ll 1$ and $a_u \ll 1$, which is typical for our experiment, the first term in the series is an adequate approximation of the

ion motion, given by

$$u(\tau) \simeq A_u^{(1)} \cos(\omega_u \tau + \varphi_u) \left(1 + \frac{q_u}{2} \cos(\Omega\tau)\right) \tag{2.11}$$

where

$$\omega_u = \frac{\Omega}{4}\sqrt{a_u + \frac{q_u^2}{2}} \tag{2.12}$$

is the so-called secular frequency. $A_u^{(1)}$ is the amplitude of secular oscillation and φ_u is the corresponding phase. Both are parameterized by the initial conditions of the ion.

Eq. (2.11) depicts oscillations associated with two different timescales, aside from the case where $q_z = 0$. The slower oscillation occurs with angular frequency ω_u and is called the secular motion. Secular motion can be intuitively understood as the harmonic motion caused by the time-averaged rotating saddle point potential. The faster motion occurs with angular frequency Ω, the driving RF frequency, is called micromotion. Micromotion is from the ponderomotive force that the saddle exerts on the ion as it changes in time. There is no static potential analogy for micromotion; it can only be caused by a dynamically changing potential. Additionally, if the amplitude of secular motion of an ion is zero, so too is its micromotion. This occurs when ions are along the z-axis of the trap, which is co-incident with the saddle point of the RF potential, also called the RF-node.

2.1.1 Pseudo-potential approximation

Since $a_u \ll 1$ and $q_u \ll 1$ are typical trapping conditions, $\omega_u \ll \Omega_u$ by Eq. (2.12). The timescales of the two oscillatory motions can thus be adiabatically separated. Doing so mathematically amounts to time averaging over the RF oscillation of the potential. This reduces the equations of motion to purely harmonic potentials, which is known as the trap pseudo-potential. A detailed derivation of the pseudo-potential can be found in [64]. The result is

$$\phi^*(x, y, z) = \frac{eV_{RF}^2}{m\Omega^2 r_0^4}(x^2 + y^2) + \phi_{EC}(x, y, z) \tag{2.13}$$

This approximation is particularly useful for estimating the trap depth for our ions in the x and y-directions

$$PE_{x,y} \leq \frac{q_{x,y} V_{RF}}{4}, \tag{2.14}$$

where the equality holds for an ion at the center of the radial potential. An ion with a large amplitude of oscillation – away from the center of the trap – is less bounded. This is essentially a statement of energy conservation $E = PE + KE$ where E is a constant and KE is the kinetic energy of the ion.

2.1.2 Trapping stability

One would assume that there are a specific range of frequencies that work best for trapping ions. Intuitively, a saddle rotating too slowly will allow ions to escape. Likewise, rotating too quickly will eject ions via the ponderomotive force. Between these limits is the stable trapping regime. This can be quantitatively described by a stability analysis of the Mathieu equation (Eq. (2.6)). The stability regime is parameterized by a_u and q_u, which can be related back to real world trapping parameters via Eq. (2.7). A detailed stability analysis can be found in [64]. The result of which is often given in terms of another unitless parameter

$$\beta \approx \sqrt{a_u + \frac{q_u^2}{2}} \tag{2.15}$$

also called the mathieu characteristic parameter. Stable trapping in the region defined by $0 < \beta_u < 1$. However, Eq. (2.15) only holds for $a_u \ll 1$ and $q_u \ll 1$ and thus $\beta \ll 1$. Fortunately, almost every major programming package has the mathieu characteristic parameter built in, and a general analytic formula for β is unnecessary. Using a computational resource for β (Mathematica), one can produce the stability diagram relevant to our experiment seen in Fig. 2.2.

We do not need to consider stability in the z direction because the purely harmonic potential has a permanent, stable minimum.

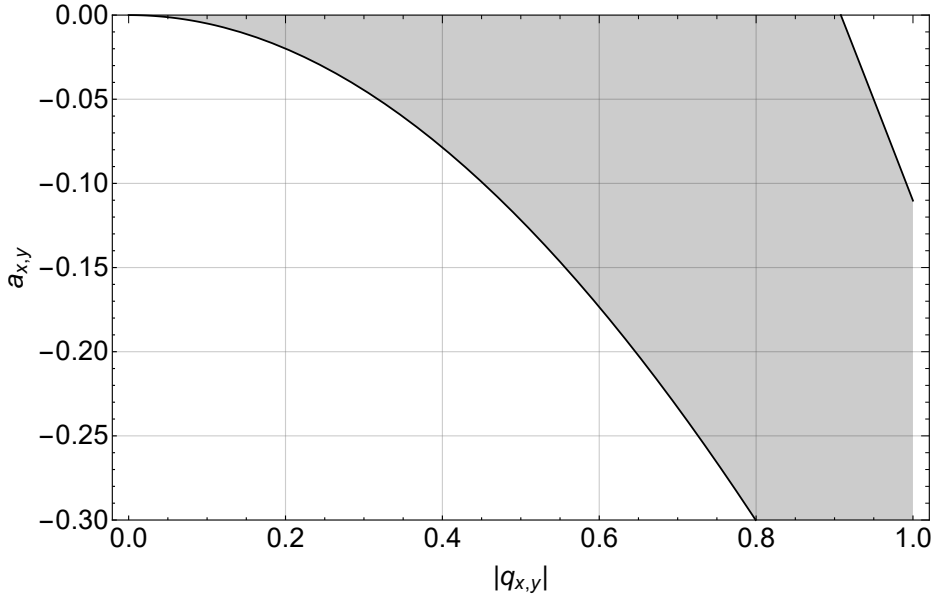

Figure 2.2: Mathieu Stability diagram for experimentally accessible values of $a_{x,y}$ and $q_{x,y}$. Stable trapping conditions are represented by the shaded region. The intercept on the $q_{x,y}$-axis is ~ 0.908.

2.1.3 Ion kinetic energy

From Eq. (2.11), we can calculate the kinetic energy averaged over one period of the secular motion

$$KE_u = \frac{1}{2}m\langle \dot{u}^2 \rangle = \frac{1}{4}mA_u^{(1)^2}(\omega_u^2 + \frac{1}{8}q_u^2\Omega_u^2). \tag{2.16}$$

Applying Eq. (2.12) gives

$$KE_u \simeq \frac{1}{4}mA_u^{(1)^2}\omega_u^2(1 + \frac{q_u^2}{q_u^2 + 2a_u}). \tag{2.17}$$

In the x and y directions, we can further simplify with the condition $a_{x,y} \ll q_{x,y}$ giving

$$KE_{x,y} \simeq \frac{1}{2}mA_{x,y}^{(1)^2}\omega_{x,y}^2, \tag{2.18}$$

which shows that in typical trapping conditions, secular motion and micromotion contribute approximately equally to the kinetic energy of the ion. Furthermore, Eq. (2.17) shows that the condition required for cold ions is a low amplitude of oscillation. This can be realized by direct laser cooling, which is discussed in the next section.

2.2 Laser cooling of Ca^+

Doppler laser cooling is a technique utilized in virtually every cold atom experiment. In our case, we use it to cool calcium-40 cations, $^{40}Ca^+$, which are the workhorse ions present in the trap for all of our ion-molecule reactions. A useful model for understanding Doppler laser cooling of Ca^+ is a two-level atom. I will provide some semi-classical results of the derivation found in [65] for the purpose of building an intuition and connecting with experiment.

A two level atom irradiated by a laser near its resonance frequency will scatter light from the beam. The spontaneously emitted light, having no preferential direction, means that there is a momentum transfer from the laser beam to the atom. Given the proper conditions, the resulting force felt by the atom can be guaranteed to be opposite the direction of the atoms velocity. The net effect is a dissipative force that removes kinetic energy from the atom.

The quantum mechanical process behind the force is spontaneous emission. To build up to the force, we must first define characteristics of the atom and of the laser irradiating it. To start is the spontaneous emission rate of the atom, $\Gamma \equiv 1/\tau$, where τ is the excited state lifetime. The excited state lifetime sets the saturation intensity of the process

$$I_s = \frac{\pi hc}{3\lambda^3 \tau}, \tag{2.19}$$

where λ is the laser wavelength on resonance. The saturation parameter defines the relative interaction strength of the laser with the atom

$$s = \frac{s_0}{1 + (2\Delta/\Gamma)^2}, \tag{2.20}$$

where $\Delta \equiv \nu - \nu_0$ is the laser frequency detuning from resonance, ν_0, and s_0 is the on resonance saturation parameter

$$s_0 = \frac{I}{I_0} = \frac{2|\Omega|^2}{\Gamma^2}, \tag{2.21}$$

where Ω is the Rabi frequency, which is another way to parameterize the light-matter interaction strength. Finally, the force an atom feels from a laser near resonance is given by

$$\vec{F} = \hbar\vec{k}\ \frac{s\Gamma/2}{1+s}\ \left(1 + \frac{2\Delta\vec{v}\cdot\vec{k}}{(1+s)(\Delta^2 + \Gamma^2/4)}\right) = \vec{F}_0 - \beta\vec{v}, \tag{2.22}$$

where $\vec{k} = \frac{2\pi}{\lambda}\hat{k}$ is the laser's k-vector, $\vec{v}$ is the velocity of the atom, and β is a damping coefficient to be defined next. The equation has been suggestively parameterized into two terms. The velocity-independent term, F_0, is the classical radiation pressure from the laser. The velocity dependent term is the dissapative force responsible for laser cooling. It's form is identical to that of a friction term. Solving for β gives us the damping coefficient

$$\beta = -\hbar k^2 \frac{4s_0(\Delta/\Gamma)}{(1 + s_0 + (2\Delta/\Gamma)^2)^2}, \tag{2.23}$$

which depends only on the laser intensity (through s_0), detuning, and excited state lifetime. We can now see that for $\Delta < 0$ (red detuned), the force is guaranteed to be damping and lead to cooling.

In the experiment we use two, counter-propogating beams to cool. Assuming the k-vectors are equal and opposite, the resulting force generated by the two beams is

$$\vec{F}_{tot} = -\beta_{tot}\vec{v}, \tag{2.24}$$

where $\beta_{tot} = 2\beta$. Intuitively, the radiation pressure force from each side cancels and the damping coefficient doubles.

In general, six laser beams are needed to produce the most efficient cooling in three dimensions. Because of the symmetry of linear Paul ion trap, only the radial and axial directions need cooling, which relaxes the number of beams needed to four. In practice, our lasers cool along the axial direction of our trap. A slight misalignment in the overlap of the counter-propagating lasers provides enough cooling in the radial dimension to further relax the condition to the two beams used in the experiment. Radial cooling is dramatically enhanced for large ion clouds extending off of the RF-node. The strongly interacting ions (through coulomb repulsion) effectively couple the laser cooling to all transnational degrees of freedom. A notable exception to this scenario is when few enough ions are trapped that they can all be arranged along the RF-node. In this case, an additional radial laser beam is added to help cool the resulting ion string. It is not strictly necessary, due to imperfections in alignment of the axial beams, but it noticeably improves laser cooling efficiency.

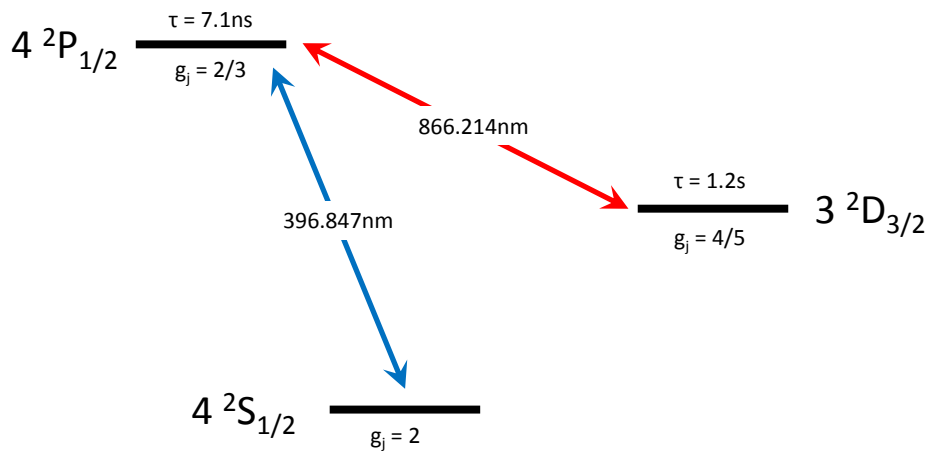

Figure 2.3: Energy level diagram for $^{40}Ca^{+}$. Transition wavelengths are measured in air, the lifetimes are total excited state lifetimes, and g_j are the Landé g-factors.

Eq. (2.24) would suggest Doppler laser cooling is able to bring the atoms to rest. Since this would correspond to a temperature of absolute zero, it would violate the second law of thermodynamics and surely cannot be the case. What is missing from the model is the fact that momentum/energy is removed in discrete quanta of photons, which results in a finite minimum velocity attainable. The actual Doppler cooling limit associated with this minimum velocity, expressed as a temperature, reduces to the form

$$T_D = \frac{\hbar\Gamma}{2k_B}. \tag{2.25}$$

The best candidates for Doppler laser cooling will be closed cycle systems with very short excited state lifetime. The shortest excited state lifetimes occur in dipole allowed transitions, like that of an electron going from the P to S orbitals in hydrogen. The alkaline earth column of the periodic table is a sensible place to look for hydrogen-like cations, because the cations will only have one valence electron.

Since Ca^{+} is not an ideal two-level system, we must consider its specific energy levels. We choose the mass 40u isotope of calcium because it is naturally the most abundant (98%) and it has no nuclear spin (no hyperfine structure). A graphic description of the lowest lying energy levels and

all their properties tabulated in the NIST atomic spectra database is shown in Fig. 2.3. The main cooling transition is the $S_{1/2}$ to $P_{1/2}$. There is a 7.5% chance the $P_{1/2}$ state will spontaneously decay to the low-lying $D_{3/2}$ state, which does not have a dipole-allowed transition back to the $S_{1/2}$ state. To prevent shelving of ions in the $D_{3/2}$ state, a single repump laser is necessary to close the cooling-cycle. In practice, only two lasers are needed (main cooling and repump) to cool Ca^+ to the Doppler limit.

Since Ca^+ is constantly cycling between the $S_{1/2}$, $P_{1/2}$, and $D_{3/2}$ states, a steady-state population builds up in each of the three states when considering time-scales longer than the excited state lifetime (ns). The steady-state population of the excited states can be predicted by using the optical Bloch equations (OBE). The OBE are relevant to experiments where the quantum state populations of Ca^+ need to be known. The OBE are explicitly laid out for Ca^+ in [54].

2.3 Coulomb crystals and sympathetic cooling

Coulomb crystals, also called Wigner crystals, are cold, single-component plasmas confined by an external field. They are periodic (or quasi-periodic) structures that form when the kinetic energy of the plasma becomes less than the potential energy of the ions in confinement. With much less kinetic energy than the potential of the confining field, the ion locations become locked into place. The overall structure of the ions is determined by the balance of the confining force on each ion with that of the coulomb-repulsion between ions. This is precisely what occurs when Doppler laser cooling trapped ions.

The transition from a cloud of trapped ions to a coulomb crystal is parameterized by the plasma parameter

$$\Gamma_{pl} = \frac{PE}{KE} = \frac{e^2}{a_{ws} k_b T} \tag{2.26}$$

where a_{ws} is the Wigner-Seitz radius, related to the zero-temperature plasma density n_0 by

$$n_0 = \frac{V_{RF}^2}{4\pi m \Omega^2 r_0^4} = \frac{1}{\frac{4}{3}\pi a_{ws}^3}. \tag{2.27}$$

It has been both experimentally and computationally verified that for $\Gamma_{pl} \gtrsim 2$ the ion cloud will

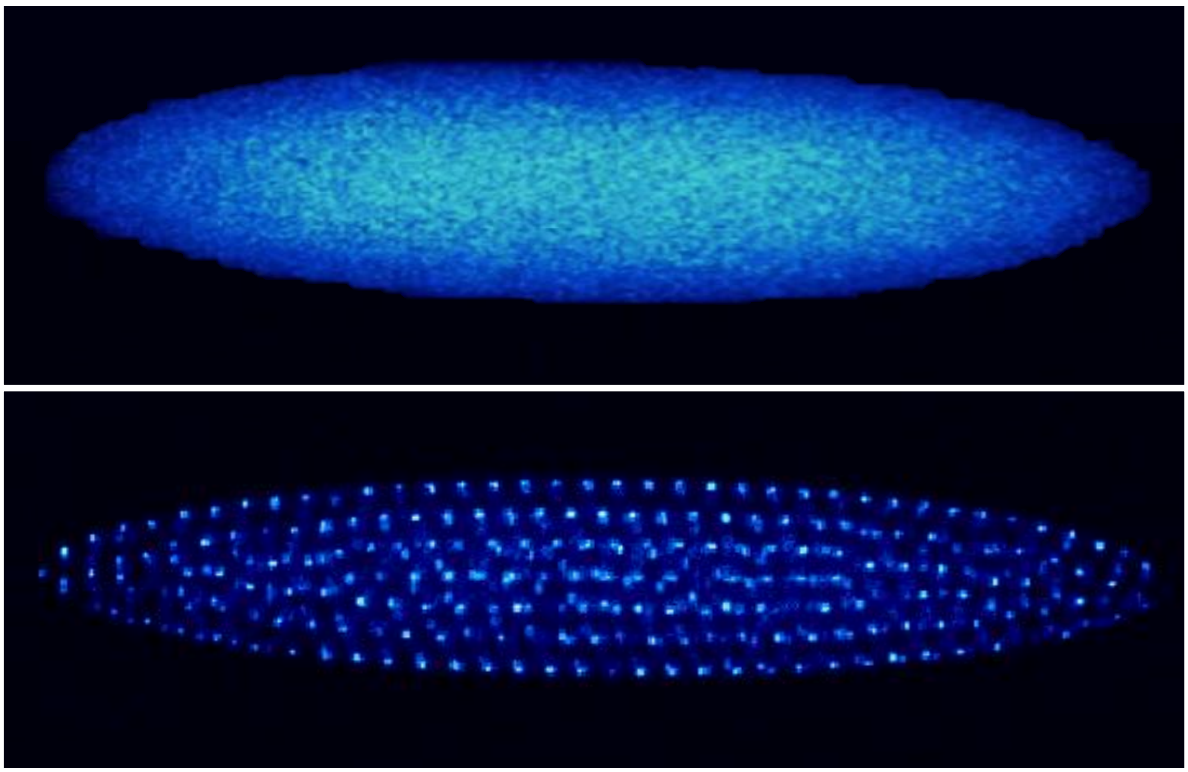

Figure 2.4: False-color fluorescence microscope images of two separate coulomb crystals with different values of the plasma parameter. The top image shows the charged fluid phase and the bottom image shows the crystalline phase.

undergo a phase-transition into a charged fluid phase. At this point, the boundary of the ion cloud is now clearly defined but individual ion sites are not resolvable and only short-range order exists. This is because the ion cloud has too much kinetic energy to settle on a single structure. The constant re-arrangement of ion sites is on a faster time-scale than that of the camera exposure. For $\Gamma_{pl} \gtrsim 150 - 170$ the ion sites become locked into place and the crystal structure is clearly seen with long-range order. Solving Eq. (2.26) for T with an ion density of $n_0 = 10^8 \frac{1}{\text{cm}^3}$ estimates the crystalline phase transition to occur at $T \sim 100\text{mK}$. A visual example of the transition from our apparatus is shown in Fig. 2.1.

When ions are added to a trap where a coulomb crystal is already present, the new ions are cooled by elastic collisions with the crystal. Momentum transferred to the crystal is quickly removed by the laser cooling in a process dubbed sympathetic cooling. The sympathetically cooled

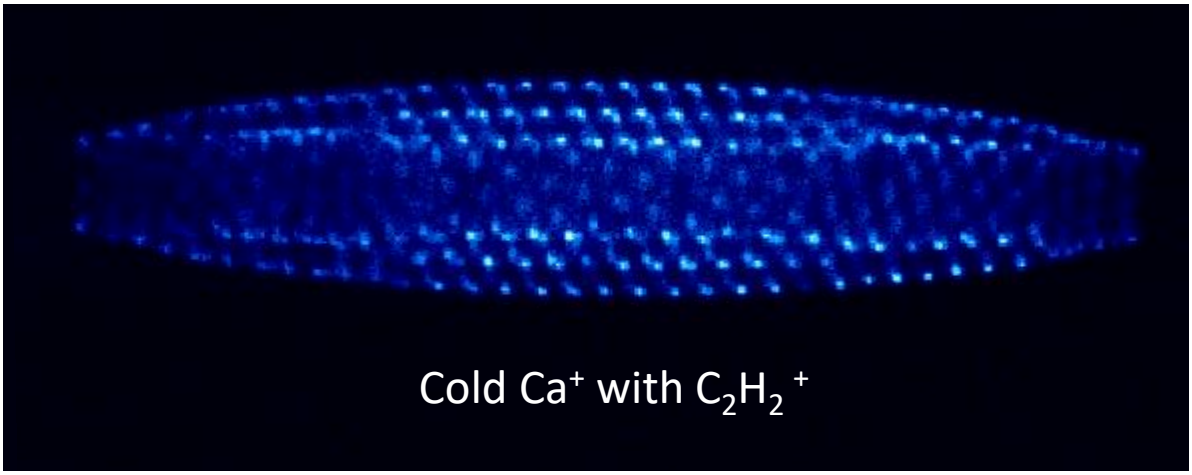

Figure 2.5: False-color fluorescence microscope images of a bi-component coulomb crystal containing Ca^+ and $C_2H_2{}^+$ ions.

ion will typically reach a kinetic energy on the same order of magnitude as the directly laser cooled ions. Depending on how efficient the sympathetic cooling is, the sympathetically cooled ions will also crystallize. This is one clever way of achieving cooling of molecular ions that cannot be directly laser cooled. It should be stressed here that only the external degrees of freedom (translations) of molecular ions are cooled. Internal degrees of freedom (vibrations and rotations) of molecular ions cannot be cooled by collisions between the ions as they do not ever get close enough to one another to do so.

Ions not addressed by the laser will not fluoresce and are often refered to as dark ions. Their location can be inferred by the displacement of laser cooled Ca^+ observed in fluorescence microscope images. When a coulomb crystal contains more than one species of ion it is said to be multi-component, borrowing the term from multi-componenet plasmas. An example of a bi-component crystal is depicted in Fig. 2.5. An immediately noticeable feature of the bi-component crystal is that all the $C_2H_2{}^+$ (26u) are gathered at the core of this crystal. The structure is qualitatively predicted by the pesudo-potential approximation, Eq. (2.13), which shows $\phi^* \propto \frac{1}{m}$. In other words, the radial potential is stronger for lighter mass ions in our trap, and they will fall to the bottom of the well. Ions that are heavier than Ca^+ (40u) will collect at larger radii. Because

ions arrange radially by mass, energy transfer will be most efficient between ions of neighboring masses.

The quantitative structure and energetics of multi-component crystal cannot be predicted analytically. The system is inherently far from thermodynamic equilibrium. The RF trapping field is driving energy into the system via micromotion, while laser cooling removes it. A steady-state structure and energy distribution are none-the-less eventually achieved and can be modeled computationally. Quantitative insight can be gained from these models in the form of effective heating and cooling rates as shown in [66]. These rates, however, are very dependent on the number and masses of constituent ions in a crystal. In order to fully describe a multi-component crystal, one must be able to unambiguously identify the crystal's constituent ions. The tool we use for this task is a time-of-flight mass spectrometer, covered in the next section.

2.4 Time-of-flight mass spectrometry

Many methods have been developed for performing mass spectrometry on trapped ions. The most applicable to the area of trapped ion-molecule reactions are secular mass excitation [32–34] and time-of-flight mass spectrometry (TOFMS) [35–38]. The former relies on exciting the mass-dependent secular frequency of a trapped species; it is, in principle, non-destructive and can be preformed *in situ*. The latter ejects ions from the trap with a large, static DC potential and measures the mass-dependent flight times required to reach an ion detector far away from the trap. While the measurement is destructive (empties the trap), it accurately detects both the mass of species in the trap and how many ions in each constituent mass were trapped.

The underlying principle of TOFMS comes from the motion of an ion in a constant electric field. Consider and ion between two parallel plate-like mesh screens holding a potential difference V_{TOF}. An ion near the higher potential mesh will be pushed towards the mesh at lower potential and ejected from the region of constant electric field with kinetic energy

$$KE_{TOF} = eV_{TOF} = \frac{1}{2}mv^2. \tag{2.28}$$

solving for the ion's velocity v gives

$$v = \sqrt{\frac{2eV_{TOF}}{m}}. \tag{2.29}$$

The time it would then take to reach a detector a distance x away would be

$$t = \frac{x}{v} = x\sqrt{\frac{m}{2eV_{TOF}}}. \tag{2.30}$$

The important result is that the ion arrival time is proportional to the square root of its mass-to-charge ratio: $t \propto \sqrt{\frac{m}{e}}$.

The resolution of a TOFMS is a measure of the relative separation of neighboring mass peaks. It is defined as

$$R \equiv \frac{m}{\Delta m} = \frac{t}{2\Delta t} \tag{2.31}$$

and can be interpreted as the highest measurable mass m that can be distinguished from mass $m+1$. To estimate R, we take a derivative of Eq. (2.30) $\frac{dt}{dv} \approx \frac{\Delta t}{\Delta v}$ which leads to

$$R = \frac{1}{2\Delta v}\sqrt{\frac{2eV_{TOF}}{m}}. \tag{2.32}$$

In order to optimize the resolution of a TOFMS, one must primarily minimize Δv and secondarily maximize V_{TOF}. Δv can be interpreted as the initial spread in velocity (kinetic energy) of a cloud of ions. Laser cooling directly reduces this, leading to excellent TOFMS resolution. Also, the larger V_{TOF}, the better. This is typically constrained by the geometry of the meshes or the electronics driving them.

Counter-intuitively, the free-flight distance of a TOFMS, x, does not affect its resolution. It does however set the scale of t and Δt. These values have an important practical concern based on the response time of the ion detection system. By ensuring that these are long enough, one will be able to measure both t and Δt, and quantify the resolution. Additionally, the integrated signal from the ion detector will be proportional to number of ions in each mass channel. The more data points measured per mass peak, the more accurate that integral calculation will be.

2.5 Bimolecular reaction kinetics and dynamics

The extremely dilute environment of the ultra high vacuum (UHV) chamber ensures that the only reactions we will study are bimolecular. The basics of bimolecular kinetics and dynamics are covered very well in [67–69] and more specifically for ion molecule chemistry in [70].

2.5.1 Kinetics

Here is a quick overview forming the theory basis for our reaction data analysis. Consider reaction of the form

$$\mathrm{A}^+ + \mathrm{B} \xrightarrow{\mathrm{k}} \mathrm{C}^+ + ... \tag{2.33}$$

where $\mathrm{A}^+$is an ionic reactant, B is a neutral reactant, C^+ is the ionic product, and k is the reaction rate constant. By charge conservation, one ionic product is guaranteed from this reaction and any other neutrals produced will be lost from the trap. The probability that a neutral product will participate further in the reaction is practically zero. The rate constant, k, is related to the rate of reaction

$$\begin{aligned} r_A &= \frac{d\mathrm{A}^+}{dt} = -k\,\mathrm{A}^+\,\mathrm{B}, \\ r_C &= \frac{d\mathrm{C}^+}{dt} = k\,\mathrm{A}^+\,\mathrm{B}. \end{aligned} \tag{2.34}$$

It is always the case in our experiment that the neutral reactant is in excess, $\mathrm{B}(t) = const$, and thus we can define an effective rate constant

$$k_{eff} \equiv k\mathrm{B}. \tag{2.35}$$

A neutral reactant in excess makes the kinetics identical to that of a unimolecular process and thus the reaction is called pseudo first-order. Solving Eq. (2.34) gives

$$\begin{aligned} \mathrm{A}^+(t) &= \mathrm{A}_0^+ e^{-k_{eff}t} \\ \mathrm{C}^+(t) &= \mathrm{A}_0^+ \left(1 - e^{-k_{eff}t}\right) \end{aligned} \tag{2.36}$$

where A_0^+ is the initial number of A^+ ions and $\mathrm{C}_0^+ = 0$.

Parallel reactions are described by the model

$$\begin{aligned} \mathrm{A}^+ + \mathrm{B} &\xrightarrow{\mathrm{k}_c} \mathrm{C}^+ + ... \\ \mathrm{A}^+ + \mathrm{B} &\xrightarrow{\mathrm{k}_d} \mathrm{D}^+ + ... \end{aligned} \tag{2.37}$$

which give three first-order linear differential equations

$$\begin{aligned} r_A &= \frac{d\mathrm{A}^+}{dt} = -(\mathrm{k}_c + \mathrm{k}_d)\,\mathrm{A}^+\,\mathrm{B} \\ r_C &= \frac{d\mathrm{C}^+}{dt} = \mathrm{k}_c\,\mathrm{A}^+\,\mathrm{B} \\ r_D &= \frac{d\mathrm{D}^+}{dt} = \mathrm{k}_d\,\mathrm{A}^+\,\mathrm{B} \end{aligned} \tag{2.38}$$

along with the conservation of mass condition $\mathrm{A}_0^+ = \mathrm{A}^+ + \mathrm{C}^+ + \mathrm{D}^+$. The pseudo first-order solutions are

$$\begin{aligned} \mathrm{A}^+(t) &= \mathrm{A}_0^+ e^{-(k_c+k_d)\mathrm{B}t} \\ \mathrm{C}^+(t) &= \mathrm{A}_0^+ \frac{k_c}{k_c+k_d}\left(1 - e^{-(k_c+k_d)\mathrm{B}t}\right) \\ \mathrm{D}^+(t) &= \mathrm{A}_0^+ \frac{k_d}{k_c+k_d}\left(1 - e^{-(k_c+k_d)\mathrm{B}t}\right). \end{aligned} \tag{2.39}$$

The new scale factors are called branching ratios

$$BR_c \equiv \frac{k_c}{k_c+k_d}; BR_d \equiv \frac{k_d}{k_c+k_d}. \tag{2.40}$$

Because the neutral is always in excess, we often observe sequential reactions described by the model

$$\begin{aligned} \mathrm{A}^+ + \mathrm{B} &\xrightarrow{\mathrm{k}_c} \mathrm{C}^+ + ... \\ \mathrm{C}^+ + \mathrm{B} &\xrightarrow{\mathrm{k}_d} \mathrm{D}^+ + ... \end{aligned} \tag{2.41}$$

which give three first-order linear differential equations

$$\begin{aligned} r_A &= \frac{d\mathrm{A}^+}{dt} = -\mathrm{k}_c\,\mathrm{A}^+\,\mathrm{B} \\ r_C &= \frac{d\mathrm{C}^+}{dt} = \mathrm{k}_c\,\mathrm{A}^+\,\mathrm{B} - \mathrm{k}_d\,\mathrm{C}^+\,\mathrm{B} \\ r_D &= \frac{d\mathrm{D}^+}{dt} = \mathrm{k}_d\,\mathrm{C}^+\,\mathrm{B} \end{aligned} \tag{2.42}$$

along with the same conservation of mass condition $\mathrm{A}_0^+ = \mathrm{A}^+ + \mathrm{C}^+ + \mathrm{D}^+$. The pseudo first-order solutions are

$$\begin{aligned} \mathrm{A}^+(t) &= \mathrm{A}_0^+ e^{-(k_c)\mathrm{B}t} \\ \mathrm{C}^+(t) &= \mathrm{A}_0^+ \frac{k_c}{k_d - k_c}\left(e^{-k_c\mathrm{B}t} - e^{-k_d\mathrm{B}t}\right) \\ \mathrm{D}^+(t) &= \mathrm{A}_0^+ \left(1 - \frac{k_d}{k_d - k_c}e^{-k_c\mathrm{B}t} + \frac{k_c}{k_d - k_c}e^{-k_d\mathrm{B}t}\right). \end{aligned} \tag{2.43}$$

The kinetics of a sequential reaction falls into one of three different regimes: $k_c \ll k_d$, $k_c \sim k_d$, and $k_c \gg k_d$. When one of the rate constants is approximately 10 times less than the other, the associated step in the reaction model is called the rate-limiting step.

In practice, a realistic reaction model may be a large combination of parallel and sequential reactions. Since this will always result in a system of linear, first-order differential equations, an analytic solution always exists. The solution in analytic form is far more cumbersome than the system of differential equations, however. When dealing with a complicated model, the data can be directly fit by the system of differential equations. See App. C for a MATLAB script that does just that.

2.5.2 Dynamics

The dynamics of gas-phase reactions are the short-range physics that describe the process of reactants leading to products. Better understanding of reaction mechanisms and the better models that result from them, are the overall goals of this research. That said, there are many useful models that have already been developed. The textbooks mentioned at the start of this section are the most useful references on the subject of dynamics. I will point out the most applicable model to this work.

Most models aim to predict the temperature dependence of reaction rate constants $k = k(T)$. One very famous and successful model is called the Langevin model. This models the long range interaction between an ion and a molecule as a point charge and a polarizable dipole. The effective interaction potential that results contains only a centrifugal barrier. Assuming that all interactions

that make it past that barrier will react delivers the striking result is that the rate constant isn't a function of temperature at all

$$k = \sqrt{\frac{4\pi^2 e^2 \alpha}{\mu}} \tag{2.44}$$

where α is the polarizability of the molecule and μ is the reduced mass $\frac{1}{\mu} \equiv \frac{1}{m_{ion}} + \frac{1}{m_{neutral}}$. Experimentally, however, it was observed that some ion-molecule reactions would accelerate at low temperatures. The increase was attributed to a permanent dipole moment, μ_d, of the neutral reactant increasing the interaction strength. This is due to the average orientation of the dipole being biased towards the ion when fewer rotational states of the neutral are populated. It results in the aptly named average dipole orientation (ADO) model

$$k(T)_{ADO} = \frac{2\pi e}{\sqrt{\mu}} \left(\sqrt{\alpha} + C\mu_d \sqrt{\frac{2}{\pi k_B T}} \right) \tag{2.45}$$

where C is the dipole locking constant, usually $C \sim 0.1$. A detailed derivation of this model can be found in [46]. Comparing this model to our data requires us to define a temperature of our reactions. For the purposes of the ADO model, one needs to define a rotational temperature. This is room temperature for our experiment because the neutral reactant is leaked into the vacuum without any means to cool it.

Generally speaking there is much more to reaction dynamics than the rate constant predicted by the ADO model. For example, both branching ratios of products and isotopic substitution effects are not predicted by ADO. These effects are details of what happens after reactants make it over the centrifugal barrier of the long range potential and are also functions of temperature. Unfortunately, a temperature relevant to these dynamics is not well defined, because a multi-component coulomb crystal system is decidedly far from thermodynamic equilibrium. Since it does reach a steady state with constant energy E, however, we can consider a microscopic picture of the rate constant

$$k = k(E) = \sigma(E) v_{rel} \tag{2.46}$$

where $\sigma(E)$ is the cross-section for reaction and v_{rel} is the relative velocity of reactants within the center-of-mass frame. The microscopic picture separates the internal degrees of freedom of

a molecule (electronic, vibrations, rotations, spin) from the external ones (translations). The distinction is exactly what we need to connect our experiments to the temperature dependence of various models. The internal degrees of freedom are in thermal equilibrium with the black-body background of our room temperature UHV chamber, $\sim$ 300K. The external degrees of freedom can be compared to a classical temperature by average kinetic energy of the system divided by the Boltzmann constant

$$T_{reaction} = \frac{\langle E_{coll} \rangle}{k_B} = \frac{\mu \langle v_{rel}^2 \rangle}{2k_B}. \tag{2.47}$$

If $v_{ion} \sim 0$ then $v_{rel} \sim v_{neutral}$, and

$$T_{reaction} = \frac{T_{neutral}}{1 + \frac{m_{neutral}}{m_{ion}}}. \tag{2.48}$$

For $T_{neutral} \sim 300K$, Eq. 2.48 is an adequate approximation. If $T_{neutral} \leq$ 10K, then the ion kinetic energy distribution must be modeled using molecular-dynamics simulations as demonstrated in [49]. The convolution of the neutral and ion velocity distributions is then used to tabulate the average collision energy.

To model the details of the reaction cross-section and its energy dependence requires quantum chemical calculations of reaction potential energy surfaces. Rice–Ramsperger–Kassel–Marcus (RRKM) theory can then be used to predict branching ratios and build up $\sigma(E)$ from the microscopic picture [71]. Because $\sim$ 300K is already pushing the limits of theoretical accuracy for quantum chemical computations [3], we do not emphasize this analysis. As such, the details of quantum chemical calculations required are beyond the scope of this thesis.

Chapter 3

Experimental Apparatus

A large part of my thesis work was designing, building, rebuilding, and improving the ion trap apparatus. This chapter will describe the apparatus in detail, which has enabled the study of the molecule-ion reactions that follow in later chapters. What follows is adapted from [38]. I will also include updates and improvements we have implemented since then.

Our experimental apparatus consists of a ultra-high vaucuum (UHV) chamber containing a segmented linear quadrupole ion trap and a linear TOFMS, coupled (radially) to the ion trap. We trap $^{40}Ca^{+}$ and perform laser cooling to form Coulomb crystals with temperatures < 1 K. Molecular ions can be co-trapped and sympathetically cooled by the atomic ions.

Trapped ions are detected either by the fluorescence of the atomic ions or by ejecting all trapped ions into the TOFMS. To detect mass spectra with high mass resolution over a wide mass range, the trapping RF amplitude must be switched off within a couple RF periods before the HV extraction pulses are applied to the trap electrodes. Here, dedicated RF drive electronics were built and characterized. The next sections describe in detail these individual components of the apparatus.

3.1 Vacuum chamber

To facilitate high cooling rates and have Coulomb crystal lifetimes of several hours, the vacuum chamber is maintained at a base pressure of $<5\times10^{-10}$ torr using a 600 l/s turbo pump (Pfeiffer HiPace 700) backed by a dry roughing pump (Edwards XDS 35i). A titanium sublimation

pump is used in addition for enhanced pumping of certain residual reactive contaminants. Finally, to eliminate background water in the chamber, a cold finger filled with liquid nitrogen is used occasionally.

3.2 Linear ion trap – time-of-flight mass spectrometer (LIT-TOFMS)

The central component of the experimental apparatus is a segmented, linear quadrupole ion trap built from four rods (see Fig. 3.1). RF potentials of several hundred volts peak-to-peak are applied to the rods to produce a time-averaged trapping potential in the radial dimension. Additionally, each rod is divided into three electrically isolated segments, which allow for the application of individual DC voltages on each segment to confine the ions along the longitudinal axis. The DC voltages can also be used to make small adjustments to the position of the ion cloud in three dimensions to center the ions on the node of the RF potential, thus minimizing RF heating of the ions.

Our trap has an inscribed radius of $r_0 = 3.91$ mm and a trap rod radius of R = 4.5 mm. This ratio produces a nearly perfect radial quadrupole field in the center of the trap [61], reducing the micromotion heating of the ions. The central segments of the ion trap have a length of $2\times z_0 = 7$ mm, while the outer segments have a length of $6\times z_0 = 21$ mm. These lengths give rise to an approximately harmonic axial potential in the center of the trap. To trap the laser-cooled atomic ions, the RF frequency applied to the electrodes is $\Omega_{RF} \approx 2\pi\times 3.5$ MHz with an amplitude up to V = 250 V. Axial confinement is achieved with DC potentials of $V_{DC} \leq 10$ V applied to the outer segments of the rods (Fig. 3.1). A summary of typical trapping parameters is given in Tab. 3.1.

Table 3.1: Typical trapping parameters and trap geometry specifics. Also included are some calculated values (not measured) for $^{40}Ca^{+}$ using the typical trap parameters and the equations found in Ch. 2.

Trap parameters			Calculated trap values		
RF frequency	Ω_{RF}	$2\pi\times$3.552MHz	Mathieu q param	$\lvert q_{x,y}\rvert$	0.25
RF voltage	V_{RF}	200V	Mathieu a param	$\lvert a_{x,y}\rvert$	0.0012
endcap voltage	V_{EC}	3.5V	radial frequency	$\omega_{x,y}$	$2\pi\times$162kHz
endcap separation	$2z_0$	7mm	radial trap depth	$D_{x,y}$	12.6eV
inscribed raduis	r_0	3.91mm	longitudinal frequency	ω_z	$2\pi\times$43.8kHz
geometric factor	κ	0.22	longitudinal trap depth	D_z	0.77eV
rod radius	R	4.5mm	ion density	n_0	4.58×10^7 1/cm^3

To produce calcium atoms for loading into the trap, we use an effusive calcium beam generated by a home-built, resistively heated Ca oven. The oven is made out of a thin-walled stainless steel tube, crimped on both ends, with an 1 mm^2 opening at one end. The oven is mounted 300 mm from the trap center and uses a collimating aperture in the beam path to minimize Ca deposition on the trap rods. A beam flag is placed in the atomic beam path as a shutter to block the Ca impinging on the trap after the loading process. This allows the Ca oven to be kept at a consistent temperature at all times, while reducing the influence of the oven products on the trapped ions. The atomic beam of ^{40}Ca is then ionized in the trap center using non-resonant photo-ionization at 355 nm (Continuum Minilite II, 10 Hz, 5 ns pulse length, up to 7 mJ/pulse, focused $f = 20cm$). In addition to the Ca oven, we installed a set of three alkali atom sources dispensers (SAES) — K, Rb and Cs — for calibration of the TOFMS spectra. A shield prevents direct line of sight between the dispensers and the trap.

The trapped atomic ions are laser cooled on the $4^2S_{\frac{1}{2}}$- $4^2P_{\frac{1}{2}}$ transition of $^{40}Ca^{+}$ using a fiber-coupled 397 nm diode laser (NewFocus, 3.5 mW, 600 μm beam diameter). The ions are repumped from a dark state on the $4^2P_{\frac{1}{2}}$ - $3^2D_{\frac{3}{2}}$ transition using a second fiber-coupled diode laser at 866

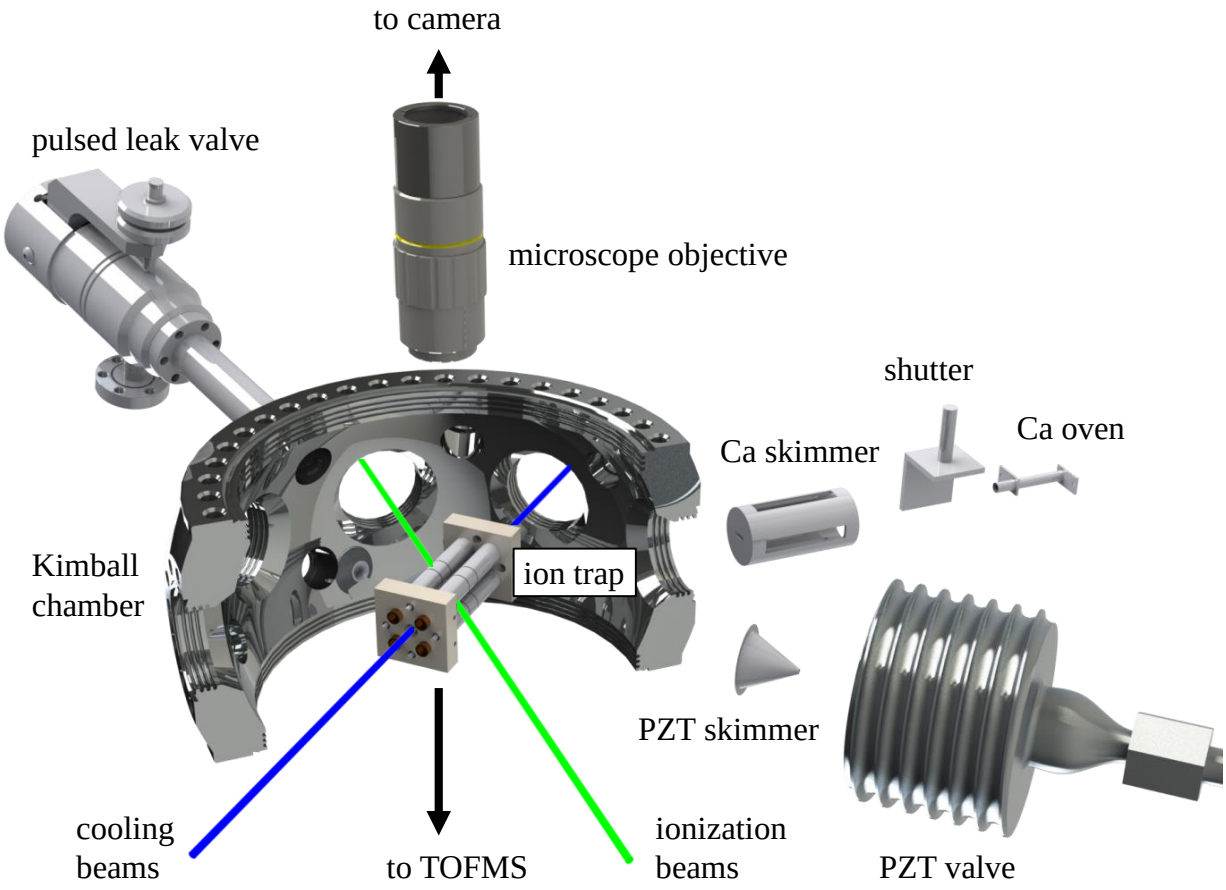

Figure 3.1: Exploded schematic of the ion trap and detection optics. The ion trap has four rods, which are broken into three segments each. RF potentials are applied to all 12 segments. In addition, small DC potentials are applied to form a trapping field along the longitudinal axis. Directly above the ion trap sits a 10x microscope objective to image the fluorescence from the Ca ions onto a EMCCD camera. The drift tube (not shown) of the TOFMS is located directly below the ion trap.

nm (NewFocus, 9 mW, 2 mm beam diameter). The two diode laser frequencies are measured by a wavemeter (High Finnesse/Ångstrom WSU-30), which is calibrated daily to an additional diode laser at 780 nm locked via saturated absorption spectroscopy to a transition in ^{87}Rb (see Fig. 3.2). The calcium cooling laser frequencies are locked via a slow LabVIEW controlled servo based on the wavemeter readings.

For efficient cooling of ion crystals down to the single ion level, the 397 nm laser beam is directed into the center of the trap from up to three directions (two counter-propagating beams

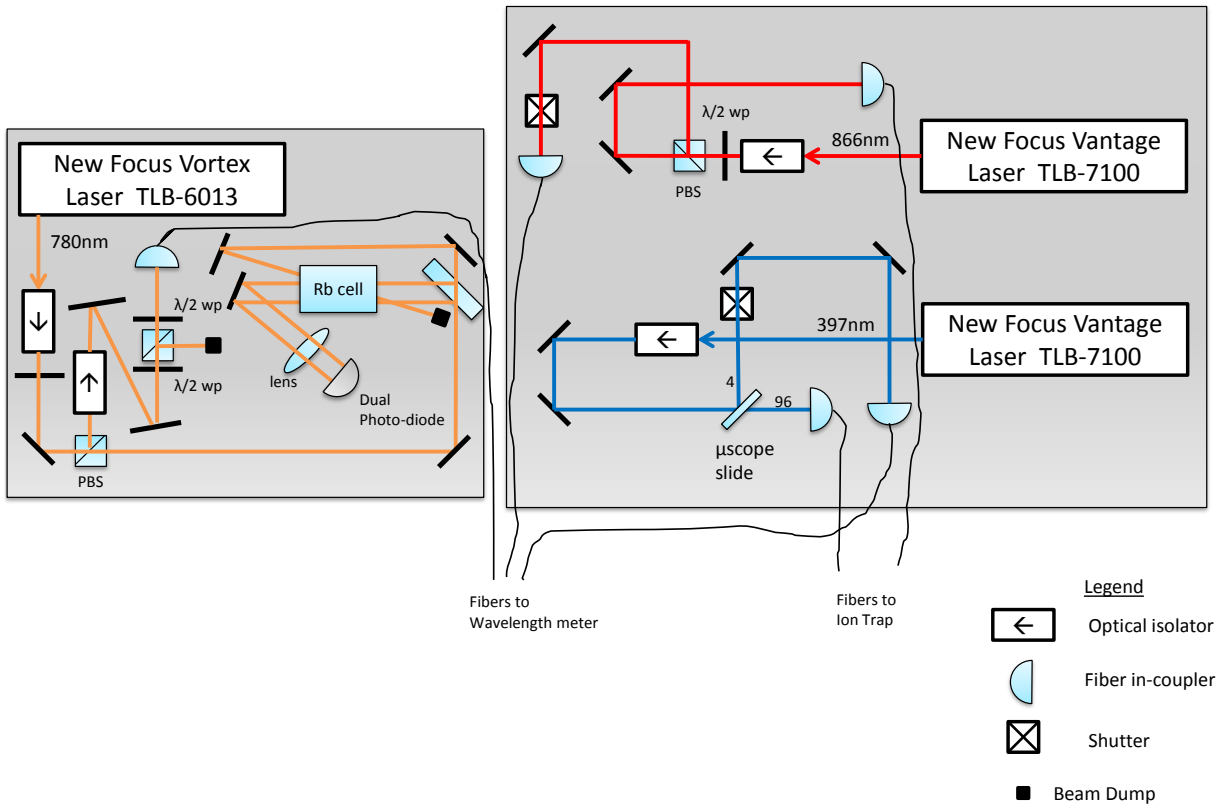

Figure 3.2: Laser breadboard layouts for diode lasers used in the experiment.

along the axial dimension and sometimes one beam along ionization beam-path, acting to cool radial dimension). The axial beams are of equal intensity, while the radial beam has about 2% of the total power. The radial beam is required to efficiently cool only small strings of ions, but is unnecessary for large crystals. The emitted fluorescence at 397 nm from $^{40}Ca^{+}$ is collected by a 10× microscope objective (Mitutoyo) and imaged onto an EMCCD camera (Andor iXon 897). This allows real-time, non-destructive detection of ions stored in the trap. See Fig 3.3 for a schematic layout of the laser and imaging system.

In addition to imaging the fluorescence to determine the number of Ca ions, we have incorporated a radially extracted TOFMS to the ion trap to greatly increase the accuracy of measurements of non-fluorescing ions. The TOFMS consists of two stages of longitudinal electric fields that ex-

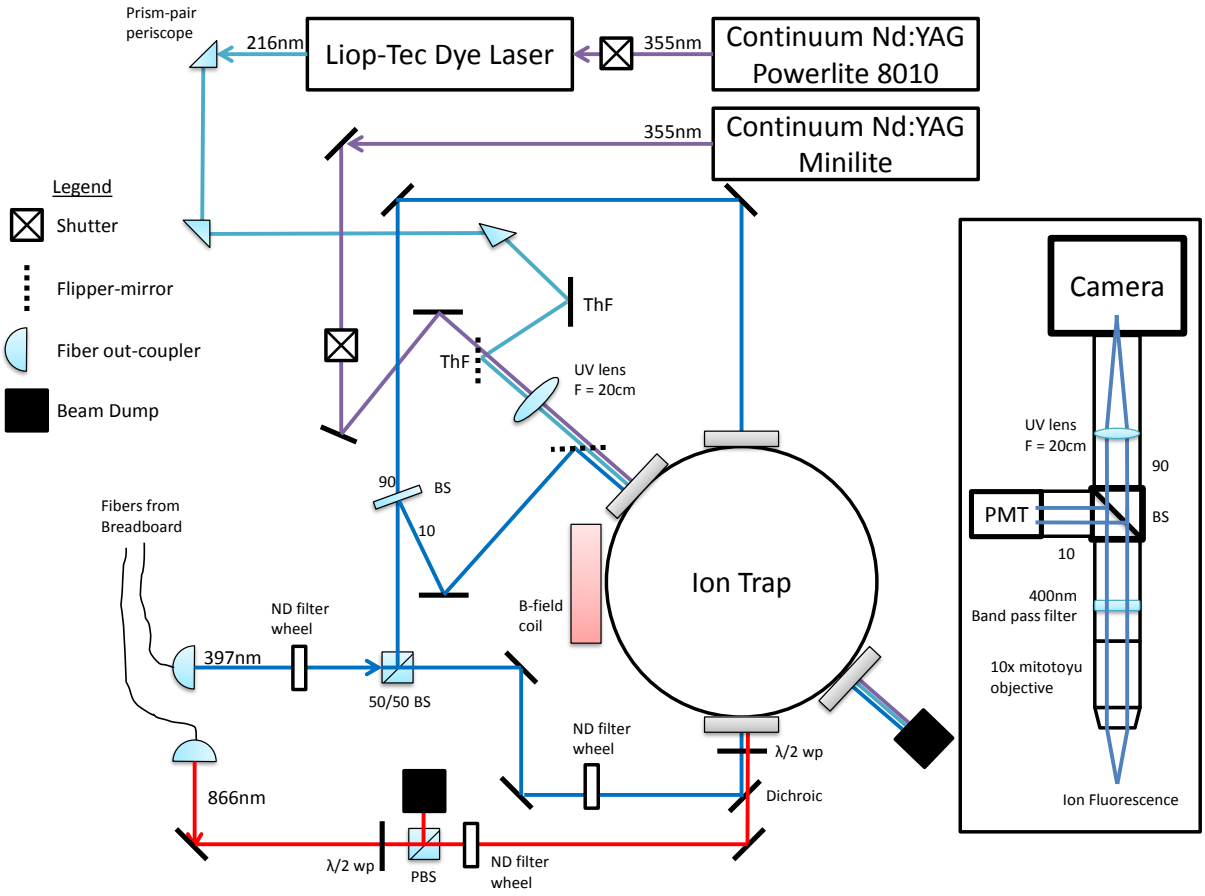

Figure 3.3: Optical beampaths of ionization lasers and cooling lasers used in this thesis. Two flipper mirrors are used in conjunction with the shutters to send one of the two ionization lasers into the chamber at a time or the radial cooling beam for the calcium.

tract the ions from the trap and accelerate them into a longitudinal zero potential drift tube. The entire length of the TOFMS is 540 mm. The trap electrodes themselves create the repeller and extractor fields for the TOFMS. This is accomplished by applying large DC potentials to the four trap rods, where the two rods farthest away from the entrance of the drift tube (i.e., repeller rods) are at one positive potential, and the two trap rods closest to the drift tube (i.e., extractor rods) are at another, lower, positive potential (see Fig. 3.4, left, for more details). A drift tube, held at ground potential, is placed between the ion trap and the ion detector to minimize the influence of stray fields on the post-accelerated ions. The entrance into the drift tube, which is 22 mm from the center of the trap, is limited by a 2 $\times$ 5 mm elliptical hole located directly below the center

of the trap. Using a small opening reduces the fringe fields from the trap electrodes penetrating into the drift tube. Directly after the entrance of the drift tube are a set of four deflection plates for beam steering and a cylindrical Einzel lens for beam focusing. At the end of the drift tube, a 40 mm diameter micro-channel plate (MCP) detector (double-stack in Chevron configuration, Jordan-TOF) produces a TOF spectrum from the ions.

During an experimental run, the process to detect the ions is as follows. First, the RF trapping field is rapidly quenched over ∼2 RF cycles. Second, after an optimized time delay, high voltage is pulsed onto the four trap rods (see Fig. 3.4 for more details). This creates a two-stage acceleration field in a Wiley-McLaren configuration [72], increasing the mass resolution of the recorded spectra. Third, the ions pass through deflection plates and an Einzel lens, neither of which are currently used. Finally, the ions hit the MCP detector creating a current that is split by a 50/50 RF power splitter (MiniCircuits ZSC-2-1). The currents are converted to voltages using two separate channels of a fast (1GHz) digital storage oscilloscope. The two channels of the oscilloscope are set with different vertical scaling to allow for the dynamic range required to simultaneously measure the large number of calcium ions (25 – 1500) on one channel, while still having the sensitivity on the other channel to measure lower numbers of (molecular) product ions (1 – 25).

3.3 Electronics

The electronics for operating a combined ion trap/TOFMS instrument need to perform three distinct operations : (1) application of RF and small DC fields for ion trapping, (2) rapid quenching of the RF voltage to create zero electric fields to prepare for ion extraction, and (3) rapid application of high DC voltages for ion extraction. First, during the normal trapping mode, the electronics must produce two RF sine waves at the same frequency (a few MHz), but with a 180° phase shift between the two signals. The amplitude of these signals must be variable up to 250 V. Second, for optimal extraction of the ions into the TOFMS, the RF fields must be turned off within 1-2 RF cycles. Otherwise, the RF fields will distort the extraction field, reducing the mass resolution of

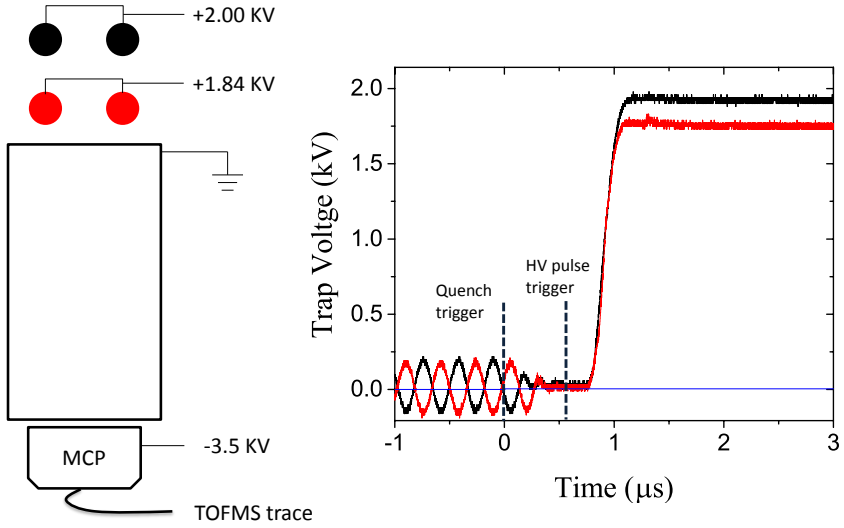

Figure 3.4: Left: Schematic representation of the TOFMS. Shown in red and black are the repeller and extractor configuration of the trap rods for radial ejection of trapped ions into the TOFMS. Right: The corresponding repeller and extractor voltages as a function of time, required to go from trapping to TOFMS. Vertical dotted lines represent the timings of the quench and HV pulse control triggers.

the TOFMS. Finally, to direct the ions into the drift tube with well-defined starting conditions, two HV pulses with fast rise times and different amplitudes must be applied to the four trap rods to extract and accelerate the ions towards the MCP.

In the following, we present a simplified version of an electronic circuit to drive an ion trap TOFMS with the schematic shown in Fig. 3.5. Complete circuit diagrams can be found in App. A. The electronics are capable of generating two RF potentials 180° out of phase with an amplitude of several hundred volts for a single resonant frequency in the 1-5 MHz range. The RF amplitude can be quenched within 1-2 RF cycles and two fast HV pulses of different amplitudes up to 2.5 kV can be produced. Unlike other published implementations of such a combined system, our design can have an arbitrary time delay between the RF quench and the HV pulses. This preserves the Wiley-McLaren condition [72] for the TOFMS.

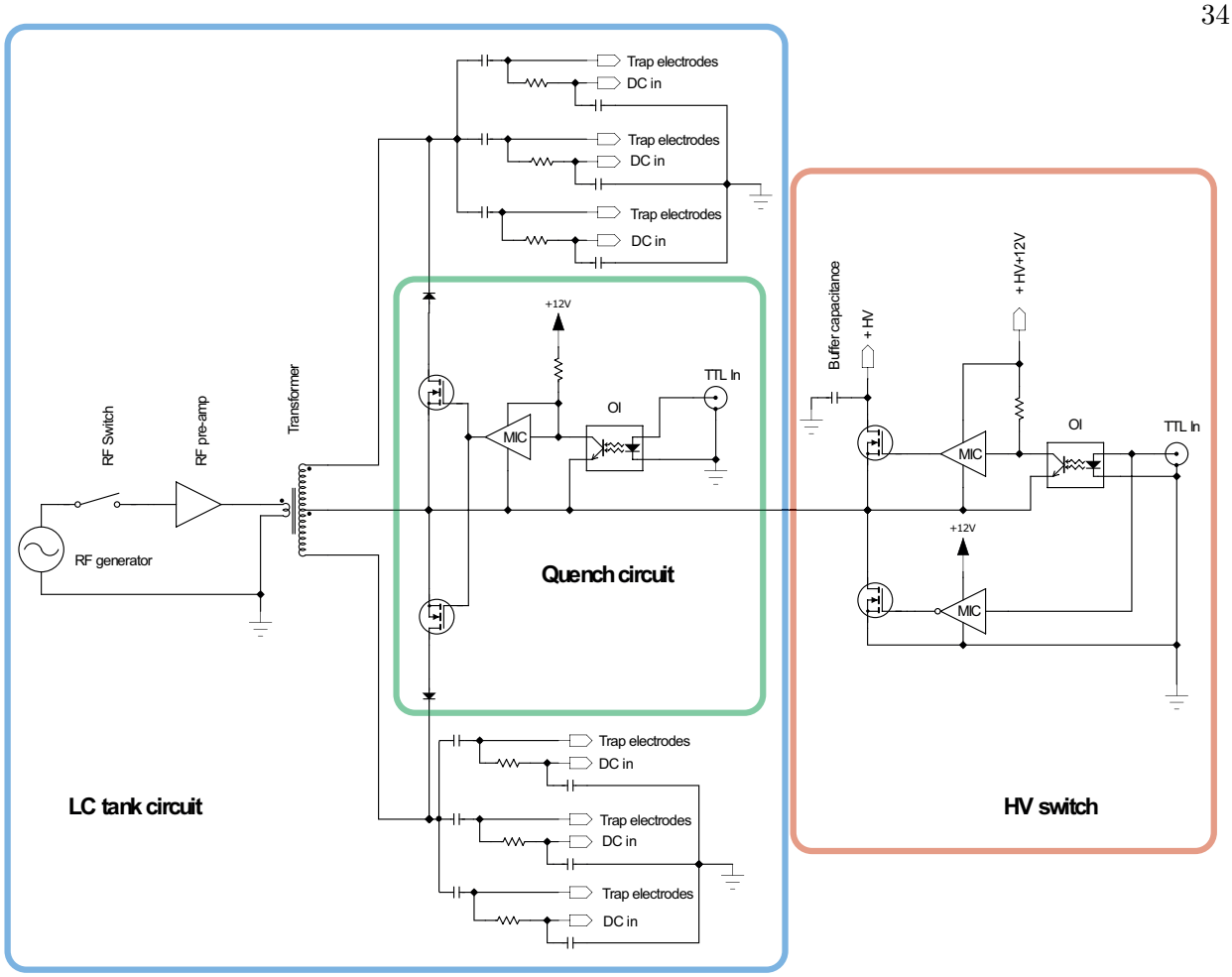

Figure 3.5: A schematic diagram of the RF drive electronics. The diagram shows the three different parts (marked by colored boxes) required for ion trapping and extraction into the TOFMS (only single side of bifilar winding is shown).

Our design can be divided roughly into three distinct sections: a LC tank circuit for generating the RF trapping potentials, a quench circuit for rapidly switching off the RF, and an HV switch for creating the extraction pulses for the TOFMS. In the following sections, the individual parts of the circuit are described in more detail.

3.3.1 LC tank circuit

For driving the ion trap with the required RF field, we use a LC tank circuit, as shown in Fig. 3.5. The inductor, L, is a hand-wound transformer coil, while the ion trap electrodes and

SHV cables form the capacitance of the circuit. Low voltage RF is generated by a signal generator (Stanford Research Systems, DS345) and amplified by a home-built RF pre-amplifier before driving the primary side of a toroidal transformer core (Mircometal, T200-2). For the secondary side, we use a center-tapped bifilar winding, which is required for the application of the two individual HV pulses for ion extraction. The center-tap creates two RF signals with 180° phase shift. During ion trapping operation, the center-tap is kept at ground potential and pulsed to HV for mass analysis with the TOFMS. Each electrode is also AC coupled by individual blocking capacitors. By choosing the appropriate values of L and C, the RF frequency is set to $\Omega \approx 2\pi \times 3.552$ MHz. To apply individual DC voltages on each ion trap segment, a low-pass filter couples the DC to the RF on the trap side of the blocking capacitors.

3.3.2 Quench circuit

Fast quenching of the RF before ion extraction is required for high resolution TOFMS mass spectra. If the RF is turned off by removing the input signal only, a long ring-down period of several tens of microseconds will be observed due to the high quality factor of the LC tank circuit. To reduce the turn-off time to within 1-2 RF cycles, we implement an active damping circuit (quench) into our LC tank circuit. The high voltage sides of each secondary winding are connected to the respective center-tap by a diode-MOSFET chain. When the MOSFET closes it creates a low-resistance current path, effectively shorting the coil. This stops the RF output in minimal time. Quenching is implemented on the secondary winding of each side of the center tap simultaneously to reduce the quench time by nearly a factor of two. Additionally, the input RF is turned off via an RF switch (Mini-Circuits ZYSW-2-50DR) on the primary side of the coil at the same time as the quench. This further reduces the turn-off time of the RF potentials on the trapping electrodes.

The arrival time of the ions at the MCP depends sensitively on the phase of the RF cycle when the quench is triggered, thus we trigger the quench circuit at a zero crossing of the RF signal. This ensures that the ions always experience similar electric field distributions, reducing RF phase-dependent jitter in the mass spectra. The timing of the trigger signal with respect to the zero

crossing introduces an overall 20-30 ns jitter in the arrival times of all ions within a single mass spectrum.

Additionally, because the HV pulses are applied on the center-taps, the quench circuit must be able to float up to 2 kV together with the coil during ion extraction. To accomplish this, the MOSFETs (MTP2N50E) are controlled by a driver chip (MIC4429, MIC in Fig. 3.5) triggered by an optocoupler (6N137, OI in Fig 3.5), where the entire circuit is powered by floating 12 V rechargeable battery pack (Tenergy NiMH 12V 2000mAh). This configuration allows the circuit to float to the required HV during the extraction.

A quick addendum on floating power: Batteries are the ideal floating power supply for this circuit because it produces extremely low-noise DC power. DC-DC switch mode power supplies were used previously but they introduce $\sim$ 100 kHz noise into the circuit. This noise would find its way onto the trap rods and excite secular resonances of the trapped ions.

3.3.3 HV switches

After the RF signal is quenched, a fast rise time HV pulse is applied to extract the ions out of the trap and accelerate them into the drift tube. To produce the HV pulse (2 kV), we use a home-built HV switch, shown in Fig. 3.5. The central elements are two MOSFETs (IYXS IXTL2N450) in a push-pull configuration. The low-voltage side MOSFET is driven by a single MOSFET gate driver (MIC4429, MIC in Fig. 3.5) and the gate of the high-voltage side MOFSET is driven by a opto-coupled gate driver (MIC4420, MIC in Fig. 3.5), which is powered by the same battery pack as the quench circuit. This floating design is similar to the quench circuit.

Two of these HV switches are used to apply different potentials to the repeller and extractor rods. The two switches are connected directly to the center-tap of each of the bifilar windings. During the RF trapping configuration, the high-voltage side MOSFET is open while the low-voltage side MOSFET is closed, thus providing a ground connection for the center-tap of the secondary windings.

The output of the combined quench and HV switch circuits is shown in the right half of

Fig. 3.4. The two phases of the RF are measured by attaching a pair of 100× oscilloscope probes to two trap electrodes. Time = 0 indicates the MOSFET trigger to short the coil and switch off the input signal. The RF amplitude then decays within two RF cycles. We measure a 100% to 10% decay time of 360 ns, which is nearly independent of the initial RF amplitude. We adjust the time between the quench and HV pulse triggers to optimize the detection efficiency and mass resolution of our TOFMS. The delay of the HV switch with respect to the quench trigger was set to 600 ns. The HV pulses on repeller and extractor have identical turn-on characteristics and reach the design amplitude of 2 and 1.84 kV at the same time (the mismatch between objective and measured amplitudes is due to the oscilloscope probe capacitance). The 10% to 90% rise time of the HV pulses is measured to be 220 ns and displays a smooth increase in voltage. The rapid quench and HV pulses coupled with a controllable delay between the the two operations leads to a high mass resolution in the TOFMS spectra.

3.4 TOFMS performance

In addition to loading Ca ions into the trap to be laser cooled, we can load in other atomic (or molecular) ions where they will be sympathetically cooled by interactions with the Ca ions. Using SAES atom dispensers as the source of neutral atoms, we were able to ionize, co-trap, and cool various alkali atoms in our trap, including $^{39}K^+$, $^{85,87}Rb^+$, and $^{133}Cs^+$. These ions serve as a convenient source of different mass ions to be able to calibrate our mass spectrometer. Fig. 3.6 shows a typical single shot (non-averaged) mass spectrum of a multi-component Coulomb crystal and its corresponding fluorescence signal. Because the mass range of interest is centered around 40 u, we optimized the TOFMS voltages and timings to this region.

The mass spectrum in Fig. 3.6 shows several distinct ion peaks, which can be directly assigned to the ionized atoms. The peak with the strongest intensity is created by $^{40}Ca^+$. The smaller peak to the left is $^{39}K^+$, while the very small peak on the right hand side of $^{40}Ca^+$ is another isotope of calcium, $^{44}Ca^+$. The relative peak heights of $^{40}Ca^+$ and $^{44}Ca^+$ represent the natural isotopic abundance. At higher masses, $^{85}Rb^+$, $^{87}Rb^+$, and $^{133}Cs^+$ can be identified. Apart from these

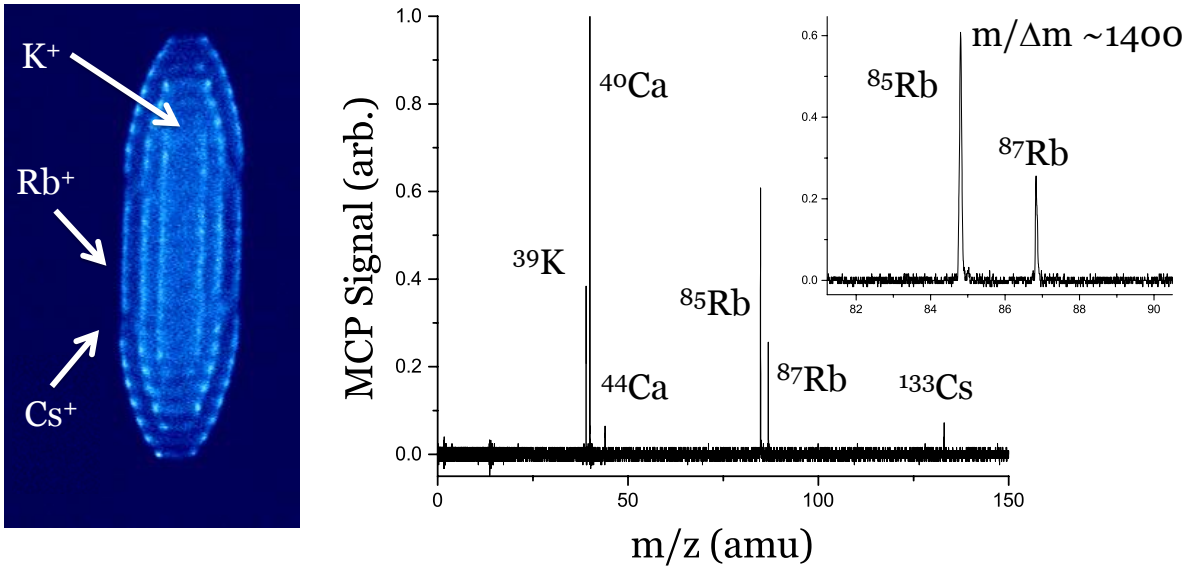

Figure 3.6: A single-shot TOFMS mass spectrum (right) of trapped, laser-cooled $^{40}Ca^+$ and co-trapped $^{39}K^+$, $^{44}Ca^+$, $^{85,87}Rb^+$ and $^{133}Cs^+$. This Coulomb crystal (left) contained 986 ions with 594 of them being $^{40}Ca^+$. Apart from these ions, no further mass peaks can be identified.

masses, no further ions are present. The inset shows the resolving power of the TOFMS by the clear separation of the $^{85}Rb^+$ and $^{87}Rb^+$ peak.

We determine the mass resolution of our TOFMS and how it depends on the mass of the ion being detected and on the number of ions in the trap. The mass resolution is defined as $R = t/(2\Delta t) = m/\Delta m$. In the following experiments, the mass resolutions from single, individual mass spectrum are reported. This is motivated by the planned experiments on measuring chemical reactions, which require the recording of non-averaged mass spectra. For our current experimental triggering system, we have a 20-30 ns jitter in the arrival time between two individual, subsequent mass spectra. However, we can calibrate each mass spectrum to $^{40}Ca^+$, thus reducing the uncertainty in the accuracy of the mass identification. The residual uncertainty is 0.01 u for ^{85}Rb, as an example. Using the definition of mass resolution from above, every peak in the mass spectrum in Fig. 3.6 has a mass resolution of R>1200, with the exception of $^{40}Ca^+$. The ion number for $^{40}Ca^+$ is too

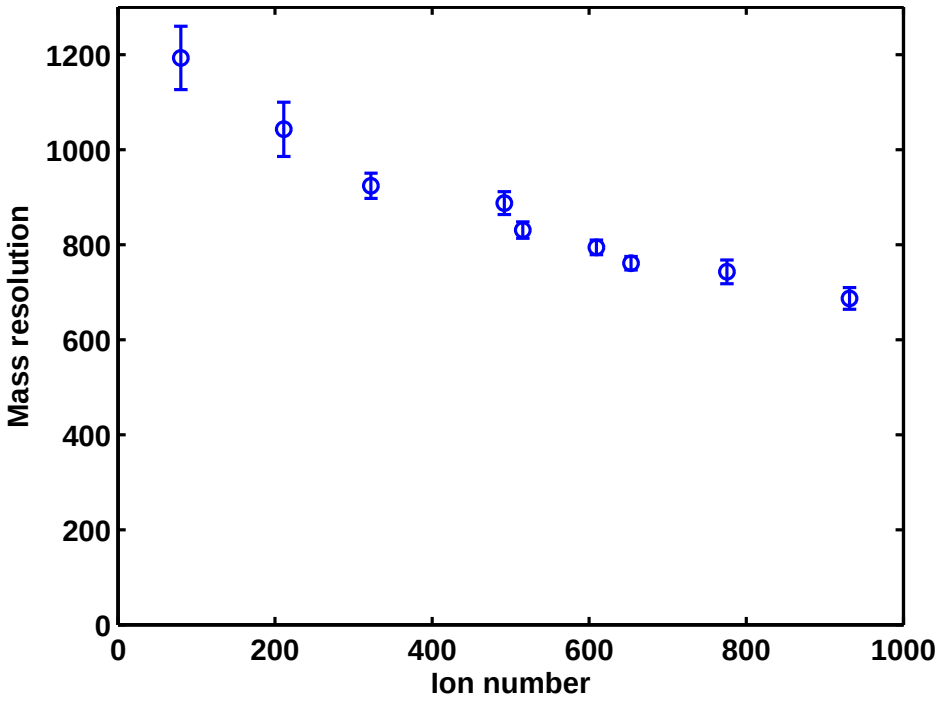

Figure 3.7: Dependence of mass resolution on trapped ion numbers. Pure $^{40}Ca^{+}$ Coulomb crystals of different sizes are trapped and detected in the TOFMS. We observe a decrease of mass resolution with increasing ion number.

great to observe equally high mass resolutions. Coulomb explosion in the drift tube means the mass resolution is expected to decrease with increasing ion mass and ion numbers. To investigate this relationship in our system, we plot the measured mass resolution as a function of ion number for $^{40}Ca^{+}$. The results of this are plotted in Fig. 3.7

3.5 Ion number calibration

Mass spectra must be calibrated to allow extraction of absolute numbers of ions present at each mass for a single shot. We use information from the fluorescence images of the crystals to calibrate our mass spectrometer. The trapped calcium ions represent a deterministic ion source, as the number of ions can be directly counted for small crystals using the fluorescence images. To determine the transfer function of our TOFMS, we start by loading a small crystal (1 –40 ions) into the trap and counting the number of ions in the resulting fluorescence image via a MATLAB

script. Then, we eject the ions into the TOFMS and record a spectrum. We integrate the peak in the spectrum corresponding to $^{40}Ca^{+}$, which produces a number with units of nVs. The results of this procedure are shown in Fig. 3.8. The plot shows a linear relationship between the number of ions in the trap and the integrated signal from the MCP. The fitted slope of $1.73\pm0.07\times10^{-3}$ nVs/ion is then used to determine the number of ions during subsequent reaction experiments. This calibrated ion number is also valid for larger Coulomb crystals, as long as the MCP shows a linear response with the increasing ion numbers. To test this linearity, we loaded pure $^{40}Ca^{+}$ crystals with different sizes into the trap. As Coulomb crystals have nearly a constant ion density, we expect a linear relationship between the size of the Coulomb crystal (as determined by the CCD image) and the integrated MCP signal. From the measured data, we have seen little deviation from linear behavior up to 1500 ions (See Fig. 3.9).

Using a single trapped ion, we can also measure the probability of detecting a ion. We extract a single ion into the TOFMS and observe a signal from the MCP about 38±3% of the time. This is the transfer efficiency of the entire system. The largest contribution to the decrease in detection efficiency is the quantum efficiency of the MCP detector, which is 50–55% [73].

To use the LIT-TOFMS as a platform for studying chemical reactions, one must be able to determine the initial number of trapped ions before the reactions. Although the number of ions loaded into the trap is relatively reproducible, there is some variation and a direct measurement of the initial trap number will help to reduce the uncertainty in the reaction measurements. Since the TOFMS measurements are destructive, we need to use data from the fluorescence images to determine the initial number of ions. We calculate the number of ions by multiplying the density in the trap by the volume of the Coulomb crystal. The Coulomb crystal volume is determined by an ellipsoidal fit of the CCD image. The density is then found by fitting a line to the measurements of the integrated MCP signal (calibrated ion number) vs. the volume of the crystal (Fig. 3.9). From these data, we calculate the ion density for our ion trap to be $7.8\pm0.2\times10^{7}$ ions cm^{-3}. This density depends on only the trapping potential and is fixed for any one reaction experiment.

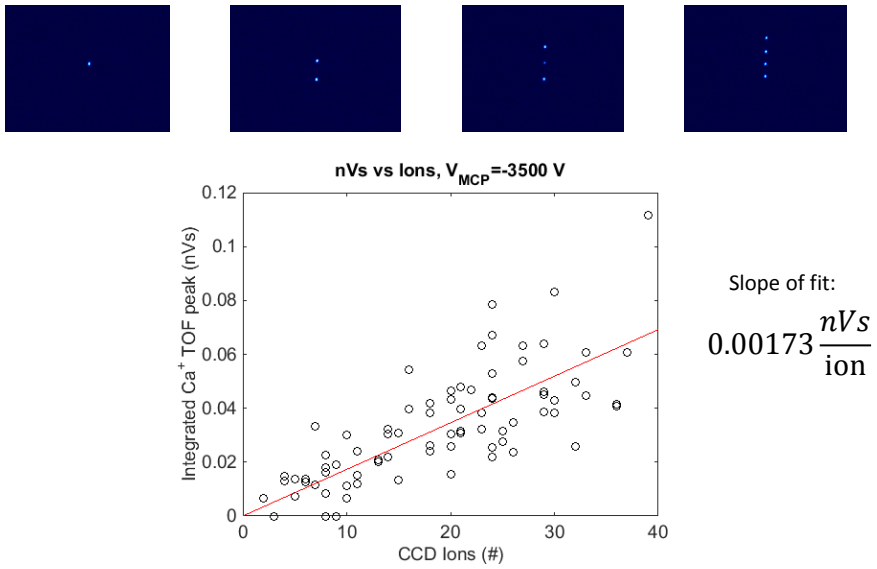

Figure 3.8: Calibration of the MCP signal to ion number. To calibrate the MCP signal, we start by loading small crystals into our trap and counting the number of ions on the image. Then, by extracting those ions into the TOFMS and integrating the resulting MCP signal, we determine how the MCP signal relates to the number of ions in the trap. Using this calibration, we can determine the absolute number of ions in the trap for subsequent experiments.

3.6 Calcium state population calibration

Doppler laser cooling enables quantum control of the electronic degree of freedom in Ca^+. We can directly manipulate the steady-state populations of the three states in Ca^+ accessible by our cooling lasers (see Fig. 2.3). We utilize this control in the experiment to reveal any quantum-state dependence in reactions involving Ca^+. In practice, quantum control is accomplished by changing the cooling laser detunings from resonance. To be confident in the state populations generated by a given pair of detunings, the state populations must be calibrated.

Our calibration procedure is closely based off of the procedure in [1]. We even use their Matlab code in our analysis (see App. C). Our extension to their procedure begins by identifying the five experimentally controlled variables that affect the state populations and the five free parameters in OBE used to predict the state populations. These variables and parameters, along with their

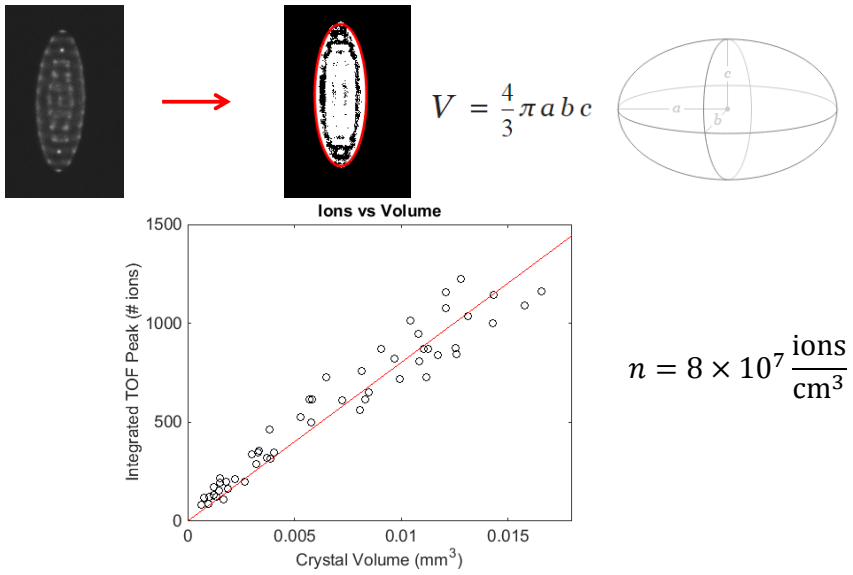

Figure 3.9: Determination of the ion density in our ion trap. We correlate the measured ion number from the TOFMS to the fitted Coulomb crystal volume taken from the recorded CCD images. From a fit to these data, we can determine the ion density in our trap. The inset shows a Coulomb crystal with an ellipsoidal fit.

typical values, are summarized in Tab. 3.2. Since the effects of each of the variables on the state populations are highly coupled, our setup cannot calibrate each of the five fit parameters individually. Instead, we collect a lot of data and globally fit all five parameters. The data that are collected attempts to explore as large of the variable space as possible by only varying one variable at a time, while holding the values of all the other variables constant. The procedure is essentially a principle component style analysis.

The dependent variable in the analysis is the coulomb crystal fluorescence intensity as measured by the camera. This is measured by taking a background subtracted image of the coulomb crystal and summing up the value of every pixel. Since the camera counts are recorded on an absolute scale, the counts will be proportional to the fluorescence intensity, which in-turn, is proportional to the $P_{1/2}$-state population. As long as all the calibration data are taken with the same Coulomb crystal, a global scale factor between the OBE $P_{1/2}$-state and the measured fluorescence

can be defined. The fit procedure does this automatically, but it will not be the same from crystal to crystal if the ion numbers are different. This is only a practical concern for calibration. Once calibrated, the OBE model calculates the state-populations that apply to any number of ions. It cannot predict, however, the corresponding fluorescence. An example dataset with global fits generated by the OBE are shown in Fig. 3.10. This fit corresponds to the parameters given in Tab. 3.2.

Table 3.2: Variables used to calibrate OBE fit parameters with typical trap parameters in Tab. 3.1

Experimental variables			OBE fit parameters		
397nm laser power	P_{397}	1.7mW	397nm power correction factor	c_{397}	0.6
866nm laser power	P_{866}	13.2mW	866nm effective intensity	c_{866}	1.0
397nm detuning	Δ_{397}	-30MHz	397nm effective linewidth	Γ_{397}	10 MHz
866nm detuning	Δ_{866}	20MHz	866nm effective linewidth	Γ_{866}	8 MHz
866nm polarization	α	$\frac{\pi}{4}$	B-field magnitude	B_{mag}	1.9 Gauss

3.7 Gas Handling

The two other major labeled components in Fig. 3.1, not discussed thus far, concern introduction of gases into the UHV chamber. They are the pulsed leak valve and a piezo-transducer driven (PZT) valve.

3.7.1 Pulsed leak valve

The pulsed leak valve is for delivering a neutral reactant to the trap center. Since the valve opening does not have a direct line of sight to the ion trap center, gas is delivered by flooding the chamber. The neutral reactant gas is nominally in thermal equilibrium with the UHV chamber ($\sim 300K$). The pulsed leak valve is the combination of two valves: a high-precision, all-metal leak valve (Duniway VLVE-2000) backed by a solenoid actuated, 3-way valve (Parker XM30VBG45A).

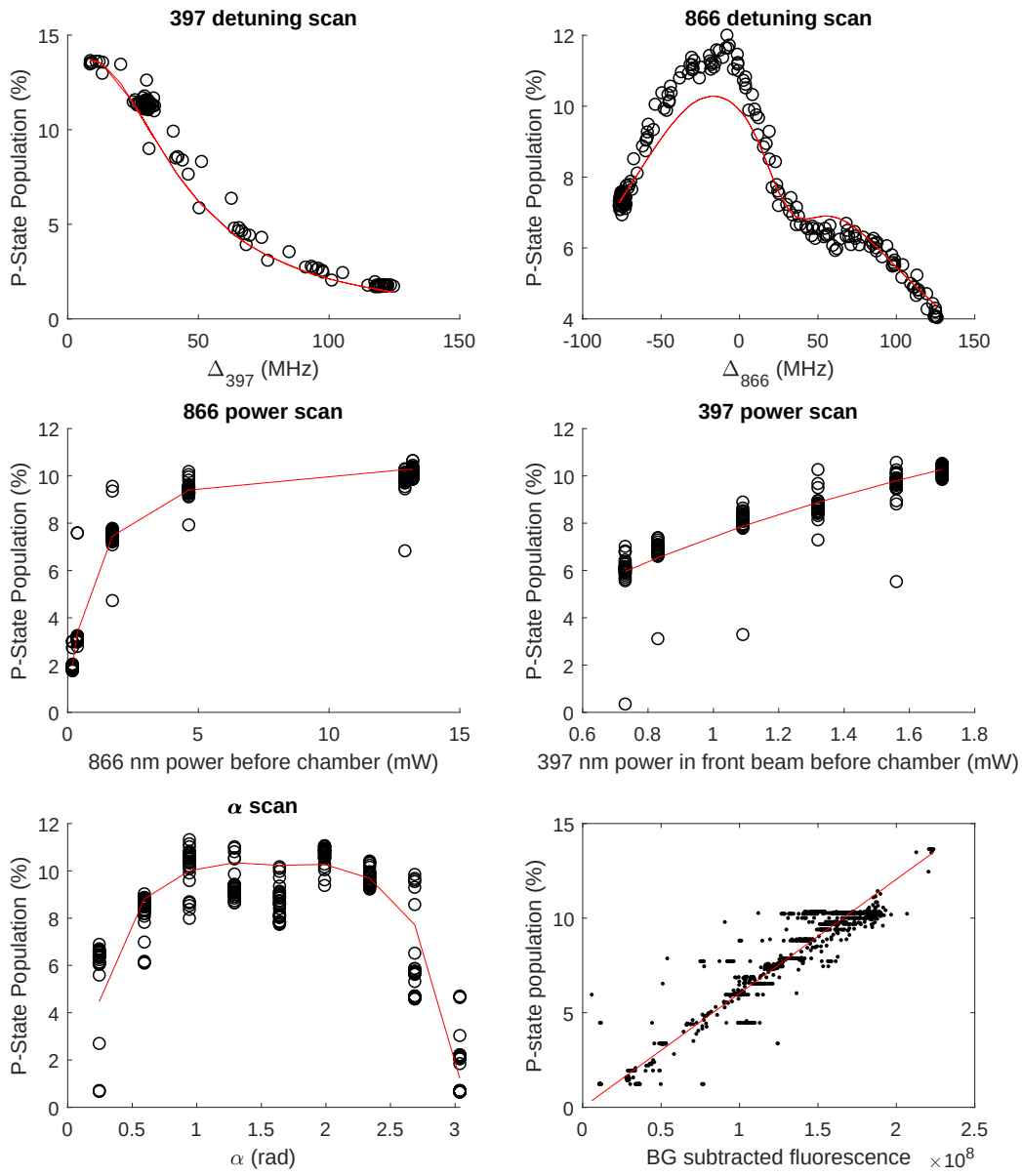

Figure 3.10: Five calibration data sets to constrain the parameters of the OBE. These five plots are fit simultaneously (red lines) to determine the p-state population. The sixth plot is the global scaling of intensity to p-state population. **NOTE:** the detunings plotted are defined opposite from the majority of the literature, *i.e.:* $\Delta_{model} = -1 \times \Delta$. This is a holdover from the base code taken from [1].

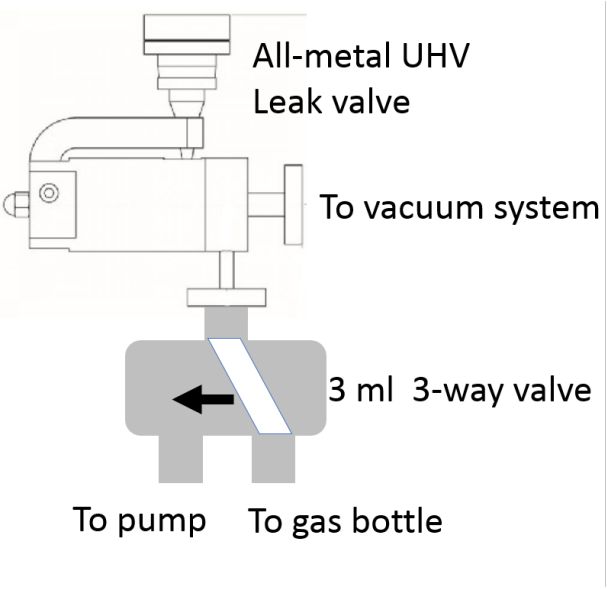

Figure 3.11: Schematic diagram of pulsed leak valve setup. The high precision all-metal leak valve is backed by a solenoid actuated 3-way valve. This arrangement allows pulsed gas admission into the UHV chamber.

The 3-way valve connects the gas-inlet of the leak valve to either a gas reservoir, or a rough vacuum pump. The arrangement allows the leak valve to be left at a constant opening. When the 3-way valve is opened, the inlet of the leak valve becomes pressurized by the reservoir gas, and the UHV chamber is flooded with a small, constant gas pressure. When the 3-way valve is closed, the gas is pumped away from the inlet of the leak-valve allowing the UHV chamber to return to its base pressure. Functionally, the opening and closing of the 3-way turns on or off the presence of a neutral reactant in the chamber, thereby pulsing the leak valve on and off, hence the name: pulsed leak valve.

The chamber reaction time to switching the on/off state of the valve is quite rapid. A steady state pressure is typically reached in < 2 s. The UHV chamber pressure is consistent enough that we consider our reactions to take place at a constant density that remains in excess. This is the basis of the pseudo first-order approximation (see 2.5.1). Fig. 3.12 shows typical valve behavior with helium gas. The pulsed leak valve behavior deteriorates when gases not chemically compatible with the 3-way valve are used. In these cases, diluting the gases in a noble carrier gas can return

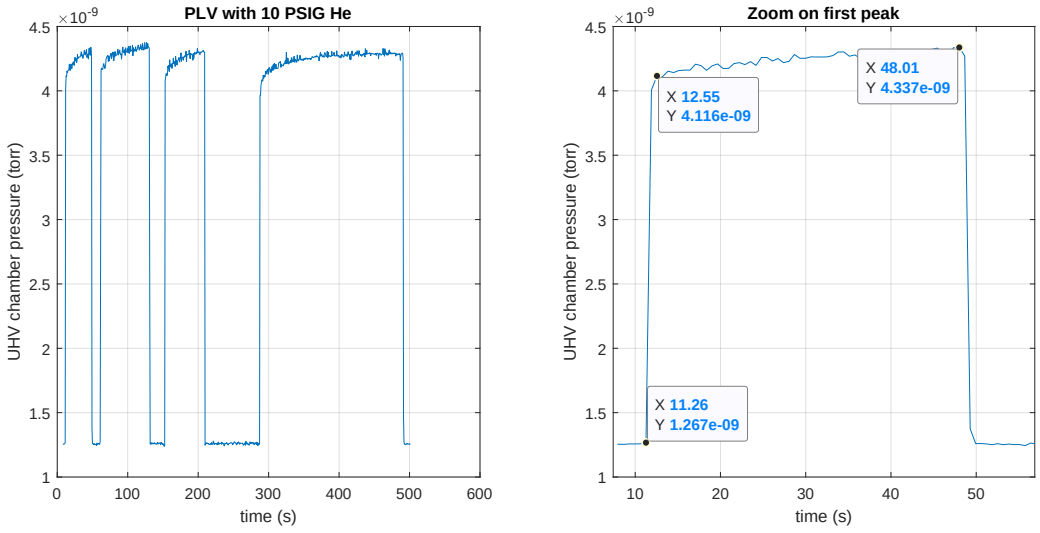

Figure 3.12: UHV chamber pressure reacting to opening and closing of the PLV. These tests were performed with 10 PSIG of pure helium backing the valve. The plot on the right is a zoom in of the first pulse plotted to the left with markers to highlight the valve opening time.

normal operation of the valve. At time of writing, we are upgrading the 3-way valve to an all-teflon 3-way valve (Valcor SV75P48T-1) to mitigate future chemical compatibility issues.

Liquids with large vapor pressures at room temperature can also be used as neutral reactants in our experiments. A liquid sample is delivered into the UHV chamber via mixture of its vapor pressure with a noble gas in the line pressurizing the 3-way valve. Liquids can contain significant quantities of impurities (typically water) that are removed via freeze-pump-thaw cycles. The liquid sample holder is frozen via submersion in liguid nitrogen, pumped on via a rough vacuum pump while frozen, and then allowed to thaw after closing the connection to the pump. Repeating this cycle 3-5 times noticeably improves sample purity in our experiments. When gas impurities are present, a coil filled with molecular sieve (Sigma-Aldrich 3Å) is added to the line between gas reservoir and 3-way valve. The coil is externally cooled by a cold bath to freeze out gaseous impurities. All of our gas lines are stainless-steel or teflon.

The constant density of gas is inferred from changes in the UHV chamber pressure as measured by a hot-cathode ion gauge. These gauges are not calibrated in the 10^{-10} to 10^{-8} torr regime we typically operate in. The accuracy of the readings can be off by upwards of a factor of two or more, depending on the gauge, controller, and gas being measured. This seriously impacts the accuracy of reaction rate constants measured in the apparatus. However, relative uncertainties in rate-constants across experiments with the same gas are unaffected. Reaction branching ratios are also insensitive to inaccurate density measurements of neutral gases. In order to improve the accuracy of absolute measurements of rate-constants, one will need to overcome the challenge of measuring density at an extremely low absolute pressure.

3.7.2 PZT valve

The method we utilize to introduce many different species of molecular ions into the trap is via a supersonic beam. A dilute gas mixture is prepared of our molecule of interest in a noble, atomic gas (typically 2-6% in He or Ar). The gas mixture pressurizes a PZT valve that actuates a Kalrez O-ring to form a seal with the UHV chamber. 150μs pulses of -200V to -400V are sent at 10Hz to the PZT valve to open it. The supersonic expansion into vacuum cools the molecule of interest to $\sim 4K$, while giving it a large longitudinal velocity. A molecular beam is formed by skimming the supersonic expansion. The beam exits the skimmer and has direct line of sight with the ion trap center. At the trap center the gas pulse is intersected by a focused laser pulse to produce molecular ions that are immediately trapped. Between the ionization laser and the molecular beam, there is a large parameter space that can be explored for loading optimization. A detailed description of PZT valve behavior and the resulting molecular beam can be found in [74]. In most cases, hundreds of the ion of interest can be loaded in only 10 gas/laser pulses. This is largely attributed to the high density of each gas pulse.

The UHV region between the skimmer and the PZT valve is pumped separately from the main ion trap chamber by a turbopump (Pfeiffer HiPace 80). The small aperture of the skimmer (2 mm) creates differential pumping during a gas pulse. The short pulse durations and differential

pumping keep the ion trap chamber pressure low for reaction experiments that occur after ion loading. These conditions also minimize chemistry between ions produced by the beam and their neutral precursors. Pulsed molecular beam loading enables us to isolate highly reactive species in our ion trap for reaction studies (e.g., $C_2H_2^+$ and CCl^+).

Liquids with reasonable vapor pressures at room temperature can also be used for molecular ion precursors. The method is identical to loading from the pulsed leak valve. Since a dilute mixture is ideal for producing a good supersonic beam, many liquid molecular sources are conveniently accessible.

Chapter 4

Quantum controlled reaction with Ca^+

The following sections are two ion-molecule reactions we studied between laser-cooled Ca^+ and oxygen (O_2) and nitric oxide (NO). Both papers take advantage of the quantum control we have over Ca^+ excited state populations. Presented here are the data and write-ups published in the literature with edits to the bibliographical references and formatting to match that of the thesis. The abstracts and acknowledgments have been omitted. A short addendum has also been added.

4.1 $Ca^+ + NO$

This paper [2] was the first reaction studied in the LIT-TOFMS apparatus. In addition to helping build the apparatus, control software, and analysis code, I took most of the data and wrote most of the text.

4.1.1 Introduction

Ions and free radicals play important roles in the chemistry of the interstellar medium [5, 75], in many combustion processes [9, 10], and in planetary atmospheres [7, 8]. Therefore, studying reactions between these species in the laboratory is useful for developing models of the chemical dynamics in these environments. In addition to the importance to interstellar medium chemistry, radical - ion chemistry is interesting to explore, as reactions may proceed in a fundamentally different manner from stable molecule - ion reactions. For example, radical species such as OH,

CH, NH may abstract an H atom or other neutral entities from the ion. Alternatively, they might readily add to multiple bonds in the ion acting as a classical electrophile, or insert into single bonds to form 3-centered 3-electron intermediates. Perhaps most significant, reactions between radicals and ions are predicted to be barrierless [76–79]; therefore rapid and appreciable reactions can occur at the low temperatures of important astronomical environments, and these likely play a role in the foundations of the chemical complexity of the universe. Consequently, it is imperative to study these reactions in low-temperature environments, where an exquisite level of detail can be extracted about these fully quantum mechanical systems. Finally, the same level of detail that can be extracted from low-temperature experiments offers the chance to anchor advanced theoretical treatments of molecular phenomena [80–82].

Even with the considerable potential for increasing our understanding of gas-phase chemical reactions, experimental studies of ion-radical reactions are extremely rare[83–85]. This is because laboratory measurements of ion-radical reactions have been notoriously challenging to make, due to the difficulty of creating dense, pure samples of these reactants. Ion densities are limited by the Coulomb repulsion between molecules. Radicals, in most cases, must be created *in situ* by breaking apart stable species, which leads to low density, contaminated samples. Because both of these species are created at low densities, the interaction times for experiments that rely on molecular beams or flow tubes are often too short to have a significant fraction of the molecules react. Acquiring clean samples of radicals in the gas phase and reacting them with ions at low temperatures poses significant difficulties. However, in the last decade, new experimental techniques have become available[22, 23, 78, 86–88], which have the promise to overcome some of the experimental challenges.

Recently, these techniques were used to study ion-neutral (non-radical) reactions at low temperatures using laser-cooled ions stored in linear traps. Reactions between laser-cooled atomic ions and neutral species have been demonstrated in several systems[20, 34, 48, 89–92]. Additionally, reactions using sympathetically cooled molecular ions stored in ion traps have been carried out[25, 31, 33, 36, 42, 93]. Recent experiments also investigated the influence of the internal state of the ions

on the reaction kinetics. In that work, the quantum state of the laser-cooled atomic ion was varied [28, 32, 34, 54, 94–96], while in other measurements, the reactivity of the molecular ro-vibrational state[34, 48, 52, 53] or the conformer was tested[50].

4.1.2 Ca^+ + NO reactions

In this work, we present results from reactions between neutral radical molecules and laser-cooled, electrodynamically trapped ions, where the reaction rates are controlled by changing the quantum-state population of the ions. In particular, we study the reactions of laser-cooled $^{40}Ca^+$ at millikelvin temperatures with nitric oxide radicals at room temperature. Since the ions are nearly at rest compared to the neutral molecules, the average collision energy is calculated to be $\bar{E}_{coll}/k_B\mathrm{T}\sim$ 180 K. There are two possible charged reaction products in this system, CaO^+ and NO^+ (see Eq. 4.1), where k_{NO} and k_{CaO} are the rate constants for producing NO^+ and CaO^+ respectively.

$$\begin{aligned} \mathrm{Ca^+ + NO} \quad &\xrightarrow{k_{NO}} \mathrm{NO^+ + Ca} \\ &\xrightarrow{k_{CaO}} \mathrm{CaO^+ + N} \end{aligned} \tag{4.1}$$

Subsequent reactions between CaO^+ product ions and NO are energetically forbidden and thus not considered.

The thermochemistry associated with the reactions between Ca^+ and NO was computed with high-level coupled-cluster theory and the HEAT thermochemical protocol [3]. Using these energies, we can determine the exothermic reaction pathways for our system. Laser cooling of Ca^+ simultaneously populates three electronic states: $S_{1/2}$, $D_{3/2}$, and $P_{1/2}$ (Fig. 4.1). At zero temperature, no reactions can occur when Ca^+ is in either the ground ($S_{1/2}$) or next lowest-lying excited state ($D_{3/2}$). However, reactions can proceed when Ca^+ is in the $P_{1/2}$ state. Here, the oxygen abstraction process is slightly exothermic ($\Delta E = -45(10)$ meV), while the charge-exchange process is still energetically forbidden by ΔE = +34(10) meV. For reactions at 180 K, $\bar{E}_{coll} \sim 16$

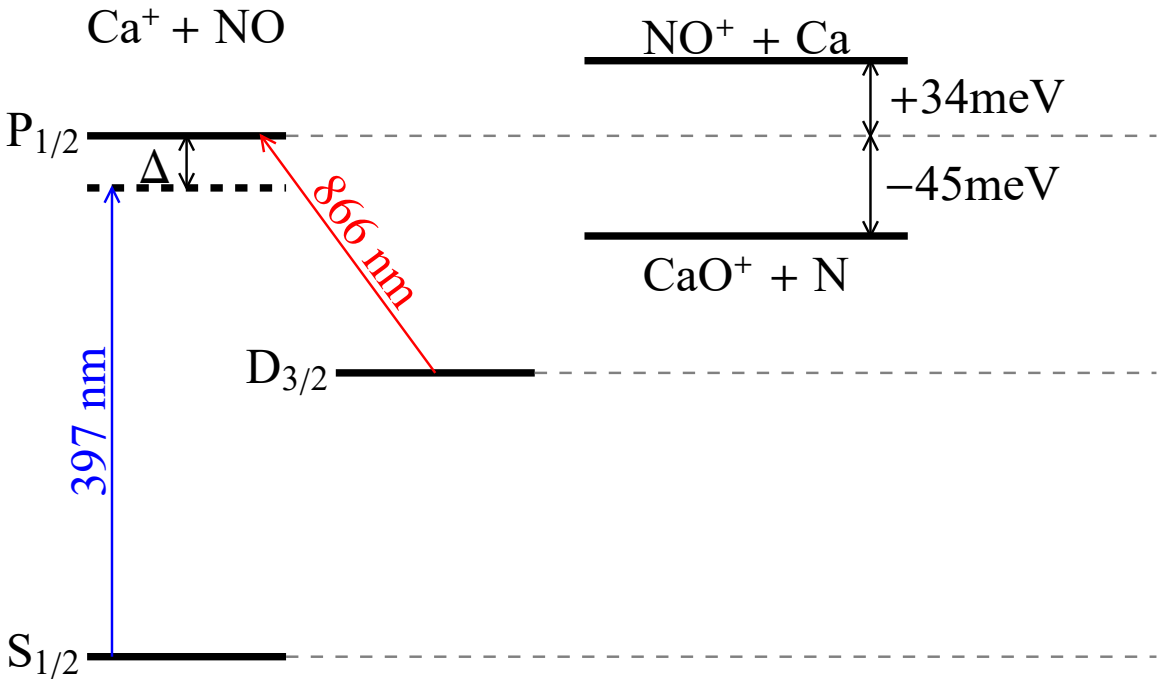

Figure 4.1: Comparison of reactant and product energies for the Ca^+ + NO system. The exothermicity of the reaction depends on the quantum state of Ca^+. Excited states of Ca^+ can be populated by excitation on the two cooling laser transitions at 397 nm and 866 nm. To achieve cooling, the 397 nm laser is red-detuned from resonance by an amount Δ. Only Ca^+ in the $P_{1/2}$ state is energetically allowed to react. The charge exchange product channel barrier is overcome by the thermal energy of neutral NO at 180 K.(Energies not to scale.)

meV, this channel will also be possible, though only with molecules whose thermal energy exceeds the barrier. Control over both reaction rates is possible by changing the time Ca^+ spends in the $P_{1/2}$ state. In our experiment, this control is accomplished by changing the detuning of the primary cooling laser ($\lambda \sim 397$ nm) from resonance (See Fig. 4.1).

4.1.3 Ion trap apparatus

The experimental apparatus used to study ion-radical reactions uses a combination of a linear Paul ion trap and a time-of-flight mass spectrometer (TOFMS)[38], similar to Refs. [35–37]. The trap allows for accumulation of charged products over the course of a reaction (i.e., several minutes) due to the long lifetime afforded by the large trap depth (2 – 4 eV). Accumulation of products over

such a long timescale makes measurements of ion-radical reactions possible even for reaction rates as slow as one per minute. Additionally, this allows for measurements of accumulated product ions and not just measurements of the depletion of the reactant. This provides the opportunity to map out simultaneous, competing reaction pathways. Once a reaction is complete, the products can be identified by time-of-flight mass spectrometry. Using measurements of the number of ions at each mass-to-charge ratio, the reaction rates and products of the reaction can be determined. The combination of an ion trap and TOFMS makes studies of very low density samples of ions and radicals possible.

An experimental run begins by non-resonantly photoionizing (355 nm) a neutral calcium beam and loading the resultant ions into the trap, located in an ultra-high vacuum chamber ($< 5 \times 10^{-10}$ torr). $^{40}Ca^{+}$ ions are then laser cooled on the $S_{1/2} \rightarrow P_{1/2}$ transition at 397 nm, where the laser is red-detuned by $\Delta = 30$ – 100 MHz (Fig. 4.1). Additionally, a repump laser tuned near resonace with the $D_{3/2} \rightarrow P_{1/2}$ transition at 866 nm is used to pump ions that have fallen into the $D_{3/2}$ state back into the cooling cycle. The ions are cooled to a low enough temperature to form a Coulomb crystal[97]. The fluorescence from the Coulomb crystal is imaged onto an intensified CCD camera, so that the initial, absolute number of calcium ions can be determined. Next, NO gas is introduced into the vacuum chamber via a precision leak valve at typical concentrations of 10^7 to 10^8 cm^{-3}. The NO (98.5% purity, Sigma-Aldrich) is passed through an ascarite cell ($NaOH:SiO_2$ mixture) to remove any residual water and a copper coil filled with molecular sieve ($3\mathring{A}$ pore diameter) submerged in a cold bath at -115°C to freeze out any N_2O and NO_2. The pressure of NO is measured by a Bayard-Alpert style ion gauge and Agilent controller(XGS-600). The large ion trap depth ensures that all charged products will remain trapped and have time to sympathetically cool via interactions with the laser-cooled atomic ions. Once the desired reaction time has elapsed, the trapping potentials are rapidly turned off (< 500 ns) and high potentials (~ 2 kV) are pulsed onto the trap rods to eject ions radially into the TOFMS [38]. The ion current from the microchannel plate detector is converted into a voltage and recorded by a fast oscilloscope (1 GHz). Arrival times and integrated peak areas in the TOFMS spectra are then used to determine the absolute number

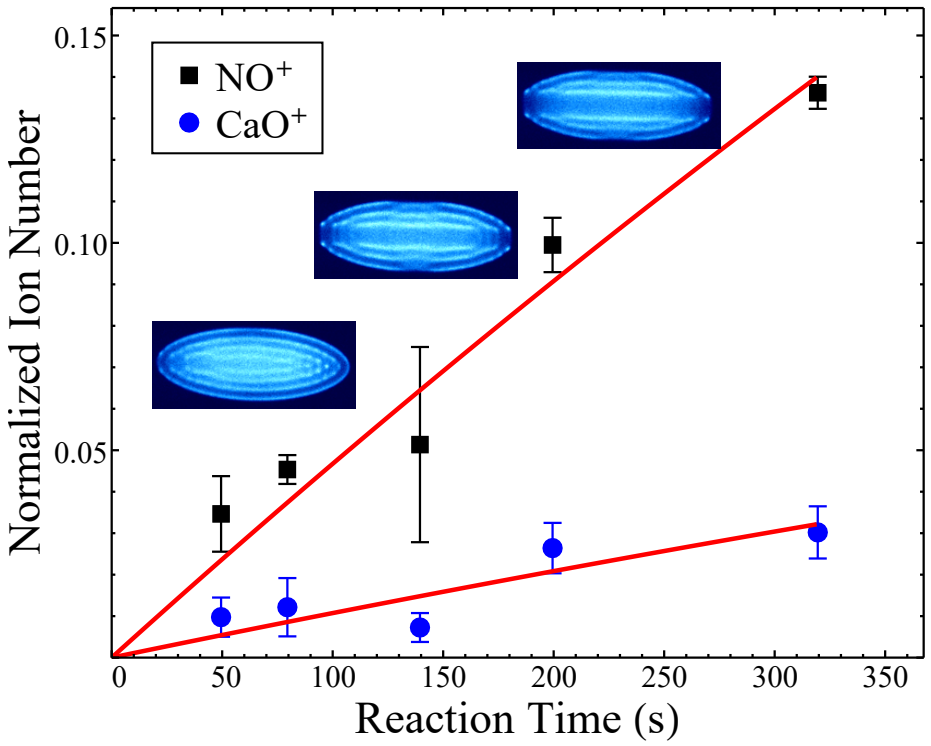

Figure 4.2: NO^+ and CaO^+ measured ion numbers as a function of time. The ion numbers are normalized by the initial number of Ca^+ determined from the image captured at t = 0. The error bars represent the standard error of the mean of measured ion numbers from five experimental runs at each time point. The solid lines indicate fits to the data using a pseudo first-order reaction rate model. Also shown are three false-color fluorescence images of the Coulomb crystals taken immediately before ejecting the ions into the TOFMS. The images were taken at t = 50 s, 200 s, and 320 s. The dark bands in the center and along the outer edges of the crystals indicate the presence of ions that are lighter and heavier than Ca^+ respectively. These ions are the reaction products.

of ions at each mass-to-charge ratio[38].

4.1.4 Reaction Rate Measurements

Reaction rates are determined by repeating experimental runs at different reaction times, while holding the neutral radical concentration and Ca^+ $P_{1/2}$ state population fixed. An example reaction curve is shown in Fig. 4.2. Here, the ion numbers are normalized to the initial number of Ca^+, which is determined from the fluorescence image taken at time t = 0. Example images of the crystals after reactions with NO are shown at three different times along the reaction curve.

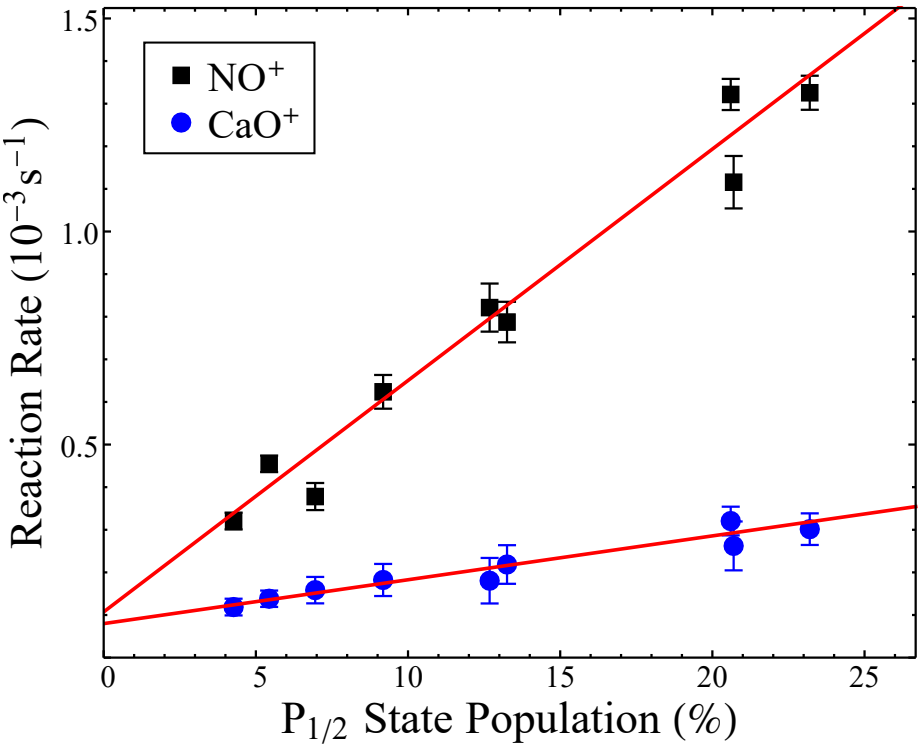

Figure 4.3: Measured reaction rates for the two product channels, NO^+ and CaO^+, as a function of Ca^+ $P_{1/2}$ state population. The NO concentration was $2.3(1)\times10^8$ cm^{-3} for all of these data. The initial number of Ca^+ ions in the trap was around 600. The slopes of the fit lines are used to determine the 180 K reaction rate constants. The statistical uncertainty in the $P_{1/2}$ state population is smaller than the points. There is a an offset for the reaction rate at zero excited state population. However, it corresponds to only a 1 – 2% offset in the $P_{1/2}$ state population, which is likely due to a small systematic in determining the absolute state population from the florescence.

The dark bands in the center and along the outer edges of the crystals indicate the presence of non-fluorescing product ions. The solid lines are fits to the data using a pseudo first-order reaction rate model for each reaction. Explicitly, the model is given by

$$\frac{NO^+(t)}{Ca^+(0)} = \frac{k_{NO}}{k_{NO}+k_{CaO}}\left(1-e^{-k_{NO}[NO]f_P t}\right) \tag{4.2}$$

$$\frac{CaO^+(t)}{Ca^+(0)} = \frac{k_{CaO}}{k_{NO}+k_{CaO}}\left(1-e^{-k_{CaO}[NO]f_P t}\right), \tag{4.3}$$

where the number of NO^+ and CaO^+ product ions at a given time, t, are normalized by the number of calcium ions at $t = 0$. $[NO]$ is the concentration of neutral NO molecules, and f_P is the fraction of Ca^+ in the $P_{1/2}$ state.

To demonstrate control of the reaction rates by changing the quantum-state populations of the Ca^+, we adjust the 397 nm laser detuning between measurements. The detuning controls the fraction of time an ion spends in the excited $P_{1/2}$ state, and thus its reactivity. The fraction of time is determined experimentally with the help of the optical Bloch equations [54]. First, we integrate the intensity of the florescence of the entire pure Ca^+ crystal image from the CCD camera as a function of detuning. Next, we fit these data to the three-level optical Bloch equations. Using this fit, we can calculate the fraction of time the atomic ions spend in the $P_{1/2}$ state based on a single image of the crystal at a known laser detuning. Since the lifetime of the excited state is on the order of a nanosceond, one can model this excitation as a steady-state system, where the fraction of time in the excited state is equal to the fraction of ions that can react.

The results of the quantum-state controlled reaction can be seen in Fig. 4.3. Here, we keep the NO concentration fixed at $2.3(1)\times10^8$ cm^{-3} and vary the fraction of ions in the excited $P_{1/2}$ state. We can vary the reaction rate by up to a factor of five. In our experiment, we were limited in the range of accessible $P_{1/2}$ state populations on the lower end by the decreased cooling rate, which leads to loss of ion crystallization, and on the upper end by the maximum fraction of ions that can be in the $P_{1/2}$ state of the three-level system, assuming the repump laser is on resonance. In total, we are able to vary the population between approximately 5 and 25%.

We were also able to extract branching ratios and reaction rate constants for the charge exchange channel, k_{NO}, and for the oxygen abstraction channel, k_{CaO}, using the slopes of the linear fits and the fixed NO concentration (see Table 4.1.) Note that the NO concentration was estimated from an ion gauge reading with the gas correction factor for NO. To explore a possible systematic effect of the pressure measurement, we completed an additional experiment to determine the rate constants where any systematic effects likely contribute in different ways.

The second experiment measured the reaction rates for producing NO^+ and CaO^+ at a fixed laser detuning, while varying the NO concentration. The results of these measurements can be seen in Fig. 4.4. Here, we varied the pressure between 3.4×10^{-9} and 1×10^{-8} torr with a fixed fraction of Ca^+ in the $P_{1/2}$ state of 19.1(1.8)%. The lower end of the range was chosen to be well above the

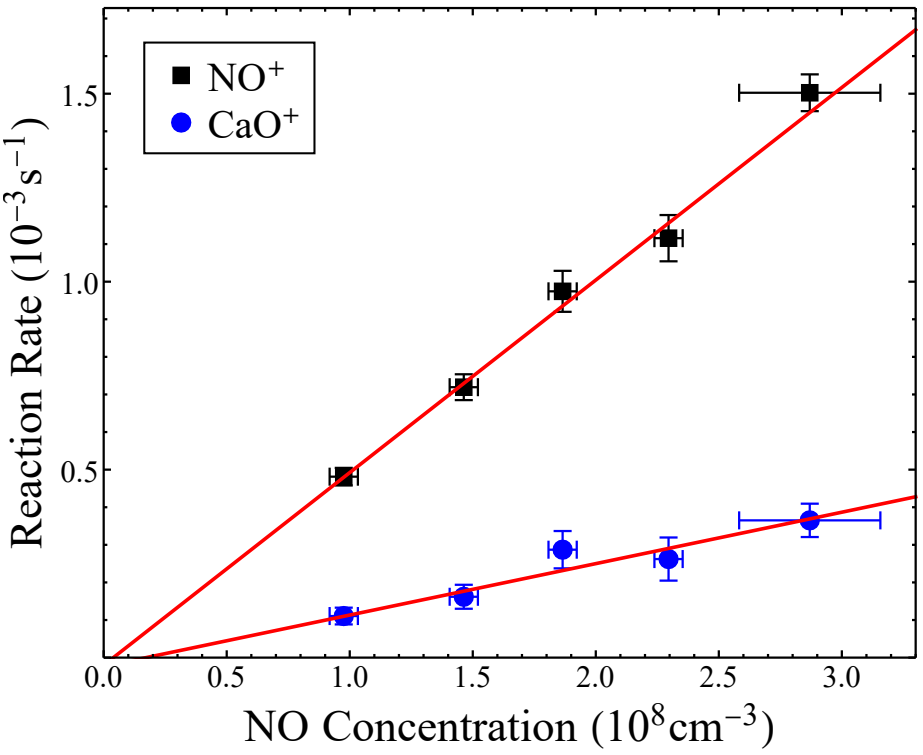

Figure 4.4: Measured reaction rates for product channels NO^+ and CaO^+ as a function of neutral NO concentration in the chamber. The NO pressure in the chamber was varied between 3.4×10^{-9} and 1×10^{-8} torr to change the NO concentration. For all of these data, the $P_{1/2}$ state population was 19.1(1.8)%. The slopes of the fit lines correspond to the 180 K reaction rate constants.

background pressure before introduction of NO, and the upper end of the range was chosen such that the ions still formed a well-resolved Coulomb crystal. Once again, the rate constants from these measurements were determined by slopes from linear fits to the data and the excited state population calculated from the fluorescence images (Table 4.1). The rate constants and branching ratios from the two experiments agree to within statistical uncertainties. This agreement gives us confidence in the limited impact of any uncontrolled systematic effects.

4.1.5 Discussion

Typical predictions of rate constants using the Langevin capture model do not apply in this situation. This is because one of the channels is endothermic and involves a charge exchange process, neither of which are well characterized by the simple model. Instead, we present a mechanistic

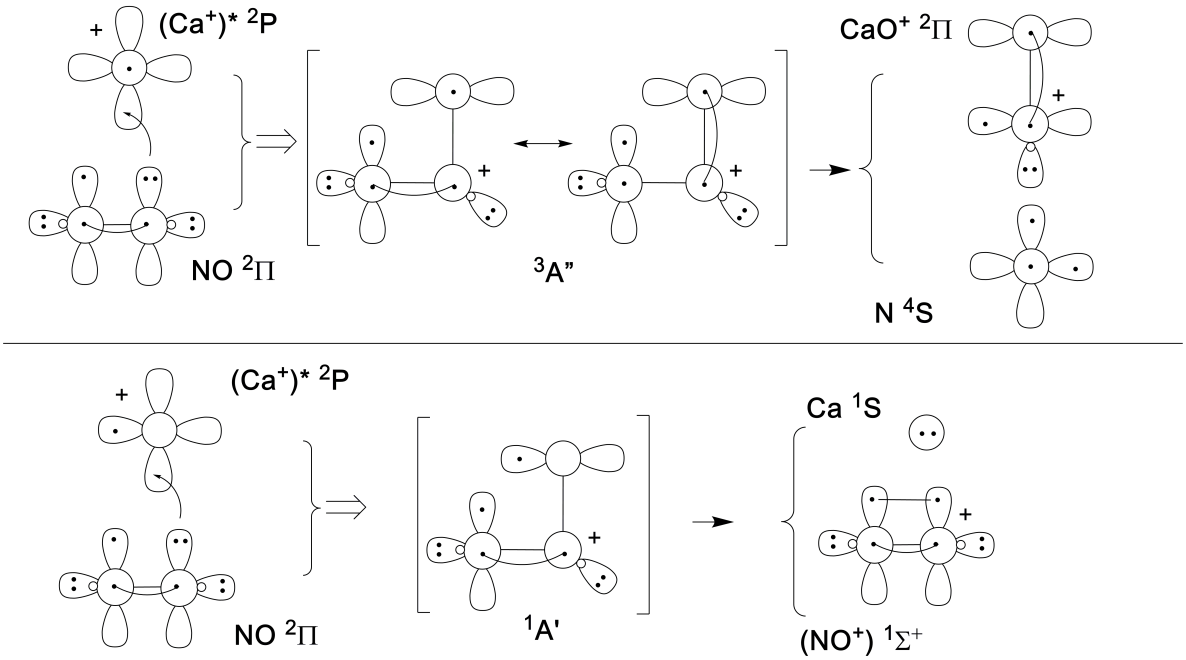

Figure 4.5: Generalized valence-bond (GVB) diagrams that illustrate the processes whereby ^2P calcium atoms react with NO molecules to form CaO^+ and nitrogen atom in their ground states (top); and the charge exchange process that yields Ca atoms and ground state NO^+ (bottom).

model for the reactions. Likely mechanisms for the slightly exothermic chemical reaction and the charge exchange process are shown in Fig. 4.5. The calcium ions and the NO molecules can combine in four distinct ways, involving A' and A'' electronic states of either singlet or triplet multiplicity. Interaction along the $^3A''$ pathway correlates with the production of a ground state nitrogen atom and the CaO^+ molecule, while interaction along a $^1A'$ is consistent with the observed charge exchange process. A detailed theoretical characterization of the $^3A''$ and $^1A'$ intermediates is desirable and is the focus of extensive future work. However, the proposed mechanism is plausible and consistent with the observed products.

Table 4.1: Table of results for the two independent determinations of reaction rate constants and branching ratios. The listed uncertainties represent the statistical uncertainty.

	NO concentration	$P_{1/2}$ fraction
$k_{NO}(\frac{\text{cm}^3}{\text{s}})$	$2.3(2) \times 10^{-11}$	$2.7(3) \times 10^{-11}$
$k_{CaO}(\frac{\text{cm}^3}{\text{s}})$	$4.4(7) \times 10^{-12}$	$7(2) \times 10^{-12}$
BR_{NO}	0.8(2)	0.8(1)
BR_{CaO}	0.21(5)	0.16(3)

4.1.6 Conclusion

In conclusion, we have demonstrated quantum-state controlled reactions between laser-cooled Ca^+ ions and neutral NO radicals. We utilized an ion trap to accumulate the charged reaction products over the course of the reaction. By coupling a time-of-flight mass spectrometer to the ion trap, we were able to make simultaneous measurements of the product channels. Using this technique, we made two independent measurements of the reaction rate constants and branching ratios for NO^+ and CaO^+ products at 180 K. A realistic mechanistic model for the two product channels was also presented. In the future, reactants of other important radicals, such as OH and CH can be introduced to the trapped ions while controlling both the internal ro-vibrational states, as well as the collision energy through the use of a Stark decelerator. These studies will allow for complete control over the reactants, and thus lead to a new level of understanding of radical-ion reactions.

4.2 $Ca^+ + O_2$

This paper [39] was the second reaction studied in the LIT-TOFMS apparatus. In addition to helping build the apparatus, control software, and analysis code, I had to retake all of the data and redo the analysis upon realizing we needed to use an 8-level OBE model. After this, I helped rewrite the relevant sections of the paper, which ultimately did not have an impact on the overall

story.

4.2.1 Introduction

The study of cold, controlled molecular reactions and collisions in the gas phase is a steadily growing field, offering many opportunities for detailed studies of interactions [98–101]. Several different experimental pathways are currently used to explore cold molecular interactions with neutral molecules. These include, but are not limited to, crossed-beam experiments using a Stark decelerator [102, 103], merged-beam experiments [104, 105], co-trapped atoms and moleucles [106, 107], buffer-gas cooled molecules inside magnetic traps [108], trapped Rydberg molecules [13], laser-cooled molecules [109–113] and ultracold bi-alkali atom molecules [114, 115]. Another set of experiments uses laser-cooled atomic ions confined in radio-frequency (rf) traps as reactants, or as a cold bath to sympathetically cool molecular ions for reaction studies [23, 116].

While most of these experiments benefit from reducing the translational motion via cooling to temperatures below T$\leq$1 K, controlling the internal states of the reactants can offer additional insights into understanding the reactions. Preparing the reactants in a single quantum state [117–120] could elucidate the state's influence on reaction pathways. There have been some experiments that explore cold reactions where the internal states of the atomic reactant have been controlled including, but not limited to, $Ca^+ + O_2$ [121], $Ca^+ + H_2$ [94], $Ca^+ + H_2O$ [34], $Ca^+ +$ Rb [91], $Yb^+ +$ Rb [28], $Ba^+ + {}^{87}$Rb [96], or $Ca^+ + (CH_3F, CH_2F_2,$ or $CH_3Cl)$ [54], $Ca^+ + {}^6$Li [122], $Yb^+ + {}^6$Li [123], and $Be^+ + H_2O$ [45]. These experiments take advantage of the control of electronic states of the atomic ion using cooling lasers. However, preparation of pure state-selective molecular samples is significantly more challenging [13, 50, 52].

Here, we explore the reaction between laser-cooled Ca^+ ions and neutral O_2, where the reaction can proceed only when Ca^+ is in one of two excited electronic states ($^2P_{1/2}$ or$^2D_{3/2}$). We control the relative populations in the different quantum states by the wavelengths of the cooling lasers. Although the reaction of $Ca^+ + O_2$ has been observed previously [121], no details on the reaction kinetics or the influence of the quantum states of Ca^+ have been reported. In this work, we

present a detailed study on the reaction $Ca^+ + O_2 \rightarrow CaO^+ + O$, including the absolute reaction rate constants for reactions starting with Ca^+ in either the $^2P_{1/2}$-state or $^2D_{3/2}$-state.

In this paper, we begin by discussing the energetics of the reaction (Sec. 4.2.2) before discussing the experimental setup (Sec. 4.2.3). Next, we present results of the reaction measurements and the dependence of the rates on the quantum state of Ca^+ (Sec. 4.2.4). We then discuss the implications of our results (Sec. 4.2.5), and conclude by giving an outlook for future experiments (Sec. 4.2.6).

4.2.2 $Ca^+ + O_2$ Reactions

In the experiments presented here, we show measurements of the reactions between Ca^+ ions, which have been laser-cooled to millikelvin temperatures, and O_2 molecules at room temperature. This leads to an average collision energy of $\sim$ 160 K. This estimation neglects the effect of the micromotion on the collision energy. Based on the images of our ion crystals and previously published values for the temperature of similar sized crystals [49], we estimate an upper limit to the effective kinetic temperature from micromotion to be $<E_{eff}>/k_B < 10$ K. Although the inclusion of micromotion slightly increases the effective kinetic temperature of the ionic reactants, its value is still negligible compared to the energy of the O_2 molecules.

The reaction of Ca^+ with O_2 is highly endothermic (+1.7 eV) when Ca^+ is in the ground $^2S_{1/2}$-state [124], but becomes feasible when the excited states of the atomic cation are involved. With the $^2P_{1/2}$ state, the reaction is exothermic, and for $^2D_{3/2}$, it is thermoneutral to within the accuracy of a high-level calculation. The numbers here are based on a thermochemical cycle that involves the bond energy (4.202 eV) and ionization potential (6.895 eV) of CaO, the bond energy of O_2, and the ionization potential and relative cation energies of the Ca atom. The numbers associated with CaO are from high-level theory, and are taken from a previous study [38], while the others are precise and well-established numbers from the literature.

$$Ca^+ (^2P_{1/2}) + O_2 \longrightarrow CaO^+ + O \quad \Delta E = -1.43(2) \text{ eV} \tag{4.4}$$

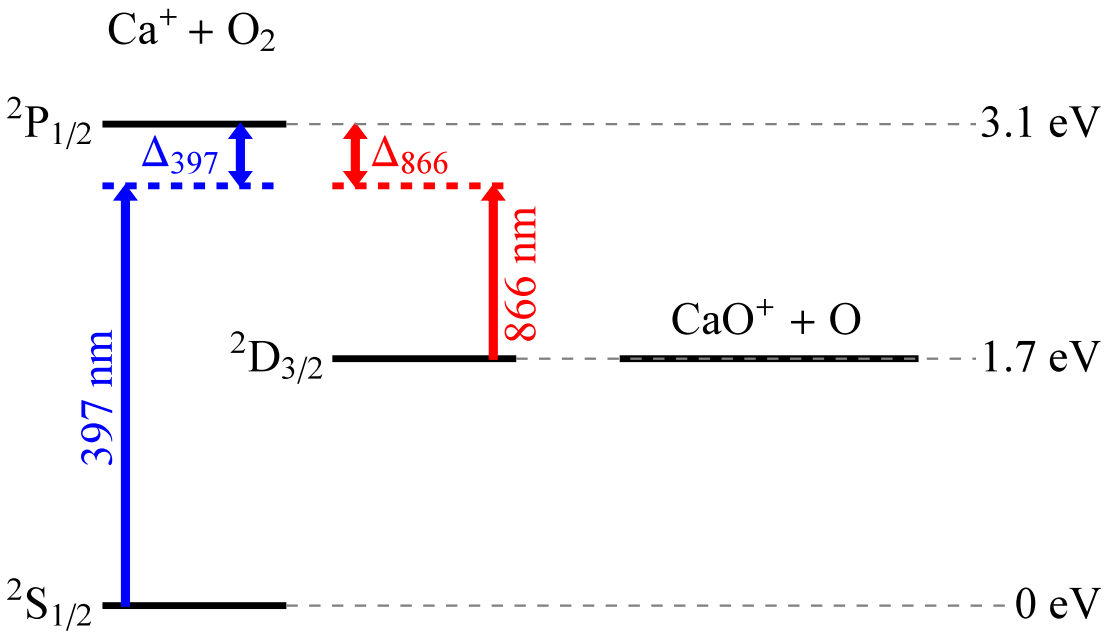

Figure 4.6: Diagram of the Ca^+ energy structure and product channel energy (energies are not to scale). The main laser cooling transition for Ca^+ at 397 nm excites the ion to the $^2P_{1/2}$-state. The ion can decay to the ground $^2S_{1/2}$- or the excited $^2D_{3/2}$-state. A second laser at 866 nm repumps population that accumulates in the dark $^2D_{3/2}$-state back into the cooling cycle. Here, Δ_{397} and Δ_{866} represent the detuning of the cooling lasers with respect to the two cooling transition frequencies. The reaction with O_2 is energetically possible in either of the two excited states, but not in the ground state.

$$Ca^+ (^2D_{3/2}) + O_2 \longrightarrow CaO^+ + O \quad \Delta E = +0.01(2) \text{ eV} \tag{4.5}$$

We note that the endothermicity of the $^2D_{3/2}$-state reaction is comparable to the uncertainty in the calculated energy. However, the collision energy is observed to be sufficient to counter this endothermicity, if indeed it is present. Thus, the reaction rate for $Ca^+ + O_2$ will depend on the population of both excited states of Ca^+.

We control the relative populations of Ca^+ in its two excited states by adjusting the detuning of both the main cooling laser at 397 nm and the repump laser at 866 nm (Fig. 4.6). To determine the fraction of the time the Ca^+ spends in each of its three electronic states, we use the 8-level optical Bloch equations (OBE) calibrated to the magnitude of the fluorescence from the Coulomb

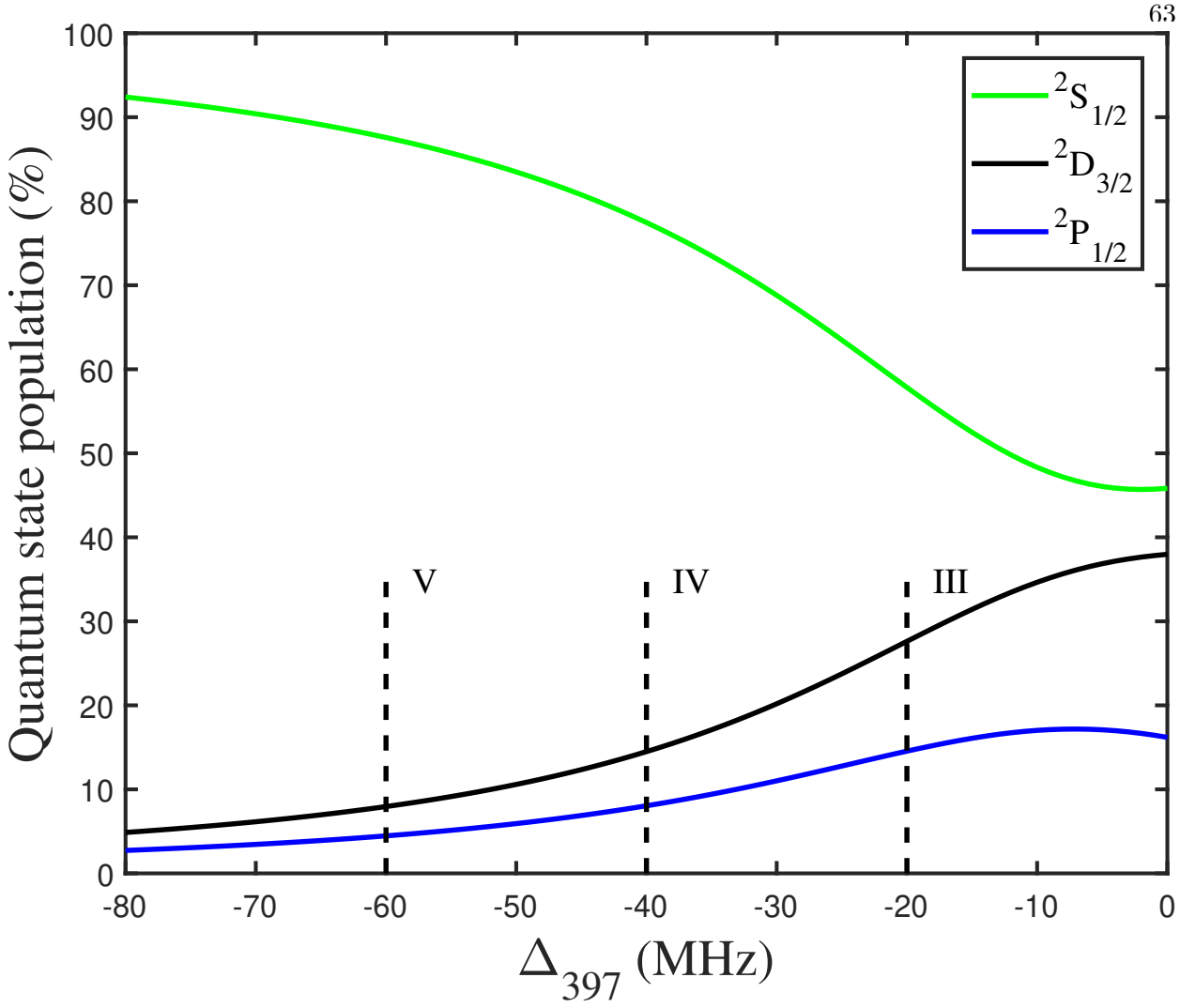

Figure 4.7: Predictions of the state distribution of the Ca^+ ion from the 8-level OBE with a fixed 866 nm detuning (+42 MHz). The state populations for the $^2S_{1/2}$, $^2P_{1/2}$, and $^2D_{3/2}$ states are shown. The vertical lines represent the parameters used for three measurements used to determine the rate constants presented in Section 4.2.4 (see Table 4.2). To obtain the other state distributions shown in Table 4.2, we also changed the 886 nm laser detuning.

crystal following the method described in [54]. Once calibrated, the 8-level OBE are used to predict the populations in each state based on the detunings of both lasers used for laser cooling. An example set of curves for the three states is shown in Fig. 4.7. Here, the repump laser detuning is fixed, while the main cooling laser detuning is varied.

4.2.3 Ion Trap Apparatus

Details of the experimental setup for measuring reactions between cations and neutrals have been described recently [2, 38]. In the following, we present a short description of the apparatus with an emphasis on aspects relevant for the present experiment.

Ca^+ ions are created from non-resonant photo-ionization of calcium atoms at 355 nm (7 mJ/pulse, 10 Hz, beam diameter $\approx$ 1 mm^2) and trapped using a segmented, linear quadrupole ion trap [38]. The trapped Ca^+ ions are laser cooled [125] to secular temperatures close to the Doppler cooling limit resulting in the formation of Coulomb crystals [97]. Laser cooling is performed on the $^2S_{1/2}$- $^2P_{1/2}$ transition, driven at 397 nm by a fiber-coupled diode laser (NewFocus, 3.5 mW, 600 μm beam diameter). A second fiber-coupled diode laser at 866 nm (NewFocus, 9 mW, 2 mm beam diameter) is used to repump the ions back into the cooling cycle on the $^2P_{1/2}$ - $^2D_{3/2}$ transition.[1] Both laser frequencies are measured and locked using a wavemeter (HighFinesse/ Ångstrom WSU-30) with a precision of $\pm$ 2.5 MHz around the center frequency. The wavemeter is calibrated daily to a 780 nm laser, locked to a transition in ^{87}Rb by saturation absorption spectroscopy.

Detection of the trapped ions is done by two different methods. We can image the fluorescence from the Coulomb crystal onto an intensified CCD camera or eject the ions into a time-of-flight mass spectrometer (TOF-MS), which is radially coupled to the linear ion trap [38]. Optical detection has the advantage of being non-destructive, but is sensitive to only Ca^+. Non-fluorescing ions can be inferred only by a change in the shape of the Coulomb crystal in combination with results from molecular dynamics simulations [126]. In the present experiment, we use the optical detection of pure Ca^+ crystals to determine the initial number of trapped atomic ions by fitting the area of the crystal and knowing the density of ions in the trap [38]. To accurately determine the number of all trapped reactant and product ions, we eject all ions in the trap into the TOF-MS. This allows us to determine the absolute number of ions at each mass in a single shot [38]. Thus, we can study the reactions by the increase of products, as well as by the loss of reactants.

[1] $^{40}Ca^+$ has a second possible cooling scheme, which uses the $^2S_{1/2}$ - $^2P_{3/2}$ transition for cooling and the $^2P_{3/2}$ - $^2D_{5/2}$ transition for repumping. The two transition wavelengths — 393 nm and 854 nm — are not within the bandwidth of our laser systems. We therefore neglect these electronic states for the scope of this work.

An experimental sequence starts by loading a Ca^+ Coulomb crystal into the ion trap and removing any impurity ions by varying the trapping fields. Next, an image of the crystal is taken to determine the initial number of Ca^+ ions. At this point, O_2 is introduced into the chamber through a leak valve for a predetermined length of time. After the set reaction time has been reached, all trapped ions are ejected into the TOF-MS and a mass spectrum is produced. The total number of ions (product + reactant) is also determined from the full mass spectrum [38] at each time point to ensure the number of ions remains constant during a reaction measurement and ions are not lost from the trap. To test the conservation of ions in the trap, we sum the number of ions in every mass channel and compare this sum at each time step in the reaction to the initial number of Ca^+ ions. This check is especially important when measuring the highly exothermic, excited-state reaction of $Ca^+ + O_2$, where the charged products may have > 1 eV of kinetic energy.

There is one notable improvement to the apparatus compared to our previous work [38], which concerns how we introduce the neutral reactant. Instead of having the O_2 present during the trap loading sequence, we now implement a pulsed-leak valve [127]. The valve consists of an all-metal leak valve (Kurt Lesker LVM series) with a 3-way solenoid valve (Parker Hannifin) connected to the input port. The 3-way valve connects the input port of the leak valve to either a roughing pump or a bottle of O_2 diluted to 60% in N_2. In this configuration, the leak valve is held open at a desired leak rate at all times and the 3-way valve controls whether or not O_2 flows into the chamber. Using the 3-way valve to initiate the introduction of O_2 into the trapping chamber, we achieve a stable background O_2 pressure in around $1--2$ seconds. This time sets the uncertainty in the initial time for the reactions.We note that the pressure of O_2 was measured using an ion gauge, which can give readings that are accurate to within only a factor of 2-3. This systematic will not affect the relative rates between the two states, however.

Although care is taken to introduce pure O_2 gas into the vacuum chamber, there is always the possibility that contaminants can be entrained in the gas flow. Since all trapped ions are detected in the TOF-MS spectrum simultaneously, we can measure any background reactions between Ca^+ and H_2O (the dominant contaminant), which lead to the production of $CaOH^+$. Therefore, we can

account for parasitic background reactions in our modeling of the reaction rates.

4.2.4 Reaction Rate Constant Measurements

We model the reactions in our experiment using pseudo-first-order kinetics, where we assume that the density of O_2 does not change during a reaction measurement. We model the system by including reactions that start with the Ca^+ in the two excited states. Equation (4.6) describes the growth of the charged product, CaO^+.

$$[CaO^+] = [Ca_0^+](1\text{-}e^{-k_{eff}[O_2]t}) \tag{4.6}$$

Here, $[CaO^+]$ is the number of CaO^+ ions as a function of reaction time, t, $[Ca_0^+]$ is the initial number of trapped Ca^+ ions, k_{eff} is the effective reaction rate constant, and $[O_2]$ is the oxygen concentration in the chamber. The effective reaction rate constant, k_{eff}, is given by

$$k_{eff} = k_P f_P + k_P f_D, \tag{4.7}$$

where $k_P(k_D)$ is the rate constant for reactions with Ca^+ in the P (D)-state, and $f_P(f_D)$ is the fraction of the Ca^+ ions in the P (D)-state.

To extract the quantum-state dependent reaction rate constants, we first measure k_{eff} at several different state populations. We accomplish this by varying the detunings of the cooling lasers, while maintaining a constant O_2 concentration. An example of one such rate measurement is shown in Fig. 4.8. With our experimental parameters, the $^2P_{1/2}$-state population can be varied between 4% and 16%, while the $^2D_{3/2}$-state range is between 8% and 50%. We are not able to work outside this range, as either the heating rates become too large such that we can not maintain a stable Coulomb crystal due to the energy imparted by collisions with the background gas or the population is not possible due to the coupling in an eight-level system. A summary of the determined k_{eff} for the different state populations is given in Table 4.2. We perform a two-dimensional fit to these data using Eqn. 4.7 as the model to extract two fit parameters, k_P and k_D. The data and the fit can be seen Fig. 4.9. The measurements are shown as diamond

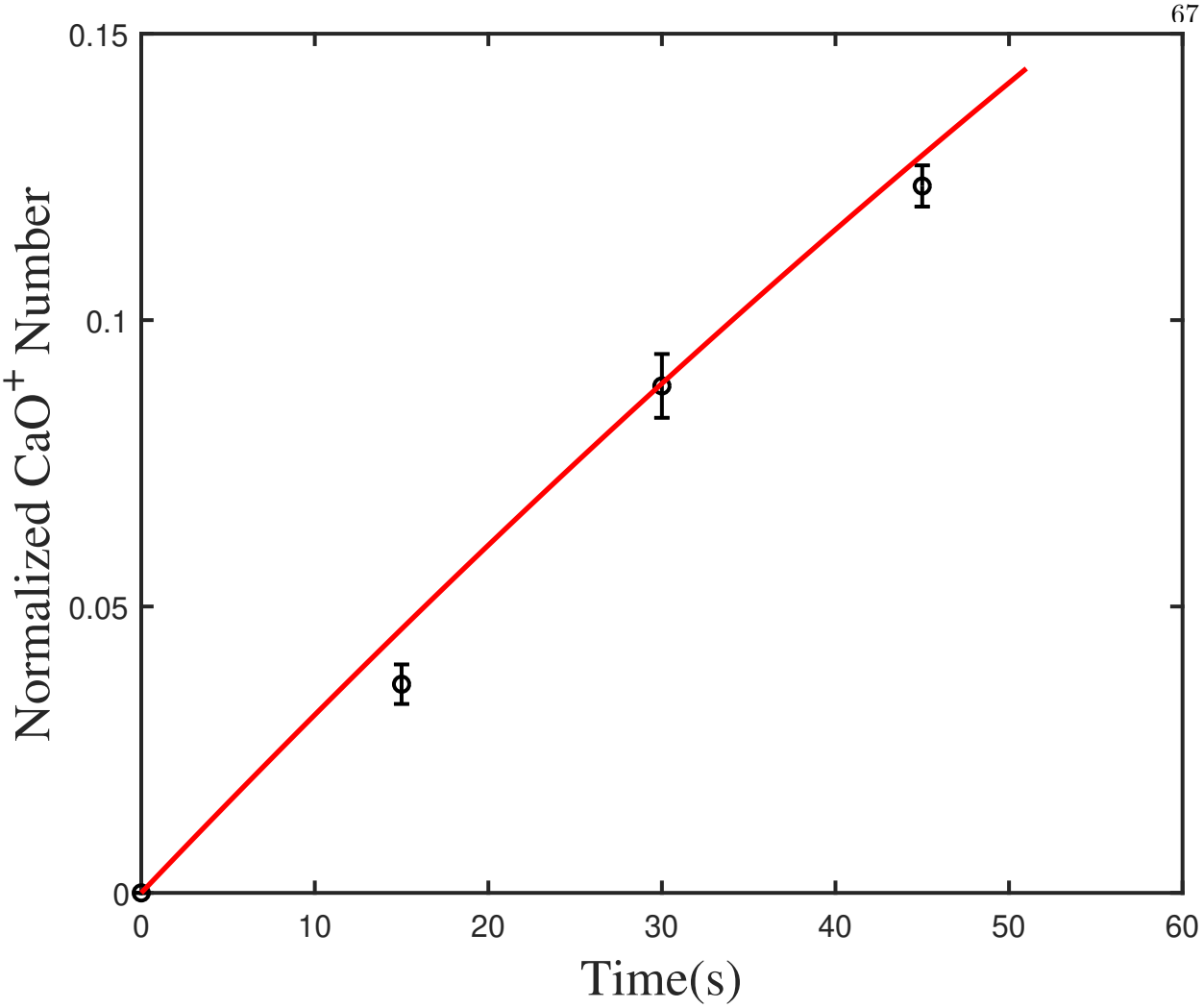

Figure 4.8: Example reaction measurement showing the growth of CaO^+ product ions, normalized by the initial number of Ca^+ ions ($\sim$ 800). The fraction in the $^2P_{1/2}$-state is 0.16 and $^2D_{3/2}$-state is 0.22, with an O_2 density of $8.9\times10^7 cm^{-3}$. The solid line is a fit using Eqn. (4.6), where k_{eff} is the only free parameter. The error bars correspond to the standard error of the mean of 7 measurements at each time point.

points, where the color represents k_{eff}. The fit is shown as contour lines of constant k_{eff}. The rate constants from the fit are given in Table 4.3. The rate constant for Ca^+ in its $^2D_{3/2}$-state is about three times lower than $^2P_{1/2}$-state reactions.

Table 4.2: Measured reaction rate constants for pairs of Ca^+ excited state populations shown in Fig. 4.9. The fractional populations in the $^2P_{1/2}$-state (f_P) and $^2D_{3/2}$-state (f_D) are shown with the corresponding measured effective rate constant (k_{eff}). The data point numbers correspond to measurements shown in Fig. 4.9.

Data point	f_P	f_D	k_{eff} (10^{-11} cm^3 s^{-1})
I	0.13	0.32	4.1(7)
II	0.16	0.22	3.5(4)
III	0.15	0.28	4.1(6)
IV	0.08	0.15	2.3(1)
V	0.04	0.08	1.4(1)
VI	0.07	0.50	3.6(4)

Table 4.3: The resulting rate constants k_P (k_D) for the three quantum states of Ca^+. Uncertainties are from the 90% confidence interval for the fit parameters, k_P (k_D)

.

Ca^+ state	k (10^{-10}cm^3 s^{-1})
$^2S_{1/2}$	0
$^2P_{1/2}$	1.8(4)
$^2D_{3/2}$	0.5(2)

4.2.5 Discussion

There are two possible explanations as to why the rate constants for the different quantum states are not the same. The first, and most likely, of these is related to the energy of the $^2D_{3/2}$-state. The calculated energy of the $Ca^+(^2D_{3/2}) + O_2$ entrance channel is coincident, to within the estimated uncertainty, to that of the $CaO^+ + O$ outgoing channel. If the reaction is indeed

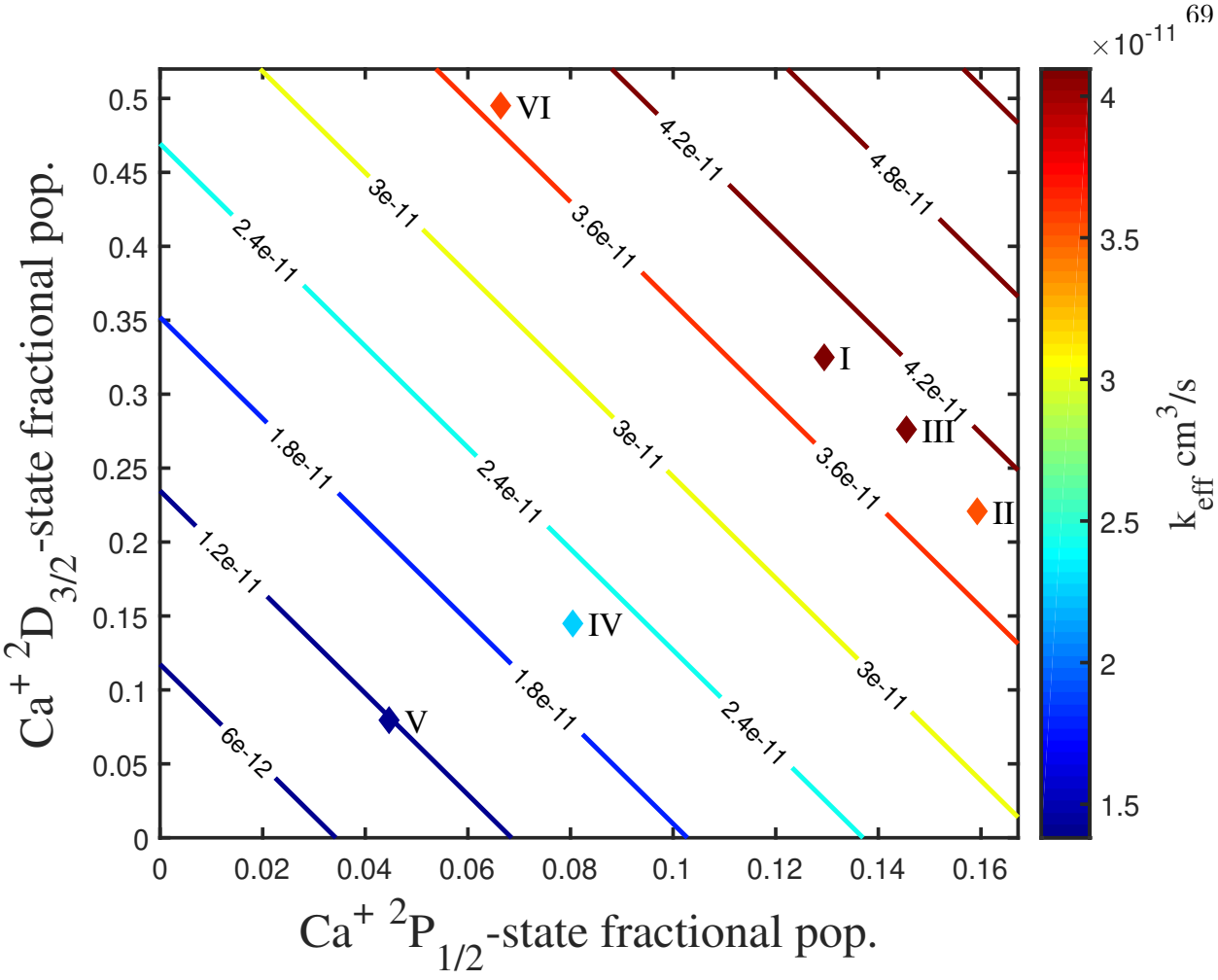

Figure 4.9: Dependence of the effective rate constant, k_{eff}, on the $^2P_{1/2}$- and $^2D_{3/2}$-state populations of Ca^+. The experimental measurements are shown as diamonds, where the color of the point represents the value of k_{eff}. For all data shown, the O_2 concentration was kept constant at 8.9×10^7 cm^{-3}. We perform a two-dimensional fit to the data using Eqn. 4.7, which allows us to extract k_P and k_D. The contour lines represent constant k_{eff} values of the fit.

endothermic by an amount comparable to the collision energy, then only a portion of the Boltzmann distribution of the O_2 molecules have enough energy to react. Assuming the ions are at rest and the O_2 is at 300 K, the estimated collision energy is 160 K. To have a reduction of the rate constant by a factor of three (i.e., only one-third of the collisions have enough energy to react), an energy barrier of ca. 15 meV would have to exist. Given that this is in quantitative agreement with the calculated energy, this is an entirely plausible explanation for the observations. However, the uncertainty in the calculation includes the possibility that the reaction is actually exothermic, so

one needs to be conservative in making such an assertion.

If the possible endothermicity of the reaction involving $Ca^+(^2D_{3/2})$ is not the explanation for the slower rate, then a mechanistic rationalization is needed. The association of the calcium ion and O_2 will involve some sort of intermediate complex, and thus it is necessary to consider the full triatomic potential energy surface. Given that the reaction involves an excited state calcium atom, the lowest electronic states of "CaO_2^+" lay well below the energy of the entrance channel, and a reaction pathway involving many highly excited electronic states is likely. While a detailed theoretical study of such a process is well beyond the scope of this paper, some indication of the structures and electronic states involved can be gleaned from Fig. 4.10. This displays calculated energetics obtained with coupled-cluster theory based on single, double, and perturbative triple excitations (CCSD(T)) [128, 129] together with the cc-pCVTZ basis set [130]. This level of theory is somewhat less rigorous than that used to calculate the reaction energetics documented earlier, differences are likely small (*i.e.,* +0.01 eV for the effectively thermoneutral channel *v.* -0.02 with CCSD(T)/cc-pCVTZ) and the results are expected to be accurate to within *ca.* 0.02−−0.04 eV for the states shown in the figure. Only the lowest doublet and quartet states of various symmetries are shown, all of which are both *bona fide* minima on the potential energy surface and qualitatively described by a single Slater determinant (thus treated well by CCSD(T)).

Figure 4.10 shows that the association of Ca^+ and O_2 can potentially lead to states belonging to several manifolds of spin multiplicity and spatial symmetry, the lowest of which lies very far below the association asymptote. Favorable association of the $^2P_{1/2}$ and $^2D_{3/2}$ states of the atomic calcium ion with ground state O_2 correlates with $^2A_2$ and $^2B_2$ states of the C_{2v} intermediate, where the former arises from pairing of in-plane electrons (forming a σ bond) and the latter from a π interaction. The lowest states of these symmetries will correlate adiabatically with $Ca^+(^2S)$ + $O_2(^3\Sigma)$, with higher-lying $^2A_2$ and $^2B_2$ states correlating adiabatically with the $Ca^+(^2P_{1/2})$ or $^2D_{3/2}$ + $O_2(^3\Sigma)$ reactants. The minimum-energy path for the approach of the $^2P_{1/2}$ state will be in C_s symmetry on excited ^{2}A' and ^{2}A" surfaces that correlates with $^2B_2$ and $^2A_2$ states of the favored cyclic structure, respectively; the approach of the $^2D_{3/2}$-state atomic cation is symmetry allowed in

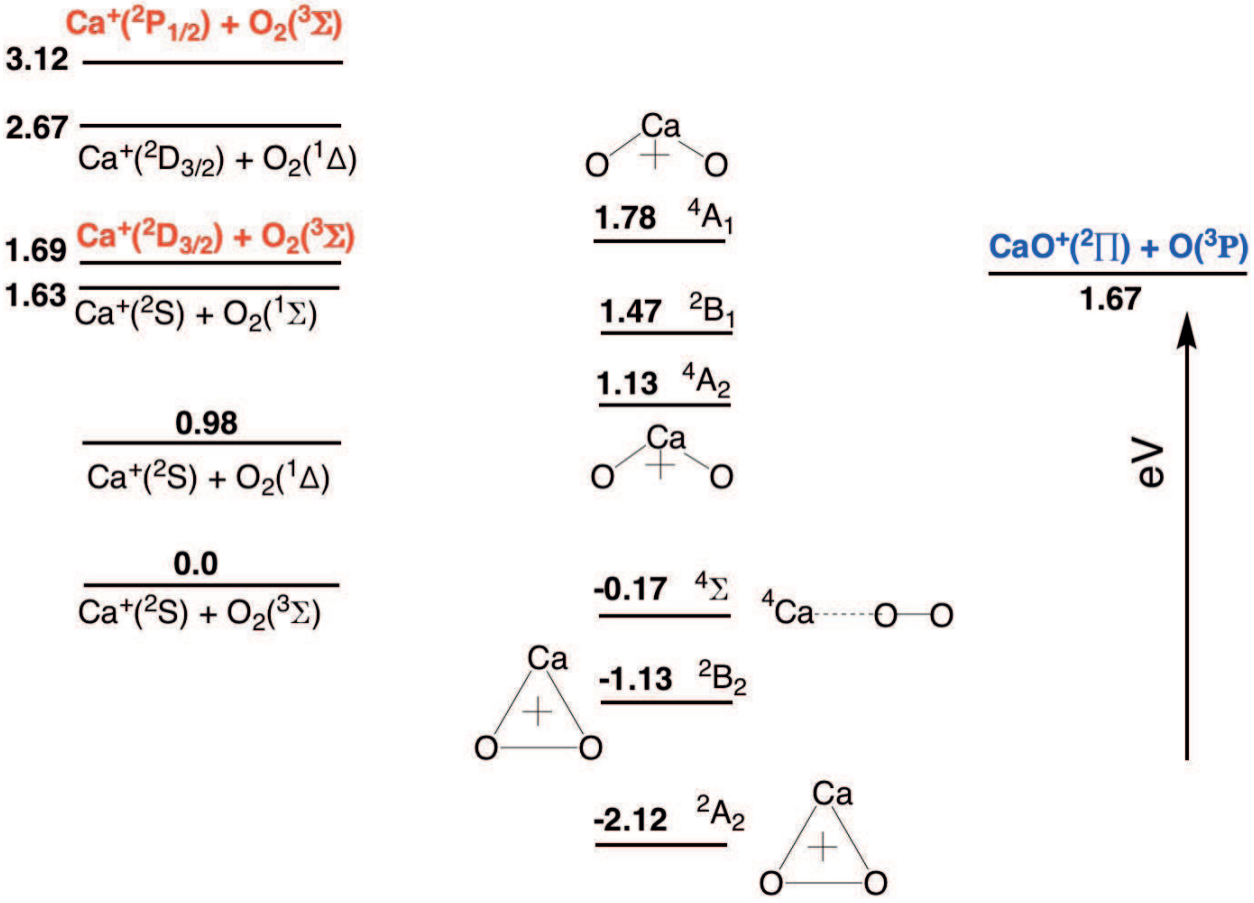

Figure 4.10: An energy-level diagram featuring electronic states of reactants, intermediates, and the observed $CaO^+ + O(^3P)$ product channel. All energies calculated at the CCSD(T) level, apart from those levels involving excited states of molecular oxygen, that use experimental excitation energies.

C_{2v}. Although the excited states that adiabatically correlate to reactants have not been calculated in this cursory exploration, it is likely that rapid internal conversion will produce vibrationally hot complexes associated with the lowest two electronic states (Fig. 4.10) that can then dissociate to observed products. Dissociation of complexes associated with these cyclic geometries would certainly encounter a barrier, but the complex will form with roughly 4−−5 eV of internal energy, which should be sufficient to surmount it. However, the possibility remains that the barriers for these processes are sufficiently great that they are above the entrance channel associated with $Ca^+(^2D_{3/2})$. If so, then another state of the complex that might come into play is the $^2B_1$ state

of the open form, which likely dissociates without a barrier. In such a scenario, the lower-energy entrance channel would react by a completely different pathway, and perhaps at the slower rate observed experimentally.

Note that the possibility discussed above is based on a very simple thermodynamic observation (the fact that the $^2B_1$ intermediate lies below products) and the assumption that its dissociation to CaO^+ and atomic oxygen is barrierless. Taking a theoretical investigation of the reaction process beyond this would involve a significant amount of effort; it is perhaps more productive to focus on reducing the uncertainty for the calculated reaction energy for Ca^+ ($^2D_{3/2}$) + O_2, the established endothermicity of which could successfully account for the difference in rate.

4.2.6 Summary

We measured the ionic products from the photo-induced reaction of $Ca^+ + O_2 \rightarrow CaO^+ + O$ using laser-cooled and trapped samples of Ca^+ ions. The product ions were trapped and sympathetically cooled by the atomic ions and detected using a TOF-MS. The reaction is energetically allowed only when the Ca^+ is in one of two electronically excited states ($^2P_{1/2}$ or $^2D_{3/2}$). By adjusting the detunings of the cooling lasers, the quantum-state population of the Ca^+ ions can be controlled. Using this control, we were able to determine reaction rate coefficients for reactions starting in either the $^2P_{1/2}$- or $^2D_{3/2}$-state. The $^2P_{1/2}$-state rate constant is a factor of three larger than for the $^2D_{3/2}$-state. We propose two possible explanations for this difference. The $^2D_{3/2}$-state reaction might be endothermic by a very small amount or, perhaps, proceeds through a different mechanism involving the $^2B_1$ state of the charged CaO_2 intermediate.

In future work, we plan to extend these types of measurements to more complex systems, such as reactions with organic molecules, and with additional control over the neutral reactant using a Stark decelerator. We will attach a traveling-wave Stark decelerator [131, 132] to the ion trap apparatus, similar to the experiments of the Oxford group [133] and the recent proposal by the Willitsch group [134]. This will allow us to tune the velocity of the neutral reactant down to 10 ms^{-1}, enabling studies of ion-molecule reactions below 10 K. A Stark decelerator can also

produce molecules in a single quantum state, thus enabling studies of the influence of the internal molecular states on the reaction. Ultimately, by introducing state-selective molecular ions into the trap [135, 136], fully quantum-state resolved molecular reactions at cold temperatures will be possible.

4.2.7 $Ca^+ + H_2O$

In order to accurately measure the state-dependent rate constants for $Ca^+ + O_2$, we needed to account for a parallel reaction occuring: $Ca^+ + H_2O \longrightarrow CaOH^+ + H$. Water is the largest contaminant in our vacuum chamber and this reaction can be observed even when the chamber pressure drops below 5×10^{-10} torr. As an added bonus to the published reaction, we measured the state-dependent rates of $Ca^+ + H_2O$. We cannot report the rate constants because we do not know the absolute concentration of water in the chamber. Instead, we measure the associated reaction rate and its dependence on Ca^+ quantum-state populations. In doing so, we verified the curious result reported in [34], where the reaction rate is dramatically faster for Ca^+ in the d-state than the rate is for Ca^+ in the p-state. This is shown in Fig. 4.11, which is a state-dependent rate fit for $Ca^+ + H_2O$. The rates themselves are summarized in Tab. 4.4. Their relatively large uncertainties come from the fact that tiny numbers of $CaOH^+$ ions were created from the parallel reaction. The $CaOH^+$ signal was typically 10 times smaller than the corresponding CaO^+ signal.

Table 4.4: The resulting reaction rates for the three quantum states of Ca^+. Uncertainties are from the 90% confidence interval for the fit parameters.

Ca^+ state	rate ($10^{-3}s^{-1}$)
$^2S_{1/2}$	0
$^2P_{1/2}$	1(4)
$^2D_{3/2}$	2(2)

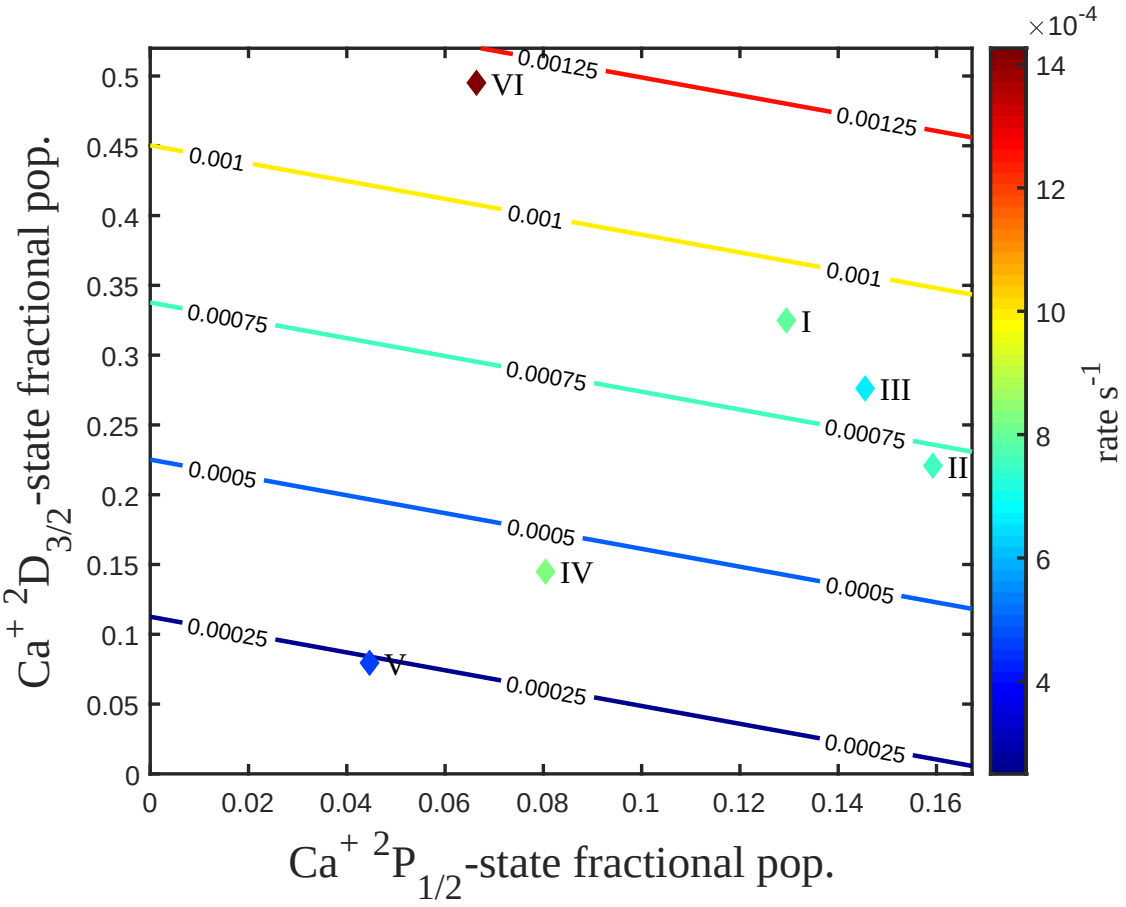

Figure 4.11: Dependence of the reaction rate on the $^2P_{1/2}$- and $^2D_{3/2}$-state populations of Ca^+ for the reaction $Ca^+ + H_2O$. The experimental measurements are shown as diamonds, where the color of the point represents the value of the rate. We perform a two-dimensional fit to the data, which allows us to estimate the state dependent rates. The contour lines represent constant reaction rate values of the fit.

4.2.8 Addendum

During the publication process of this paper, we were alerted to the fact that a 3-level OBE model does not accurately reflect the state-populations of calcium. In the presence of a magnetic field, the energy levels of Ca^+ split into 8 distinct Zeeman levels and thus an 8-level OBE must be used. This introduces two new variables that were present but not measured in the original experiment: the magnetic field experienced by the crystal, and the 866nm repump laser polarization

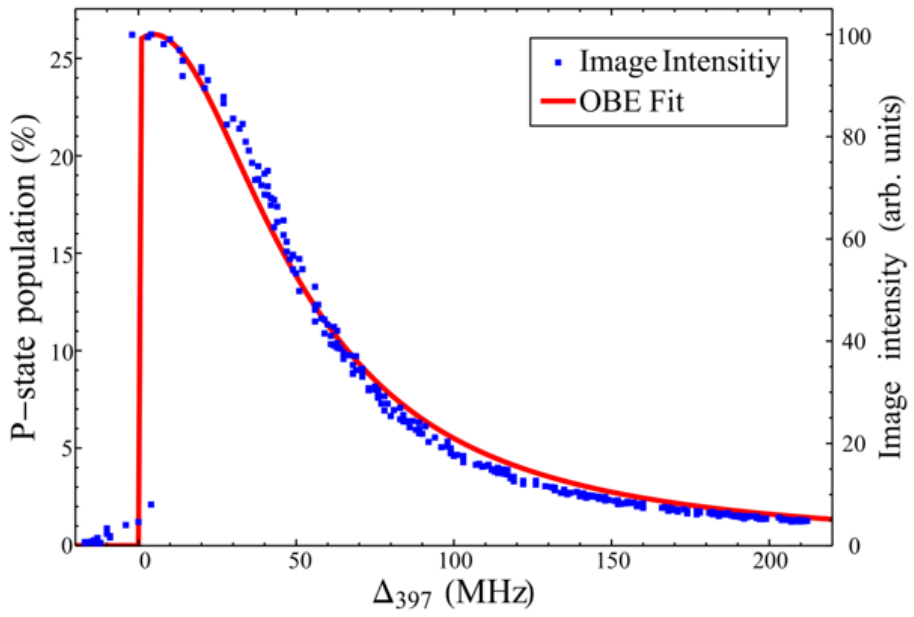

Figure 4.12: Calibration data used to predict calcium p-state populations by coulomb crystal fluorescence. The red line is the output of the 3-level OBE model used in [2]. Retroactive use of the 8-level OBE is not possible and thus the y-axis scaling of the p-state is too large by as much as a factor of 2.

angle with respect to the magnetic field determined quantization axis. These were measured and applied correctly for the $Ca^+ + O_2$ study [39], but not for the $Ca^+ + NO$ study [2]. Unfortunately, we cannot go back in time to measure the two variables required and retroactively apply the 8-level OBE. Fortunately, it will not have much of an impact on the results reported in [2]. The 3-level OBE still qualitatively predicts the excited state population of calcium as a function of coulomb crystal fluorescence intensity. This can be seen in the callibration data taken for $Ca^+ + NO$ shown in Fig. 4.12. What would change, however, is the quantitative predictions of the state-populations. Specifically, the the state-populations are too large by as much as a factor of 2. This would also affect the calculations of the absolute rate-constants reported. They should be increased by the corresponding factor.

Chapter 5

Isomer specific chemistry and isotopologue reactions of $C_2H_2^+ + C_3H_4$

The following is a pre-print draft of a paper yet to be submitted. This study investigates the isomer specific chemistry between sympathetically cooled $C_2H_2^+$ cations and two isomers of C_3H_4: allene and propyne. Paramount to this investigation was the use of isotope substitution of both the ionic and neutral reactants. Presented here are the data and analysis drafted for future publication. In addition to helping build the apparatus, control software, and analysis code, I acquired most of the data presented and wrote the majority of the text. Electronic structure calculations were provided by our fantastic theory collaborators John Stanton, James Thorpe, and Lam Nguyen at the University of Florida Gainesville.

5.1 Introduction

Small carbocations and neutral organic species such as $C_2H_2^+$ and C_3H_4 form some of the basic building blocks in organic chemistry and contribute to a diverse field of chemical environments. For example, acetylene has been observed in the interstellar medium (ISM)[137], where it is likely to play a central role in the formation of complex organic molecules through condensation reactions leading to larger carbocations.[75, 138, 139] Characterization of reaction mechanisms that contribute to condensation reactions can help to explain the diverse species of complex organic matter observed in the ISM.[140] Propyne and allene (C_3H_4) are also expected to play a role in similar polymerization reactions in the ISM.[141] An additional chemical environment of interest is planetary atmospheres. C_3H_4 was recently detected in the atmosphere of Titan, and is expected to

have a role in the formation of tholins that make up its dense haze layer.[142] All three reactants are also common constituents in fuels. The chemistry of acetylene flames have been studied in detail to investigate soot formation mechanisms.[143–145] The role of propyne and allene isomerization in flames have also been characterized, previously.[146] Our work adds valuable insight to the broad knowledgebase on these fundamental hydrocarbons using new experimental techniques of cooling of molecular ions co-trapped with laser-cooled atomic ions in ion traps.

Linear Paul ion traps (LIT) have proven to be fruitful environments to study gas-phase ion chemistry of molecular ions. Laser-cooled atomic ions can be used to sympathetically cool co-trapped molecular ions to translational temperatures below 10K. The cold, trapped ion ensemble forms a Coulomb crystal structure that can be stably trapped and interrogated for minutes to hours. By exposing the Coulomb crystal to a neutral reactant gas, chemistry can be observed to occur at low concentrations (10^6 cm^{-3}, $< 10^{-8}$ Torr) and over long timescales.[23] Another advantage of LITs is the ability to purify reactants using radio frequency (RF) secular excitation, which enables mass dependent ejection of ions from the trap.[147, 148] We use this technique to isolate acetylene ions in our trap from other carbocations trapped in the molecular ion loading process.

In addition to the ability to create clean, cold molecular ion samples, the LIT offers a way to determine the reaction products with high mass resolution and sensitivity. Recently, reaction studies in the Coulomb crystal environment have been improved by (radially) coupling to a time-of-flight mass spectrometer (TOFMS) to the LIT.[35–38, 149, 150] Low translational temperatures provide the initial conditions necessary for a high-resolution determination of the mass-to-charge ratio ($\frac{m}{\Delta m} > 1000$) and an accurate count of each constituent mass. The TOFMS also detects all constituent masses in the ion trap simultaneously. Because reaction product ions are also trapped and sympathetically cooled, one can follow reactions both by the depletion of reactants and by the growth of product channels. This enables a more complete description of reaction kinetics.

These detection methods also allow for extensions beyond reaction kinetics into the realm of chemical dynamics, which can be characterized by isotope substitution studies.[43, 44] Even for small organic molecules, there can be a large combination of isotope substituted reactants

available. Following the isotopic distribution of product channels is a powerful extension to basic kinetic studies. These data can validate and/or exclude kinetic pathways proposed by potential energy surface calculations. Overall, this degree of control and measurement sensitivity is critical to tracking reaction pathways in the experiment. With these experimental techniques, we were able to study here the previously unexplored reactions between acetylene cations and C_3H_4.

What follows in this article is a detailed investigation into the isomer specific chemical mechanisms observed in the reactions between acetylene cations, allene, and propyne. This begins with an overview of the experimental and computational methods we used to study the reactions. After that, the paper is divided into two major sections, one for reactions involving propyne and another for reactions with allene. Each reaction section is structured the same way. First is the description of experimental results, which include a model of the observed reaction kinetics, measured reaction rate constants, branching ratios for primary products, and select branching ratios for secondary products. Second is a description of computational results, which cover the reaction potential energy surface and supporting calculations. Last is a discussion of how the experimental results validate the computational results. The discussion section also includes a comparison of the results in this inquiry to those in the literature (where possible), as well as possible sources of uncertainty. Finally, the paper concludes with a summary of the presented results and an outlook on future work.

5.2 Methods

Experimental: The details of our LIT-TOFMS apparatus have been described in previous work.[2, 38, 39] We will give a short overview of the experimental apparatus, emphasizing the new aspects and experimental procedures. See Fig. 5.1 for a schematic layout of the apparatus.

A major addition from previous descriptions was a molecular beam source, which was needed to study reactions with molecular ions. A piezo actuated (PZT) valve backed by acetylene gas diluted in argon (6%, 30 PSIG) produced a pulsed, supersonic beam in a diferentially pumped region of the vacuum system. The molecular beam was skimmed using a 2 mm diameter skimmer,

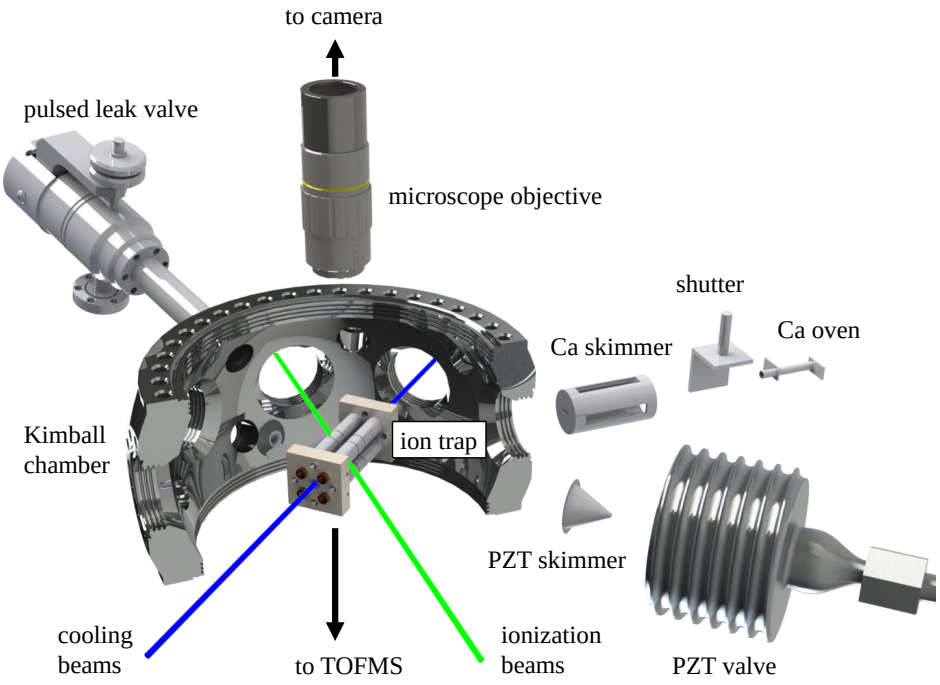

Figure 5.1: Schematic render of the LIT-TOFMS apparatus. A cross-sectional view of the spherical octagon vacuum chamber reveals the ion trap at the center of our experiment. The source of Ca^+ is an effusive beam of neutral calcium, generated by an oven. The source of molecular ions is a pulsed, supersonic gas jet of neutral acetylene seeded in a noble carrier gas. These neutral beams are intersected by pulsed ionization lasers in the center of our trap to load atomic and molecular ions. Ca^+ ions are addressed by the cooling lasers. To observe the laser induced fluorescence from Ca^+, a microscope objective (outside the UHV chamber) is implemented. A pulsed leak valve (also outside the UHV chamber) is used for the introduction of the neutral reactant.

which allowed the ion trap chamber to recover to a UHV pressure ($\sim 10^{-10}$ Torr) quickly after operation of the pulsed valve. The resultant molecular beam passed through the center of the ion trap along the radial direction, where constituents of the beam could be ionized and loaded into the trap. In particular, acetylene cations were produced by the intersection of a focused, pulsed dye laser (LIOP-TEC, 2mJ/pulse, $f = 20$ cm) and the molecular beam at the center of the ion trap. A (1+1') resonance enhanced multi-photon ionization (REMPI) scheme was used at ~216nm to load $C_2H_2{}^+$. [151] For $C_2D_2{}^+$, ~218nm was used to address the same intermediate excited state.[152] Both the dye laser and PZT valve were run synchronously at a 10 Hz rep rate, which loaded hundreds of molecular ions into the trap in <1s. Due to the high reactivity of acetylene cations

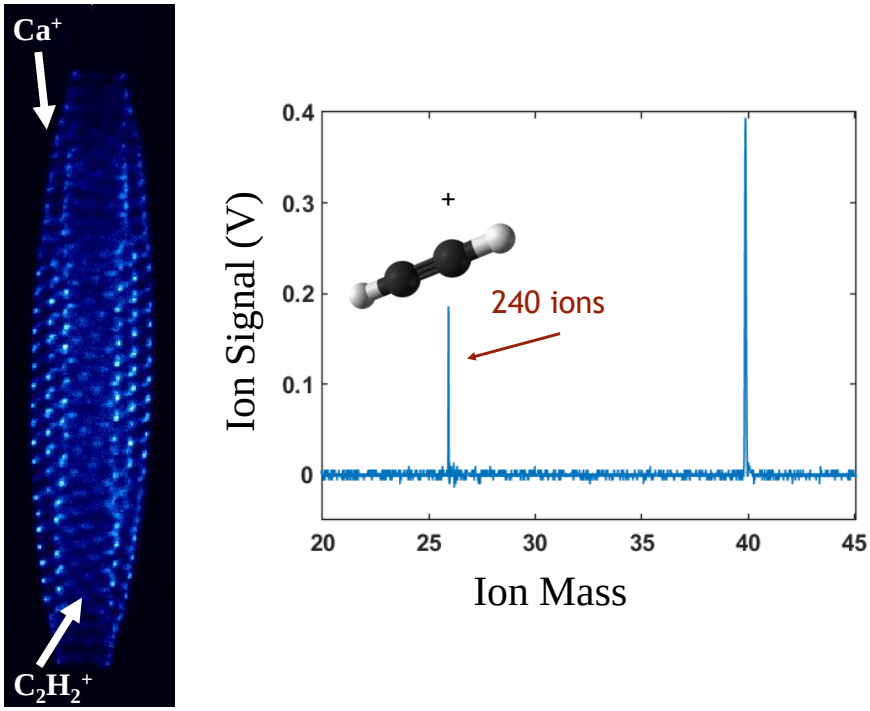

Figure 5.2: Left: False-color fluorescence microscope image of a typical two-component Coulomb crystal and its corresponding TOFMS trace (right). The TOFMS data were produced by a single trap loading, i.e., not averaged over multiple experimental cycles. The mass spectrum shows ∼240 $C_2H_2^+$ ions were co-trapped with ∼600 Ca^+ ions.

and the high ionization photon energy, this loading scheme also loaded many contaminant ions. To remove all contaminant ions, a resonant secular mass excitation scheme was implemented.[147, 148] Radio-frequency (RF) excitations were used to remove all unwanted masses, thus purifying the acetylene sample for the reaction study. Typically, 150–250 acetylene ions remained in the trap after purification, and contaminant ions constituted $\lesssim$5% of the acetylene number.

Calcium ions (600–900) were then loaded into the trap and laser cooled to $\lesssim$ 1 K.[38] The cooled calcium ions sympathetically cooled the acetylene ions via the Coulomb-Coulomb interaction to translational temperatures below 10K, similar to previous work.[49] Additional RF secular excitations were applied to remove from the trap the isotopes of calcium not addressed by the cooling lasers. This point in the experimental procedure marked the initial condition (time, t=0) for reaction measurements. See Fig. 5.2 for a typical trapped ensemble after loading and purification.

Reactions were then carried out by admitting a neutral reactant gas into the vacuum chamber

by a pulsed leak valve scheme.[127] This raised the UHV chamber base pressure of 10^{-10} Torr to a constant pressure of about $\sim 3 \times 10^{-9}$ Torr within 2 s. The neutral gas was a 7% mixture of allene or propyne diluted in a noble gas (argon or helium). After the Coulomb crystal was exposed to the neutral reactant for a variable reaction time of 10–300 s, the pulsed leak valve was closed and the neutral gas was pumped out of the UHV chamber, which quickly (< 2 s) returned to the base pressure. Pressures were measured by a hot-cathode ion gauge. Subsequently, the crystal was ejected into the TOFMS to determine the number of ions in the trap, as well as their mass-to-charge ratio. This measurement scheme was repeated for various reaction times (10-15 times per reaction time), which allowed us to create reaction curves simultaneously for the reactants and products (e.g., Fig. 5.3).

Because reaction curves were measured at a constant chamber pressure – and thus, constant neutral reactant concentration ($[n] \sim 10^6$ cm^{-3}) – reaction rate constants could be determined. Fitting reaction curves to a reaction model (e.g., Fig. 5.5) gave the effective rate constant, k_{eff} for each pathway. All reaction pathways were treated as pseudo-first order with the neutral reactant being in excess. The absolute rate constant, k, was then given by the relationship $k_{eff} = k \cdot [n]$.

To measure the effects of isotope substituted reactants and more carefully map out reaction pathways, deuterium labelled reactants (CDN isotopes, >98% D) were used. For the rest of the paper, we will refer to the explicit chemical formulas of the reactants to emphasize which hydrogen sites were substituted for deuterium. In addition to unlabelled acetylene (C_2H_2), allene ($H_2C_3H_2$), and propyne (HC_3H_3), we utilized C_2D_2, DC_3H_3, HC_3D_3, and DC_3D_3 gasses diluted in argon (7%). $D_2C_3D_2$ was also used, but diluted in helium (10%) for unrelated technical reasons. Reaction curves were mapped out and fit to models in the same way as described above. The product channel distributions for the isotopologue reactions were then compared to help verify the potential energy surfaces.

Computational: Potential energy surfaces were assembled via quantum chemical calculations. We calculated the propyne surface using our hybrid model: CCSD(T)/ANO1//ANO0. This means that we calculate molecular geometries and vibrational frequencies using CCSD(T)/ANO0, and

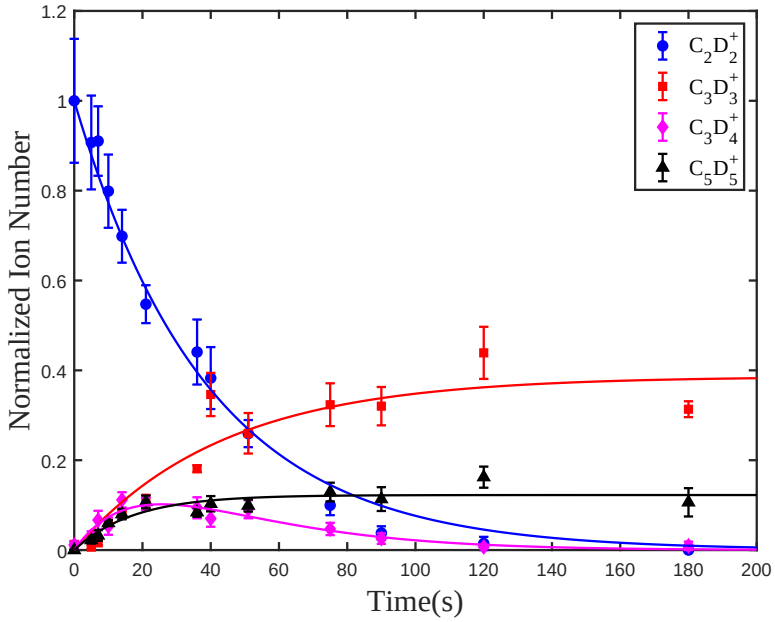

Figure 5.3: Primary products of the reaction $C_2D_2^+ + DC_3D_3$ as a function of time. Each point represents the mean and standard error of 12 measurements. Secondary reaction products have been omitted for clarity. Ion numbers are normalized to the initial number of acetylene ions in the trap ($\sim$ 200 ions).

then a single point energy from CCSD(T)/ANO1 using this geometry. We have not performed rigorous analysis of the errors of this model, but relative errors should around ±2 kcal/mol (90 meV). For the allene surface, the mHeat+[3] method was used to improve the accuracy of the calculations to about ±0.23 kcal/mol (10 meV). Kinetics were performed on the propyne surface to estimate branching ratios of the products. We calculated rate coefficients from the standard Rice–Ramsperger–Kassel–Marcus (RRKM) equation.

5.3 Propyne – HC_3H_3

5.3.1 Experimental results

Over the course of the reaction time (ranging from 100–300s), all trapped acetylene cations reacted away into product ions (see Fig. 5.3). The primary product ions for the reaction $C_2H_2^+ + HC_3H_3$ are $C_3H_3^+$, $C_3H_4^+$, and $C_5H_5^+$. Because $C_3H_4^+$ and Ca^+ are both mass 40 u, the two

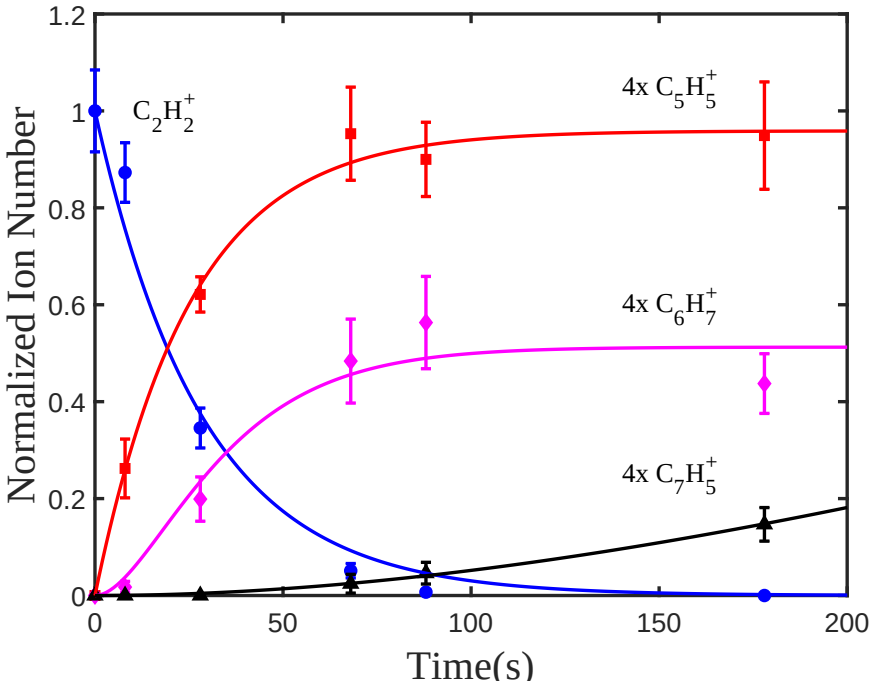

Figure 5.4: Example detection of multiple orders of products from $C_2H_2^+ + HC_3H_3$. The product order is apparent by the delay of onset in appearance and their mass is too large to be a product of $C_2H_2^+ + C_3H_4$. $C_5H_5^+$ was first order, $C_6H_7^+$ second, and $C_7H_5^+$ was third. Ion numbers have been normalized to initial $C_2H_2^+$ number. Product channels have been multiplied by 4 to enhance clarity of the differences in reaction order. Note that not all measured product channels are shown in this plot.

ion species are not readily distinguished from each other. The product assignment was directly confirmed by the isotopologue reaction $C_2D_2^+ + DC_3D_3$, which shifted the product $C_3H_4^+$ to $C_3D_4^+$ (mass 44 u) and allowed the product channel to be assigned unambiguously (see Fig. 5.3). The product $C_3H_4^+$ can also be inferred by the detection of heavier-mass product ions, $C_6H_5^+$ and $C_6H_7^+$, resulting from the secondary reaction $C_3H_4^+ + HC_3H_3$.[141] These products were evidently second order in comparison to the primary products, because their onset occurs later in time and their mass-to-charge ratio was too large to be a product of $C_2H_2^+ + C_3H_4$ (See Fig. 5.4). Of the three primary order products, only $C_3H_4^+$ was observed to react further with the neutral propyne in excess in the chamber. Third order reactions also occurred, which resulted in product ions $C_7H_5^+$ and $C_7H_7^+$, as shown in Fig. 5.4.

From the results of $C_2H_2^+ + HC_3H_3$, a reaction model was developed depicting the relationship between reactant and product ions (see Fig. 5.5). The large amount of branching in the reaction led to very small ion numbers per product channel, especially for higher order products. Detailed relationships between higher order products were ambiguous and are left as such in the model (represented by curly brackets). Branching becomes even more prevalent in analogous models for the isotopologue reactions studied, as H/D scrambling is observed within each product order.

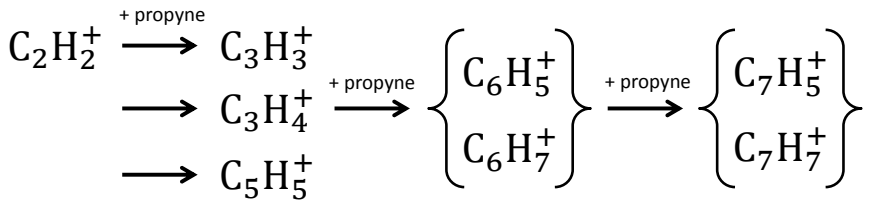

Figure 5.5: Reaction model for propyne. Each arrow represents a bimolecular gas-phase reaction between the ion and a neutral propyne. Vertically stacked ions are of the same reaction order. The exact relationship between higher order products was undetermined and beyond scope of this work. This ambiguity is represented by the curly brackets.

After developing a reaction model, absolute rate constants for each isotopologue reaction were determined. Ion numbers were normalized by the initial acetylene ion number for each reaction. The decay of the normalized reactant ion number vs. time was fit to determine the rate. The rate constant was then obtained by dividing the rate by the neutral gas concentration. The results are tabulated in Tab. 5.1. The uncertainties reported are derived using the 90% confidence interval of the rate fit parameter. The uncertainties are purely statistical and do not include any possible inaccuracy introduced by the method of concentration measurement.

Branching ratios for the primary products $C_5H_xD_y^+$ $(x + y = 5)$ and $C_3H_xD_y^+$ $(x + y = 3)$ were determined by a fit of normalized product ion numbers to the reaction model. These results are reported as percentages in Tab. 5.2 for the $C_5H_xD_y^+$ $(x + y = 5)$ channel and Tab. 5.3 for

the $C_3H_xD_y^+$ $(x+y=3)$ channel. The rate constant for each of these pathways can be calculated by multiplying the branching ratio with its corresponding isotopologue rate constant in Tab. 5.1. The branching ratio of the $C_3H_4^+$ channel, and its analogous isotopologues, can be inferred by subtracting the branching ratios of the two other primary products from 100%.

Table 5.1: Reaction rate constants for all measured isotopologue reactions. All rate constants determined by fit of the loss of charged reactants. Uncertainties are derived from the 90% confidence interval of the fit and do not account for possible inaccuracies in the neutral concentration measurement.

Reactants	$k\left(10^{-9}\frac{\mathrm{cm}^3}{\mathrm{s}}\right)$
$C_2H_2^+ + HC_3H_3$	6(1)
$C_2H_2^+ + DC_3H_3$	6(1)
$C_2H_2^+ + HC_3D_3$	7(1)
$C_2H_2^+ + DC_3D_3$	6(1)
$C_2D_2^+ + HC_3H_3$	8(2)
$C_2D_2^+ + DC_3H_3$	8(3)
$C_2D_2^+ + HC_3D_3$	6(2)
$C_2D_2^+ + DC_3D_3$	7(2)

Table 5.2: Branching ratios for the reaction $C_2H_2^+ + HC_3H_3 \longrightarrow C_5H_5^+ + H$ and its isotopologues that led to $C_5H_xD_y^+$ ($x+y=5$). Numbers are the branching ratios (in %) for each mass channel as determined by the fit of the model. Uncertainties are the 90% confidence interval of the branching ratio fit. Blank spaces indicate the mass channel was either not populated or not statistically different from zero at the 10% significance level.

Products	$C_5H_5^+$	$C_5H_4D^+$	$C_5H_3D_2^+$	$C_5H_2D_3^+$	$C_5HD_4^+$	$C_5D_5^+$
Mass (U)	65	66	67	68	69	70
$C_2H_2^+ + HC_3H_3$	21(3)					
$C_2H_2^+ + DC_3H_3$	3(2)	17(2)				
$C_2H_2^+ + HC_3D_3$			11(2)	7(1)		
$C_2H_2^+ + DC_3D_3$				12(2)	6(1)	
$C_2D_2^+ + HC_3H_3$		4(2)	11(2)			
$C_2D_2^+ + DC_3H_3$			8(5)	14(5)		
$C_2D_2^+ + HC_3D_3$					16(4)	5(5)
$C_2D_2^+ + DC_3D_3$						13(3)

Table 5.3: Branching ratios for the reaction $C_2H_2^+ + HC_3H_3 \longrightarrow C_3H_3^+ + C_2H_3$ and its isotopologues that led to $C_3H_xD_y^+$ $(x + y = 3)$. Numbers are the branching ratios (in %) for each mass channel as determined by the fit of the model. Uncertainties are the 90% confidence interval of the branching ratio fit. Blank spaces indicate the mass channel was either not populated or not statistically different from zero at the 10% significance level.

Products	$C_3H_3^+$	$C_3H_2D^+$	$C_3HD_2^+$	$C_3D_3^+$
Mass (U)	39	40	41	42
$C_2H_2^+ + HC_3H_3$	53(9)			
$C_2H_2^+ + DC_3H_3$	27(4)	40(20)		
$C_2H_2^+ + HC_3D_3$	5(1)	33(8)	19(3)	6(1)
$C_2H_2^+ + DC_3D_3$			18(3)	30(20)
$C_2D_2^+ + HC_3H_3$	31(5)	24(9)	5(1)	
$C_2D_2^+ + DC_3H_3$		40(20)	11(2)	
$C_2D_2^+ + HC_3D_3$			27(3)	25(5)
$C_2D_2^+ + DC_3D_3$			5(2)	36(4)

It was also possible to estimate the branching ratios for selected second order products that stemmed from the reaction $C_3H_4^+ + HC_3H_3$. This was done by fitting a truncated version of the model that assumed the products $C_6H_5^+$ and $C_6H_7^+$ are the final products and do not react further. As such, the branching ratios tabulated in Tab. 5.4 are likely lower bounds on the actual branching ratios. More product branches were observed from these isotopologue reactions than are reported. Some of the detected mass-to-charge ratios could not be assigned a unique chemical formula due to the possibility of H/D swapping. Since the secondary reactions were not the focus of this study, those products have been omitted.

Table 5.4: Estimated branching ratios for the reaction $C_3H_4^+ + HC_3H_3 \longrightarrow$ products and its selected isotopologues. Numbers are the branching ratios (in %) for each mass channel, as determined by the fit of the truncated model. Uncertainties are the 90% confidence interval of the branching ratio fit. Blank entries indicate the mass channel was not statistically different from zero at the 10% significance level. Detected mass-to-charge ratios that could not be assigned a unique chemical formula have been omitted.

Products	$C_6H_5^+$	$C_6H_7^+$	$C_6D_5^+$	$C_6D_7^+$
Mass (U)	77	79	82	86
$C_2H_2^+ + HC_3H_3$	2(1)	13(3)		
$C_2H_2^+ + DC_3D_3$			2(1)	6(1)
$C_2D_2^+ + HC_3H_3$	2(1)	7(2)		
$C_2D_2^+ + DC_3D_3$			4(1)	9(3)

5.3.2 Computational results

The experimentally observed formation of $C_3H_3^+$ and $C_5H_5^+$ from the reaction of $C_2H_2^+$ with propyne is indicative of a reaction pathway featuring a short-range, bound reaction complex. Figure 5.6 displays a coupled-cluster, CCSD(T), potential energy surface (PES) that comprises the salient stationary points (minima and transition states) for this system, where the (zero-point corrected) energies refer to the undeuterated species.

The formation of the acetylene-propyne cation complex is initiated by a charge transfer from acetylene cation to propyne, culminating in the complex labelled as INT0 in Figure 5.6. This process is exothermic by about $\sim$1 eV; the lack of collisional cooling in the ion trap, coupled with barrier heights below the entrance energy, enables the vibrationally hot complex to rapidly interconvert between the many minima displayed in Figure 5.6. This reaction ultimately produces $C_5H_5^+$, $C_3H_4^+$, and $C_3H_3^+$ via the loss of a hydrogen atom (PRD1, PRD3, and PRD5), the loss of a neutral acetylene (PRD4), and the loss of a vinyl radical (PRD2), respectively.

The product yields can be simulated by employing a collisionless treatment of the chemical

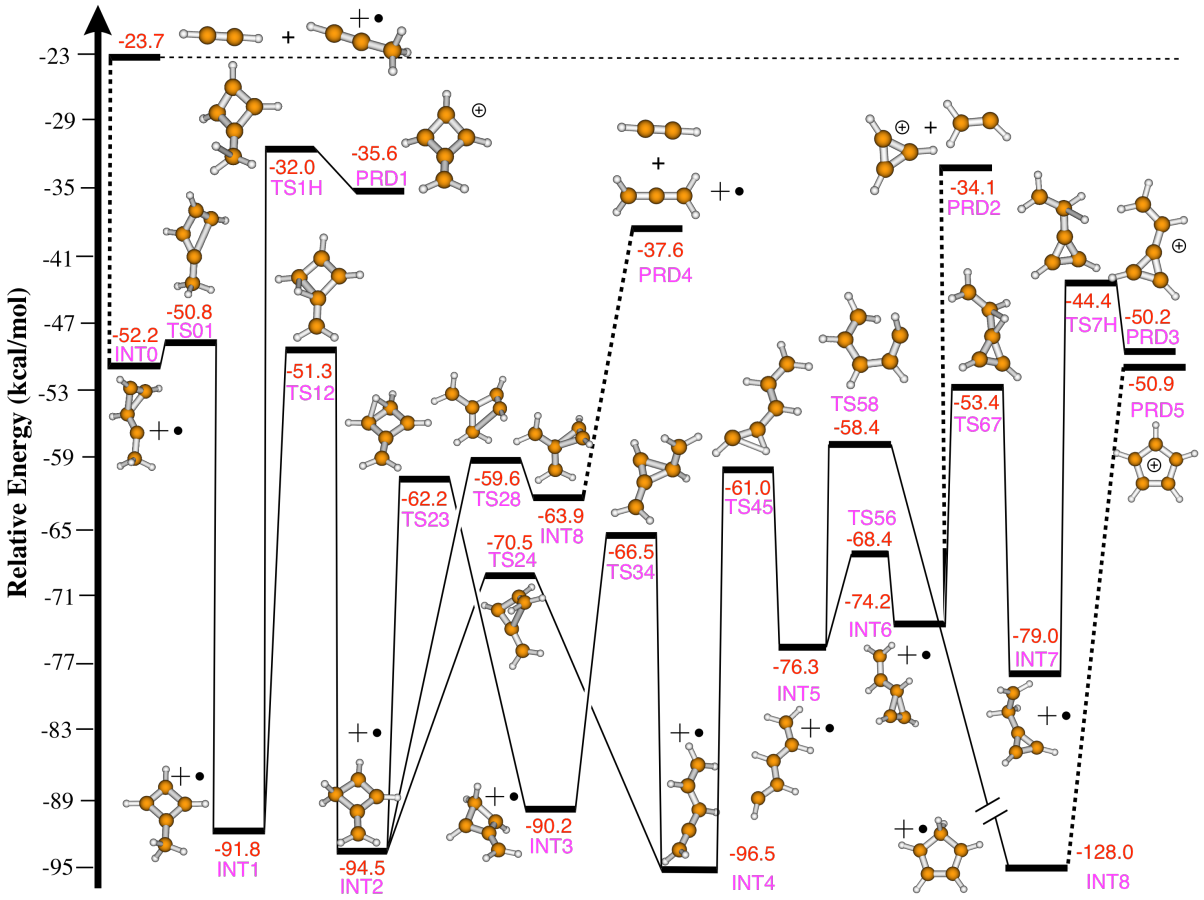

Figure 5.6: Potential energy surface (PES) connecting the propyne and acetylene cation to experimentally observed primary products. The energy of each stationary point is calculated using CCSD(T) in the scheme described in the main text. All energies are relative to separated acetylene cation and propyne. Dashed lines between stationary points indicate reactions that occur via a barrierless process. Note that the initial point of the PES is given for after the first charge exchange has taken place already.

master equation in conjunction with RRKM theory.[71]

We estimate that reactions between propyne and acetylene cations, which proceed through the complex displayed in Figure 5.6 result in product yields of roughly 40 % $C_3H_3^+$ and 60 % $C_5H_5^+$, in contrast to the experimentally observed product ratios of roughly 70 % $C_3H_3^+$ and 30 % $C_5H_5^+$. This suggests that another pathway may be in play, namely one where charge transfer between propyne and acetylene occurs, but formation of a reactive complex is suppressed. This is supported by the experimentally observed build-up of $C_3D_4^+$ in Fig. 5.3. Combinations of long-

range charge exchange mechanisms and short range, bound, complex formation can be dependent on the reaction impact parameter. These effects have been studied in other ion-molecule systems velocity map imaged (VMI) products from crossed-beam experiments.[153] Without a measured angle-dependent reactive cross-section, it is difficult to predict *a priori* the percentage of ionized propyne molecules that would take this second path.

5.3.3 Discussion

The distribution of products for the $C_5H_xD_y^+$ ($x+y=5$) product channel exhibited all of the isotopic combinations of hydrogen and deuterium possible (see Tab. 5.2). These H/D scrambled products suggested the formation of a $C_5H_6^+$ complex with a PES conducive to H/D swapping. Such a surface would need shallow minima along the pathway where hydrogen sites exchange. This condition is met by the transition states in Fig. 5.6 are all submerged well below the energy of charge exchange. One of many examples of isomerization that leads to swapping can be seen following steps (INT2) thru (INT4) in Fig. 5.6. Hydrogen-site swapping in these steps is shown from the methyl group of propyne to the other end of the complex. There is also ambiguity in the source and destination of the transferred hydrogen atom. Combined with similar pathways on the PES, any of the hydrogen/deuterium atoms from either acetylene or propyne could end up in the final product. Because there is only loss of a single hydrogen from the system to form $C_5H_xD_y^+$ ($x+y=5$), a maximum of two isotopic arrangements can exist for each isotopologue reaction. We also observed that the loss of a methyl group hydrogen is preferred (largest branching ratio) in every isotopologue reaction. This may be informative when considering future RRKM calculations.

The $C_3H_xD_y^+$ ($x+y=3$) product channel in the isotopologue experiments told a very similar story to that of $C_5H_xD_y^+$ ($x+y=5$). We observed experimentally of all but three of the allowed combinations (see Tab. 5.3). The three missing combinations are $C_2D_2^+ + DC_3H_3 \longrightarrow$ 39 u ($C_3H_3^+$) and 42 u ($C_3D_3^+$), and $C_2H_2^+ + DC_3D_3 \longrightarrow$ 40 u ($C_3H_2D^+$). These are likely missing because the low ion numbers in each of the different product channels allow us to differentiate only a branching ratio of $\geq$5% from zero for the $C_3H_3^+$ channel. Additionally, the neutral reactant gasses

are specified to >98% isotopic purity only from the factory. We cannot rule out the possibility H/D swapping occurred in the stainless steel lines delivering the gas to the vacuum chamber. Accordingly, reactions may result in products with hydrogen atoms that do not originate from the assumed reactants. This was notably the case for the reaction of $C_2D_2^+ + DC_3D_3$, where we observe the product $C_3HD_2^+$, which should not be possible. While this was a clear influence of contamination, the levels were low enough to believe that the main results of the measured isotopolouge reactions were not appreciably influenced. The combined observations of $C_5H_xD_y^+$ $(x+y=5)$ and $C_3H_xD_y^+$ $(x+y=3)$ product channel isotopic distributions validate the proposed PES pathways.

The lack of secondary reactions observed in the experiment between propyne and the $C_3H_3^+$ and $C_5H_5^+$ primary product channels notably indicated stable isomers of the products. The most stable isomers for both carbocations involve resonant ring structures (PRD2 and PRD5 in Fig. 5.6). Thermodynamic calculations verify that the cyclopropenyl cation is the only isomer of $C_3H_3^+$ that is exothermic with respect to the reactants. Thus, PRD2 is very likely the only observed product isomer of $C_3H_3^+$. For $C_5H_5^+$, there are three isomers that thermodynamic calculations show are exothermic with respect to the reactants (PRD1,PRD3, and PRD5), all of which involve ring structures. The barriers leading to any of these products are all well below the initial reaction energy and thus do not rule out any of the isomers. A future study involving a titration reaction or spectroscopy is needed to identify the $C_5H_5^+$ structures produced by the $C_2H_2^+ + HC_3H_3$ reaction.

Another prediction of the computational results was that both long-range and short-range charge exchange could lead to the $C_3H_4^+$ product. By long-range we mean no bond is formed between reactants in the process of charge exchange. By short-range, we mean the $C_5H_6^+$ bound complex is formed (see Fig. 5.6), and the reaction exits the surface via either PRD4 or the unnamed entrance channel with propyne cation, which ultimately produces a $C_3H_4^+$ product. The former, long-range process, would show no signs of H/D scrambling in the isotopic distribution of charge exchange products, while the latter, short-range process, could. Unfortunately, our isotopologue reaction measurements cannot distinguish these two possibilities for two reasons: First, the possible

mass channels for charge exchange products overlap considerably with those of $C_3H_3^+$ products. Second, secondary reactions between $C_3H_4^+$ and propyne continually deplete the charge exchange product formed by the primary reaction.[141] This prevented sufficient build-up of detectable primary reaction products in many (but not all) isotopologue reactions. Those two factors prevented unambiguous determination of $C_3H_4^+$ product channels. A possible way around these limitations would be to monitor the second order products from the resulting $C_3H_4^+ + HC_3H_3$ reaction and its isotopologues. That method is also untenable in our experiment due to the immense branching and isotopic scrambling of the second order products leading to branching ratios typically $\leq$3%. There is no way to unambiguously assign chemical formulas to such secondary product mass channels with the levels of ionic and neutral contaminants present in this study.

Impurities also contribute to the Uncertainty in the branching ratios. As stated in the methods section, a small number of ionic impurities, relative to acetylene ion numbers ($\lesssim$5%), remain trapped after RF secular excitation cleaning. For $C_2H_2^+$, the largest impurity occurred at mass 27 u ($C_2H_3^+$). For $C_2D_2^+$, the largest impurities were masses 27 and 29 ($C_2H_3^+$,C_2HD^+, and/or $C_2D_2H^+$). Bimolecular reactions between these contaminant cations and neutral propyne are expected to form products that overlap with the primary product channels of interest.[154]

Some of the experimentally observed products from secondary reactions, however, can be assigned chemical formulas. We can thus compare these results with previous measurements of the reaction $C_3H_4^+ + HC_3H_3$ by Anicich *et. al.*[141]. Both experiments observed the $C_6H_7^+$ and $C_6H_5^+$ products. Notably, we did not see the $C_3H_5^+$ product channel that Anicich *et. al.* did. Since the product channel is exothermic, we suggest two explanations why we do not see it. One possibility is there is a barrier to this process that cannot be overcome by the translationally cold collision temperatures in our apparatus, $\sim$150 K, while those in the cited ion cyclotron resonance (ICR) experiment could be on the order of $\sim$1000 K due to their method of ion production. Another possibility is that our reaction took place in a lower pressure environment, $\lesssim 10^{-9}$ Torr, than that of the ICR reaction, $\geq 10^{-6}$ Torr. Their experiment investigated the effects of pressure on product branching ratios and found that as the pressure is reduced from 10^{-6} Torr to 10^{-8} Torr, the $C_6H_7^+$

product becomes preferred over the $C_3H_5^+$ product. The more than two orders of magnitude extra gas pressure could kinetically stabilize a pathway on the potential energy surface leading to this product. Building a potential energy surface to investigate secondary reaction pathways would likely provide insight into this discrepancy.

Lower absolute concentrations in our experiment also caused some challenges. These are reflected in measured overall reaction rate constants of the isotopologue reactions. All of the rate constants are considerably larger than predicted by the Langevin model for $C_2H_2^+ + HC_3H_3$, $k_L \approx 2 \times 10^{-9} \frac{cm^3}{s}$. We attribute this discrepancy to the inaccuracy of our absolute pressure measurement made at extremely low gas densities. This inaccuracy is ultimately due to systematic effects inherent to the ion gauge used to measure the introduced neutral gas pressure, which can be upwards of a factor of two or more in the $< 10^{-8}$ Torr pressure regime.[155] Despite this fact, relative differences in the rate constants could have revealed kinetic isotope effects. However, None of the rate constants measured appear to show isotope effects within their respective statistical uncertainties.

5.4 Allene – $H_2C_3H_2$

5.4.1 Experimental Results

The measurements in the system $C_2D_2^+ + H_2CCCH_2$ followed the same steps as described for propyne above. The observed primary product ions for the reaction $C_2H_2^+ + H_2C_3H_2$ were $C_3H_3^+$ and $C_3H_4^+$ (see Fig. 5.7). Compared to the reaction with propyne, $C_5H_5^+$ was notably not observed. Also in contrast to the propyne case, the products of the deuterium substituted aceyetlene reaction did not show isotopic scrambling. Similar to the propyne case, $C_3H_4^+$ and Ca^+ are both mass 40 u, which were not readily distinguished from each other. However, the assignment of this product was directly confirmed by the isotopologue reaction $C_2D_2^+ + D_2C_3D_2$, which shifted the product $C_3H_4^+$ to $C_3D_4^+$ (mass 44 u) and allowed the product channel to be assigned unambiguously. The $C_3H_4^+$ product channel can also be inferred by the existence of

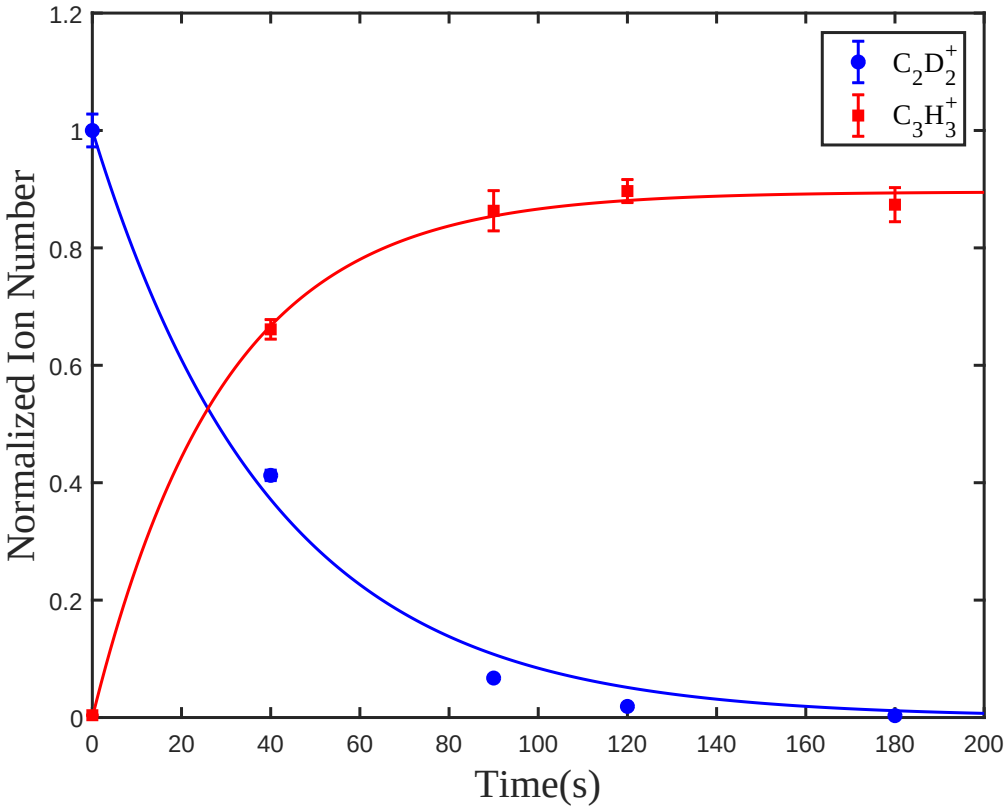

Figure 5.7: Primary product of the reaction $C_2D_2^+ + H_2C_3H_2$ as a function of time. Each point represents the mean and standard error of 10 measurements. Secondary and higher order products have been omitted for clarity. Ion numbers are normalized to the initial acetylene in the trap 120 ions.

heavier-mass product ions, $C_6H_5^+$ and $C_6H_7^+$. These products were the result of the reaction $C_3H_4^+ + H_2C_3H_2$[141] and were evidently second order in comparison to the primary products and their mass-to-charge ratio is too large to be a product of $C_2H_2^+ + C_3H_4$ (see Fig. 5.8). Only $C_3H_4^+$ was observed to react further with the neutral allene in excess in the chamber. We also observed third order reactions resulting in product ions $C_7H_5^+$ and $C_7H_7^+$.

From the results of $C_2H_2^+ + H_2C_3H_2$, a reaction model was developed depicting the relationship between reactant and product ions (see Fig. 5.9). Branching in the reaction led to very small ion numbers per product channel for higher order products. Detailed relationships between higher

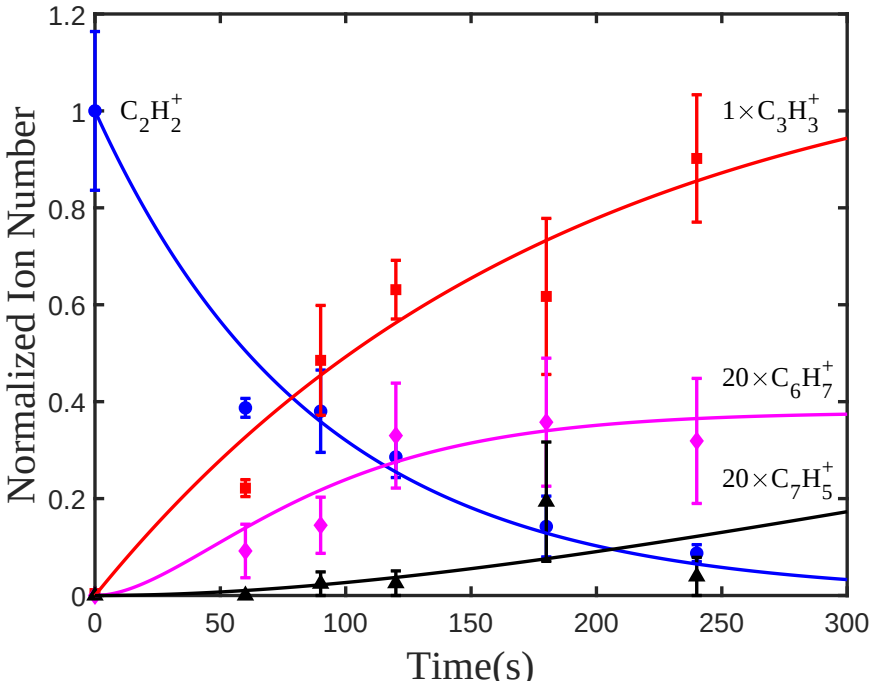

Figure 5.8: Example detection of multiple orders of products from $C_2H_2^+ + H_2C_3H_2$. Which product order is apparent by delay of onset in appearance and their mass was too large to be a product of $C_2H_2^+ + C_3H_4$. $C_3H_3^+$ was first order, $C_6H_7^+$ second, and $C_7H_5^+$ was third. Ion numbers have been normalized to initial $C_2H_2^+$ number. Second and third order product channels have been multiplied by 20 to enhance the clarity of the differences in reaction order. Note that not all measured product channels are shown in this plot.

order products were ambiguous and are left as such in the model (depicted by curly brackets).

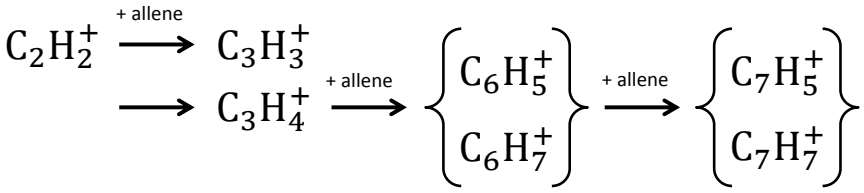

Figure 5.9: Reaction model for allene. Each arrow represents a bimolecular gas-phase reaction with the ion and a neutral allene. Vertically stacked ions are of the same reaction order. The exact relationship between higher order products was undetermined and beyond scope of this work. This ambiguity is represented by the curly brackets.

After developing a reaction model with allene, absolute rate constants for each isotopologue reaction were determined in the same way as for propyne. Ion numbers were normalized by the initial acetylene ion number for each reaction and the decay of the normalized reactant ion number vs. time was fit to determine the rate. The rate constant was then obtained by dividing the rate by the neutral gas concentration. The results are tabulated in Tab. 5.5 with the uncertainties derived from the 90% confidence interval of the rate fit parameter. The uncertainties are purely statistical and do not include any possible inaccuracy introduced by the method of concentration measurement.

Branching ratios were determined for the primary product $C_3H_3^+$ – in an identical manner to propyne – by a fit of normalized product ion numbers to the reaction model. These results are reported as percentages in Tab. 5.6. The rate constant for each of these pathways can be calculated by multiplying the branching ratio with its corresponding isotopologue rate constant in Tab. 5.5. The branching ratio of the $C_3H_4^+$ channel, and its analogous isotopologues, can be inferred by subtracting the branching ratios in Tab. 5.6 from 100%.

Table 5.5: Reaction rate constants for all measured isotopologue reactions. All rate constants determined by fit of the loss of charged reactants. Uncertainties are derived from the 90% confidence interval of the fit and do not account for possible inaccuracies in the neutral concentration measurement.

Reactants	$k\left(10^{-9}\frac{\mathrm{cm}^3}{\mathrm{s}}\right)$
$C_2H_2^+ + H_2C_3H_2$	6(1)
$C_2H_2^+ + D_2C_3D_2$	1.3(2)
$C_2D_2^+ + H_2C_3H_2$	6(2)

Table 5.6: Branching ratios for the reaction $C_2H_2^+ + H_2C_3H_3 \longrightarrow C_3H_3^+ + C_2H_3$ and its isotopologues. Numbers are the branching ratios (in%) for each mass channel as determined by the fit of the model. Uncertainties are the 90% confidence interval of the branching ratio fit. Blank spaces indicate the mass channel was not statistically different from zero at the 10% significance level.

Products	$C_3H_3^+$	$C_3H_2D^+$	$C_3HD_2^+$	$C_3D_3^+$
Mass (U)	39	40	41	42
$C_2H_2^+ + H_2C_3H_2$	100(20)			
$C_2H_2^+ + D_2C_3D_2$		40(20)	6(1)	44(5)
$C_2D_2^+ + H_2C_3H_2$	90(10)			

It was also possible to estimate the branching ratios for some second order products resulting from the reaction $C_3H_4^+ + H_2C_3H_2$. This was done by fitting a truncated version of the model that assumed the products $C_6H_5^+$ and $C_6H_7^+$ are the final products and do not react further. As such, the branching ratios tabulated in Tab. 5.4 are likely lower bounds on the actual branching ratios. Like for the propyne data, detected mass-to-charge ratios that could not be assigned a unique chemical formula have been omitted.

Table 5.7: Selected isotopologue data for $C_6H_5^+$ and $C_6H_7^+$ products from allene. Numbers are the branching ratios (%) for each mass channel as determined by the fit of the truncated model. Uncertainties are the 90% confidence interval of the branching ratio fit. Blank spaces indicate the mass channel was not statistically different from zero at the 10% significance level.

Products	$C_6H_5^+$	$C_6H_7^+$	$C_6D_5^+$	$C_6D_7^+$
Mass (U)	77	79	82	86
$C_2H_2^+ + H_2C_3H_2$	3(1)	12(2)		
$C_2H_2^+ + D_2C_3D_2$			1.0(6)	
$C_2D_2^+ + H_2C_3H_2$	2(1)	10(2)		

5.4.2 Computational Results

In contrast to propyne, the only product (with appreciable yield) of the reaction $C_2D_2^+ + H_2C_3H_2$ is $C_3H_3^+$. It is significant to note that only fully hydrogenated $C_3H_3^+$ is observed, with no evidence of H/D scrambling noticeable. This suggests that no intimate reaction complex between the two species is formed, else the reaction would proceed on the identical reaction pathway on the PES of propyne, starting at PRD4, as shown on in Figure 5.6. This would invariably lead to some $C_5H_5^+$ products and/or isotope scrambling of $C_3H_3^+$ products, similar to propyne. Thus, the allene reaction pathway must be described by a different portion of the full PES than propyne.

We propose the acetylene cation and allene must undergo charge-exchange at long-range exclusively. A PES of the subsequent reaction of undeuterated allene cation, calculated using the

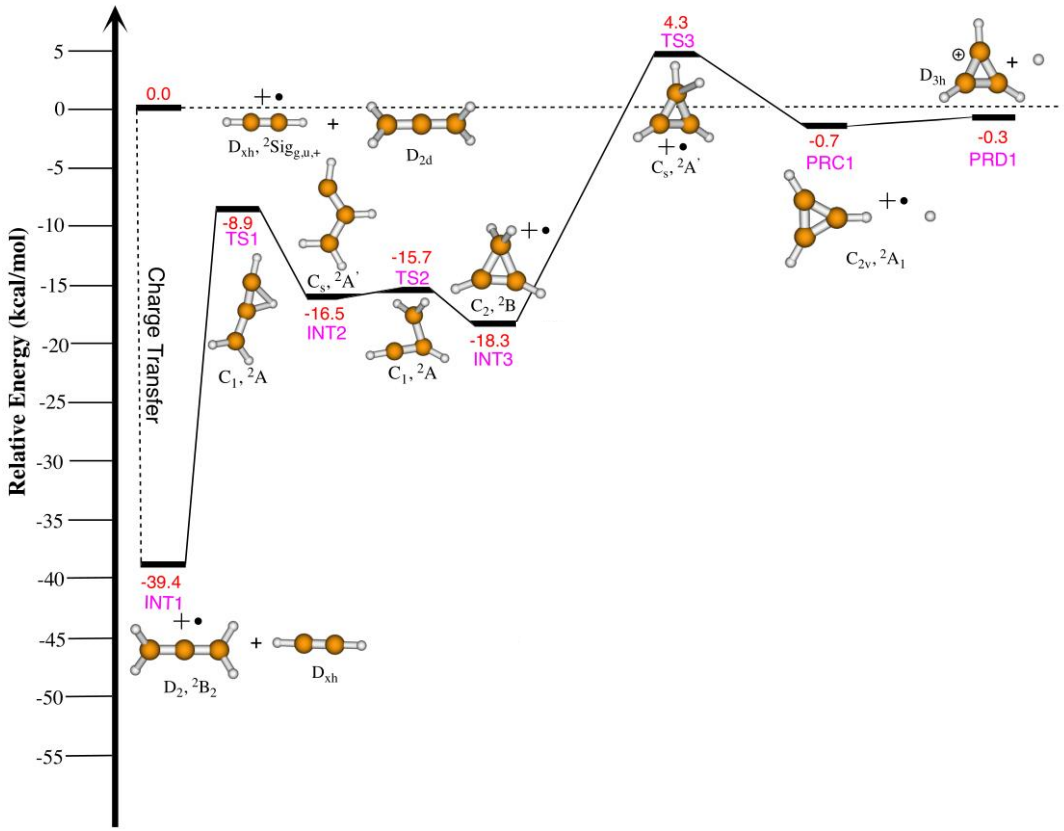

Figure 5.10: Potential energy surface connecting the of allene and acetylene cation to experimentally observed primary products. The energy of each stationary point is calculated using the mHEAT+ method.[3] All energies are relative to separated acetylene cation and allene.

mHEAT+ method,[3] is displayed in Figure 5.10. If nearly all of the internal energy released in the charge-transfer process is converted into $C_3H_4^+$ vibrations, the allene cation has sufficient energy to rapidly isomerize to INT3 in Figure 5.10, and subsequently tunnel through TS3 to release a hydrogen atom and form cyclic $C_3H_3^+$ (PRD1). Since the allene cation is a Jahn-Teller system and distorts significantly from the neutral,[156] this is a plausible hypothesis. It should be noted that this process was first proposed by Mebel and Bandrauk,[157] but recalculated here with a higher level of theory. An analogous process has also been suggested in a VMI study of the charge transfer reaction $C^+ + NH_3$. The authors observed evidence of a resonant energy transfer from the excess charge-exchange energy into the umbrella bending mode that connects the geometry of NH_3

to NH_3^+.[158]

The PES in Fig. 5.10 was calculated for the non-deuterated case only. While zero-point energy corrections were not explored for deuterium substitutions on the entire surface, it was determined that the thermochemistry of the c-$C_3H_3^+$ (PRD1) product channel reaction remains exothermic for any choice of the studied isotopologue reactants.

5.4.3 Discussion

Almost all the allene cations formed undergo the proposed mechanism leading to cyclic $C_3H_3^+$. While it is a somewhat surprising result that all the internal energy available from charge transfer is converted to internal energy of the allene cation, it is entirely consistent with the appearance potential of $C_3H_3^+$ observed in photoionization studies of allene,[159] where $C_3H_3^+$ appears at energies ∼1.79 eV above the threshold for ionization of allene. If the excess energy from the charge transfer is localized in the allene cation, it would be 1.71 eV above the threshold, and the results observed here might be expected. Moreover, in the photoionization experiments, samples of allene were ionized and detected much more quickly than the ions studied in this experiment. Thus, the tunneling process is apparently quite efficient, and appears dominant under the conditions of the Coulomb crystal experiment.

The results of the $C_2H_2^+ + D_2C_3D_2$ isotopologue reaction (see Tab. 5.6) bolster the proposed mechanism leading to primarily $C_3D_3^+$ products. While tunneling of a D atom should be much less efficient than an H atom, it is still observed experimentally. This is likely due to the fact that kinetically there is only one other option, which is to vibrationally relax into $C_3D_4^+$. Given the extremely low background pressure environment, $\lesssim 10^{-8}$ torr, the vibrationally excited $C_3D_4^+$ would not kinetically stabilize on a short enough timescale to prohibit tunneling. We can also conclude that the tunneling time-scale is shorter than the vibrational relaxation time for $C_3D_4^+$ due to radiative decay.

The other two observed products from the $C_2H_2^+ + D_2C_3D_2$ isotopologue reaction, masses 40 u and 41 u, are not predicted by the proposed reaction mechanism. Mass 41 u is very likely

the result of ionic contaminants or neutral reactant contaminants in the form of H/D swapping in the gas delivery lines. This is identical to the sources of uncertainty described in the propyne discussion section. Mass 40 u, however, is observed in such abundance that it must be the result of a reaction involving $C_2H_2^+$. We assume the neutral reactant to be an unidentified contaminant in our $D_2C_3D_2$ sample, as the mass 40 u product occurs only when using the fully deuterated isotopologue of allene and in no other combination (see Tab. 5.6).

We can also compare our results of secondary reactions between $C_3H_4^+$ + allene to those of Anicich *et. al.*[141]. For isotopologue reactions involving $H_2C_3H_2$, we report good quantitative agreement with the major products and branching ratios. For the deuterium substituted reaction with $D_2C_3D_2$, the resulting ion numbers in the different product channels were too few to make a quantitative comparison.

The reaction rate constants tabulated in Tab. 5.5 provide largely the same insights for acetylene cations reacting with allene as they do for reactions with propyne. We attribute the large difference between reactions with $H_2C_3H_2$ and $D_2C_3D_2$ to be from the inaccuracies of the ion gauge at low pressures being different for different gasses. $H_2C_3H_2$ was diluted in argon and $D_2C_3D_2$ was diluted in helium. It is likely that the systematic inaccuracy of the two gas pressure measurements are different. In light of this possibility, the rate constants do not appear to be affected by isotopic substitution of the acetylene cation within the reported statistical uncertainties. Alternatively, however, the reaction with $D_2C_3D_2$ really could be kinetically slower, due to the longer tunneling time of a deuterium atom compared to that of an hydrogen atom.

5.5 Summary and outlook

Isotopic substitution is a powerful and well-tested method for gaining insight into chemical reaction processes. We applied this methodology to bimolecular reactions of $C_2H_2^+ + C_3H_4$ in the gas phase in the extremely isolated and specific environment of a Coulomb crystal. For reactions with different isomers of C_3H_4, propyne and allene, we measured a fundamentally different reaction mechanism leading to isomer specific reaction products. Together with high-level theory

calculations, we gained understanding into the isomer specific reaction mechanism.

The reaction $C_2H_2^+ + HC_3H_3$ and its isotopologues showed the likely formation of the $C_5H_6^+$ reaction complex. This complex produced primary products $C_3H_3^+$ and $C_5H_5^+$. Reaction rate constants, branching ratios, and isotopic product distributions were measured for the primary products. These results were used to validate the calculated PES, which demonstrated pathways leading to extensive H/D swapping. Secondary reactions between $C_3H_4^+$ and propyne were measured and compared to results in the literature.

The reaction $C_2H_2^+ + H_2C_3H_2$ and its isotopologues exhibited only $C_3H_3^+$ as its major product channel, which suggests no short-range reaction complex was formed. This was further bolstered by a lack of H/D scrambling in observed products. These results validated a calculated PES based on the unimolecular decay of $C_3H_4^+$ after it converted the energy of the charge-transfer process almost entirely into vibrational energy. Reaction rate constants, branching ratios, and isotopic product distributions were also measured for the primary products. Secondary reactions also occurred between $C_3H_4^+$ and allene and the results, where possible, were compared to the literature.

Given the copious added insight from isotopologue reactions in this system, this methodology will become an indispensable tool in the characterization of future reactions studied in our ion trap. The ability to unambiguously assign reaction products will aid in modeling reaction pathways contributing to ISM chemistry and interactions in isolated environments. Further revelations of unique ion-molecule reaction mechanisms will contribute to the basic understanding of how chemical bonds are formed and broken.

In the future, we plan to couple a Stark decelerator to slow the neutral reactant and control the collision energy available for reaction.[132, 160] This will enable detailed studies of reaction dynamics. Isotopic substitution will be another useful handle in such experiments that allow for precise changes in reaction energetics through zero-point energy corrections. While such changes in energy are typically negligible, the highly controlled reaction environment of a combined ion trap–Stark decelerator apparatus will have the goal to leverage those changes to do precise ther-

mochemistry measurements; the resulting experiments may set new benchmarks for theory and quantum chemical calculations.

Chapter 6

Translationally cold trapped CCl^+ reactions with acetylene (C_2H_2)

The following is a pre-print draft of a paper submitted The Journal of Chemical Physics for publication. This study investigates the reaction mechanisms of $CCl^+ + C_2H_2$, which revealed previously unknown pathways to two cations actively studied in the chemistry of the ISM: C_3H^+ and $C_3H_2{}^+$. Presented here are the data and analysis drafted and under review for publication. In addition to helping build the apparatus, control software, and analysis code, I acquired some of the data presented and aided in writing the text. Electronic structure calculations were carried out at JILA by our excellent post-doc Katherine Catani.

6.1 Introduction

Chlorine containing compounds have been found to exist in extraterrestrial environments including the dense and diffuse clouds of the interstellar medium (ISM). Interest in chlorine chemistry in these areas was initially fueled by detection of HCl, HCl^+, and H_2Cl^+ in these areas. However, these small molecules are acknowledged to account for only a minor fraction of the overall chlorine abundance.[161–170] More recently, CH_3Cl was detected towards the low mass protostar IRAS 16293-2422 and comet Churyumov-Gerasimento.[171] Organohalogens, including CF^+ have been detected in these remote environments, but their overall chemical roles are not completely understood. A possible reservoir containing both carbon and chlorine is the carbon monochloride cation (CCl^+). CCl^+ has been proposed as an intermediate in the overall chlorine cycle in diffuse clouds, although its overall abundance is not known. The major predicted pathways to CCl^+ formation

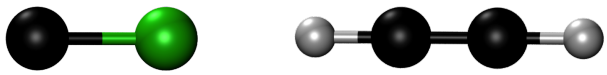

$CCl^+\ X\ ^1\Sigma^+$ $C_2H_2\ X\ ^1\Sigma_g^+$

Figure 6.1: Ground-state structures of CCl^+ and C_2H_2.

are through reactions of C^+ with HCl and H_2Cl.[161, 162, 172–177] Previous kinetic measurements, mainly using ion cyclotron resonance (ICR) spectrometry and selected ion flow tube (SIFT) techniques, found CCl^+ to be stable and non-reactive.[161, 162, 178] Products were observed for reactions with NH_3, H_2CO, CH_3Cl, $CHCl_3$, CCl_4, $CHCl_2F$, and $CHClF_2$.[161, 162, 178] However, with NO, H_2, CH_4, N_2, O_2, CO, and CO_2, no reactions were observed.[161, 162, 178] Although only a few reactions with relevant interstellar species have been measured, it is conceivable that CCl^+ could undergo reactive collisions with varying neutrals, such as acetylene (C_2H_2; previously detected and thought to be abundant).[142, 179–182] Reactions of CCl^+ with neutral carbonaceous species would likely produce larger carbocation species.

Simple carbocation species like C_2H_2, c-$C_3H_2{}^+$, and l-C_3H^+ (observed cationic reaction products), have long been speculated to be present in the ISM. Recently, l-C_3H^+ was detected towards dark nebula in Orion and confirmed with laboratory spectroscopic measurements.[183–188] The role of $C_3H_2{}^+$ in these environments is less certain. Both neutral l-C_3H_2 and c-C_3H_2 have been detected towards dark clouds in the interstellar medium by their radioemission lines.[189] c-C_3H_2, in particular, has been detected in diffuse clouds, where ionizing radiation is more prevalent, and the role of its cation has been speculated as its probable precursor. Insight into additional formation pathways of these fundamental carbocations could prove useful for refining chemical models that rely on energetic and electronic information.

Understanding the details of these and other ion-neutral chemical reactions benefit from studies at low temperatures and are beginning to be explored using new experimental techniques. In particular, trapped Coulomb crystals have become increasingly popular as a way of studying cold ion-neutral chemical reactions.[2, 25, 39, 43–45, 47, 50, 51, 53] Here, the reactant ion is sympa-

thetically cooled to low translational temperatures by elastic collisions with co-trapped laser-cooled calcium ions. This technique allows for controlled interrogation of cold ion-neutral reactions over long timescales.

To characterize the CCl^+ cation and its reactivity in remote environments, we have measured the reactive pathways of gas-phase CCl^+ with C_2H_2 in a linear Paul ion trap coupled to a time-of-flight mass spectrometer (TOF-MS). The coupled ion trap enables co-trapping of sympathetically cooled CCl^+ with laser cooled Ca^+. This creates a controlled environment to study reactions with C_2H_2 that may be present is some areas of the ISM, planetary atmospheres, or comets. The reaction of $CCl^+ + C_2H_2$ leads to a possible pathway to the formation of c-$C_3H_2{}^+$ and l-C_3H^+ and to a measurement of the branching ratio of these two products. Complementary electronic structure calculations are used to aid in the discussion of the experimental results.

6.2 Experimental Methods

Kinetic data for the reactions of $CCl^+ + C_2H_2$ were recorded at different interaction time steps by monitoring the masses of all ions present in a custom built linear Paul ion trap radially coupled to a time-of-flight mass spectrometer (TOF-MS). Details of the apparatus have been described previously,[2, 38, 39] and only a brief outline is presented here. CCl^+ was formed through non-resonant multiphoton ionization of tetrachloroethylene (TCE; C_2Cl_4). Vapor from TCE was seeded in a pulsed supersonic expansion of helium gas (3 % TCE in ∼1000 Torr He). The skimmed molecular beam was overlapped with 216 nm photons from a frequency-doubled, 10 Hz pulsed dye laser (LIOP-TEC LiopStar; 10 ns pulse, 100 μJ/pulse) in the center of the ion trap forming $C^{35}Cl^+$, $C^{37}Cl^+$, $C_2{}^+$, C_2H^+, $^{35}Cl^+$, and $^{37}Cl^+$. Radio frequency (RF) secular excitation of contaminant ion masses was used to eject all cation species from the trap except $C^{35}Cl^+$ cations (subsequently denoted as CCl^+). Next, calcium was added to the chamber via effusive beam from a resistively heated oven and non-resonantly photoionized with 355 nm light from the third harmonic of a Nd:YAG laser (Minilite, 10 Hz, 7 mJ/pulse). Trapped calcium ions were Doppler laser cooled with two external cavity diode lasers (ECDLs) forming a Coulomb crystal composed of Ca^+ and a pure sample

of CCl^+. Both ECDLs were fiber-coupled with one tuned to the $^2S_{1/2} - ^2P_{1/2}$ transition of Ca^+ (397 nm; New Focus, 3.5 mW, 600 μm beam diameter) and the other to re-pump Ca^+ ions back into the cooling cycle on the $^2P_{1/2} - ^2D_{3/2}$ transition (866 nm; New Focus, 9 mW, 600 μm beam diameter). Both laser frequencies were measured and locked using a wavemeter (HighFinesse/Ångstrom WSU-30).

Upon formation of a mixed-species Coulomb crystal, the RF trapping amplitude was dropped to allow any ions in metastable higher angular-momentum orbits to escape from the trap. This was repeated three times, leaving only cold Ca^+ and sympathetically cooled CCl^+. During the course of each experimental run, trapped Ca^+ ions were monitored continuously via their fluorescence using an intensified CCD camera. CCl^+ and other product ions do not fluoresce and were not directly seen in the images, but rather were inferred due to changes in the shape of the Coulomb crystal. Non-fluorescing ions were detected and quantified by ejecting the trapped species into a TOF-MS, which enabled unambiguous determination of chemical formula based on the ion mass-to-charge ratio (m/z).

In a typical experimental run, $\sim$ 100 CCl^+ ions were loaded and sympathetically cooled by $\sim$ 800 calcium ions. Once the mixed Coulomb crystal was formed, neutral C_2H_2 ($\sim$ 4.7% in Ar at 298 K) was leaked into the vacuum system containing the trap at a constant pressure of $\sim 4.6(3) \times 10^{-9}$ Torr via a pulsed leak valve scheme.[127] The gas pulse duration was one of multiple neutral gas exposure time steps (0, 5, 10, 20, 40, 80, 160, and 260 s). At the end of each time step, a mass spectrum was measured and ion numbers for each mass channel were recorded. An experimental run for every time step was repeated four times and the number of ions from each mass channel of interest was averaged at each time step. Each mass channel of interest was normalized by the initial number of CCl^+ ions, and the average normalized ion numbers and standard error of the mean are plotted as a function of the different time steps as shown in Figure 6.2.

6.3 Computational Methods

Structures, vibrational frequencies, and relaxed potential energy scans for $CCl^+ + C_2H_2$ were determined using the M06-2X/aug-cc-pVTZ level of theory. Potential energy surfaces were scanned along bond lengths, rotations, and angles to identify minima and saddle points. The M06-2X stationary points were used for CCSD/aug-cc-pVTZ calculations of structures and harmonic vibrational frequencies. The optimized structures were then used for single point energy calculations at the CCSD(T) level of theory with extrapolation to the complete basis set (CBS) limit using the aug-cc-pVXZ (X = T,Q) basis sets.[190–192] The energies were corrected for vibrational zero-point energy from the calculated CCSD/aug-cc-pVTZ level of theory. Energies extrapolated to the CBS limit should account for possible basis set superposition errors. Structures for CCl^+ and C_2H_2 are shown in Figure 6.1, with further geometric parameters and calculated harmonic vibrational frequencies (CCSD/aug-cc-pVTZ) provided in the Supplemental Information.

Other computational studies on CCl^+ itself recommend using multireference methods.[193–196] The computational cost of using multireference methods for the larger potential energy surface would be prohibitive, therefore we use the CCSD/aug-cc-pVTZ level of theory, which gives reasonable agreement with previously published computational and experimental data for CCl^+ and C_2H_2 separately.[193–197] Reported CCSD(T)/CBS energies should be accurate to within 0.04 eV. Computations were compared to previous theoretical work and experimental data where available for the reactants and products in order to determine the best level of theory to determine accurate energetics. DFT and CCSD calculations were performed using both the Gaussian 16 and the Psi4 version 1.3.2 computational packages.[198, 199] Relaxed potential energy scans for the complexes at the M06-2X/aug-cc-pVTZ level of theory were undertaken using Gaussian 16.

6.4 Results and Discussion

6.4.1 $CCl^+ + C_2H_2$ reaction measurements

Using room temperature (298 K) C_2H_2, the average collision energy with translationally cold ($\sim$ 10 K) CCl^+ is 17 meV ($\sim$ 197 K). The excess collision energy should not be a significant source of energy to the reactions as the predicted products, c-$C_3H_2{}^+ + Cl$ and l-$C_3H^+ + HCl$ are -0.15 and -0.07 eV exothermic, respectively (Equations 6.1 and 6.3) based on CCSD(T)/CBS level calculations:

$$\begin{aligned} CCl^+ + C_2H_2 &\longrightarrow c\text{-}C_3H_2{}^+ + Cl \\ \Delta E &= -0.15\,\text{eV} \end{aligned} \tag{6.1}$$

$$\begin{aligned} CCl^+ + C_2H_2 &\longrightarrow l\text{-}C_3H_2{}^+ + Cl \\ \Delta E &= 0.08\,\text{eV} \end{aligned} \tag{6.2}$$

$$\begin{aligned} CCl^+ + C_2H_2 &\longrightarrow l\text{-}C_3H^+ + HCl \\ \Delta E &= -0.07\,\text{eV} \end{aligned} \tag{6.3}$$

Several other product channels were explored theoretically, however, their endothermicities were significantly greater than the calculated average collision energy (greater than 1 eV above the reactant energies), and therefore disqualified from the discussion of products. In addition, the l-$C_3H_2{}^+$ isomer could contribute to the m/z 38 signal, however, the pathway is endothermic by about 0.08 eV, making it very unlikely to be formed (see Equation 6.2).

As shown in Figure 6.2, the initial ionic products that are formed as CCl^+ reacts away are indeed C_3H^+ and $C_3H_2{}^+$ (m/z 37 and 38, respectively). At about 40 seconds, the rates into the intermediate C_3H^+ and $C_3H_2{}^+$ species are overtaken by the rates of these intermediate species reacting with the excess C_2H_2 present. This is illustrated by the turning over of the two corresponding curves (green and black traces) and growth of the secondary products of larger carbonaceous species (red trace), mainly comprising $C_5H_2{}^+$ and $C_5H_3{}^+$. The red trace plotted in Figure 6.2 includes

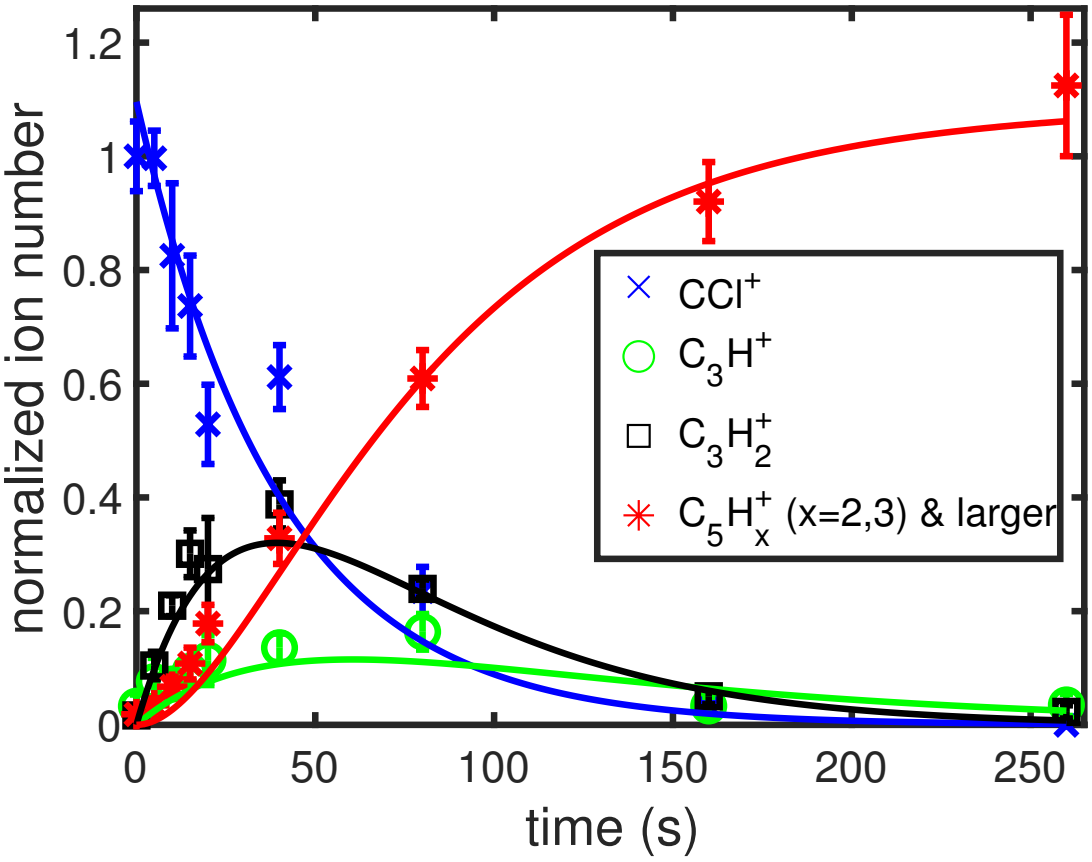

Figure 6.2: Measured ion numbers of CCl^+ (blue ×), *l*-C_3H^+ (green ○), *c*-$C_3H_2{}^+$ (black □), and $C_5H_x{}^+$ (x = 2, 3, and higher; red ∗) as a function of time. Data are normalized by the initial ion number of CCl^+ (~ 100). Each data point represents the mean and standard error from four experimental runs per time point. The averaged data are fit using a pseudo-first order reaction rate model (solid lines).

all mass channels above m/z 61, which should account for any secondary and tertiary reaction products (or larger). Additions of C_2H_2 to $C_3H_x{}^+$ (x = 1, 2) have been characterized previously, and are not modeled computationally.[200–204]

Experimental reaction rates are determined by fitting the reaction data, shown in Figure 6.2 to a pseudo-first-order reaction rate model; the fits are represented by solid lines. For the formation of intermediate and secondary products, the model is explicitly defined as:

$$\frac{d[CCl^+]}{dt} = -(k_{37} + k_{38})[CCl^+] \tag{6.4}$$

$$\frac{d[C_3H^+]}{dt} = k_{37}[CCl^+] - k_{37\_63}[C_3H^+] \tag{6.5}$$

$$\frac{d[C_3H_2{}^+]}{dt} = k_{38}[CCl^+] - k_{38\_63}[C_3H_2{}^+] \tag{6.6}$$

$$\frac{d[C_5H_x{}^+]}{dt} = k_{37\_63}[C_3H^+] + k_{38\_63}[C_3H_2{}^+] \tag{6.7}$$

where the product ions of C_3H^+ (m/z 37), $C_3H_2{}^+$ (m/z 38), and $C_5H_x{}^+$ (x=2,3, and higher; $m/z \geq 62$) at time t are normalized with respect to the number of CCl^+ (~ 100) ions at $t = 0$. Rate constants are estimated using the measured concentration of neutral C_2H_2, which is measured using a Bayard-Alpert ion gauge $\approx 5(1) \times 10^6\,\mathrm{cm}^3$. It should be noted that the uncertainty quoted here is statistical, there is larger systematic uncertainty introduced by using an ion gauge in the 10^{-10} Torr regime. The resulting reaction rates and rate constants are given in Table 6.1. These calculated rate constants are on the order of the rate calculated using Langevin collision theory, 1.07×10^{-9} $\mathrm{cm}^3\mathrm{s}^{-1}$.

Table 6.1: Results from the fits to the pseudo-first order reaction rate models for the formation of intermediate and secondary products from the reaction of $CCl^+ + C_2H_2$. Included are the rate constants for the single pressure measurement of $C_2H_2 \approx 5(1) \times 10^6\,\mathrm{cm}^3$.

Species	m/z	k (s^{-1})	$k/[C_2H_2]$ ($\mathrm{cm}^3\mathrm{s}^{-1}$)
C_3H^+	37	$0.5(3) \times 10^{-2}$	$0.9(5) \times 10^{-9}$
$C_3H_2{}^+$	38	$2.0(3) \times 10^{-2}$	$4(1) \times 10^{-9}$
$C_5H_x{}^{+a}$	62 (and larger)	$4(1) \times 10^{-2}$	$7(2) \times 10^{-9}$

[a] formation of $C_5H_x{}^+$ and higher order products from both $C_3H_2{}^+$ and C_3H^+

From the calculated rate constants, the branching ratio between the two intermediate products is determined to be about 4:1, with the Cl loss product channel (formation of c-$C_3H_2{}^+$) favored over the HCl loss product channel (formation of l-C_3H^+).

Further confirmation of the intermediate and secondary products was obtained by reaction of CCl^+ with C_2D_2, where the product masses shifted to m/z 38 for C_3D^+ and m/z 40 for $C_3D_2{}^+$ as expected. Additionally, for both reactions with C_2H_2 and C_2D_2, the total ion numbers as a function of trap time were also collected to ensure conservation of trapped ions. These data are included in the Supplementary Information.

6.4.2 Modeling the $CCl^+ + C_2H_2$ reaction

In order to determine the relative energetics of the different pathways, an abridged potential energy surface of the $CCl^+ + C_2H_2$ reaction was explored; the key features that lead to the preferable intermediate products are shown in Figure 6.3. Starting from the two reactants, at varying approaches, a stable $C_3H_2Cl^+$ C_{2v} complex forms, which is exothermic by about 4.73 eV [CCSD(T)/CBS]. From this complex, the main experimentally observed products correspond to Cl and HCl loss respectively, discussed below. Geometric parameters of each stationary point, harmonic vibrational frequencies, and energies (CCSD/aug-cc-pVTZ), as well as a lower level M06-2X/aug-cc-pVTZ potential energy surface are given in the Supplementary Information.

6.4.2.1 Cl loss

The favored products, c-$C_3H_2{}^+ + Cl$, are obtained through a barrierless dissociation pathway, with the products residing about -0.15 eV below the reactants. The c-$C_3H_2{}^+$ isomer is favored over the l-$C_3H_2{}^+$ by about 0.23 eV (22 kJ/mol) and the barrier to rearrangement from linear to cyclic has been calculated in previous studies to be between 1.62-1.75 eV.[205] Indeed, it may be possible that both isomers are present, however, as noted above the l-$C_3H_2{}^+ + Cl$ products are slightly endothermic, by about 0.08 eV, making it very unlikely to be formed.

6.4.2.2 HCl loss

The other intermediate product channel, forming l-C_3H^+ through HCl loss, goes through the same cyclic intermediate as the Cl loss channel [2]. From the cyclic minima, several rearrangements

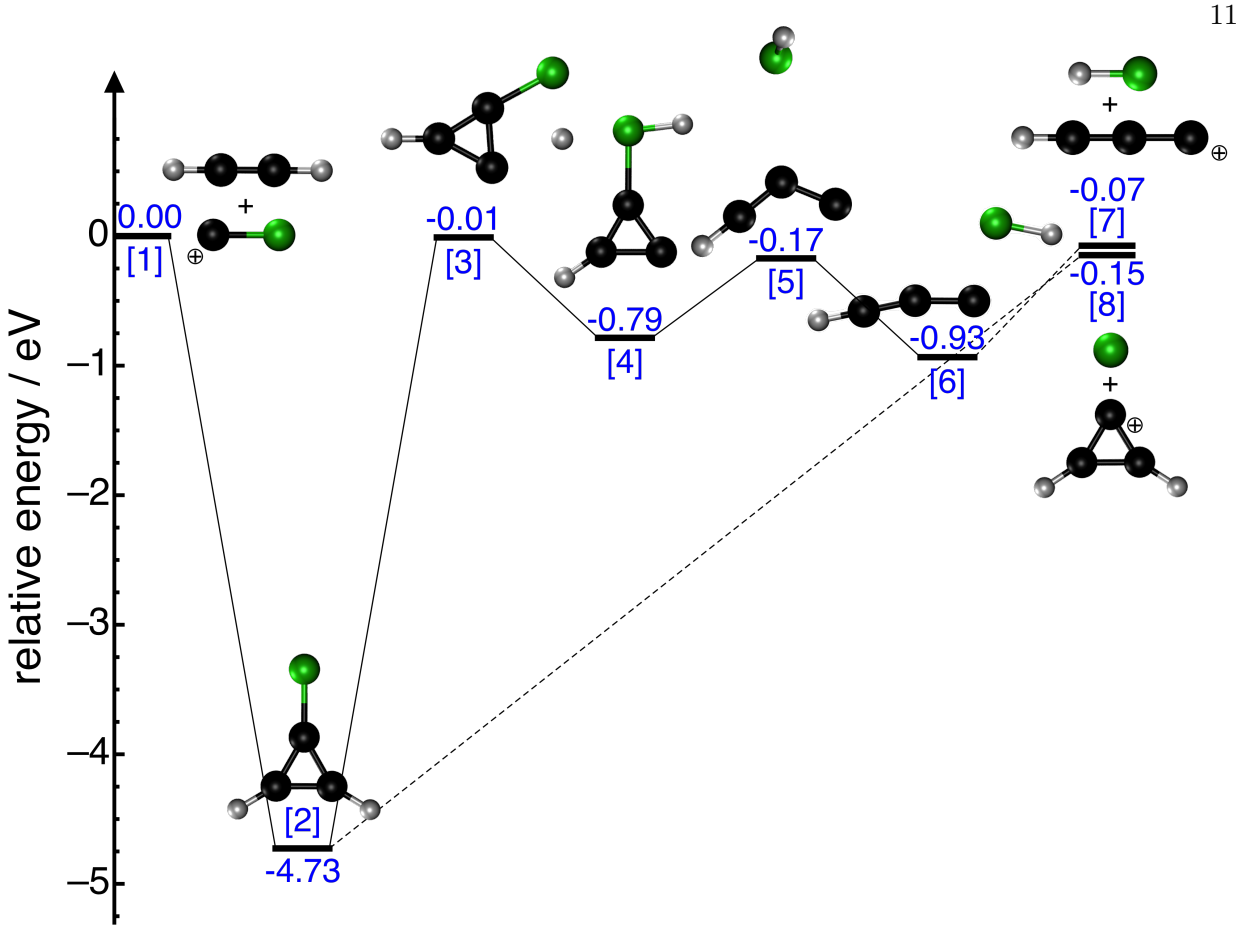

Figure 6.3: The main features of the potential energy surface for $CCl^+ + C_2H_2$ calculated at the CCSD(T)/CBS level of theory. The favored Cl loss product, dissociates without a barrier, forming c-$C_3H_2{}^+ + Cl$ [8]. The HCl loss channel leading to l-$C_3H^+ + HCl$ [7] involves a few stationary points with lower energies than the dissociation limit of -0.1 eV. Here, the bare '+' indicates infinite separation.

are required before eventually losing neutral HCl from l-C_3H^+. A few shallow minima were found where the HCl moiety rearranges along the conjugated pi-system of l-C_3H^+, the lowest energy isomer is shown [6]. The structures and energies (CCSD/aug-cc-pVTZ) of these different isomers are given in the Supplementary Information.

The experimentally observed branching ratio favors c-$C_3H_2{}^+$ over l-C_3H^+ by about a factor of four. In the absence of Rice-Ramsperger-Kassel-Marcus (RRKM) theory/master equation simulations, it is difficult to probe the potential energy surface barriers and their possible contribution to this observed branching ratio between the two primary product channels. The comparison is

supported by the increased number of steps required for the HCl loss channel compared to the Cl loss channel. It should be noted that over several levels of theory the barrier height of the H abstraction before HCl loss ([3] in Figure 6.3) is variable based on the level of theory employed, with the CCSD(T)/CBS level giving the largest barrier. The uncertainty in the level of theory (0.04 eV) could push this barrier slightly endothermic, which would kinetically favor the Cl loss channel.

6.5 Conclusions

The reaction of C_2H_2 with sympathetically cooled CCl^+ was examined using a linear Paul ion trap coupled to a TOF-MS. Although CCl^+ has been previously predicted to be non-reactive, it is clear that collisions with C_2H_2 result in either Cl or HCl loss. The primary products formed from these two loss channels are the astrochemically relevant c-$C_3H_2{}^+$ and l-C_3H^+, respectively. The rate constants measured for the formation of the two primary products are on the order of those predicted through Langevin modeling. Furthermore, the Cl loss channel, occurring through a barrierless dissociation pathway, is favored by a factor of four compared to HCl loss channel, which requires several rearrangements before losing HCl.

The theoretical work presented in this study would benefit from further exploration at a higher level of theory, possibly with multireference methods to characterize CCl^+ and its initial complexation with C_2H_2. In addition, kinetic modeling, possibly using RRKM theory, would be beneficial for a comprehensive comparison to experimentally measured branching ratios.

In future work, we plan to explore further the reactivity of CCl^+ with other astrochemically relevant neutrals. In addition, a natural extension to this work would be to study similar reactions of CCl^+ with more control over the neutral reactant, using state-selected molecular ions from a traveling wave Stark decelerator.[132, 160] This will allow further study of ion-neutral reactions in low temperature regimes, where the internal quantum states and external motion can be controlled with high precision.

6.6 Supplementary information

Data included in this supplementary information consist of reaction curves from reactions of CCl^+ + acetylene (C_2H_2) and CCl^+ + deuterated acetylene (C_2D_2; used to verify reaction products). Also included are measured total ion numbers (a sum of all detected ion channels in a given TOF-MS trace) for each reaction; used to demonstrate conservation of ions in the linear Paul ion trap over the entire reaction. The full calculated potential energy surface for the discussion of the $CCl^+ + C_2H_2$ reaction is included at the CCSD/aug-cc-pVTZ level of theory with additional structural and energetic information provided for each stationary point.

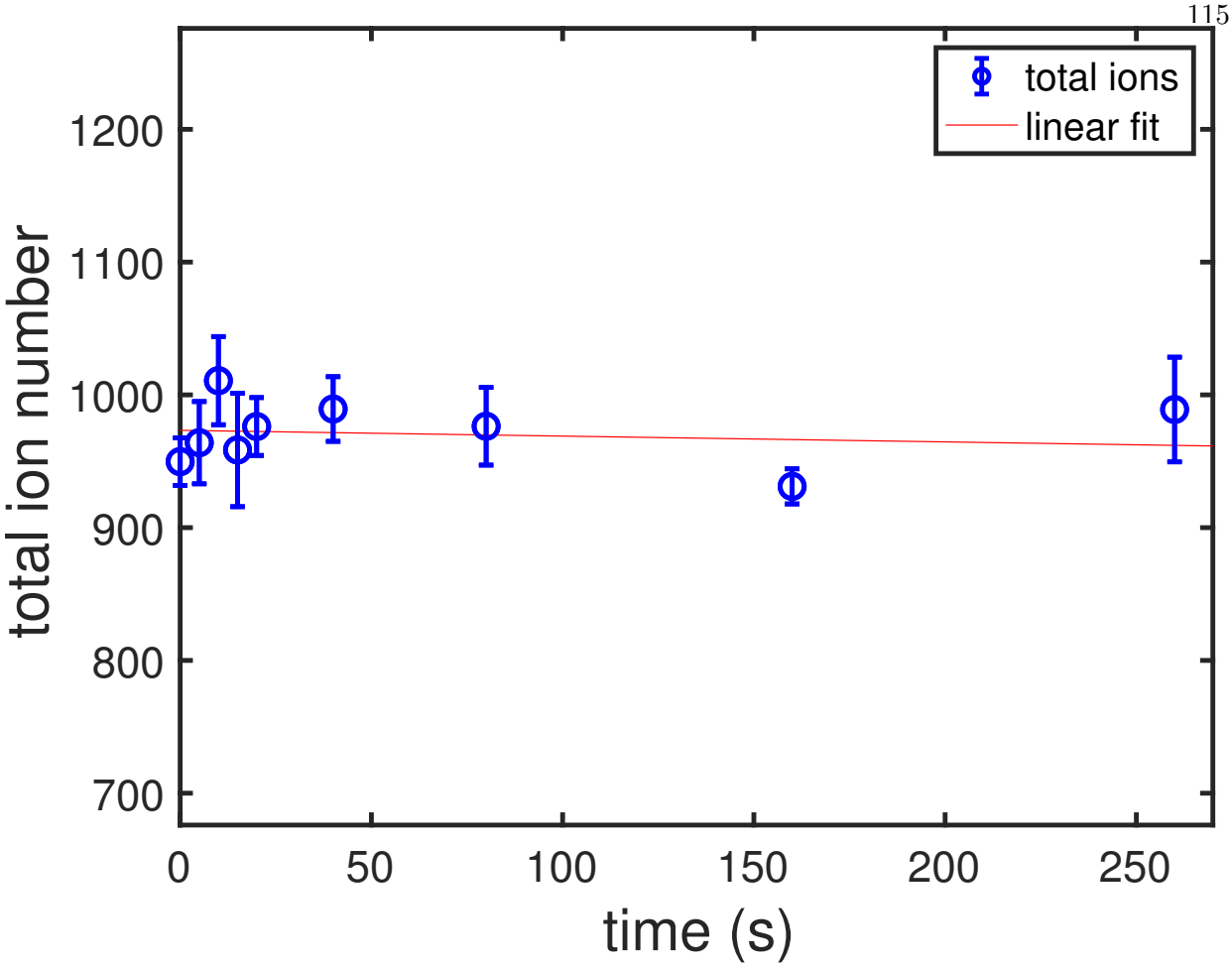

Figure 6.4: Measured total ion numbers of the $CCl^+ + C_2H_2$ reaction as a function of time. Each data point represents the mean and standard error from 4 experimental runs per time point. The total ion data are fit using a 1st order polynomial giving a slope of -0.04 with an uncertainty of 0.3 (the 95% confidence interval of the fit parameter) indicating the number of ions are conserved over the reaction.

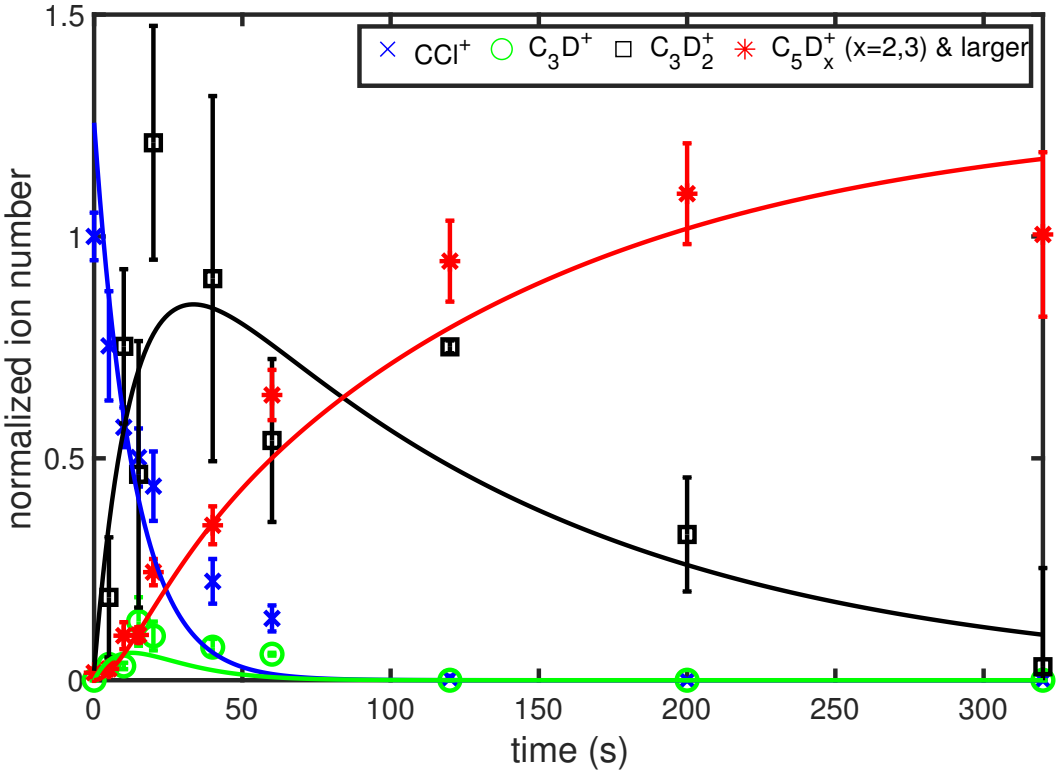

Figure 6.5: Measured ion numbers of CCl^+ (blue $\times$), C_3D^+ (green $\circ$), $C_3D_2{}^+$ (black $\square$), and C_5D_x (x = 2, 3 and higher; red $*$) as a function of time for the reaction of CCL^+ with duetrated acetylene C_2H_2. The product masses shift as expected due to deuterium substitution. Data are normalized by the initial ion numbers of CCl^+ ($\sim$ 100). Each data point represents the mean and standard error from 4 experimental runs per time point. The average data are fit using a pseudo-first order reaction rate model (solid lines). $C_3D_2{}^+$ (m/z 40) overlaps with the Ca^+ channel. To fit this channel, the initial average Ca^+ ion numbers are subtracted from the m/z 40 channel at each time step. There is some variability in the loaded numbers of Ca^+, making the ion numbers and rates extracted from the 40 channel less certain.

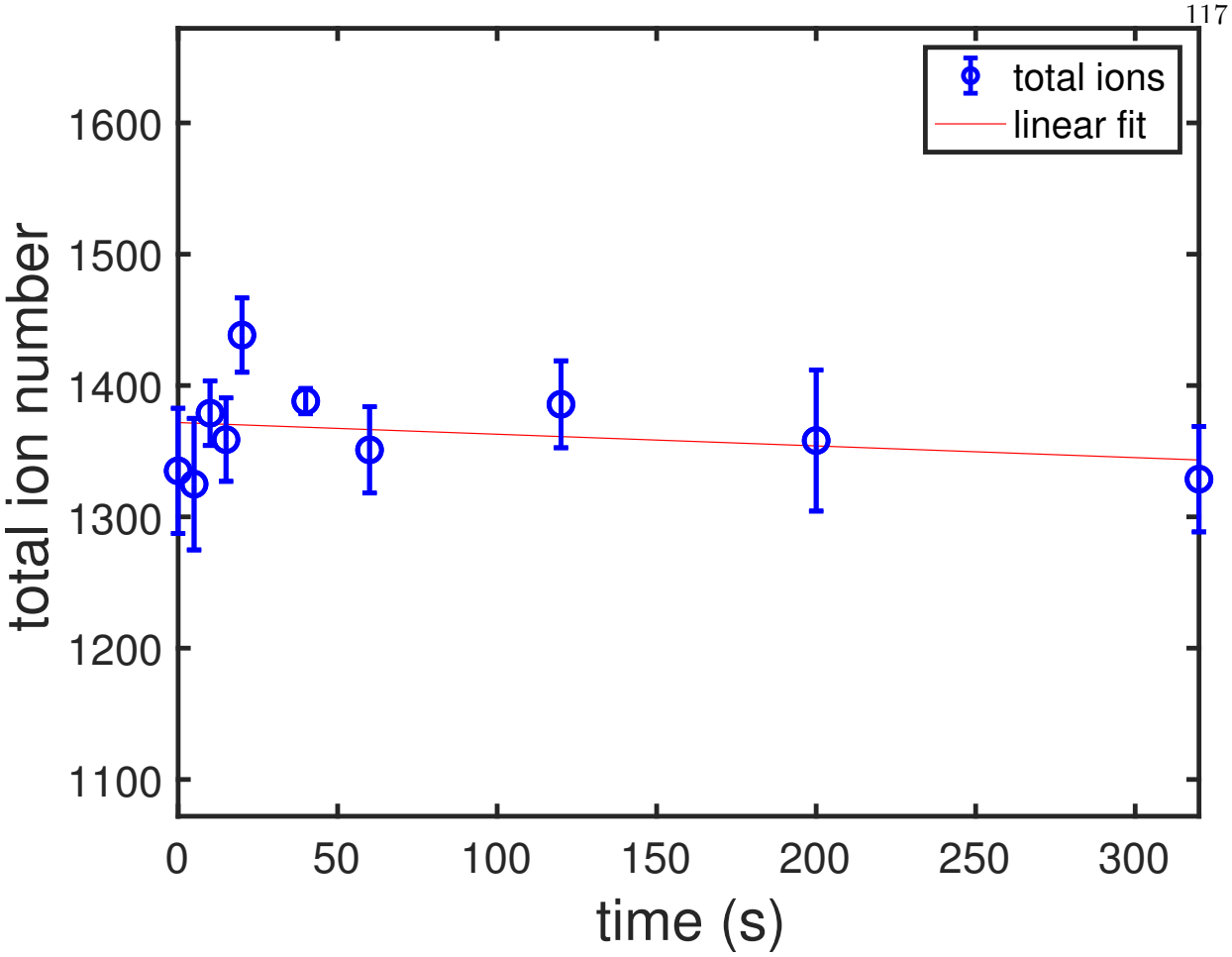

Figure 6.6: Measured total ion numbers of the $CCl^+ + C_2D_2$ reaction as a function of time. Each data point represents the mean and standard error from 4 experimental runs per time point. The raw total ion data are fit using a 1st order polynomial giving a slope of -0.09 with an uncertainty of 0.2 (the 95% confidence interval of the fit parameter) indicating the number of ions are conserved over the reaction.

Table 6.2: Results from the fits to the pseudo-first order reaction rate models for the formation of intermediate and secondary products from the reaction of CCl^+ with C_2H_2 (from Table I in main text) and C_2D_2. Included are the rate constants for the single pressure measurement of $C_2H_2 \approx 5(1) \times 10^6\,cm^3$ and $C_2D_2 \approx 7(1) \times 10^6\,cm^3$. For the C_2D_2 case, rates extracted from the data are less certain and the majority of the reported error is due to the calcium ion number uncertainties, as the $C_3D_2{}^+$ product channel overlaps with the Ca+ channel

$CCl^+ + C_2H_2$

Species	m/z	k (s^{-1})	$k/[C_2H_2]$ (cm^3s^{-1})
C_3H^+	37	$0.5(3) \times 10^{-2}$	$0.9(5) \times 10^{-9}$
$C_3H_2{}^+$	38	$2.0(3) \times 10^{-2}$	$4(1) \times 10^{-9}$
$C_5H_x{}^{+a}$	62 (and larger)	$4(1) \times 10^{-2}$	$7(2) \times 10^{-9}$

$CCl^+ + C_2D_2$

Species	m/z	k (s^{-1})	$k/[C_2D_2]$ (cm^3s^{-1})
C_3D^+	38	$1(1) \times 10^{-2}$	$1(2) \times 10^{-9}$
$C_3D_2{}^+$	40	$6(2) \times 10^{-2}$	$8(4) \times 10^{-9}$
$C_5D_x{}^{+b}$	64 (and larger)	$9(24) \times 10^{-2}$	$1(3) \times 10^{-8}$

[a] formation of $C_5H_x{}^+$ and higher order products from both $C_3H_2{}^+$ and C_3H^+

[b] formation of $C_5D_x{}^+$ and higher order products from both $C_3D_2{}^+$ and C_3D^+

Table 6.3: Previously measured and calculated constants of CCl^+ for comparison with current computational results.

CCl^+	r_e (Å)	ω_e (cm^{-1})	D_e (eV)	Ref
$\mathbf{X}^+\,^1\mathbf{\Sigma}^+$ $...(5\sigma)^2(6\sigma)^2(2\pi_x)^2(2\pi_y)^2(7\sigma)^2$				
Exp.	1.5378	1178	6.55	[197]
MRCI	1.5421	1172		[195]
M06-2X/aug-cc-pVTZ[a]	1.5341	1212		
CCSD/aug-cc-pVTZ[a]	1.5330	1169	6.59	

[a] this work

Table 6.4: Electronic energies and vibrational zero-point corrections from calculations at the CCSD/aug-cc-pVTZ level of theory with accompanying CCSD(T)/CBS single point energies, all in Hartrees. Stationary point numbers correspond to those on the $CCl^+ + C_2H_2$ potential energy surface in Figure 6.3. Structures 6 and 10-12 are energetically similar isomers where the HCl moiety rearranges along the l-C_3H^+ backbone. The other linear isomer of $C_3H_2{}^+$ is also included for reference. All structures are illustrated in Figure 6.8.

Stationary Point	Electronic Energy CCSD/aug-cc-pVTZ	Vibrational ZPE correction CCSD/aug-cc-pVTZ	Single Point Energy CCSD(T)/CBS
[1a] CCl^+	-497.3093456	0.0027851	-497.4439045
[1b] C_2H_2	-77.2104448	0.0271492	-77.2986219
[2]	-574.7086427	0.0375602	-574.9238578
[3]	-574.5202927	0.0294604	-574.7423639
[4]	-574.5572188	0.0326468	-574.7740926
[5]	-574.5254313	0.0277394	-574.7466993
[6]	-574.5569850	0.0310633	-574.7779988
[7a] HCl	-460.3686914	0.0068998	-460.4594045
[7b] l-C_3H^+	-114.1521467	0.0201516	-114.2829693
[8a] Cl	-459.7017467	0.0000000	-459.7883079
[8b] c-$C_3H_2{}^+$	-114.8378178	0.0333737	-114.9630686
[9] l-$C_3H_2{}^+$	-114.8212372	0.0265948	-114.9479331
[10]	-574.5530070	0.0306167	-574.7741961
[11]	-574.5339041	0.0311430	-574.7528099
[12]	-574.5325391	0.0306695	-574.7513854

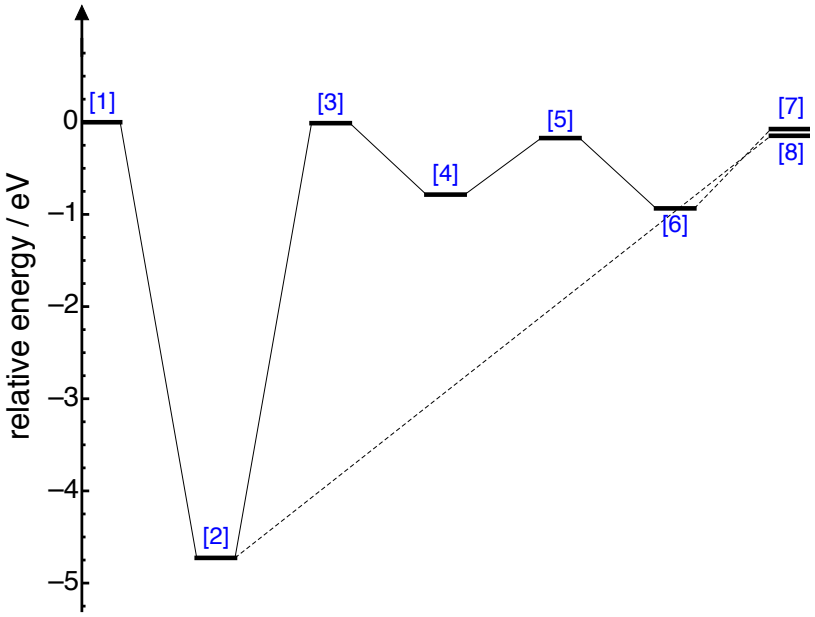

Figure 6.7: Potential energy surface calculated at the CCSD/aug-cc-pVTZ level of theory for the reaction of CCl^+ with C_2H_2. Energies (in eV) are from single point CCSD(T)/aug-cc-pVTZ calculations extrapolated to the complete basis set limit. Structures, energies, and geometries are given in Figure 6.8 and Tables 6.4 and 6.5, respectively.

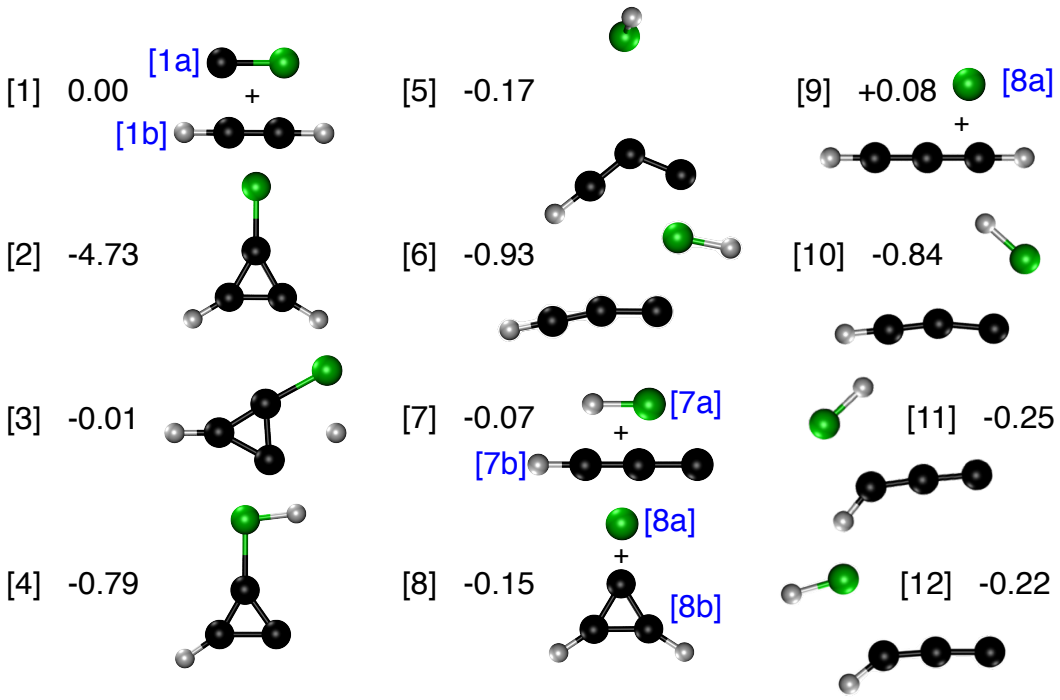

Figure 6.8: Structures of stationary points on the potential energy surface in Figure 6.7. In each case, energies are given relative to the $CCl^+ + C_2H_2$ limit [1]. Geometries were computed at the CCSD/aug-cc-pVTZ level. Structures 6 and 10-12 are the several minima with different rearrangements of the HCl moiety along the C_3H^+ backbone. Also included is the *l*-$C_3H_2{}^+$ isomer energy. Geometries for each stationary point are provided in Table 6.4.

Table 6.5: CCSD/aug-cc-pVTZ calculated geometries for stationary points on potential energy surface represented in Figure 6.5. Structures for each point are depicted in Figure 6.8 and electronic and zero point energies are provided in Table 6.4

stationary point	atom	x	y	z
[1a]	C	0	0	-1.14136
	Cl	0	0	0.39167
[1b]	C	0	0	0.599904
	H	0	0	1.656109
	C	0	0	-0.599904

stationary point	atom	x	y	z
	H	0	0	-1.656109
[2]	C	0	0	-0.345000
	Cl	0	0	1.286760
	C	0	0.678367	-1.527787
	H	0	1.600247	-2.078554
	C	0	-0.678367	-1.527787
	H	0	-1.600247	-2.078554
[3]	C	0.018354	0.536955	0
	Cl	-0.768290	-0.963326	0
	C	1.394966	0.458316	0
	H	0.755356	-1.120267	0
	C	0.703112	1.675055	0
	H	0.702256	2.750014	0
[4]	C	0.005983	0.474440	0
	Cl	-0.085875	-1.279367	0
	C	0.860059	1.562082	0
	C	-0.594289	1.627523	0
	H	-1.455953	2.265192	0
	H	1.199848	-1.501703	0
[5]	C	-1.162870	0.048628	0.038439
	Cl	1.682021	-0.086273	-0.050671
	C	-1.744158	1.243183	-0.008853
	H	2.149974	0.074659	1.128091
	C	-1.954728	-0.900496	0.022612
	H	-2.623554	-1.740519	0.008556
[6]	C	1.223681	0.310537	0

stationary point	atom	x	y	z
	Cl	-1.280714	-0.425591	0
	C	0.019856	0.951579	0
	H	-2.290150	0.383234	0
	C	2.394211	-0.025809	0
	H	3.413458	-0.336866	0
[7a]	Cl	0	0	0.035656
	H	0	0	-1.237164
[7b]	C	0	0	1.197535
	H	0	0	2.270605
	C	0	0	-0.027009
	C	0	0	-1.361224
[8a]	Cl	0	0	0
[8b]	C	0	0.693545	0.333591
	C	0	-0.693545	0.333591
	C	0	0	-0.821531
	H	0	-1.595173	0.918901
	H	0	1.595173	0.918901

Chapter 7

Conclusion

7.1 Summary

The work presented in this thesis represents a new branch in a growing tree of experiments, which are working towards cold, controlled, ion-molecule collision studies. Our approach combined a linear Paul ion trap with a TOFMS. While we were not the first to do so, we developed a simplified version of LIT-TOFMS electronics without sacrificing any performance. The experiment also did not rely on molecular dynamics simulations for calibration or ion detection.

The new apparatus was used to first study reactions between laser-cooled Ca^+ with the only radical molecules available in gas bottles, NO and O_2. Reactions with both of these neutral species observed rates dependent on the electronic quantum state of Ca^+. Via the cooling lasers, the quantum state of Ca^+ was manipulated, and state dependent reaction rate constants were measured. The resulting products of these reactions were also interesting in their own right. There is not much chemical intuition to draw upon for what bonds will break or form when two electrophiles react. More reactions between ions and radicals is a very exciting direction for future studies.

We have developed methods of loading clean, isolated samples of highly reactive molecular ions. This lead to isomer specific reaction studies of $C_2H_2{}^+ + C_3H_4$ that had not been previously studied. Two stable isomers of C_3H_4, propyne and allene, displayed very different chemistry with $C_2H_2{}^+$. Such a study was made possible by the highly specified creation and detection of ions in our apparatus. Through the use of isotope substitution, we completed a thorough investigation of the potential energy surface used to model the reaction. Such in-depth studies of isomer specific

reaction models provide insight into the foundational question of how structure determines function.

Another study of molecules relevant to the ISM performed was that of $CCl^+ + C_2H_2$. Benefiting from the methods developed in the previous studies, clean loading of CCl^+ was achieved. This reaction produced two very interesting carbocations, C_3H^+ and $C_3H_2{}^+$, which are central components of ISM chemistry. This study showed that halogenic compounds outside of flourine likely contribute to the chemistry of intersteller clouds and are worth further study.

7.2 Outlook

The use of an ion trap and laser-cooled Ca^+ produces cold, controlled ions. The next step in studying cold, controlled molecular-ion collisions is to gain similar levels of control over neutral molecules. Conveniently, such a technology has been developed and thoroughly investigated in the Lewandowski lab. Stark decelerators produce cold, velocity-tunable, quantum state selected, beams of neutral molecules. As an added bonus, neutral radicals are particularly well suited for Stark deceleration. A large leap forward in cold-controlled radical-ion reaction studies would be made by connecting the ion trap apparatus to a Stark decelerator in the lab. This is way easier said than done. As mentioned in the introduction of this thesis, multiple groups have been pursuing the exact proposal of a combined ion trap-decelerator experiment for years.

We hope to succeed in this endeavor through the use of an in-vacuum shutter and an electrostatic hexapole guide. The main elements of the molecular beam line are shown in Fig. 7.1. The in-vacuum shutter will separate the decelerated beam of neutral radicals from its non-decelerated carrier gas. The electrostatic hexapole will then guide the decelerated beam into the ion trap center. The pictured decelerator is a traveling-wave ring decelerator (TWRD) [131, 132]. The end result would be the ability to study ion-radical reactions with control over the collision energy and quantum state of the neutral molecule.

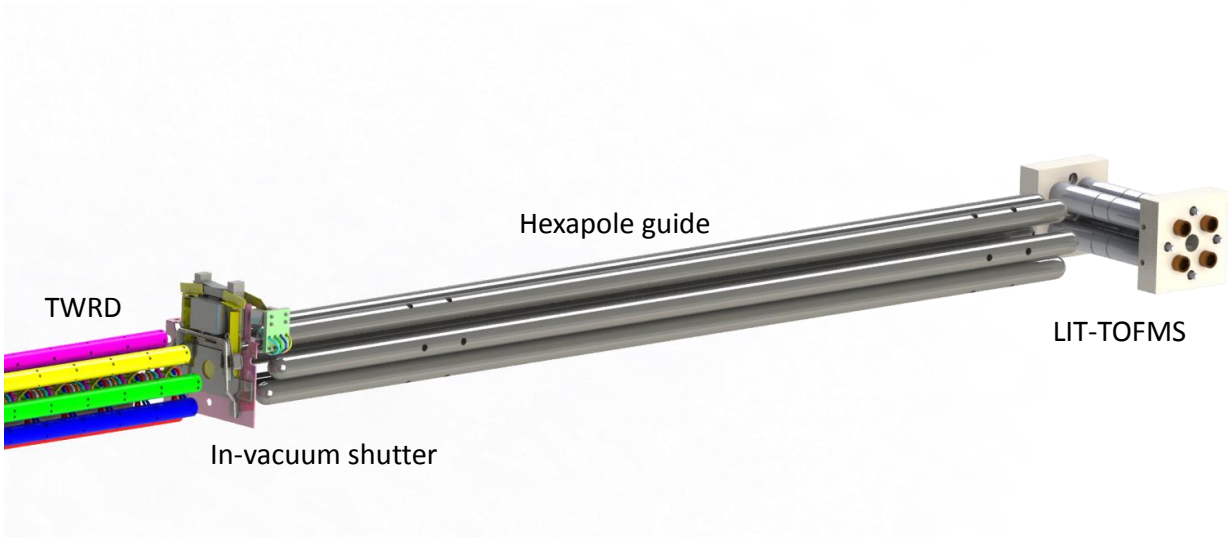

Figure 7.1: Schematic render of the partially constructed coupling between a TWRD and the ion trap from this thesis. An in-vacuum molecular beam shutter separates the line of site from the TWRD to the guiding hexapole. The guiding hexapole delivers the molecular beamline to the trap center.

Bibliography

[1] Alexander D Gingell. Applications of Coulomb crystals in cold chemistry. PhD thesis, Oxford University, UK, 2010.

[2] James Greenberg, Philipp C Schmid, Mikhail Miller, John F Stanton, and HJ Lewandowski. Quantum-state-controlled reactions between molecular radicals and ions. Physical Review A, 98(3):032702, 2018.

[3] Attila Tajti, Péter G Szalay, Attila G Császár, Mihály Kállay, Jürgen Gauss, Edward F Valeev, Bradley A Flowers, Juana Vázquez, and John F Stanton. Heat: High accuracy extrapolated ab initio thermochemistry. The Journal of chemical physics, 121(23):11599–11613, 2004.

[4] Christian P Endres, Stephan Schlemmer, Peter Schilke, Jürgen Stutzki, and Holger SP Müller. The cologne database for molecular spectroscopy, cdms, in the virtual atomic and molecular data centre, vamdc. Journal of Molecular Spectroscopy, 327:95–104, 2016.

[5] Valentine Wakelam, J-C Loison, E Herbst, B Pavone, A Bergeat, K Béroff, M Chabot, A Faure, D Galli, Wolf D Geppert, et al. The 2014 kida network for interstellar chemistry. The Astrophysical Journal Supplement Series, 217(2):20, 2015.

[6] Vincent G Anicich. An index of the literature for bimolecular gas phase cation-molecule reaction kinetics. 2003.

[7] V Vuitton, RV Yelle, and MJ McEwan. Ion chemistry and n-containing molecules in titan's upper atmosphere. Icarus, 191(2):722–742, 2007.

[8] JH Westlake, JH Waite, Nathalie Carrasco, M Richard, and T Cravens. The role of ion-molecule reactions in the growth of heavy ions in titan's ionosphere. Journal of Geophysical Research: Space Physics, 119(7):5951–5963, 2014.

[9] KERMIT C SMYTH, SG Lias, and P Ausloos. The ion-molecule chemistry of c3h3+ and the implications for soot formation. Combustion Science and Technology, 28(3-4):147–154, 1982.

[10] John R Eyler. Reactivities and structures of some hydrocarbon ions and their relationship to soot formation. ACS Publications, 1984.

[11] John L Bohn, Ana Maria Rey, and Jun Ye. Cold molecules: Progress in quantum engineering of chemistry and quantum matter. Science, 357(6355):1002–1010, 2017.

[12] Roland Wester. Velocity map imaging of ion–molecule reactions. Physical Chemistry Chemical Physics, 16(2):396–405, 2014.

[13] Pitt Allmendinger, Johannes Deiglmayr, Otto Schullian, Katharina Höveler, Josef A Agner, Hansjürg Schmutz, and Frédéric Merkt. New method to study ion–molecule reactions at low temperatures and application to the h2++ h2→ h3++ h reaction. ChemPhysChem, 17(22):3596, 2016.

[14] Thomas Glenewinkel-Meyer and Dieter Gerlich. Single and merged beam studies of the reaction h2+ (v= 0, 1; j= 0, 4)+ h2→ h3++ h. Israel journal of chemistry, 37(4):343–352, 1997.

[15] Stephan Schlemmer and Oskar Asvany. Laser induced reactions in a 22-pole ion trap. In Journal of Physics: Conference Series, volume 4, page 134. IOP Publishing, 2005.

[16] Alan Günther, Pablo Nieto, David Müller, Alexander Sheldrick, Dieter Gerlich, and Otto Dopfer. Berlintrap: A new cryogenic 22-pole ion trap spectrometer. Journal of Molecular Spectroscopy, 332:8–15, 2017.

[17] Roland Wester. Radiofrequency multipole traps: tools for spectroscopy and dynamics of cold molecular ions. Journal of Physics B: Atomic, Molecular and Optical Physics, 42(15):154001, 2009.

[18] Oskar Asvany, Sandra Brünken, Lars Kluge, and Stephan Schlemmer. Coltrap: a 22-pole ion trapping machine for spectroscopy at 4 k. Applied Physics B, 114(1-2):203–211, 2014.

[19] Steven J Schowalter, Alexander J Dunning, Kuang Chen, Prateek Puri, Christian Schneider, and Eric R Hudson. Blue-sky bifurcation of ion energies and the limits of neutral-gas sympathetic cooling of trapped ions. Nature communications, 7(1):1–8, 2016.

[20] B Roth, P Blythe, H Daerr, L Patacchini, and S Schiller. Production of ultracold diatomic and triatomic molecular ions of spectroscopic and astrophysical interest. Journal of Physics B: Atomic, Molecular and Optical Physics, 39(19):S1241, 2006.

[21] B Roth, D Offenberg, CB Zhang, and S Schiller. Chemical reactions between cold trapped ba+ ions and neutral molecules in the gas phase. Physical Review A, 78(4):042709, 2008.

[22] Stefan Willitsch. Chemistry with controlled ions. Adv. Chem. Phys, 162:307–340, 2017.

[23] Brianna R Heazlewood and Timothy P Softley. Low-temperature kinetics and dynamics with coulomb crystals. Annual review of physical chemistry, 66:475–495, 2015.

[24] Scott Trevor Sullivan. The motion trap: a hybrid atom-ion trap system for experiments in cold-chemistry and the production of cold polar molecular ions. PhD thesis, UCLA, 2013.

[25] Prateek Puri, Michael Mills, Christian Schneider, Ionel Simbotin, John A Montgomery, Robin Côté, Arthur G Suits, and Eric R Hudson. Synthesis of mixed hypermetallic oxide baoca+ from laser-cooled reagents in an atom-ion hybrid trap. Science, 357(6358):1370–1375, 2017.

[26] Felix Henry Joynson Hall. Cold ion-neutral reactions. PhD thesis, University_of_Basel, 2013.

[27] Alexander D Dörfler, Pascal Eberle, Debasish Koner, Michał Tomza, Markus Meuwly, and Stefan Willitsch. Long-range versus short-range effects in cold molecular ion-neutral collisions. Nature communications, 10(1):1–10, 2019.

[28] Lothar Ratschbacher, Christoph Zipkes, Carlo Sias, and Michael Köhl. Controlling chemical reactions of a single particle. Nature Physics, 8(9):649–652, 2012.

[29] Prateek Puri, Michael Mills, Ionel Simbotin, John A Montgomery, Robin Côté, Christian Schneider, Arthur G Suits, and Eric R Hudson. Reaction blockading in a reaction between an excited atom and a charged molecule at low collision energy. Nature chemistry, 11(7):615, 2019.

[30] Pascal Eberle, Alexander D Dörfler, Claudio von Planta, Krishnamurthy Ravi, and Stefan Willitsch. A dynamic ion–atom hybrid trap for high-resolution cold-collision studies. ChemPhysChem, 17(22):3769–3775, 2016.

[31] Felix HJ Hall and Stefan Willitsch. Millikelvin reactive collisions between sympathetically cooled molecular ions and laser-cooled atoms in an ion-atom hybrid trap. Physical review letters, 109(23):233202, 2012.

[32] Kristian Mølhave and Michael Drewsen. Formation of translationally cold mgh+ and mgd+ molecules in an ion trap. Physical Review A, 62(1):011401, 2000.

[33] B Roth, P Blythe, H Wenz, H Daerr, and S Schiller. Ion-neutral chemical reactions between ultracold localized ions and neutral molecules with single-particle resolution. Physical Review A, 73(4):042712, 2006.

[34] K Okada, M Wada, L Boesten, T Nakamura, I Katayama, and S Ohtani. Acceleration of the chemical reaction of trapped ca+ ions with h2o molecules by laser excitation. Journal of Physics B: Atomic, Molecular and Optical Physics, 36(1):33, 2002.

[35] Christian Schneider, Steven J Schowalter, Peter Yu, and Eric R Hudson. Electronics of an ion trap with integrated time-of-flight mass spectrometer. International Journal of Mass Spectrometry, 394:1–8, 2016.

[36] KAE Meyer, LL Pollum, LS Petralia, A Tauschinsky, CJ Rennick, TP Softley, and BR Heazlewood. Ejection of coulomb crystals from a linear paul ion trap for ion–molecule reaction studies. The Journal of Physical Chemistry A, 119(50):12449–12456, 2015.

[37] Daniel Rösch, Hong Gao, Ardita Kilaj, and Stefan Willitsch. Design and characterization of a linear quadrupole ion trap for high-resolution coulomb-crystal time-of-flight mass spectrometry. EPJ Techniques and Instrumentation, 3(1):5, 2016.

[38] Philipp C Schmid, J Greenberg, MI Miller, K Loeffler, and Heather J Lewandowski. An ion trap time-of-flight mass spectrometer with high mass resolution for cold trapped ion experiments. Review of Scientific Instruments, 88(12):123107, 2017.

[39] Philipp C Schmid, Mikhail I Miller, James Greenberg, Thanh L Nguyen, John F Stanton, and HJ Lewandowski. Quantum-state-specific reaction rate measurements for the photo-induced reaction ca++ o2→ cao++ o. Molecular Physics, 117(21):3036–3042, 2019.

[40] Katherine J. Catani, James Greenberg, Benjamin V. Saarel, and Heather J. Lewandowski. Translationally cold trapped ccl+ reactions with acetylene (c2h2), 2020.

[41] Bernhard Roth and Stephan Schiller. Sympathetically cooled molecular ions: from principles to first applications. arXiv preprint arXiv:0812.1154, 2008.

[42] Takashi Baba and Izumi Waki. Chemical reaction of sympathetically laser-cooled molecular ions. The Journal of chemical physics, 116(5):1858–1861, 2002.

[43] L. S. Petralia, A. Tsikritea, J. Loreau, T. P. Softley, and B. R. Heazlewood. Strong inverse kinetic isotope effect observed in ammonia charge exchange reactions. Nat. Commun., 11:173, 2020.

[44] Gary K Chen, Changjian Xie, Tiangang Yang, Anyang Li, Arthur G Suits, Eric R Hudson, Wesley C Campbell, and Hua Guo. Isotope-selective chemistry in the be+(2 s 1/2)+ hod→ beod+/beoh++ h/d reaction. Physical Chemistry Chemical Physics, 21(26):14005–14011, 2019.

[45] Tiangang Yang, Anyang Li, Gary K Chen, Changjian Xie, Arthur G Suits, Wesley C Campbell, Hua Guo, and Eric R Hudson. Optical control of reactions between water and laser-cooled be+ ions. The journal of physical chemistry letters, 9(13):3555–3560, 2018.

[46] Gary Chen. A New Tool For Col Ion-Molecule Chemistry. PhD thesis, UCLA, 2019.

[47] Kunihiro Okada, Takuya Suganuma, Takahiro Furukawa, Toshinobu Takayanagi, Michiharu Wada, and Hans A Schuessler. Cold ion–polar-molecule reactions studied with a combined stark-velocity-filter–ion-trap apparatus. Physical Review A, 87(4):043427, 2013.

[48] Stefan Willitsch, Martin T Bell, Alexander D Gingell, Simon R Procter, and Timothy P Softley. Cold reactive collisions between laser-cooled ions and velocity-selected neutral molecules. Physical review letters, 100(4):043203, 2008.

[49] Martin T Bell, Alexander D Gingell, James M Oldham, Timothy P Softley, and Stefan Willitsch. Ion-molecule chemistry at very low temperatures: cold chemical reactions between coulomb-crystallized ions and velocity-selected neutral molecules. Faraday discussions, 142:73–91, 2009.

[50] Yuan-Pin Chang, Karol Długołęcki, Jochen Küpper, Daniel Rösch, Dieter Wild, and Stefan Willitsch. Specific chemical reactivities of spatially separated 3-aminophenol conformers with cold ca+ ions. Science, 342(6154):98–101, 2013.

[51] Daniel Rösch, Stefan Willitsch, Yuan-Pin Chang, and Jochen Küpper. Chemical reactions of conformationally selected 3-aminophenol molecules in a beam with coulomb-crystallized ca+ ions. The Journal of chemical physics, 140(12):03B624_1, 2014.

[52] Xin Tong, Tibor Nagy, Juvenal Yosa Reyes, Matthias Germann, Markus Meuwly, and Stefan Willitsch. State-selected ion–molecule reactions with coulomb-crystallized molecular ions in traps. Chemical Physics Letters, 547:1–8, 2012.

[53] Ardita Kilaj, Hong Gao, Daniel Rösch, Uxia Rivero, Jochen Küpper, and Stefan Willitsch. Observation of different reactivities of para and ortho-water towards trapped diazenylium ions. Nature communications, 9(1):1–7, 2018.

[54] Alexander D Gingell, Martin T Bell, James M Oldham, Timothy P Softley, and Jeremy N Harvey. Cold chemistry with electronically excited ca+ coulomb crystals. The Journal of chemical physics, 133(19):194302, 2010.

[55] Kunihiro Okada, Yusuke Takada, Naoki Kimura, Michiharu Wada, and Hans A Schuessler. Development of a wavy stark velocity filter for studying interstellar chemistry. Review of Scientific Instruments, 88(8):083106, 2017.

[56] Dominik Haas, Claudio von Planta, Thomas Kierspel, Dongdong Zhang, and Stefan Willitsch. Long-term trapping of stark-decelerated molecules. Communications Physics, 2(1):1–7, 2019.

[57] Jutta Toscano, Christopher Rennick, Michal Hejduk, Timothy Softley, and Brianna Heazlewood. Making a pure beam of cold, state-selected particles with tuneable velocity. Bulletin of the American Physical Society, 2020.

[58] Klaas Bergmann, Hanns-Christoph Nägerl, Cristian Panda, Gerald Gabrielse, Eduard Miloglyadov, Martin Quack, Georg Seyfang, Gunther Wichmann, Silke Ospelkaus, Axel Kuhn, et al. Roadmap on stirap applications. Journal of Physics B: Atomic, Molecular and Optical Physics, 52(20):202001, 2019.

[59] Samuel Earnshaw. On the nature of the molecular forces. In Cambridge Philosophical Society, volume 7, pages 97–112, 1842.

[60] Wolfgang Paul. Electromagnetic traps for charged and neutral particles. Rev. Mod. Phys., 62:531–540, Jul 1990.

[61] D. R. Denison. Operating parameters of a quadrupole in a grounded cylindrical housing. Journal of Vacuum Science & Technology, 8(1):266–269, 1971.

[62] John Raymond Gibson and Stephen Taylor. Numerical investigation of the effect of electrode size on the behaviour of quadrupole mass filters. Rapid Communications in Mass Spectrometry, 15(20):1960–1964, 2001.

[63] DJ Berkeland, JD Miller, James C Bergquist, Wayne M Itano, and David J Wineland. Minimization of ion micromotion in a paul trap. Journal of applied physics, 83(10):5025–5033, 1998.

[64] Dieter Gerlich. Inhomogeneous rf fields: A versatile tool for the study of processes with slow ions. State-Selected and State-to-State Ion-Molecule Reaction Dynamics. Part 1: Experiment, 82, 1992.

[65] Harold J Metcalf and Peter van der Straten. Laser cooling and trapping of atoms. JOSA B, 20(5):887–908, 2003.

[66] C. B. Zhang, D. Offenberg, B. Roth, M. A. Wilson, and S. Schiller. Molecular-dynamics simulations of cold single-species and multispecies ion ensembles in a linear paul trap. Phys. Rev. A, 76:012719, Jul 2007.

[67] Paul L Houston. Chemical kinetics and reaction dynamics. Courier Corporation, 2012.

[68] Michael J Pilling and Paul W Seakins. Reaction kinetics. Oxford University Press, 1995.

[69] Jeffrey I Steinfeld, Joseph Salvadore Francisco, and William L Hase. Chemical kinetics and dynamics, volume 3. Prentice Hall Englewood Cliffs (New Jersey), 1989.

[70] Michael T Bowers. Gas phase ion chemistry, volume 1. Academic Press, 2016.

[71] Thanh Lam Nguyen and John F Stanton. A steady-state approximation to the two-dimensional master equation for chemical kinetics calculations. The Journal of Physical Chemistry A, 119(28):7627–7636, 2015.

[72] W. C. Wiley and I. H. McLaren. Time-of-flight mass spectrometer with improved resolution. Review of Scientific Instruments, 26(12):1150–1157, 1955.

[73] G.W. Fraser. The ion detection efficiency of microchannel plates (mcps). International Journal of Mass Spectrometry, 215:13 – 30, 2002.

[74] Travis C Briles. Production, Deceleration, and Detection of OH Radicals. PhD thesis, University of Colorado at Boulder, 2015.

[75] Theodore P Snow and Veronica M Bierbaum. Ion chemistry in the interstellar medium. Annual Review of Analytical Chemistry, 1(1):229–259, 2008.

[76] Ian WM Smith. Reactions at very low temperatures: gas kinetics at a new frontier. Angewandte Chemie International Edition, 45(18):2842–2861, 2006.

[77] Enrico Bodo. Low and ultra-low energy chemical processes involving ions. Physica Scripta, 80(4):048117, 2009.

[78] Martin T Bell and Timothy P. Softley. Ultracold molecules and ultracold chemistry. Molecular Physics, 107(2):99–132, 2009.

[79] Ian WM Smith. Gas-phase reactions in the ism: Rate coefficients, temperature dependences, and reaction products. Proceedings of the International Astronomical Union, 7(S280):361–371, 2011.

[80] Takatoshi Ichino, Jürgen Gauss, and John F Stanton. Quasidiabatic states described by coupled-cluster theory. The Journal of chemical physics, 130(17):174105, 2009.

[81] Devin A Matthews and John F Stanton. Accelerating the convergence of higher-order coupled cluster methods. The Journal of chemical physics, 143(20):204103, 2015.

[82] John F Stanton. Semiclassical transition-state theory based on fourth-order vibrational perturbation theory: the symmetrical eckart barrier. The journal of physical chemistry letters, 7(14):2708–2713, 2016.

[83] Xu Zhang, Veronica M Bierbaum, G Barney Ellison, and Shuji Kato. Gas-phase reactions of organic radicals and diradicals with ions. The Journal of chemical physics, 120(8):3531–3534, 2004.

[84] Justin P Wiens, Oscar Martinez Jr, Shaun G Ard, Brendan C Sweeny, Albert A Viggiano, and Nicholas S Shuman. Kinetics of cations with c2 hydrofluorocarbon radicals. The Journal of Physical Chemistry A, 121(42):8061–8068, 2017.

[85] Graham BI Scott, David A Fairley, Daniel B Milligan, Colin G Freeman, and Murray J McEwan. Gas phase reactions of some positive ions with atomic and molecular oxygen and nitric oxide at 300 k. The Journal of Physical Chemistry A, 103(37):7470–7473, 1999.

[86] Dieter Gerlich. Ion-neutral collisions in a 22-pole trap at very low energies. Physica Scripta, 1995(T59):256, 1995.

[87] Maria Schwarz, OO Versolato, Alexander Windberger, FR Brunner, Tim Ballance, SN Eberle, Joachim Ullrich, Piet O Schmidt, Anders Kragh Hansen, Alexander David Gingell, et al. Cryogenic linear paul trap for cold highly charged ion experiments. Review of Scientific Instruments, 83(8):083115, 2012.

[88] Christian Schneider, Steven J Schowalter, Kuang Chen, Scott T Sullivan, and Eric R Hudson. Laser-cooling-assisted mass spectrometry. Physical Review Applied, 2(3):034013, 2014.

[89] Michael Drewsen, I Jensen, Jens Lindballe, N Nissen, Randi Martinussen, Anders Mortensen, Peter Staanum, and Dirk Voigt. Ion coulomb crystals: a tool for studying ion processes. International Journal of Mass Spectrometry, 229(1-2):83–91, 2003.

[90] Peter F Staanum, Klaus Højbjerre, Roland Wester, and Michael Drewsen. Probing isotope effects in chemical reactions using single ions. Physical review letters, 100(24):243003, 2008.

[91] Felix HJ Hall, Mireille Aymar, Nadia Bouloufa-Maafa, Olivier Dulieu, and Stefan Willitsch. Light-assisted ion-neutral reactive processes in the cold regime: Radiative molecule formation versus charge exchange. Physical review letters, 107(24):243202, 2011.

[92] Wade G Rellergert, Scott T Sullivan, Svetlana Kotochigova, Alexander Petrov, Kuang Chen, Steven J Schowalter, and Eric R Hudson. Measurement of a large chemical reaction rate between ultracold closed-shell ca 40 atoms and open-shell yb+ 174 ions held in a hybrid atom-ion trap. Physical review letters, 107(24):243201, 2011.

[93] Nabanita Deb, Laura L Pollum, Alexander D Smith, Matthias Keller, Christopher J Rennick, Brianna R Heazlewood, and Timothy P Softley. Coulomb crystal mass spectrometry in a digital ion trap. Physical Review A, 91(3):033408, 2015.

[94] Naoki Kimura, Kunihiro Okada, Toshinobu Takayanagi, Michiharu Wada, Shunsuke Ohtani, and Hans A Schuessler. Sympathetic crystallization of cah+ produced by a laser-induced reaction. Physical Review A, 83(3):033422, 2011.

[95] Anders K Hansen, Magnus A Sørensen, Peter F Staanum, and Michael Drewsen. Single-ion recycling reactions. Angewandte Chemie International Edition, 51(32):7960–7962, 2012.

[96] Felix HJ Hall, Mireille Aymar, Maurice Raoult, Olivier Dulieu, and Stefan Willitsch. Light-assisted cold chemical reactions of barium ions with rubidium atoms. Molecular Physics, 111(12-13):1683–1690, 2013.

[97] Michael Drewsen. Ion coulomb crystals. Physica B: Condensed Matter, 460:105–113, 2015.

[98] O Dulieu and C Gabbanini. The formation and interactions of cold and ultracold molecules: new challenges for interdisciplinary physics. Reports on Progress in Physics, 72(8):086401, 2009.

[99] Olivier Dulieu and Andreas Osterwalder, editors. Cold Chemistry. Theoretical and Computational Chemistry Series. The Royal Society of Chemistry, 2018.

[100] Lincoln D Carr, David DeMille, Roman V Krems, and Jun Ye. Cold and ultracold molecules: science, technology and applications. New J. Phys., 11(5):055049, 2009.

[101] John M. Doyle, Bretislav Friedrich, and Edvardas Narevicius. Physics and chemistry with cold molecules. ChemPhysChem, 17(22):3581, 2018.

[102] Sjoerd N. Vogels, Jolijn Onvlee, Simon Chefdeville, Ad van der Avoird, Gerrit C. Groenenboom, and Sebastiaan Y. T. van de Meerakker. Imaging resonances in low-energy no-he inelastic collisions. Science, 350(6262):787, 2015.

[103] Zhi Gao, Tijs Karman, Sjoerd N. Vogels, Matthieu Besemer, Ad van der Avoird, Gerrit C. Groenenboom, and Sebastiaan Y. T. van de Meerakker. Observation of correlated excitations in bimolecular collisions. Nat. Chem., 10:469, 2018.

[104] Ayelet Klein, Wojciech Skomorowski Yuval Shagam, Mariusz Pawlak Piotr S. Żuchowski, Nimrod Moiseyev Liesbeth M. C. Janssen, Sebastiaan Y. T. van de Meerakker, Ad van der Avoird, Christiane P. Koch, and Edvardas Narevicius. Directly probing anisotropy in atom–molecule collisions through quantum scattering resonances. Nat. Chem., 13:35, 2017.

[105] Sean D. S. Gordon, Junwen Zou, Silvia Tanteri, Justin Jankunas, and Andreas Osterwalder. Energy dependent stereodynamics of the $Ne(^3P_2)+Ar$ reaction. Phys. Rev. Lett., 119:053001, 2017.

[106] L. P. Parazzoli, N. J. Fitch, P. S. Żuchowski, J. M. Hutson, and H. J. Lewandowski. Large effects of electric fields on atom-molecule collisions at millikelvin temperatures. Phys. Rev. Lett., 106:193201, May 2011.

[107] Nitzan Akerman, Michael Karpov, Yair Segev, Natan Bibelnik, Julia Narevicius, and Edvardas Narevicius. Trapping of molecular oxygen together with lithium atoms. Phys. Rev. Lett., 119:073204, 2017.

[108] Jonathan D Weinstein, Thierry Guillet, Bretislav Friedrich, John M Doyle, et al. Magnetic trapping of calcium monohydride molecules at millikelvin temperatures. Nature, 395(6698):148, 1998.

[109] Loïc Anderegg, Benjamin L. Augenbraun, Eunmi Chae, Boerge Hemmerling, Nicholas R. Hutzler, Aakash Ravi, Alejandra Collopy, Jun Ye, Wolfgang Ketterle, and John M. Doyle. Radio frequency magneto-optical trapping of caf with high density. Phys. Rev. Lett., 119:103201, 2017.

[110] Ivan Kozyryev, Louis Baum, Kyle Matsuda, Benjamin L. Augenbraun, Loic Anderegg, Alexander P. Sedlack, and John M. Doyle. Sisyphus laser cooling of a polyatomic molecule. Phys. Rev. Lett., 118:173201, 2017.

[111] EB Norrgard, DJ McCarron, MH Steinecker, MR Tarbutt, and D DeMille. Submillikelvin dipolar molecules in a radio-frequency magneto-optical trap. Physical review letters, 116(6):063004, 2016.

[112] H J Williams, S Truppe, M Hambach, L Caldwell, N J Fitch, E A Hinds, B E Sauer, and M R Tarbutt. Characteristics of a magneto-optical trap of molecules. New J. Phys., 19(11):113035, 2017.

[113] Matthew T. Hummon, Mark Yeo, Benjamin K. Stuhl, Alejandra L. Collopy, Yong Xia, and Jun Ye. 2d magneto-optical trapping of diatomic molecules. Phys. Rev. Lett., 110:143001, Apr 2013.

[114] T Kraemer, M Mark, P Waldburger, JG Danzl, C Chin, B Engeser, AD Lange, K Pilch, A Jaakkola, H-C Nägerl, et al. Evidence for efimov quantum states in an ultracold gas of caesium atoms. Nature, 440(7082):315, 2006.

[115] S. Ospelkaus, K.-K. Ni, D. Wang, M. H. G. de Miranda, B. Neyenhuis, G. Quéméner, P. S. Julienne, J. L. Bohn, D. S. Jin, and J. Ye. Quantum-state controlled chemical reactions of ultracold potassium-rubidium molecules. Science, 327(5967):853–857, 2010.

[116] Stefan Willitsch. Coulomb-crystallised molecular ions in traps: methods, applications, prospects. International Reviews in Physical Chemistry, 31(2):175, 2012.

[117] Xin Tong, Alexander H. Winney, and Stefan Willitsch. Sympathetic cooling of molecular ions in selected rotational and vibrational states produced by threshold photoionization. Phys. Rev. Lett., 105:143001, Sep 2010.

[118] Peter F Staanum, Klaus Højbjerre, Peter S Skyt, Anders K Hansen, and Michael Drewsen. Rotational laser cooling of vibrationally and translationally cold molecular ions. Nature Physics, 6(4):271, 2010.

[119] Tobias Schneider, B Roth, H Duncker, I Ernsting, and S Schiller. All-optical preparation of molecular ions in the rovibrational ground state. Nature Physics, 6(4):275, 2010.

[120] Chien-Yu Lien, Scott R. Williams, and Brian Odom. Optical pulse-shaping for internal cooling of molecules. Phys. Chem. Chem. Phys., 13:18825–18829, 2011.

[121] Michael Drewsen, Liv Hornekær, Niels Kjærgaard, Kristian Mølhave, Anne-Marie Thommesen, Zelinda Videsen, Anders Mortensen, and Frank Jensen. Ion coulomb crystals and some applications. AIP Conference Proceedings, 606(1):135–144, 2002.

[122] R. Saito, S. Haze, M. Sasakawa, R. Nakai, M. Raoult, H. Da Silva, O. Dulieu, and T. Mukaiyama. Characterization of charge-exchange collisions between ultracold ^{6}Li atoms and $^{40}Ca^+$ ions. Phys. Rev. A, 95:032709, Mar 2017.

[123] J. Joger, H. Fürst, N. Ewald, T. Feldker, M. Tomza, and R. Gerritsma. Observation of collisions between cold li atoms and yb^+ ions. Phys. Rev. A, 96:030703, Sep 2017.

[124] S.G. Lias. NIST Chemistry WebBook, NIST Standard Reference Database Number 69, chapter Ionization Energy Evaluation. National Institute of Standards and Technology, Gaithersburg MD, 20899, 2018.

[125] Jürgen Eschner, Giovanna Morigi, Ferdinand Schmidt-Kaler, and Rainer Blatt. Laser cooling of trapped ions. J. Opt. Soc. Am. B, 20(5):1003–1015, May 2003.

[126] Kunihiro Okada, Masanari Ichikawa, Michiharu Wada, and Hans A Schuessler. Quasiequilibrium characterization of mixed-ion coulomb crystals. Physical Review Applied, 4(5):054009, 2015.

[127] Charles Q. Jiao, Don Rufus A. Ranatunga, Weldon E. Vaughn, and Ben S. Freiser. A pulsed-leak valve for use with ion trapping mass spectrometers. Journal of the American Society for Mass Spectrometry, 7(1):118 – 122, 1996.

[128] Rodney J. Bartlett, J.D. Watts, S.A. Kucharski, and J. Noga. Non-iterative fifth-order triple and quadruple excitation energy corrections in correlated methods. Chem. Phys. Lett., 165(6):513, 1990.

[129] Krishnan Raghavachari, Gary W. Trucks, John A. Pople, and Martin Head-Gordon. A fifth-order perturbation comparison of electron correlation theories. Chem. Phys. Lett., 157(6):479, 1989.

[130] Thom H. Dunning. Gaussian basis sets for use in correlated molecular calculations. i. the atoms boron through neon and hydrogen. J. Chem. Phys., 90(2):1007, 1989.

[131] M. I. Fabrikant, Tian Li, N. J. Fitch, N. Farrow, Jonathan D. Weinstein, and H. J. Lewandowski. Method for traveling-wave deceleration of buffer-gas beams of ch. Phys. Rev. A, 90:033418, Sep 2014.

[132] Yomay Shyur, Jason A Bossert, and H J Lewandowski. Pulsed operation of a ring stark decelerator. J. Phys. B: At. Mol. Opt. Phys., 51(16):165101, 2018.

[133] James Martin Oldham. "Combination of a Cold Ion and Cold Molecular Source. PhD thesis, Oxford University, UK., 2014.

[134] Pascal Eberle, Alexander D Dörfler, Claudio von Planta, Krishnamurthy Ravi, Dominik Haas, Dong Zhang, Sebastiaan Y T van de Meerakker, and Stefan Willitsch. Ion-atom and ion-molecule hybrid systems: Ion-neutral chemistry at ultralow energies. Journal of Physics: Conference Series, 635(1):012012, 2015.

[135] Nikolay V. Vitanov, Andon A. Rangelov, Bruce W. Shore, and Klaas Bergmann. Stimulated raman adiabatic passage in physics, chemistry, and beyond. Rev. Mod. Phys., 89:015006, Mar 2017.

[136] Timothy James Barnum and Robert W Field. Preparation of state selected ions. private communication, 2018.

[137] JH Lacy, Neal J Evans, JM Achtermann, DE Bruce, JF Arens, and JS Carr. Discovery of interstellar acetylene. The Astrophysical Journal, 342:L43–L46, 1989.

[138] GR Floyd, RH Prince, and WW Duley. A method of forming complex molecules in interstellar space. Journal of the Royal Astronomical Society of Canada, 67:299, 1973.

[139] JS Knight, CG Freeman, MJ McEwan, VG Anicich, and WT Huntress. A flow tube study of ion-molecule reactions of acetylene. Journal of Physical Chemistry, 91(14):3898–3902, 1987.

[140] Eric Herbst and Ewine F. van Dishoeck. Complex organic interstellar molecules. Annual Review of Astronomy and Astrophysics, 47(1):427–480, 2009.

[141] Vincent G Anicich, Geoffrey A Blake, Jhong K Kim, Murray J McEwan, and Wesley T Huntress Jr. Ion-molecule reactions in unsaturated hydrocarbons: allene, propyne, diacetylene, and vinylacetylene. The Journal of Physical Chemistry, 88(20):4608–4617, 1984.

[142] J. H. Waite Jr., D. T. Young, T. E. Cravens, A. J. Coates, F. J. Crary, B. Magee, and J. Westlake. The process of tholin formation in titan's upper atmosphere. Science, 316(5826):870–875, 2007.

[143] P Weilmünster, A Keller, and K-H Homann. Large molecules, radicals, ions, and small soot particles in fuel-rich hydrocarbon flames: Part i: positive ions of polycyclic aromatic hydrocarbons (pah) in low-pressure premixed flames of acetylene and oxygen. Combustion and Flame, 116(1-2):62–83, 1999.

[144] John M Goodings, Scott D Tanner, and Diethard K Bohme. Hydrocarbon ions in fuel-rich, ch4–c2h2–o2 flames as a probe for the initiation of soot: interpretation of the ion chemistry. Canadian Journal of Chemistry, 60(22):2766–2776, 1982.

[145] Michael Frenklach. Reaction mechanism of soot formation in flames. Physical chemistry chemical Physics, 4(11):2028–2037, 2002.

[146] Nils Hansen, James A Miller, Phillip R Westmoreland, Tina Kasper, Katharina Kohse-Höinghaus, Juan Wang, and Terrill A Cool. Isomer-specific combustion chemistry in allene and propyne flames. Combustion and flame, 156(11):2153–2164, 2009.

[147] Raymond E. March, Adam W. McMahon, Frank A. Londry, Roland L. Alfred, John F.J. Todd, and Fernande Vedel. Resonance excitation of ions stored in a quadrupole ion trap. part 1. a simulation study. International Journal of Mass Spectrometry and Ion Processes, 95(2):119 – 156, 1989.

[148] M. Welling, H.A. Schuessler, R.I. Thompson, and H. Walther. Ion/molecule reactions, mass spectrometry and optical spectroscopy in a linear ion trap. International Journal of Mass Spectrometry and Ion Processes, 172(1):95 – 114, 1998.

[149] S. Jyothi, Tridib Ray, and S.A. Rangwala. Phase-sensitive radial extraction and mass spectrometry of trapped ions in a compact geometry. Applied Physics B, 118(1):131–138, 2015.

[150] S. Jyothi, Kisra N. Egodapitiya, Brad Bondurant, Zhubing Jia, Eric Pretzsch, Piero Chiappina, Gang Shu, and Kenneth R. Brown. A hybrid ion-atom trap with integrated high resolution mass spectrometer. Review of Scientific Instruments, 90(10):103201, 2019.

[151] JC Van Craen, Michel Herman, Réginald Colin, and JKG Watson. The ã-x̃ band system of acetylene: Analysis of medium-wavelength bands, and vibration-rotation constants for the levels nν' 3 (n= 4–6), ν' 2+ nν' 3 (n= 3–5), and ν' 1+ nν' 3 (n= 2, 3). Journal of Molecular Spectroscopy, 111(1):185–197, 1985.

[152] Andrew J Orr-Ewing, Ross A Morgan, Steven HS Wilson, Claire L Reed, and Michael NR Ashfold. (1+ 1) resonance-enhanced multiphoton ionization spectroscopy of jet-cooled c 2 h 2, c 2 hd and c 2 d 2 in the range 46 400–48 400 cm–1. Journal of the Chemical Society, Faraday Transactions, 91(19):3327–3337, 1995.

[153] Eduardo Carrascosa, Jennifer Meyer, and Roland Wester. Imaging the dynamics of ion–molecule reactions. Chemical Society Reviews, 46(24):7498–7516, 2017.

[154] Valentine Wakelam, E Herbst, J-C Loison, IWM Smith, V Chandrasekaran, B Pavone, NG Adams, M-C Bacchus-Montabonel, A Bergeat, K Béroff, et al. A kinetic database for astrochemistry (kida). The Astrophysical Journal Supplement Series, 199(1):21, 2012.

[155] K Jousten. Gauges for fine and high vacuum. CAS Cern Accelerator School, 2007.

[156] AM Schulenburg and Frédéric Merkt. Rotationally resolved photoelectron spectroscopic study of the jahn–teller effect in allene. The journal of chemical physics, 130(3):034308, 2009.

[157] AM Mebel and AD Bandrauk. Theoretical study of unimolecular decomposition of allene cations. The Journal of chemical physics, 129(22):224311, 2008.

[158] Linsen Pei and James M Farrar. Imaging ion-molecule reactions: Charge transfer and cn bond formation in the c++ nh3 system. The Journal of chemical physics, 136(20):204305, 2012.

[159] Albert C Parr, Andrew J Jason, and Roger Stockbauer. Photoionization and threshold photoelectron-photoion coincidence study of allene from onset to 20 ev. International Journal of Mass Spectrometry and Ion Physics, 26(1):23–38, 1978.

[160] Y. Shyur, N. J. Fitch, J. A. Bossert, T. Brown, and H. J. Lewandowski. A high-voltage amplifier for traveling-wave stark deceleration. Rev. Sci. Instrum., 89:084705, 2018.

[161] D Smith and N G Adams. Production and Loss Processes for Hcl in Interstellar Clouds - Some Relevant Laboratory Measurements. Astrophys. J., 298:827–829, 1985.

[162] G. A. Blake, V. G. Anicich, and W. T. Huntress. Chemistry of chlorine in dense interstellar clouds. Astrophys. J., 300:415–419, 1986.

[163] J Zmuidzinas, G A Blake, J Carlstrom, J Keene, and D Miller. HCl Absorption Toward Sagittarius B2. Astrophys. J., 447:L125–L128, 1995.

[164] D. A. Neufeld and M. G. Wolfire. The chemistry of interstellar molecules containing the halogen elements. Astrophys. J., 706:1594, 2009.

[165] D. C. Lis, J. C. Pearson, D. A. Neufeld, P. Schilke, H. S. P. Müller, H. Gupta, T. A. Bell, C. Comito, T. G. Phillips, E. A. Bergin, C. Ceccarelli P. F. Goldsmith, G. A. Blake, A. Bacmann, A. Baudry, M. Benedettini, A. Benz, J. Black, A. Boogert, S. Bottinelli, S. Cabrit, P. Caselli, A. Castets, E. Caux, J. Cernicharo, C. Codella, A. Coutens, N. Crimier, N. R. Crockett, F. Daniel, K. Demyk, C. Dominic, M.-L. Dubernet, M. Emprechtinger, P. Encrenaz, E. Falgarone, A. Fuente, M. Gerin, T. F. Giesen, J. R. Goicoechea, F. Helmich, P. Hennebelle, Th. Henning, E. Herbst, P. Hily-Blant, Å. Hjalmarson, D. Hollenbach, T. Jack, C. Joblin, D. Johnstone, C. Kahane, M. Kama, M. Kaufman, A. Klotz, W. D. Langer, B. Larsson, J. Le Bourlot, B. Lefloch, F. Le Petit, D. Li, R. Liseau, S. D. Lord, A. Lorenzani, S. Maret, P. G. Martin, G. J. Melnick, K. M. Menten, P. Morris, J. A. Murphy, Z. Nagy, B. Nisini, V. Ossenkopf, S. Pacheco, L. Pagani, B. Parise, M. Pérault, R. Plume, S.-L. Qin, E. Roueff, M. Salez, A. Sandqvist, P. Saraceno, S. Schlemmer, K. Schuster, R. Snell, J. Stutzki, A. Tielens, N. Trappe, F. F. S. van der Tak, M. H. D. van der Wiel, E. van Dishoeck, C. Vastel, S. Viti, V. Wakelam, A. Walters, S. Wang, F. Wyrowski, H. W. Yorke, S. Yu, J. Zmuidzinas, Y. Delorme, J.-P. Desbat, R. Güsten, J.-M. Krieg, and B. Delforge. Herschel/HIFI discovery of interstellar chloronium (H_2Cl^+) . Astron. Astrophys., 521:L9, 2010.

[166] David A Neufeld, Evelyne Roueff, Ronald L Snell, Dariusz Lis, Arnold O Benz, Simon Bruderer, John H Black, Massimo De Luca, Maryvonne Gerin, Paul F Goldsmith, Harshal Gupta, Nick Indriolo, Jacques Le Bourlot, Franck Le Petit, Bengt Larsson, Gary J Melnick, Karl M Menten, Raquel Monje, Zsófia Nagy, Thomas G Phillips, Aage Sandqvist, Paule Sonnentrucker, Floris van der Tak, and Mark G Wolfire. Herschel observations of interstellar chloronium. Astrophys. J., 748:37, 2012.

[167] M Goto, T Usuda, T R Geballe, K M Menten, N Indriolo, and D A Neufeld. Fundamental vibrational transitions of hydrogen chloride detected in CRL 2136. Astron. Astrophys., 558:L5, 2013.

[168] S Muller, J H Black, M Guelin, C Henkel, F Combes, M Gérin, S Aalto, A Beelen, J Darling, C Horellou, S Martín, K M Menten, Dinh V-Trung, and M A Zwaan. Detection of chloronium and measurement of the ^{35}Cl/^{37}Cl isotopic ratio at z= 0.89 toward PKS 1830–211. Astron. Astrophys., 566:1–4, 2014.

[169] M Lanza, Y Kalugina, L Wiesenfeld, A Faure, and F Lique. New insights on the HCl abundance in the interstellar medium. Mon. Not. R. Astron. Soc., 443:3351–3358, 2014.

[170] David A Neufeld, John H Black, Maryvonne Gerin, Javier R Goicoechea, Paul F Goldsmith, Cecile Gry, Harshal Gupta, Eric Herbst, Nick Indriolo, Dariusz Lis, Karl M Menten, Raquel Monje, Bhaswati Mookerjea, Carina Persson, Peter Schilke, Paule Sonnentrucker, and Mark G Wolfire. Herschel Observations of Interstellar Chloronium. II. Detections Toward G29.96-0.02, W49N, W51, and W3 (OH). Astrophys. J., 807:1–12, 2015.

[171] Edith C. Fayolle, Karin I. Öberg, Jes K. Jørgensen, Kathrin Altwegg, Hannah Calcutt, Holger S. P. Müller, Martin Rubin, Matthijs H. D. van der Wiel, Per Bjerkeli, Tyler L. Bourke, Audrey Coutens, Ewine F. van Dishoeck, Maria N. Drozdovskaya, Robin T. Garrod, Niels F. W. Ligterink, Magnus V. Persson, Susanne F. Wampfler, H. Balsiger, J. J. Berthelier, J. De Keyser, B. Fiethe, S. A. Fuselier, S. Gasc, T. I. Gombosi, T. Sémon, C. Y. Tzou, and the ROSINA team. Protostellar and cometary detections of organohalogens. Nat. Astron., 1(10):703–708, 2017.

[172] J.H. Futrell V.G. Anicich, W.T. Huntress Jr. Ion cyclotron resonance studies of some reactions of C^+ ions. Chem. Phys. Lett., 40:233–236, 1976.

[173] D. M. Sonnenfroh and J. M. Farrar. Dynamics of the reaction of C^+ with HCl. Astrophys. J., 335:491–497, 1988.

[174] C E Dateo and D C Clary. Rate constant calculations on the C^+ + HCl reaction. J. Chem. Phys., 90:7216–7228, 1989.

[175] D C Clary, C E Dateo, and D Smith. Rates for the reactions of open-shell ions with molecules. Chem. Phys. Lett., 167:1–6, 1990.

[176] J Glosik, W Freysinger, A Hansel, P Špănel, and W Lindinger. Energy dependencies of fast reactions of positive ions X^+ with HCl from near thermal to $\approx 2\,$eV center-of-mass collision energy (X^+=H + , H 2 $^+$, H 3 $^+$, N + , N 2 $^+$, Ar + , C + , CH + ,CH 2 $^+$, CH 3 $^+$, CH 4 $^+$, CH 5 $^+$). J. Chem. Phys., 98:6995–7003, 1993.

[177] J Glosik, D Smith, P Špăne̊l, W Freysinger, and W Lindinger. SIFDT studies of the reactions of C^+, CH^+ and $CH_2{}^+$ with HCl and CO_2, and CH_3; with HCl. Int. J. Mass. Spectrom. and Ion Processes, 129:131–143, 1993.

[178] V. G. Anicich. Evaluated bimolecular ion-molecule gas phase kinetics of positive ions for use in modeling planetary atmospheres, cometary comae, and interstellar clouds. J. Phys. Chem. Ref. Data, 22:1469–1569, 1993.

[179] J. H. Lacy, N. J. Evans II, J. M. Achtermann, D. E. Bruce, J. F. Arens, and J. S. Carr. Discovery of interstellar acetylene. Astrophys. J., 342:L43–L46, 1989.

[180] F. Lahuis and Ewine F. van Dishoeck. Iso–sws spectroscopy of gas–phase C_2H_2 and HCN toward massive young stellar objects. Astron. Astrophys., 355:699–712, 2000.

[181] M. J. Mumma, M. A. DiSanti, N. Dello Russo, K. Magee-Sauer, E. Gibb, and R. Novak. Remote infrared observations of planetary volatiles in comets: a window on the early solar system. Adv. Space Res., 31:2563–2575, 2003.

[182] M. Agúndez, J. Cernicharo, and J. R. Goicoechea. Formation of simple organic molecules in inner T Tauri disks. Astron. Astrophys., 483:831–837, 2008.

[183] Jérôme Pety, P Gratier, V Guzmán, E Roueff, M Gerin, JR Goicoechea, S Bardeau, A Sievers, F Le Petit, J Le Bourlot, A Belloche, and D Talbi. The IRAM-30 m line survey of the Horsehead PDR-II. First detection of the l-C_3H^+ hydrocarbon cation. Astron. Astrophys., 548:A68, 2012.

[184] Sandra Brünken, Lars Kluge, Alexander Stoffels, Oskar Asvany, and Stephan Schlemmer. Laboratory rotational spectrum of l-C_3H^+ and confirmation of its astronomical detection. Astrophys. J., 783:L4, 2014.

[185] Peter Botschwina, C Stein, P Sebald, B Schröder, and R Oswald. Strong theoretical support for the assignment of B11244 to l-C_3H^+. Astrophys. J., 787:72, 2014.

[186] V V Guzmán, J Pety, J R Goicoechea, M Gérin, E Roueff, P Gratier, and K I Öberg. Spatially resolved l-C_3H^+ emission in the horsehead photodissociation region: further evidence for a top-down hydrocarbon chemistry. Astrophys. J., 800:1–6, 2015.

[187] Brett A McGuire. 2018 census of interstellar, circumstellar, extragalactic, protoplanetary disk, and exoplanetary molecules. Astrophys. J., Suppl. Ser., 239:1–48, 2018.

[188] M Gérin, H Liszt, D Neufeld, B Godard, P Sonnentrucker, J Pety, and E Roueff. Molecular ion abundances in the diffuse ISM: CF^+, HCO^+, HOC^+, and C_3H^+. Astron. Astrophys., 622:A26, 2019.

[189] P. Thaddeus, J. M. Vrtilek, and C. A. Gottlieb. Laboratory and astronomical identification of cyclopropenylidene, C_3H_2. Astrophys. J., 299:L63–L66, 1985.

[190] David E Woon and Thom H Dunning Jr. Gaussian basis sets for use in correlated molecular calculations. iii. the atoms aluminum through argon. J. Chem. Phys., 98(2):1358–1371, 1993.

[191] Rick A Kendall, Thom H Dunning Jr., and Robert J Harrison. Electron affinities of the first-row atoms revisited. systematic basis sets and wave functions. J. Chem. Phys., 96(9):6796–6806, 1992.

[192] A. Halkier, T. Helgaker, P. Jørgensen, W. Klopper, and J. Olsen. Basis-set convergence of the energy in molecular hartree–fock calculations. Chem. Phys. Lett., 302:437–446, 1999.

[193] Y. Nishimura, T. Mizuguchi, M. Tsuji, S. Obara, and K. Morokuma. Theoretical studies on low-lying electronic states of the CCl^+, $SiCl^+$, and $GeCl^+$ ions. J. Chem. Phys., 78:7260–7264, 1983.

[194] Kirk A. Peterson and R. Claude Woods. An ab initio investigation of the spectroscopic properties of BCl, CS, CCl^+, BF, CO, CF^+, N_2, CN^-, and NO^+. J. Chem. Phys., 87:4409–4418, 1987.

[195] Kirk A. Peterson, R. Claude Woods, Pavel Rosmus, and Hans-Joachim Werner. Spectroscopic properties of the $X\,^1\Sigma^+$ and $a\,^3\Pi$ electronic states of CF^+, SiF^+, and CCl^+ by multireference configuration interaction. J. Chem. Phys., 93:1889–1894, 1990.

[196] Xiaomei Zhang, Hongsheng Zhai, Yufang Liu, and Jinfeng Sun. Extensive ab initio calculation on low-lying excited states of CCl^+ including spin-orbit interaction. J. Quant. Spectrosc. Radiat. Transfer, 119:23–31, 2013.

[197] Martin Gruebele, Mark Polak, Geoffrey A. Blake, and Richard J. Saykally. Determination of the born–oppenheimer potential function of CCl^+ by velocity modulation diode laser spectroscopy. J. Chem. Phys., 85:6276–6281, 1986.

[198] M. J. Frisch, G. W. Trucks, H. B. Schlegel, G. E. Scuseria, M. A. Robb, J. R. Cheeseman, G. Scalmani, V. Barone, G. A. Petersson, H. Nakatsuji, X. Li, M. Caricato, A. V. Marenich, J. Bloino, B. G. Janesko, R. Gomperts, B. Mennucci, H. P. Hratchian, J. V. Ortiz, A. F. Izmaylov, J. L. Sonnenberg, D. Williams-Young, F. Ding, F. Lipparini, F. Egidi, J. Goings, B. Peng, A. Petrone, T. Henderson, D. Ranasinghe, V. G. Zakrzewski, J. Gao, N. Rega, G. Zheng, W. Liang, M. Hada, M. Ehara, K. Toyota, R. Fukuda, J. Hasegawa, M. Ishida, T. Nakajima, Y. Honda, O. Kitao, H. Nakai, T. Vreven, K. Throssell, J. A. Montgomery, Jr., J. E. Peralta, F. Ogliaro, M. J. Bearpark, J. J. Heyd, E. N. Brothers, K. N. Kudin, V. N. Staroverov, T. A. Keith, R. Kobayashi, J. Normand, K. Raghavachari, A. P. Rendell, J. C. Burant, S. S. Iyengar, J. Tomasi, M. Cossi, J. M. Millam, M. Klene, C. Adamo, R. Cammi, J. W. Ochterski, R. L. Martin, K. Morokuma, O. Farkas, J. B. Foresman, and D. J. Fox. Gaussian 16 Revision A.03, 2016. Gaussian Inc. Wallingford CT.

[199] Robert M. Parrish, Lori A. Burns, Daniel G. A. Smith, Andrew C. Simmonett, A. Eugene DePrince III, Edward G. Hohenstein, Uğur Bozkaya, Alexander Yu. Sokolov, Roberto Di Remigio, Ryan M. Richard, Jérôme F. Gonthier, Andrew M. James, Harley R. McAlexander, Ashutosh Kumar, Masaaki Saitow, Xiao Wang, Benjamin P. Pritchard, Prakash Verma, Henry F. Schaefer III, Konrad Patkowski, Rollin A. King, Edward F. Valeev, Francesco A. Evangelista, Justin M. Turney, T. Daniel Crawford, and C. David Sherrill. Psi4 1.1: An open-source electronic structure program emphasizing automation, advanced libraries, and interoperability. J. Chem. Theory Comput., 13(7):3185–3197, 2017.

[200] I. Szabo and P. J. Derrick. Consective ion-molecule reactions in acetylene investigated by charge exchange mass spectrometry. Int. J. Mass. Spectrom. and Ion Phys., 7:55–69, 1971.

[201] H. I. Schiff and D. K. Bohme. An ion-molecule scheme for the synthesis of hydrocarbon-chain and organonitrogen molecules in dense interstellar clouds. Astrophys. J., 232:740–746, 1979.

[202] V. G. Anicich, W. T. Huntress Jr., and M. J. McEwan. Ion-molecule reactions of hydrocarbon ion in C_2H_2 and hcn. J. Phys. Chem., 90(2446-2450), 1986.

[203] D. Smith and N. G. Adams. Cyclic and linear isomers of $C_3H_2^+$ and $C_3H_3^+$: The $C_3H^+ + H_2$ reaction. Int. J. Mass. Spectrom. and Ion Proc., 76:307–317, 1987.

[204] S. W. McElvany. Reactions of carbon cluster ions with small hydrocarbons. J. Chem. Phys., 89(4):2063–2075, 1988.

[205] M. W. Wong and L. Radom. Thermochemistry and ion-molecule reactions of isomeric $C_3H_2^+$ cations. J. Am. Chem. Soc., 115:1507–1514, 1993.

Appendix A

Electronics circuit diagrams

Here are the most recently updated drawings of the circuit diagrams used in the experiment. With the exception of the DC shim box, these circuits are not laid out on printed circuit boards (PCBs).

A.1 Ion trap driver

The heart of the ion trap driver is a resonant step-up transformer coil. The primary side (three windings) trades high-current for high-voltage into two secondary sides, which are hand-wound in a bifilar arrangement (26 windings, each) around a toroidal core (Mircometal, T200-2). The secondary sides are center-tapped so that two, high-amplitude RF voltages are produced 180 degrees out of phase. A drawing of the ion trap driver is shown in Fig. A.1. High-Q, shim inductors ($\sim$100 nH) are hand soldered in line with some of the four, transformer secondary side outputs to balance the RF amplitude of each phase. 12 SHV cables ($\sim$30 pF/foot) deliver the high voltage to the trap via vacuum feedthroughs. These constitute almost the entirety of the capacitive trap load.

DC blocking capacitors are in series between the rods and the RF transformer. They prevent the DC shim voltages from finding their way to the cener-taps (nominally ground). The DC shim voltages are coupled to the rod output via a 1 MΩ resistor. There is an added buffer cap to create a low-pass filter for RF traveling back to the DC shim box. This is not strictly needed as the 1 MΩ resistor effectively blocks the low-current RF.

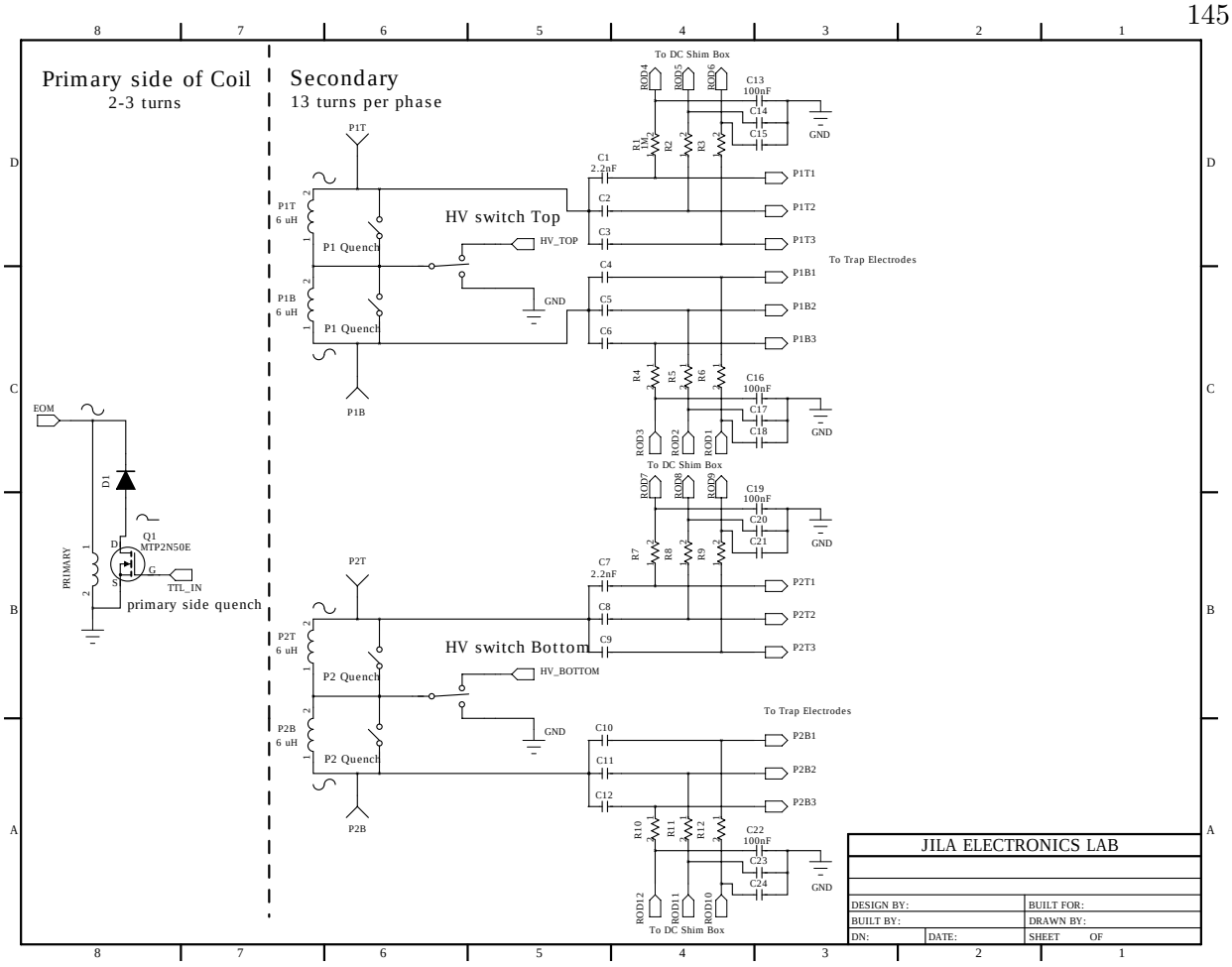

Figure A.1: Main RF driver for the ion trap. Primary and secondary sides of the step-up transformer are separated by the dashed line. The quench boards and high-voltage switches are represented schematically as two and three-way switches, respectively. Connections to the DC shim box are also labeled.

A.2 HV switches and quench boards

The HV switches and RF quench boards are needed to convert the ion trap electrodes from a trap to the repeller and extractor of a TOFMS. The RF quench shorts the secondary sides of the main transformer to the center-tap, removing the high-voltage RF quickly. The gates drivers (MIC 4420) of the main fets that short the coil must float up with the center-tap to HV DC. The way we accomplish this is by floating a battery up with the center-tap. This provides HV + 12V with

extremely low current noise. The batteries we use are recharchable (Tenergy NiMH 12V 2000mAh), and have enough capacity to last at least 12 hours of continuous experimental runs. We used to use DC-DC converters to provide the floating power. These are based on switch mode power supplies which provide continous power and are isolated via a transformer. Unfortunately, the switching frequency of almost all comercially available supplies is around 100 kHz. This produces RF noise capable of exciting secular resonances of our ions, which is unacceptable. In principle, one could return to a switch-mode power supply solution that was home-made if the frequency is >1 MHz.

The High voltage switches then pulse high voltage DC onto the ion trap rods. This is accomplished using a push-pull configuration of two N-channel Power mosfets (IXTL2N450). High current for fast switching is provided by the two series buffer capacitors. There are two copies of the circuit in Fig. A.2, one for each secondary winding. Each has a separate battery pack and high voltage power supply to provide different repeller and extractor voltages.

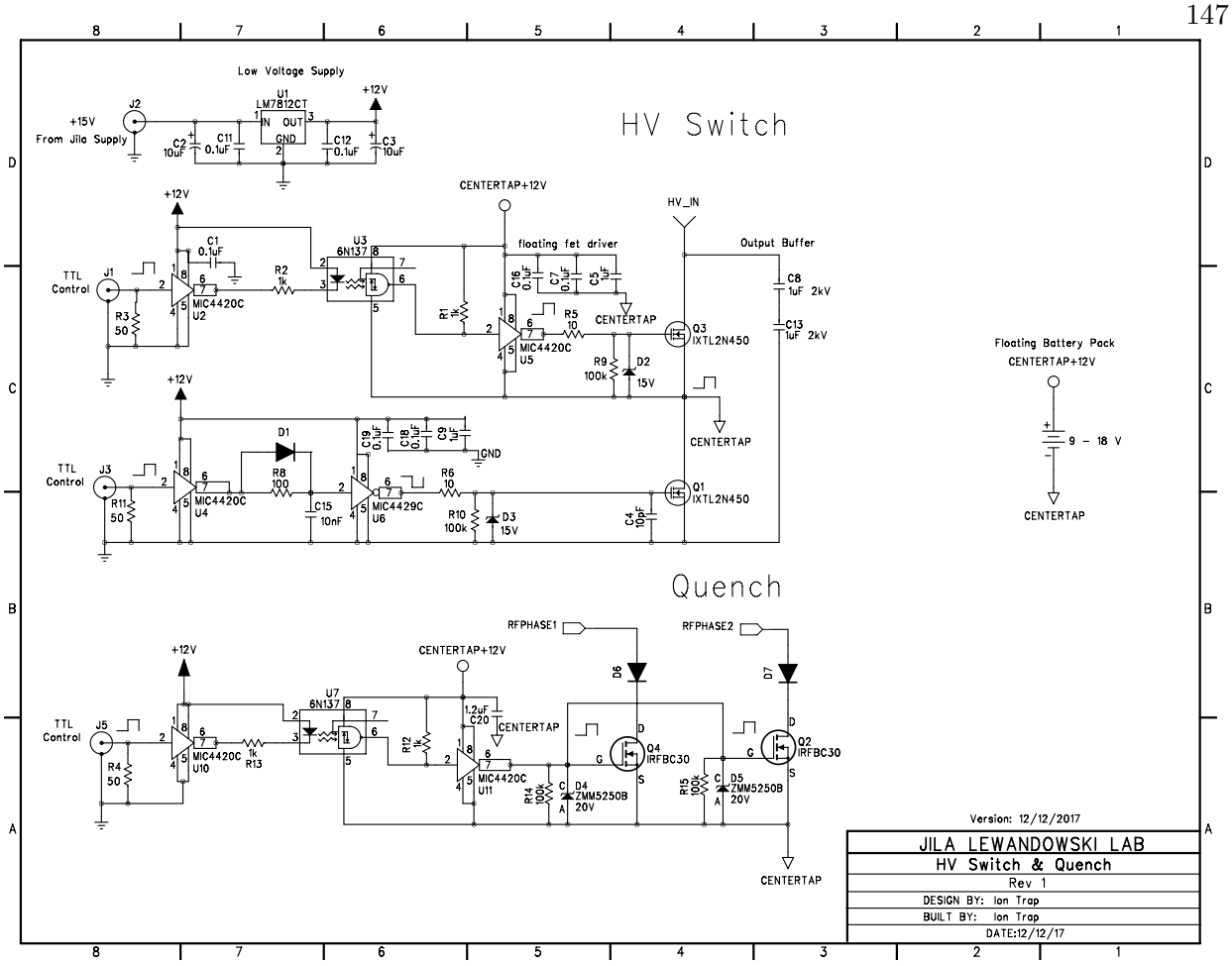

Figure A.2: High voltage switches and quench circuit diagrams. The floating power supply is a 12VDC NIHM battery pack that rests on a glass plate to allow it to float up to 2kV.

A.3 DC shim box

DC shim voltages are required to overlap the geometric center of the trap and the RF node. DC voltages are also required to produce the axial trapping potential. These voltages are supplied by the DC shim box to the trap rods through the main RF amplifier. The output voltages for groupings of rods are adjusted simultaneously by the potentiometers mounted on the front of the DC shim box. The potentiometer for the endcap voltages (axial trapping potential) has been replaced by the analog output of a NI-DAQ box. This enables digital, programatic control over the endcap potential. These control voltages are sent through a buffer circuit, one for each of the eight

potentiometers, before the control voltage is sent to the summing matrix.

The heart of the shim box is a big array of resistors leading to 12 summing op-amp circuits, one for each trap rod segment. The resistors feeding into a summing amp divides the control voltage from the potentiometer before being added. $100k\Omega \rightarrow 1\times$ and $200k\Omega \rightarrow 0.5\times$ the input voltage. The full voltage is for pots that provide 0–10V (pots 1, 4, 5, and 6). The halved voltages are for potentiometers that provide -5–5V (pots 2, 3, 7, and 8). The summing amps add the input control voltages to create the final output voltage for a rod segment. There is relatively little cross-talk, but just enough to notice with the ions. Even mV can affect the ion cloud position on the micron-scale. The summing amps also have an added current buffer on their output to provide quiet, stable DC voltages. Lots of buffer caps are used in this circuit to minimize AC noise. They are all picked to have minimal ESR.

All the amps are laid out on a PCB. The circuit diagram is shown in Fig. A.3. There is a solitary mistake on the PCB layout in the box power buffer amp. This is documented in the lab notebook.

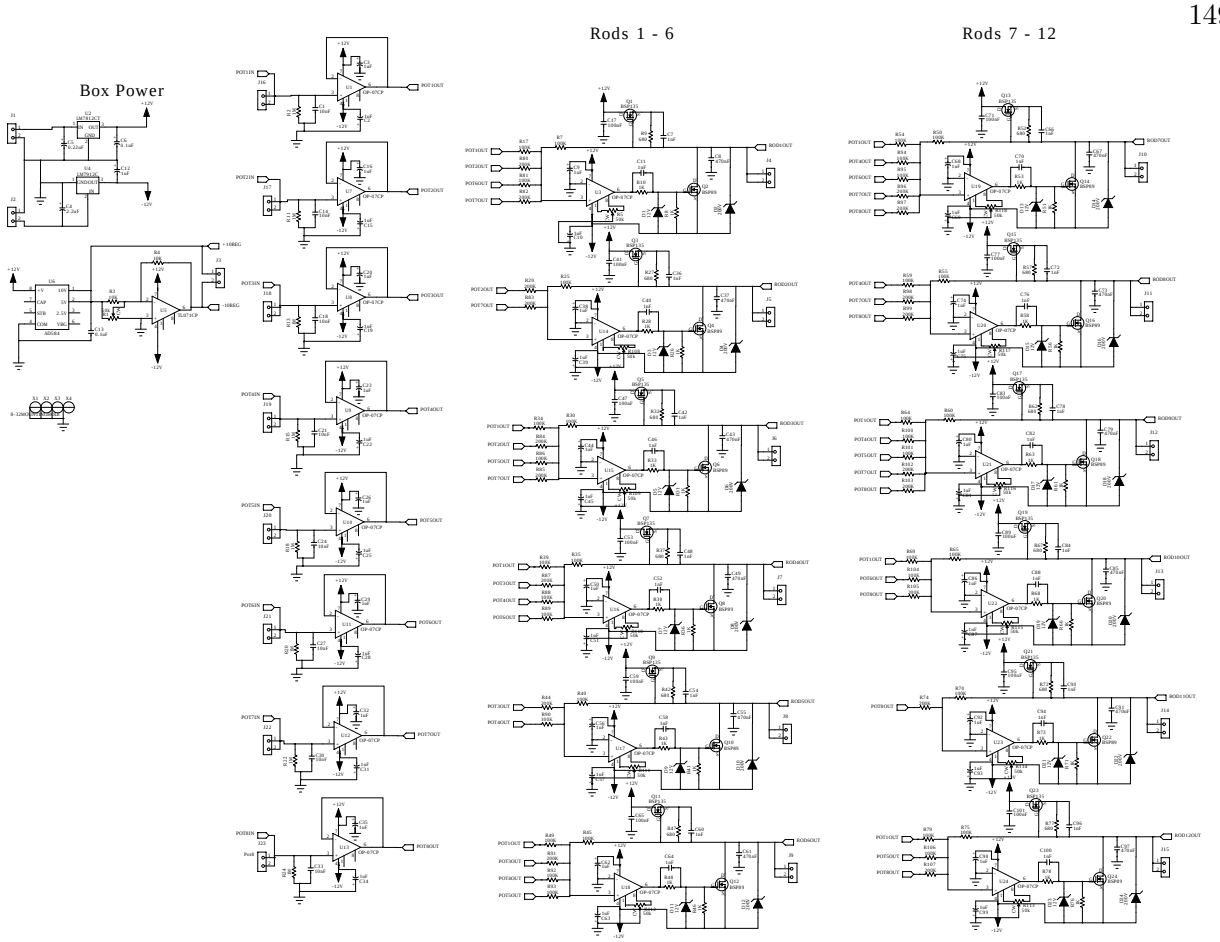

Figure A.3: Circuit diagra for DC shim box PCB. Buffer amps for potentiometer control voltages feed into the summing matrix via dividing resistors. The summing amps then generate the buffered DC voltages that are applied to the rods.

A.4 RF secular excitation

RF secular excitations are used to eject specific masses from the ion trap. They are sinusoidal frequency sweeps generated by two SRS DS345 function generators. A mini-circuits RF splitter/combiner combines the two signals into a single BNC which is coupled to one of the secondary center-taps via a HV solid state relay. The relay protects the function generators from the HV pulse used for ion extraction into the TOFMS. A schematic (hand) drawing of the circuit is shown in Fig. A.4. A time profile of the excitation sequence is given in Fig. A.5.

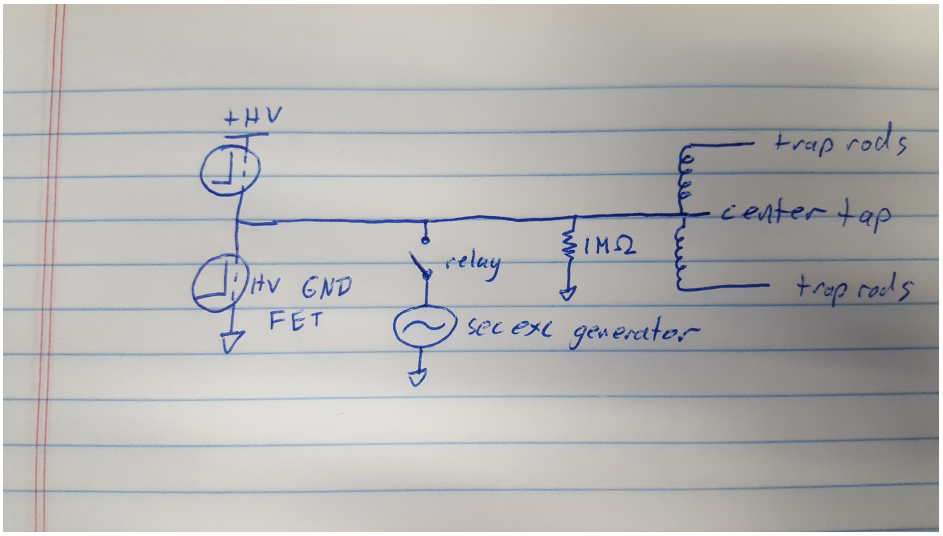

Figure A.4: Secular excitation relay circuit schematic.

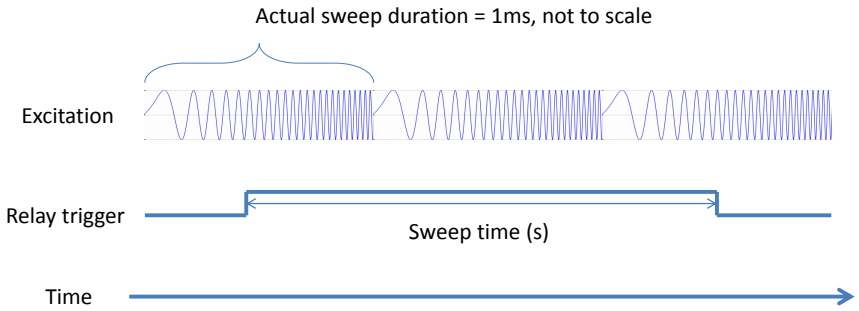

Figure A.5: Time sequence of the secular excitation and control trigger.

Appendix B

Labview control and automation

B.1 Automation

Automation is essential to the success of any experiment. People can't be trusted to reliably reproduce experiments from run to run and we rely on the help of electronics and computer controlled hardware to pull of insanely complicated things like trapping and laser cooling of ions in vacuum. To prove this point, Fig. B.1 is a block diagram of most of the actively controlled components

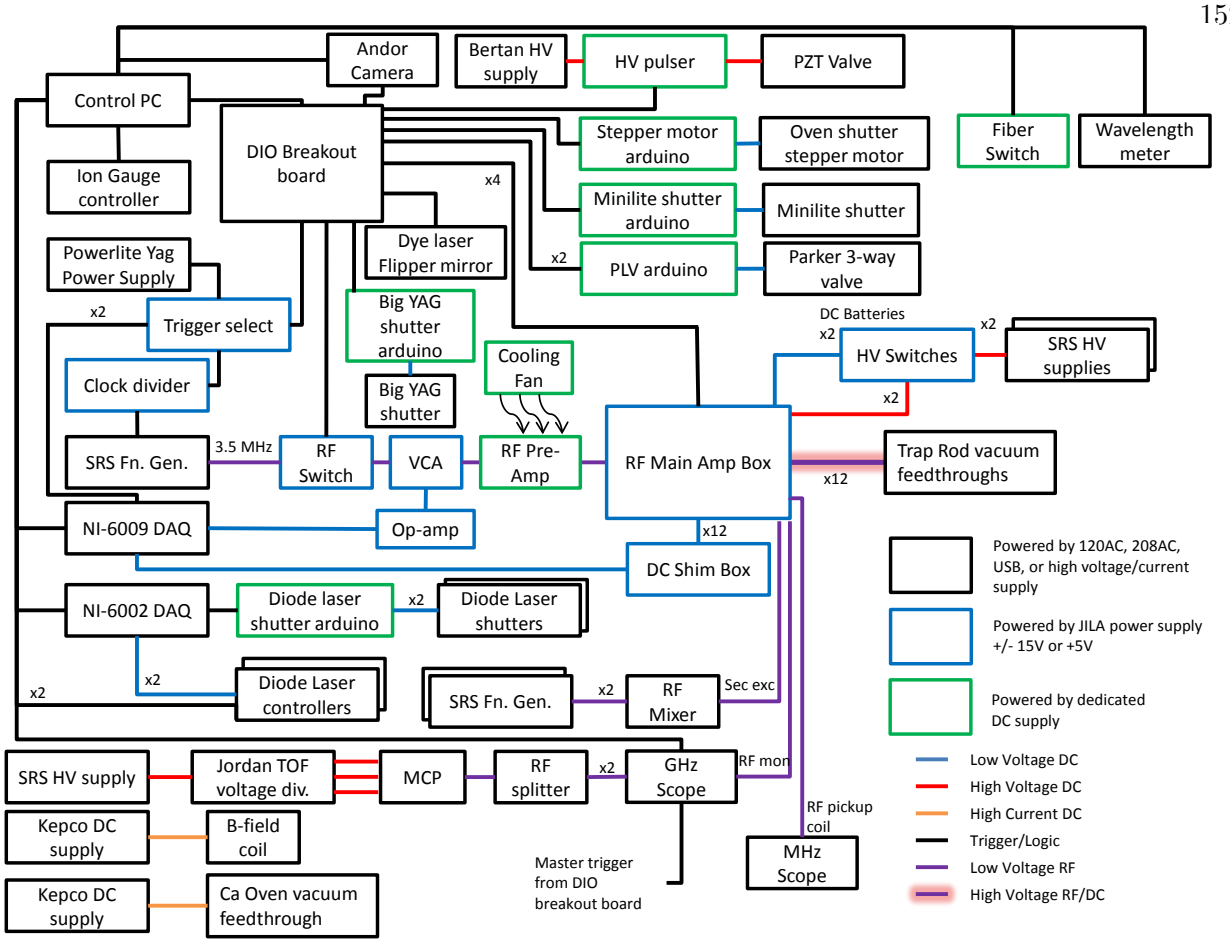

Figure B.1: Block diagram of all the control electronics in the experiment.

Automation of the experiment has other benefits as well. For example the experiment runs faster. An experiment has to run faster than any uncontrolled long term-drifts in conditions. Automation also allows for active feedback (servo) on long term-drifts that are too quick for experimental timescales. There is also, of course, the practical benefit of being less work. But let's be real, you'll spend that time doing something else and ultimately just doing more, and that's a good thing!

B.2 Labview control code

I want to say a few words about the philosophy behind the control code and some best practices that will serve you into the future when working with it. Great care was taken to

minimize the amount of work and headaches that you, dear reader, will have to experience in the future.

There is no way to future proof experimental control code. As new people and ideas come in and out of the lab, the experiment will change and the control code will have to adapt accordingly. This can easily produce a problem with version control. As edits are made to the code, one will have to carefully track which version of the code went with which state of the experiment. This is impossible. I have watched many try and fail to pull-off good version control but this system will, without fail, break down. So if you can't predict the future perfectly or keep good enough track of what has happened in the past, what recourse do you have?

The solution I have implemented relies on a philosophy of additive coding. Change nothing, only add new features. There is only one version of the code that grows ever larger as the demands of the experiment change. When slight changes are needed, resist the urge to make them on functioning code. Copy and paste it with a new name and add it to the library of other functions. If you can adhere to this original vision, I believe you will be rewarded.

B.2.1 Producer consumer architecture

To help make the additive coding philosophy a reality, the code had to be built on an architecture. This is something that all real coders do for every project. For some reason, doing this in labview is viewed as noteworthy. The architecture I have chosen is called a producer consumer architecture.

Since labview is a graphical programming language, the producer consumer architecture is represented graphically by a vertical stack of parallel (not nested!!) while loops. The general flow of data is from top to bottom. Data is generated in the top loop, to be handled by the next loop down, which can further down another loop on for more handling *ad infinitum*. In practice, I never needed to use more than three loops. The first handles user input. This passes instructions to hardware which are carried out by the second loop. If the hardware generated data that needs to be saved, it is passed to a third loop that does the actual saving.

All data/instuctions are passed from one loop to the next in the form of messages on queues. A message consists of a one word instruction (string) and can optionally carry with it any amount of data (cluster). A queue is an object that stores messages. It functions like a first-in, first-out (FIFO) buffer. This allows the loops to handle tasks asynchronously. That's a nice feature for a program that is supposed to control hardware. If you need to interrupt what the program is doing, you can add a command to the front of the queue (priority message) which is then handled next. Make sure the task associated with each message is small enough that the program doesn't ever get hung up. Never include a while loop in your tasks. This will ensure that the control code is always ready to respond to new user inputs.

Ultimately, to run the experiment, one wants to generate a list of tasks and have it carry out these tasks in-order and potentially repetitively. This is exactly what scripting languages are designed to do. Since labview is not a scripting language (runs functions simultaneously and asynchronously) I had to do my best to implement a script-like interface. The way it works is there is a table which all the details of your script are written in. Each pair of lines in the table is a task, which I call a step. Each task has a name and can have an arbitrary number of parameters names with it that are the first line. The second line are the values that go along with the named parameters. A series of these steps build an experimental script, which I call a sequence. The sequence table can be saved, loaded, and edited, in both labview and in any text editor (even in excel). Running the sequence repetitively is called a scan. You can have the program change sequence values automatically as it runs the scan. The parameters of the scan are stored in a separate scan table. All of this functionality is in the main brain module, and hopefully will never need to be written again.

B.2.2 Code hierarchy

I wanted to be able to run each piece of hardware (or small groups of hardware) used in the experiment, individually. I also wanted to be able to stop a VI and add functionality to it while other pieces of hardware were still running. This mean I had to build a system of modular VIs

that can talk to one another, but don't rely on one another. This is exactly what I did. It is roughly structured like this: Each piece of hardware has its own module (VI). Each module is an independent producer-consumer system with a queue to pass messages from the front panel controls to the hardware it is supposed to run. To allow the modules to talk to one another, the queues are made to be functional global variables (also called an action engine). This allows any module to load messages onto any other modules queue, and thus control them programatically. The only module that utilizes the ability to talk to other modules is the main brain module aside from one or two exceptions.

Fig. B.2 is a flowchart of each module and the hardware they control. This was done from memory so please excuse errors or omissions. When something goes wrong or you need new functionality, it should point you to the correct VI.

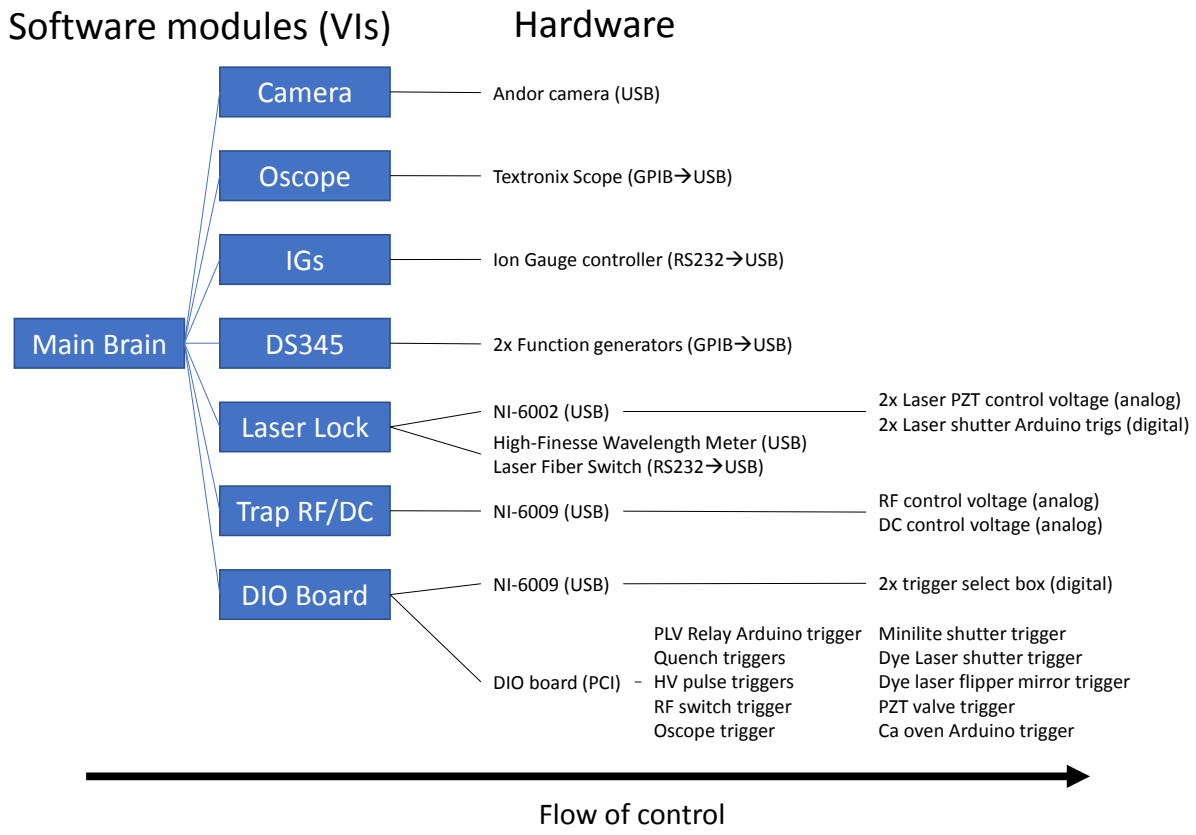

Figure B.2: Block diagram of all VI modules and what hardware they each control.

You may also find in the project file some extra, legacy modules that have been retired. The save and launcher modules had nasty bugs associated with them. Now main brain handles all save features and you can launch the module VIs by hand. Speaking of saving, everything is written to an HDF5 file. That stands for hierarchical data format, and is exactly that. It is a clever way to store multiple data types in the same data file with common, named headings that make them easy to access later. Gone are the days of counting header lines. Now you just call your dataset or attributes by name. As an added bonus, they are stored in binary and can make use of compression. This is perfect for our experiment which typically generates two images and 4 scope traces worth of data ($\sim$ 7 MB) per shot. The compressed binary HDF5 files usually are only 1.5 MB.

The same additive philosophy should be applied to the HDF5 file structure. If you are

generating data from a new source, or want to organize data from an old source in a different way, make a new folder/dataset for it! This will allow old anylsis code to be compatible with your new file structure.

B.2.3 How to add a step

To add functionality to a module, you need to make a new button on the front panel. This button will then need to generate an event in the producer loop. This event will then add a new, unique message to the consumer loop queue. The consumer loop queue will then need a new case with a name identical to the message added to the queue. The functionality is then added to the new case with the new message name. If any data needs to be included in the message –like the value of a parameter– a control must be added to the front panel with a name corresponding to that of the parameter. The parameter must then be added to the VIs type definition. The value of the parameter is then added to the message generation event. The value can then be pulled from the message using the variant-to-data VI with the type definition being fed into its data-type input. The output cluster can be un-bundled by name with the name of the control corresponding to the parameter. The value is then available to the case where the new message is being handled.

To call this new step from main brain, one has to edit two .cfg files that are in the same directory as main brain. The “main brain steps.cfg” and the “main brain step timings.cfg” are loaded by main brain when the VI is run. The first .cfg file is how the table auto-populates with parameters and default values when you add a step. The second is how main brain knows how long a step takes when running a sequence.

B.2.4 How to add a module

Use the module template found in the labview project file. Open communication to the new hardware to the left of the producer and consumer loops, and close it to the right. Make new functional global variables for any queues needed (probably only one). Follow the instructions above to add steps and also make them available to main brain.

One additional step is needed to add the new module to main brain. A call to the new queue must be added by hand along with the type-def for the new module in the "run step" sub-VI. This only needs to be done once. After the run step knows about your new global queue, it can send it any message you decide to generate in the future.

Appendix C

MATLAB analysis code

C.1 OBE global fit and model

Described in Ch. 3 is the procedure to calibrate the OBE model to fluorescence data measured by the experiment. The hierarchy of code is as follows: A script, *OBEalldatafit.m*, is used to format all of the data. It then calls the global fit function,*pop8fit.m*, to produce the calibration parameters. The parameters are then fed into *pop8model.m*, to predict the state populations. These three files are reproduced below.

OBEalldatafit.m

```
% close all
clear all
% xvar = [p397 p866 d397 d866 alpha]
% x0,k = [c397 c866 L397 L866 B_mag]
% note: laser detuning in this analysis defined as delta = w_laser - w_0
% this is a holdover from the Gingell thesis

% These functions pull and format raw data from their respective
% measurement files
[det397x,det397y] = detuningscan397();
[det866x,det866y] = detuningscan866();
[pwr866x,pwr866y] = powerscan866();
[pwr397x,pwr397y] = powerscan397();
[alphax,alphay] = alphascan();

% vectorize and normalize data for global fit
xdata = [det397x;det866x;pwr866x;pwr397x;alphax];
ydata = [det397y;det866y;pwr866y;pwr397y;alphay];
norm = max(ydata);
ydata = ydata/norm;

x0 = [1,1,6,12,3];
[k,~,resid,~,~,~,J]  = lsqcurvefit(@pop8fit,x0,xdata,ydata);
kfit = k';
ci = nlparci(kfit,resid,'jacobian',J,'alpha',0.10);
kunc = abs(ci(:,1)-ci(:,2))./2;
```

```
% build table to report fit params
param = {'c397';'c866';'L397';'L866';'B_mag'};
unit = {'none';'none';'MHz';'MHz';'Gauss'};
T=table(param,unit,kfit,kunc)

out = pop8model(k,xdata);
maxp = max(out(:,2));

% plot s,d,p-states vs blue detuning
figure
plot(det397x(:,3),pop8model(k,det397x))
legend('S','P','D');
title('397 detuning scan')
ylabel('State Populations (%)')
xlabel('\Delta_{397} (MHz)')

% plot all data and fits
figure
hold on
plot(det397x(:,3),maxp*det397y/norm,'ko')
det397model = pop8model(k,det397x);
plot(det397x(:,3),det397model(:,2),'r-')
title('397 detuning scan')
ylabel('P-State Population (%)')
xlabel('\Delta_{397} (MHz)')

figure
hold on
plot(det866x(:,4),maxp*det866y/norm,'ko')
det866model = pop8model(k,det866x);
plot(det866x(:,4),det866model(:,2),'r-')
title('866 detuning scan')
ylabel('P-State Population (%)')
xlabel('\Delta_{866} (MHz)')

figure
hold on
plot(pwr866x(:,2),maxp*pwr866y/norm,'ko')
pwr866model = pop8model(k,pwr866x);
plot(pwr866x(:,2),pwr866model(:,2),'r-')
title('866 power scan')
ylabel('P-State Population (%)')
xlabel('866 nm power before chamber (mW)')

figure
hold on
plot(pwr397x(:,1),maxp*pwr397y/norm,'ko')
pwr397model = pop8model(k,pwr397x);
plot(pwr397x(:,1),pwr397model(:,2),'r-')
title('397 power scan')
ylabel('P-State Population (%)')
xlabel('397 nm power in front beam before chamber (mW)')

figure
hold on
plot(alphax(:,5),maxp*alphay/norm,'ko')
alphamodel = pop8model(k,alphax);
plot(alphax(:,5),alphamodel(:,2),'r-')
title('\alpha scan')
```

```
ylabel('P-State Population (%)')
xlabel('\alpha (rad)')

% plot fluorescence vs p-state
figure
lb = [0,0];
ub = [Inf,0];
pvsffit = fit(ydata*norm,out(:,2),'poly1','Lower',lb,'Upper',ub);
plot(pvsffit,ydata*norm,out(:,2),'k.')
ylabel('P-state population (%)')
xlabel('BG subtracted fluorescence')
```

pop8fit.m

```
function [ppop] = pop8fit(params,vars)
% note: laser detuning in this analysis defined as delta = w_laser - w_0
% this is a holdover from the Gingell thesis code at the core of the
% analysis. I.e.: delta_analysis = -1*delta_literature
% Program to calculate the steady state populations of a trapped
% Ca+ ion in interaction with two coherent light fields, assuming
% 8 sub-levels. Calculations are made with the assumption that
% the magnetic field is perpendicular to the propagation
% direction of the lasers at angle alpha to their polarizations.
%% Laser Waists
% 1/e^2 area of blue/red in mm^2
A397 = 0.34^2*pi*1e-6; %mm^2 -> m^2 area @ 397 nm
A866 = 1.17^2*pi*1e-6; %mm^2 -> m^2 area @ 866 nm

%% Variable inputs and outputs (measured from experiment)
ppop = zeros(size(vars,1),1);
for jj = 1:size(vars,1)
    P397 = vars(jj,1); % 397nm power in mW
    P866 = vars(jj,2); % 868nm power in mW
    detb = vars(jj,3); % 397 detuning in MHz (red detune is positive)
    detr = vars(jj,4); % 866 detuning in MHz (red detune is positive)
    alpha = vars(jj,5);% angle between B-field and 866 polarization axes in
     ↪  radians
%% Model parameters (to be fit)
    c1 = params(1); % Scale factor for effective 397nm intensity
    c2 = params(2); % Scale factor for effective 866nm intensity
    l1 = params(3); % Linewidth of 397nm Diode Laser (MHz)
    l2 = params(4); % Linewidth of 866nm Diode Laser (MHz)
    B = params(5);  % B-field magnitude in gauss
%% Constants
    h = 6.626068e-34; hbar = h/(2*pi); % J*s
    ub = 9.74e-24; % bohr magneton in J/T
    g1 = 1e-6/7.7e-9;%Ca+ P->S Decay Constant MHz
    g2 = 1e-6/94.3e-9;%Ca+ P->D Decay Constant MHz
%% Generation of Rabi Frequencies from Laser Power Data
    I12 = c1*1e-3*P397/A397; % Effective intensity in Wm^-2
    I32 = c2*1e-3*P866/A866; % Effective intensity in Wm^-2
    O12 = rabi8(I12,1);
    O23 = rabi8(I32,2);
%% Conversion/Consolidation of Data with units of Frequency
    %Detunings converted to angular Mhz
    D1 = 2*pi*detb;
    D2 = 2*pi*detr;
    %Laser Linewidths
```

```
    l1 = 2*pi*l1; %Laser linewidths input in USER DATA in khz
    l2 = 2*pi*l2; %and converted to angular Mhz
    %B-field splitting
    u = 1e-6*1e-4*B*ub/hbar;
%% MAIN STEADY STATE CALCULATION
    %In the steady state, L*rho = 0
    %To enforce the correct normalisation we replace
    %one equation with the normalisation condition
    L = M8(O12,O23,D1,D2,l1,l2,g1,g2,u,alpha);
    L(1,:) = 0;
    L(1,1:9:64) = 1;
    x = zeros(64,1); x(1) = 1;
    rhoSS = L\x;
    popSS = diag(real(reshape(rhoSS,8,8)));
    popSS = 100.*popSS./sum(popSS);
    % N1 = (popSS(1) + popSS(2));   % S-state pop
    N2 = (popSS(3) + popSS(4));     % P-state pop
    % N3 = (popSS(5) + popSS(6) + popSS(7) + popSS(8)); % D-state pop
    % Espop = N2+N3;                % P + D-state pop
    %% Designate output
    ppop(jj) = N2; % normalize to P-max so intensity data can be fit
end
pmax = max(ppop);
ppop = ppop/pmax;
ppop(vars(jj,3)<=0) = 1e-6;

end

%% Function to calculate Rabi frequency
% function omega = rabi(I,which)%3-level
function omega = rabi8(I,which)%8-level
%I = Intensity in Wm^-2
%which = 1 for 397 nm, 2 for 866 nm
c = 299792458; % M/s
h = 6.626068e-34; hbar = h/(2*pi);
switch which
case 1 %397 nm laser
wl = 1/(25191.51e2);
lt = 7.7e-9; %natural lifetime
case 2 %866 nm laser
wl = 1/(25191.52e2 - 13650.19e2);
lt = 94.3e-9; %natural lifetime
end
g = 1/lt; %Spontaneous decay rate in Hz
omega = sqrt((3 * I * wl^3 * g)/(16 * pi^2 * c * hbar));%8-level
omega = omega/(1e6); % Angular Mhz
end

%% Formation of Liouvillian Matrix
% Density matrix treatment of 8 level atom in a magnetic field
function L=M8(O1,O2,D1,D2,l1,l2,g1,g2,u,alpha)
gS=2; gP=2/3; gD=4/5; % Lande factors
c=cos(alpha); s=sin(alpha); w3=3^0.5; E=eye(8);
ii=(1:8)'*ones(1,8); i1=reshape(ii',1,64); % first index
i2=reshape(ii,1,64); % second index
H=diag([D1,D1,0,0,D2,D2,D2,D2]+0.5*u*[-gS,gS,-gP,gP,-3*gD,-gD,gD,3*gD]);
HSP=-O1/w3*[ -c s ; s c ];
HDP=-O2/2/w3*[ w3*s 0 ; 2*c s ; -s 2*c ; 0 -w3*s ];
H(1:2,3:4)=HSP; H(3:4,1:2)=HSP'; H(5:8,3:4)=HDP; H(3:4,5:8)=HDP';
% Relaxation
```

```
C1=(2/3*g1)^0.5*E(:,1)*E(4,:);
C2=(2/3*g1)^0.5*E(:,2)*E(3,:);
C3=(1/3*g1)^0.5*(E(:,1)*E(3,:)-E(:,2)*E(4,:));
C4=(1/2*g2)^0.5*E(:,5)*E(3,:)+(1/6*g2)^0.5*E(:,6)*E(4,:);
C5=(1/6*g2)^0.5*E(:,7)*E(3,:)+(1/2*g2)^0.5*E(:,8)*E(4,:);
C6=(1/3*g2)^0.5*(E(:,6)*E(3,:)+E(:,7)*E(4,:));
C7=(2*l1)^0.5*(E(:,1)*E(1,:)+E(:,2)*E(2,:));
C8=(2*l2)^0.5*(E(:,5)*E(5,:)+E(:,6)*E(6,:)+...
E(:,7)*E(7,:)+E(:,8)*E(8,:));
CC=(C1'*C1+C2'*C2+C3'*C3+C4'*C4+C5'*C5+C6'*C6+C7'*C7+C8'*C8);
% Form effective Hamiltonian and Liouvillian
H=H-1i/2*CC; L = -1i*(kron(H,E) - kron(E,H'));
% Add feeding terms
L=L+C1(i1,i1).*C1(i2,i2); L=L+C2(i1,i1).*C2(i2,i2);
L=L+C3(i1,i1).*C3(i2,i2); L=L+C4(i1,i1).*C4(i2,i2);
L=L+C5(i1,i1).*C5(i2,i2); L=L+C6(i1,i1).*C6(i2,i2);
L=L+C7(i1,i1).*C7(i2,i2); L=L+C8(i1,i1).*C8(i2,i2);
end
```

pop8model.m

```
function [out] = pop8model(params,vars)
% Program to calculate the steady state populations of a trapped
% Ca+ ion in interaction with two coherent light fields, assuming
% 8 sub-levels. Calculations are made with the assumption that
% the magnetic field is perpendicular to the propagation
% direction of the lasers at angle alpha to their polarizations.
%% Laser Waists
% 1/e^2 area of blue/red in mm^2
A397 = 0.34^2*pi*1e-6; %mm^2 -> m^2 area @ 397 nm
A866 = 1.17^2*pi*1e-6; %mm^2 -> m^2 area @ 866 nm

%% Variable inputs and outputs (measured from experiment)
spop = zeros(size(vars,1),1);
ppop = zeros(size(vars,1),1);
dpop = zeros(size(vars,1),1);
for jj = 1:size(vars,1)
    P397 = vars(jj,1); % 397nm power in mW
    P866 = vars(jj,2); % 868nm power in mW
    detb = vars(jj,3); % 397 detuning in MHz (red detune is positive)
    detr = vars(jj,4); % 866 detuning in MHz (red detune is positive)
    alpha = vars(jj,5);% angle between B-field and 866 polarization axes in
    ↪  radians
%% Model parameters (to be fit)
    c1 = params(1); % Scale factor for effective 397nm intensity
    c2 = params(2); % Scale factor for effective 866nm intensity
    l1 = params(3); % Linewidth of 397nm Diode Laser (MHz)
    l2 = params(4); % Linewidth of 866nm Diode Laser (MHz)
    B = params(5);  % B-field magnitude in gauss
%% Constants
    h = 6.626068e-34; hbar = h/(2*pi); % J*s
    ub = 9.74e-24; % bohr magneton in J/T
    g1 = 1e-6/7.7e-9;%Ca+ P->S Decay Constant MHz
    g2 = 1e-6/94.3e-9;%Ca+ P->D Decay Constant MHz
%% Generation of Rabi Frequencies from Laser Power Data
    I12 = c1*1e-3*P397/A397; % Effective intensity in Wm^-2
    I32 = c2*1e-3*P866/A866; % Effective intensity in Wm^-2
    O12 = rabi8(I12,1);
```

```
    O23 = rabi8(I32,2);
%% Conversion/Consolidation of Data with units of Frequency
    %Detunings converted to angular Mhz
    D1 = 2*pi*detb;
    D2 = 2*pi*detr;
    %Laser Linewidths
    l1 = 2*pi*l1; %Laser linewidths input in USER DATA in khz
    l2 = 2*pi*l2; %and converted to angular Mhz
    %B-field splitting
    u = 1e-6*1e-4*B*ub/hbar;
%% MAIN STEADY STATE CALCULATION
    %In the steady state, L*rho = 0
    %To enforce the correct normalisation we replace
    %one equation with the normalisation condition
    L = M8(O12,O23,D1,D2,l1,l2,g1,g2,u,alpha);
    L(1,:) = 0;
    L(1,1:9:64) = 1;
    x = zeros(64,1); x(1) = 1;
    rhoSS = L\x;
    popSS = diag(real(reshape(rhoSS,8,8)));
    popSS = 100.*popSS./sum(popSS);
    N1 = (popSS(1) + popSS(2));   % S-state pop
    N2 = (popSS(3) + popSS(4));     % P-state pop
    N3 = (popSS(5) + popSS(6) + popSS(7) + popSS(8)); % D-state pop
    % Espop = N2+N3;                % P + D-state pop
    %% Designate output
    spop(jj) = N1;
    ppop(jj) = N2;
    dpop(jj) = N3;
end
    out = [spop,ppop,dpop];

end

%% Function to calculate Rabi frequency
% function omega = rabi(I,which)%3-level
function omega = rabi8(I,which)%8-level
%I = Intensity in Wm^-2
%which = 1 for 397 nm, 2 for 866 nm
c = 299792458; % M/s
h = 6.626068e-34; hbar = h/(2*pi);
switch which
case 1 %397 nm laser
wl = 1/(25191.51e2);
lt = 7.7e-9; %natural lifetime
case 2 %866 nm laser
wl = 1/(25191.52e2 - 13650.19e2);
lt = 94.3e-9; %natural lifetime
end
g = 1/lt; %Spontaneous decay rate in Hz
omega = sqrt((3 * I * wl^3 * g)/(16 * pi^2 * c * hbar));%8-level
omega = omega/(1e6); % Angular Mhz
end

%% Formation of Liouvillian Matrix
% Density matrix treatment of 8 level atom in a magnetic field
function L=M8(O1,O2,D1,D2,l1,l2,g1,g2,u,alpha)
gS=2; gP=2/3; gD=4/5; % Lande factors
c=cos(alpha); s=sin(alpha); w3=3^0.5; E=eye(8);
ii=(1:8)'*ones(1,8); i1=reshape(ii',1,64); % first index
```

```
i2=reshape(ii,1,64); % second index
H=diag([D1,D1,0,0,D2,D2,D2,D2]+0.5*u*[-gS,gS,-gP,gP,-3*gD,-gD,gD,3*gD]);
HSP=-O1/w3*[ -c s ; s c ];
HDP=-O2/2/w3*[ w3*s 0 ; 2*c s ; -s 2*c ; 0 -w3*s ];
H(1:2,3:4)=HSP; H(3:4,1:2)=HSP'; H(5:8,3:4)=HDP; H(3:4,5:8)=HDP';
% Relaxation
C1=(2/3*g1)^0.5*E(:,1)*E(4,:);
C2=(2/3*g1)^0.5*E(:,2)*E(3,:);
C3=(1/3*g1)^0.5*(E(:,1)*E(3,:)-E(:,2)*E(4,:));
C4=(1/2*g2)^0.5*E(:,5)*E(3,:)+(1/6*g2)^0.5*E(:,6)*E(4,:);
C5=(1/6*g2)^0.5*E(:,7)*E(3,:)+(1/2*g2)^0.5*E(:,8)*E(4,:);
C6=(1/3*g2)^0.5*(E(:,6)*E(3,:)+E(:,7)*E(4,:));
C7=(2*l1)^0.5*(E(:,1)*E(1,:)+E(:,2)*E(2,:));
C8=(2*l2)^0.5*(E(:,5)*E(5,:)+E(:,6)*E(6,:)+...
E(:,7)*E(7,:)+E(:,8)*E(8,:));
CC=(C1'*C1+C2'*C2+C3'*C3+C4'*C4+C5'*C5+C6'*C6+C7'*C7+C8'*C8);
% Form effective Hamiltonian and Liouvillian
H=H-1i/2*CC; L = -1i*(kron(H,E) - kron(E,H'));
% Add feeding terms
L=L+C1(i1,i1).*C1(i2,i2); L=L+C2(i1,i1).*C2(i2,i2);
L=L+C3(i1,i1).*C3(i2,i2); L=L+C4(i1,i1).*C4(i2,i2);
L=L+C5(i1,i1).*C5(i2,i2); L=L+C6(i1,i1).*C6(i2,i2);
L=L+C7(i1,i1).*C7(i2,i2); L=L+C8(i1,i1).*C8(i2,i2);
end
```

C.2 Reaction model fits

Described in Ch. 2 are the kinetic rate equations for pseudo-first order reactions. In the experiment, we often see a nasty mess of reaction pathways that do not have easy to work with analytic solutions. This can make fitting your data to extract rates a pain. So we rely on MATLAB's ode45 integrator to do the heavy lifting. If the reaction pathways are known, you can write down the set of coupled differential equations to fit your data to. Then it must be properly vectorized to make use of the ode45 integrator. After doing so, the set of differential equations can be passed to a non-linear, least squares, curve-fitting routine to extract rates and confidence intervals. Below is an example of this procedure used to analyze the $Ca^+ + O_2$ reaction presented in Ch. 4 and [39].

The hierarchy of code is as follows: A script, *O2analysis8level.m*, is used to format all of the data. It then calls the model fit function, *O2fit.m*. The model fit function then calls the set of differential equations defined in *O2model.m*. These three files are reproduced below.

O2analysis8level.m

```
clear all
close all
```

```
% basepath = 'S:\Data\2019\04 April\26\Batman\analyzed o2 data\';
det397 = [20,20,20,40,60,20,20,20,20,20,20,40,60,30];
det866 = [20,0,-20,-20,-20,20,0,-20,20,0,-20,-20,-20,60];
% obe parameters:
p397 = 1.45*ones(length(det397),1);
p866 = 12.85*ones(length(det397),1);
alpha = mod(260-25,90)*2*pi/180*ones(length(det397),1);
% k = [0.6,1.039,3,13,4.28];
k = [0.86,1.8,3,3,5.3];
xdata = [p397,p866,det397',(det866-22)',alpha];
model=pop8model(k,xdata);
ppop = model(:,2)/100;
dpop = model(:,3)/100;
% imageca = [];
% tofca = [];

for ii=1:length(det397)
    if ii>=14
        basepath = 'S:\Data\2019\04 April\30\Batman\analyzed o2 data\';
        scan = [basepath,'blu',num2str(det397(ii)),'red',num2str(det866(ii)),'h
        ↪ ip_scan.h5'];
    elseif ii>=9
        basepath = 'S:\Data\2019\04 April\29\Batman\analyzed o2 data\';
        scan = [basepath,'blu',num2str(det397(ii)),'red',num2str(det866(ii)),'h
        ↪ ip_scan.h5'];
    elseif ii>=6
        basepath = 'S:\Data\2019\04 April\25\Batman\analyzed o2 data\';
        scan = [basepath,'blu',num2str(det397(ii)),'red',num2str(det866(ii)),'_
        ↪ scan.h5'];
    else
        basepath = 'S:\Data\2019\04 April\26\Batman\analyzed o2 data\';
        scan = [basepath,'blu',num2str(det397(ii)),'red',num2str(det866(ii)),'t
        ↪ estrxn_scan.h5'];
    end
    [ratefit,ratefitunc,conc(ii),concunc(ii)] = O2fit(scan,0);
%     conc(ii) = conc(1);
%     concunc(ii) = conc(1);
        % for O2
%     rate(ii) = ratefit(1);
%     rateunc(ii) = ratefitunc(1);
        % for H2O
    rate(ii) = ratefit(2);
    rateunc(ii) = ratefitunc(2);


end
% % for O2
% kfit = rate./conc;
% kfitunc = kfit.*sqrt((rateunc./rate).^2+(concunc./conc).^2);
% for H2O
kfit = rate;
kfitunc = rateunc;

% 2D fit rate constants and propogate uncertainties
[fit2d,gof,output] = fit([ppop,dpop],kfit','poly11',...
    'Weights',1./(kfitunc').^2,'Upper',[0,+Inf,+Inf],'Lower',[0,-Inf,-Inf]);
ci = confint(fit2d,.90);
kunc = (abs(ci(1,:) - ci(2,:))/2)';
k = [fit2d.p00,fit2d.p10,fit2d.p01]';
names = {'S','P','D'};
```

```
T = table(k,kunc,'RowNames',names)


% produce reduced data set
% eqns from wiki on: Reduced chi-squared statistic
ppopred = ppop(1:5);
dpopred = dpop(1:5);
det397red = det397([1:5,14]);
det866red = det866([1:5,14]);
for ii=1:length(ppopred)
    xi = kfit(ppop==ppopred(ii) & dpop==dpopred(ii));
    wi = 1./(kfitunc(ppop==ppopred(ii)&dpop==dpopred(ii))).^2;
    kfitred(ii) = sum(xi.*wi)/sum(wi);
    kfituncred(ii) = sqrt((sum(wi.*xi.^2)*sum(wi)-(sum(xi.*wi))^2)/(sum(wi))^2);
end
ppopred(6) = ppop(14);
dpopred(6) = dpop(14);
kfitred(1,6) = kfit(14);
kfituncred(1,6) = kfitunc(14);

% 2D fit plot
figure()
hold on
colormap('jet')
scatter(ppopred,dpopred,72,kfitred,'filled')
axis([0 1.15*max(ppopred) 0 1.15*max(dpopred)]);
ph = plot(fit2d, 'Style', 'Contour');
set(ph, 'Fill', 'off', 'LineColor', 'auto','LineWidth',2);
grid off;
C = get(ph, 'ContourMatrix');
clabel(C, ph,'FontSize',10);
h = colorbar;
ylabel(h, 'k_{eff} cm^3/s','FontSize',12);
xlabel('P-State Population','FontSize',12);
ylabel('D-state Population','FontSize',12);
```

O2fit.m

```
% O2fit.m

function [kfit,kunc,conc,concunc] = O2fit(scan,zeichen)
% calculate concentration
mix = 0.6;
mixunc = mix*1/55;
[po2,po2unc] = pressuredata(scan);
% po2=1.75e-9;
% po2unc = 1.75e-12;
conc = po2*mix*3.3e16;
concunc = conc.*sqrt((po2unc./po2).^2 +(mixunc./mix).^2);

% read in data from reaction time scan
ions = h5read(scan,'/analysis/ions');
totalions = h5read(scan,'/analysis/totalions');
traptime = h5read(scan,'/analysis/scanvar');

% prepare data for fit
masses = [40,56,57];
Ndata = ions(:,masses);
Tdata = traptime;
```

```
uTdata = unique(Tdata);
% reduce data for plotting
    for jj = 1:length(uTdata)
        sub = Ndata(Tdata == uTdata(jj),:);
        Ndatamean(jj,:) = mean(sub);
        Ndatasem(jj,:) = std(sub)/sqrt(length(sub));
    end
% Time dither and sort for ODE solver
Tdata = Tdata + 0.0001*rand(numel(Tdata),1);
[Tdata,index] = sort(Tdata);
Ndata = Ndata(index,:);

% fit parameters
k0 = [1e-3*ones(1,length(masses)-1),mean(totalions)];
lb = [2*zeros(1,length(masses)-1),mean(totalions)-std(totalions)];
ub = [1*ones(1,length(masses)-1),mean(totalions)+std(totalions)];
opts = optimset('Display','off');
[kfit,~,resid,~,~,~,J] = lsqcurvefit(@O2model,k0,Tdata,Ndata,lb,ub,opts);
kfit = kfit';
ci = nlparci(kfit,resid,'jacobian',J,'alpha',0.10);
kunc = abs(ci(:,1)-ci(:,2))./2;
% rate = kfit(1);
% rateunc = kunc(1);

% build fit lines for plotting
Tfit = min(Tdata):max(Tdata);
Nfit = O2model(kfit,Tfit);

% plot reduced data and fits
if (zeichen)
    figure('Position',[5 5 800 900])
        for ii = 1:length(masses)
            subplot(4,2,ii)
            errorbar(uTdata,Ndatamean(:,ii),Ndatasem(:,ii),'bo')
            hold on
            plot(Tfit,Nfit(:,ii),'r-')
            ylabel('ions')
            title(num2str(masses(ii)))
            hold off
        end
    xlabel('time (s)')
    suptitle(scan)
end
end
```

O2model.m

```
function Nout = O2model(k,t)
% kinetics model that can be passed as a function argument for lsq-fitting
% of data
%   Model:
%       n40(t=0) = N0
%       n40dot = -(k56 + k57)*n40
%       n56dot = k56*n40
%       n57dot = k57*n40
%
%   With:
%       Variables: N(1) = n40
%                  N(2) = n56
```

```
%                   N(3) = n57
%       Parameters k(1) = k56
%                   k(2) = k57
%                   k(3) = N0

N0 = [k(3),0,0];

[~,Nout] = ode45(@DifEq,t,N0);

    function dN = DifEq(t,N)
        Ndot = zeros(length(N0),1);
        Ndot(1) = -(k(1)+k(2))*N(1);
        Ndot(2) = k(1)*N(1);
        Ndot(3) = k(2)*N(1);
        dN = Ndot;
    end

end
```

C.3 TOFMS integrator

When we acquire a raw TOFMS trace, the time axis is rescaled to mass and we can read off the mass-to-charge ratios that were in the trap. To determine the number of ions in each mass channel, the peaks must be binned and integrated. Here is the function that accomplishes this.

h5analysisintegrator.m

```
% h5analysis_integrator.m
% by James Greenberg
% 2019/01/15
% read in scope traces from a data file, integrate ion numbers, and write
% results back to the data file.

function []=h5analysis_integrator(file)

    % read in analysis attributes (integrator settings)
    p1 = h5readatt(file,'/analysis','p1');
    p2 = h5readatt(file,'/analysis','p2');
    masswindow = h5readatt(file,'/analysis','masswindow');
    zoomtracethresh = h5readatt(file,'/analysis','zoomtracethresh');
    minpeakheight = h5readatt(file,'/analysis','minpeakheight');
    nvsperion = h5readatt(file,'/analysis','nvsperion');
    dt = h5readatt(file,'/Oscope/Traces','dt');
    maxmass = h5readatt(file,'/analysis','maxmass');

    % read in traces
    toftrace = h5read(file,'/analysis/toftrace');
    tofzoomtrace = h5read(file,'/analysis/tofzoomtrace');
    toftime = h5read(file,'/analysis/toftime');

    msgid = 'signal:findpeaks:largeMinPeakHeight';
    warning('OFF',msgid);

    masses = 1:maxmass; % index of array corresponds to AMU. only integrate up
    ↪  to mass 140
```

```
    ions = zeros(size(toftime,1),length(masses));
    fwhm = zeros(size(toftime,1),length(masses));
    peaktime = zeros(size(toftime,1),length(masses));
    zoom = zeros(size(toftime,1),length(masses));

    val_min = 6.5e-6;
    val_max = 7.5e-6;

    for jj = 1:size(toftime,1)

        trace = toftrace(jj,:)';
        zoomtrace = tofzoomtrace(jj,:)';
        time = toftime(jj,:)';

        [~,idx_min] = min(abs(time-val_min));
        [~,idx_max] = min(abs(time-val_max));
        [peak,loc] = max(trace(idx_min:idx_max));
        if peak > 0.03
            p2 = sqrt(40)-(time(loc+idx_min)*1e6)*p1;
        end

        for ii = 1:length(masses)

            [~,masswinl] = min(abs(time*1e6 - (sqrt(masses(ii)-masswindow) -
            ↪  p2)/p1));
            [~,masswinr] = min(abs(time*1e6 - (sqrt(masses(ii)+masswindow) -
            ↪  p2)/p1));

            [ions(jj,ii),fwhm(jj,ii),peaktime(jj,ii),zoom(jj,ii)] =
            ↪  h5analysis_traceintegrate(trace(masswinl:masswinr),zoomtrace(ma⌋
            ↪  sswinl:masswinr),dt,zoomtracethresh,minpeakheight,nvsperion);
            peaktime(jj,ii) = peaktime(jj,ii)*dt*1e6 + time(masswinl)*1e6; %
            ↪  converts from relative points to absolute time in micro seconds

        end
    end

    tofmass = (toftime*1e6*p1 + p2).^2;
    h5write(file,'/analysis/tofmass',tofmass);
    h5write(file,'/analysis/ions',ions);
    h5write(file,'/analysis/fwhm',fwhm);
    h5write(file,'/analysis/peaktime',peaktime);
    h5write(file,'/analysis/zoom',zoom);
    h5writeatt(file,'/analysis','analyzed',1);
    h5writeatt(file,'/analysis','p2',p2);


end

function [ions,fwhm,peaktime,zoom] = h5analysis_traceintegrate(trace,zoomtrace,⌋
↪  dt,zoomtracethresh,minpeakheight,nvsperion)

            interpoints = 10;
            peakheight = max(zoomtrace);
            zoom = 1;
            if peakheight < minpeakheight
                ions = 0;
                fwhm = 0;
                peaktime = 0;
```

```
    return
end

if peakheight > zoomtracethresh
    zoom = 0;
    peaktrace = trace;
    trint = interp1(1:length(peaktrace),peaktrace,1:1/interpoints:l
    ↪ ength(peaktrace));
    [peak,center] = max(trint);
    for ii = center:-1:1
        left = ii;
        if trint(ii) < 0.004
            break
        end
    end
    for jj = center:1:length(trint)
        right = jj;
        if trint(jj) < 0.004
            break
        end
    end
    ions = simps(trint(left:right))*dt*1e9/nvsperion/interpoints;
    leftside = trint(1:center);
    rightside = trint(center:length(trint));
    [~,left_FWHM] = min(abs(leftside-peak/2));
    [~,right_FWHM] = min(abs(rightside-peak/2));
    fwhm = (center+right_FWHM-left_FWHM)*dt*1e6/interpoints;
    peaktime = center/interpoints;
else
    peaktrace = zoomtrace;
    smztr = smooth(peaktrace,3);
    [peak,center]=findpeaks(smztr,'MinPeakHeight',minpeakheight);
    if isempty(center)
        [peak,center]=findpeaks(zoomtrace,'MinPeakHeight',minpeakhe
        ↪ ight);
    end
    center = center*interpoints;
    if isempty(center) %|| length(center)>=3
        ions = 0;
        fwhm = 0;
        peaktime = 0;
        return
    end
    trint = interp1(1:length(peaktrace),peaktrace,1:1/interpoints:l
    ↪ ength(peaktrace));
    for ii = center(1):-1:1
        left = ii;
        if trint(ii) < 1e-4
            break
        end
    end
    for jj = center(length(center)):1:length(trint)
        right = jj;
        if trint(jj) < 1e-4
            break
        end
    end
    if left == right
        ions = 0;
        fwhm = 0;
        peaktime = 0;
```

```
                    return
                end
                ions = simps(trint(left:right))*dt*1e9/nvsperion/interpoints;
                [peak,kk] = max(peak);
                center = center(kk);
                leftside = trint(1:center);
                rightside = trint(center:length(trint));
                [~,left_FWHM] = min(abs(leftside-peak/2));
                [~,right_FWHM] = min(abs(rightside-peak/2));
                fwhm = (center+right_FWHM-left_FWHM)*dt*1e6/interpoints;
                peaktime = center/interpoints;
            end


end
```

C.4 Image fitting code

Since the TOFMS detection is destructive, we cannot simultaneously measure the initial number of ions for a given coulomb crystal and the final ions after exposure to a reactant gas. One way around this is to infer the initial number of ions from an image of the crystal taken before exosure to the reactant gas. This procedure is described in Ch. 3 and [38]. Here is the function that turns images into ion numbers.

h5analysisimagefit.m

```
% h5analysis_integrator.m
% by James Greenberg
% 2019/01/15
% read in images from a data file, calculate ion numbers, and write
% results back to the data file.
%modified to subtract dark ions by O. A. Krohn 02/19/2020
function []=h5analysis_imagefit(file)

    % read in analysis attributes (image fit settings)
    theta = h5readatt(file,'/imageanalysis','theta');
    countsthreshold = h5readatt(file,'/imageanalysis','countsthreshold');
    iondensity = h5readatt(file,'/imageanalysis','iondensity');

    % read in image(s)
    imageset = h5info(file,'/Images');

    numimages = numel(imageset.Datasets);
    for ii = 1:numimages
        imagename = ['/Images/',num2str(ii)];
        pic = h5read(file,imagename)';
        pic(pic<countsthreshold) = 0;
        pic = imrotate(pic,theta,'crop');

        vtol = 0.05;
        vert = sum(pic,2);
```

```
        y = (1:512)';
        vertfit = fit(y,vert,'smoothingspline','SmoothingParam',0.001);
        y = 1:0.01:512;
        vthresh = vtol*max(vert);
        vert = abs(vertfit(y)-vthresh);
        [~,vindex] = sort(vert,'ascend');
        majoraxis(ii) = abs(y(vindex(1))-y(vindex(2)))/2;
        y0(ii) = min([y(vindex(1)),y(vindex(2))]) + majoraxis(ii);

        htol = 0.1;
        horz = sum(pic,1)';

        x = (1:512)';
        horzfit = fit(x,horz,'smoothingspline','SmoothingParam',0.001);
        x = 1:0.01:512;
        hthresh = htol*max(horz);
        horz = abs(horzfit(x)-hthresh);
        [~,hindex] = sort(horz,'ascend');
        minoraxis(ii) = abs(x(hindex(1))-x(hindex(2)))/2;

        x0(ii) = min([x(hindex(1)),x(hindex(2))]) + minoraxis(ii);

        [darkpks, locs] = findpeaks(horz);
        [~,locsind] = sort(darkpks,'descend');
        darkradius(ii) = abs(x(locs(locsind(1)))-x(locs(locsind(2))))/2;

    % ellipse fit with no cylinder cut out
    %   imageions(ii) =
     ↪  iondensity*(4*pi*minoraxis(ii).^2.*majoraxis(ii)/3)*(1.6*10^-4)^3;

    %ellipse with a cylinder cut out. Added 02/19/2020
       imageions(ii) = iondensity*(4*pi*minoraxis(ii).^2.*majoraxis(ii)/3-pi*d┘
        ↪  arkradius(ii).^2*2*majoraxis(ii))*(1.6*10^-4)^3;
       darkions(ii) =
        ↪  iondensity*(pi*darkradius(ii).^2*2*majoraxis(ii))*(1.6*10^-4)^3;

    end
end
```